

AR034081.1 PHCF

TECHNICAL DIGEST

1 9 9 5

ULTRAFAST ELECTRONICS AND OPTOELECTRONICS

MARCH 13-15, 1995

DANA POINT, CALIFORNIA

1995 TECHNICAL DIGEST SERIES
VOLUME 13



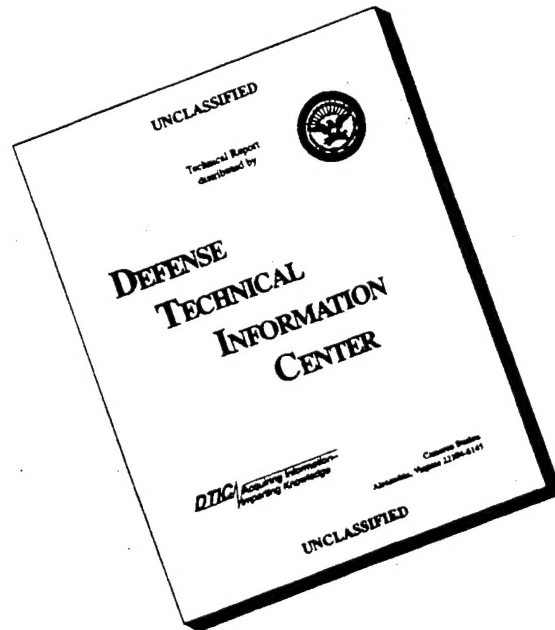
SPONSORED BY
OPTICAL SOCIETY OF AMERICA

DISTRIBUTION STATEMENT A

Approved for public release;
Distribution Unlimited

REPORT DOCUMENTATION PAGE			Form Approved OMB No. 0704-0188	
<small>Public reporting burden for this collection of information is estimated to average 1 hour per response, including the time for reviewing instructions, searching existing data sources, gathering and maintaining the data needed, and completing and reviewing the collection of information. Send comments regarding this burden estimate or any other aspect of this collection of information, including suggestions for reducing this burden, to Washington Headquarters Services, Directorate for Information Operations and Reports, 1215 Jefferson Davis Highway, Suite 1204, Arlington, VA 22202-4302, and to the Office of Management and Budget, Paperwork Reduction Project (0704-0188), Washington, DC 20503.</small>				
1. AGENCY USE ONLY (Leave blank)		2. REPORT DATE Nov 95		3. REPORT TYPE AND DATES COVERED Final 16 Mar 95 - 15 Mar 96
4. TITLE AND SUBTITLE Organization of the 1995 Ultrafast Electronics & Optoelectronics Topical Meeting			5. FUNDING NUMBERS DAAH04-95-1-0182	
6. AUTHOR(S) David W. Hennage (principal investigator)				
7. PERFORMING ORGANIZATION NAME(S) AND ADDRESS(ES) Optical Society of America Washington, DC 20036-2571			8. PERFORMING ORGANIZATION REPORT NUMBER	
9. SPONSORING / MONITORING AGENCY NAME(S) AND ADDRESS(ES) U.S. Army Research Office P.O. Box 12211 Research Triangle Park, NC 27709-2211			10. SPONSORING / MONITORING AGENCY REPORT NUMBER ARO 34081.1-PH-CF	
11. SUPPLEMENTARY NOTES The view, opinions and/or findings contained in this report are those of the author(s) and should not be construed as an official Department of the Army position, policy, or decision, unless so designated by other documentation.				
12a. DISTRIBUTION / AVAILABILITY STATEMENT Approved for public release; distribution unlimited			12b. DISTRIBUTION CODE	
13. ABSTRACT (Maximum 200 words) Summaries of papers presented at the Ultrafast Electronics and Optoelectronics Meeting, March 13-15, 1995, Dana Point, California.				
14. SUBJECT TERMS			15. NUMBER OF PAGES	
			16. PRICE CODE	
17. SECURITY CLASSIFICATION OF REPORT UNCLASSIFIED		18. SECURITY CLASSIFICATION OF THIS PAGE UNCLASSIFIED		19. SECURITY CLASSIFICATION OF ABSTRACT UNCLASSIFIED
				20. LIMITATION OF ABSTRACT UL

DISCLAIMER NOTICE



THIS DOCUMENT IS BEST QUALITY AVAILABLE. THE COPY FURNISHED TO DTIC CONTAINED A SIGNIFICANT NUMBER OF PAGES WHICH DO NOT REPRODUCE LEGIBLY.

CONFERENCE EDITION

*Summaries of the papers
presented at the topical meeting*

ULTRAFAST ELECTRONICS AND OPTOELECTRONICS

March 13–15, 1995, Dana Point, California
1995 Technical Digest Series Volume 13

SPONSORED BY
Optical Society of America



19960209 093

•—————•
COSPONSORED BY
IEEE/Lasers and Electro-Optics Society
IEEE/Electron Devices Society

*The organizers of the Ultrafast Electronics and Optoelectronics
Topical Meeting wish to acknowledge the generous contribution
from the Newport Corporation and Picometrix, Inc.*

Articles in this publication may be cited in other publications. To facilitate access to the original publication source, the following form for the citation is suggested:

Name of Author(s), "Title of Paper," in *Ultrafast Electronics and Optoelectronics*, Vol. 13, 1995
OSA Technical Digest Series (Optical Society of America, Washington DC, 1995), pp. xx-xx.

Optical Society of America

ISBN

Conference Edition	1-55752-397-5
Postconference Edition	1-55752-398-3
(Note: Postconference Edition includes postdeadline papers.)	
1995 Technical Digest Series	1-55752-368-1

Library of Congress Catalog Card Number

Conference Edition	95-67799
Postconference Edition	95-67797

Copyright © 1995, Optical Society of America

Individual readers of this digest and libraries acting for them are permitted to make fair use of the material in it, such as to copy an article for use in teaching or research, without payment of fee, provided that such copies are not sold. Copying for sale is subject to payment of copying fees. The code 1-55752-368-1/95/\$6.00 gives the per-article copying fee for each copy of the article made beyond the free copying permitted under Sections 107 and 108 of the U.S. Copyright Law. The fee should be paid through the Copyright Clearance Center, Inc., 21 Congress Street, Salem, MA 01970.

Permission is granted to quote excerpts from articles in this digest in scientific works with the customary acknowledgment of the source, including the author's name and the name of the digest, page, year, and name of the Society. Reproduction of figures and tables is likewise permitted in other articles and books provided that the same information is printed with them and notification is given to the Optical Society of America. In addition, the Optical Society may require that permission also be obtained from one of the authors. Address inquiries and notices to Director of Publications, Optical Society of America, 2010 Massachusetts Avenue, NW, Washington, DC 20036-1023. In the case of articles whose authors are employees of the United States Government or its contractors or grantees, the Optical Society of America recognizes the right of the United States Government to retain a nonexclusive, royalty free license to use the author's copyrighted article for United States Government purposes.

Printed in the U.S.A.

Contents

Agenda of Sessions	v
UMA High-Speed Devices and Circuits	1
UMB Ultrafast Carrier Dynamics and Transport	13
UMC All-Optical Switching	35
UMD High-Speed Testing	45
UTuA Ultrafast Sources	65
UTuB High-Speed Communication Systems	87
UTuC High-Frequency Electronics: Devices and Applications	97
UTuD Terahertz Dynamics	111
UTuE Poster Session	127
JWA Nanometer Probing	165
JWB Quantum Devices	181
Key to Authors and Presiders	193

**ULTRAFAST ELECTRONICS AND OPTOELECTRONICS
TECHNICAL PROGRAM COMMITTEE**

Umesh Mishra, *Conference Chair, University of California, Santa Barbara*

Martin Nuss, *Program Chair, AT&T Bell Laboratories*

Elliott Brown, *MIT Lincoln Laboratory*

Peter Delfyett, *CREOL*

Gadi Eisenstein, *TECHNION, Israel*

Dan Grischkowsky, *Oklahoma State University*

Erich Ippen, *MIT*

Tadao Ishibashi, *NTT, Japan*

Takeshi Kamiya, *University of Tokyo, Japan*

Ursula Keller, *Federal Institute of Technology, Switzerland*

Brian Kolner, *University of California, Los Angeles*

Heinrich Kurz, *RWTH, Aachen, Germany*

Ted Norris, *University of Michigan*

Yasuo Ohno, *NEC Corporation, Japan*

Mark Rodwell, *University of California, Santa Barbara*

Ran-Hong Yan, *AT&T Bell Laboratories*

**ULTRAFAST ELECTRONICS AND OPTOELECTRONICS
ADVISORY COMMITTEE**

David Bloom, *Stanford University*

Chi Lee, *University of Maryland*

Gerard Mourou, *University of Michigan*

Jagdeep Shah, *AT&T Bell Laboratories*

T.C.L.G. Sollner, *MIT Lincoln Laboratory*

BALLROOMS VI-VIII

8:25 am-8:30 am

Opening Remarks

BALLROOMS VI-VIII

8:30 am-10:00 am

UMA • High-Speed Devices and CircuitsT. C. L. G. Sollner, *Massachusetts Institute of Technology, Presider*

8:30 am (Invited)

UMA1 • Trends in ultrafast optical devices and transmission systems, John E. Bowers, *UC-Santa Barbara*. Recent trends and advances in high speed lasers, modulators, photodetectors, receivers and transmission systems will be highlighted. Electronic limitations to higher bit rate time division multiplexed systems will also be discussed. (p. 2)

9:00 am (Invited)

UMA2 • Diode laser structures for high-speed direct modulation and monolithic multiwavelength transmitter OEICs, J. D. Ralston, *Fraunhofer-Institut für Angewandte Festkörperphysik, Germany*. High-speed ($f_{3dB} > 30$ GHz) low-drive-current ($I_{33GHz} = 65$ mA) InGaAs/GaAs MQW lasers have been developed, along with fabrication processes for monolithic multiwavelength transmitter OEICs. (p. 5)

9:30 am

UMA3 • Submicron Schottky-collector AlAs/InGaAs/InP resonant tunnel diodes, M. Reddy, M. J. Mondry, M. J. W. Rodwell, *UC-Santa Barbara*; S. C. Martin, R. E. Muller, R. P. Smith, *Jet Propulsion Laboratory*; D. H. Chow, J. N. Schulman, *Hughes Research Laboratories*. We report the fabrication, DC, and microwave characteristics of submicron Schottky-collector AlAs/In_{0.53}Ga_{0.47}As/InP resonant tunnel diodes with an estimated maximum frequency of oscillation $f_{max} = 2.2$ THz. (p. 8)

9:45 am

UMA4 • Ultrahigh-speed superconductor digital circuits, V. K. Semenov, *SUNY-Stony Brook*. I will review recent progress in development of rapid single-flux-quantum integrated circuits, capable of operating at frequencies in excess of 100 GHz. (p. 11)

BALLROOM FOYER

10:00 am-10:30 am

Coffee Break

BALLROOMS VI-VIII

10:30 am-12:15 pm

UMB • Ultrafast Carrier Dynamics and TransportHiroyuki Sakaki, *University of Tokyo, Japan, Presider*

10:30 am

UMB1 • Identifying the distinct phases of carrier transport in semiconductors with 10-fs resolution, B.B. Hu, E. A. de Souza, W. H. Knox, J. E. Cunningham, M. C. Nuss, *AT&T Bell Laboratories*. A nonlinear terahertz technique with 10 fs resolution for the first time to our knowledge, resolves the primary transport processes in semiconductors: creation of polarized electron-hole pairs, ballistic transport, and velocity-overshoot. (p. 14)

10:45 am

UMB2 • Coherent charge oscillations in bulk GaAs, Arthur L. Smirl, W. Sha, Shekhar Patkar, *Univ. Iowa*; W. F. Tseng, *NIST-Gaithersburg*. Ballistic transport in bulk GaAs in the presence of a constant built-in field is observed to produce coherent electron-hole charge oscillations on subpicosecond time scales. (p. 17)

11:00 am

UMB3 • How do carrier-carrier interactions in GaAs depend on the carrier distribution? J. A. Kash, *IBM T. J. Watson Research Center*. Carrier-carrier scattering in GaAs is experimentally shown to be several times faster for a hot, nonequilibrium-plasma than for a cooler, thermalized plasma of the same density. (p. 20)

11:15 am

UMB4 • Ultrafast hole tunneling in GaInAs/AlInAs asymmetric double quantum wells, S. Ten, B. P. McGinnis, G. Khitrova, N. Peyghambarian, *Univ. Arizona*; M. F. Krol, M. J. Hayduk, *USAF Rome Laboratory*. We report the first experimental and theoretical evidence to our knowledge of subpicosecond hole tunneling in GaInAs/AlInAs asymmetric double quantum wells. Our experimental results indicate that holes generated with high momentum tunnel faster than the intrasubband relaxation time. These results are consistent with an alloy scattering model of hole tunneling. (p. 23)

11:30 am

UMB5 • Hole relaxation in p-type InGaAs/AlGaAs quantum wells observed by ultrafast mid-infrared spectroscopy, Z. Xu, P. M. Fauchet, G. W. Wicks, *Univ. Rochester*; C. W. Rella, B. A. Richman, H. A. Schwettman, *Stanford Univ.* The hole relaxation time in p-type strained In_{0.5}Ga_{0.5}As/Al_{0.5}Ga_{0.5}As quantum wells is measured by resonant pump-probe transmission experiments performed with a mid-infrared free electron laser. (p. 26)

11:45 am

UMB6 • Time-resolved photocarrier decay for mid-infrared materials with excitation correlation, Alan Kost, Linda West, T. C. Hasenberg, D. H. Chow, *Hughes Research Laboratories*. Excitation correlation is used to time-resolved photocarrier decay for a GaInSb/InAs Type II superlattice with a band gap in the mid-infrared. (p. 29)

12:00 m

UMB7 • Arsenic-ion-implanted GaAs as an ultrafast photoconductor, H. H. Wang, J. F. Whitaker, *Univ. Michigan*; H. Fujioka, *UC-Berkeley*; Z. Liliental-Weber, *Lawrence Berkeley Laboratory*. One-picosecond photoconductive lifetimes with strong bias dependence were measured in semi-insulating, arsenic-implanted GaAs. Arsenic precipitates found in the annealed material invite comparisons to low-temperature-MBE (molecular beam epitaxy) GaAs. (p. 32)

12:15 am-1:30 pm

Lunch Break

BALLROOMS VI-VIII

1:30pm-2:45pm

UMC • All-Optical Switching

Jay M. Wiesenfeld, AT&T Bell Laboratories, Presider

1:30pm (Invited)

UMC1 • All-optical signal processing technology in 100 Gbit/s optical TDM transmission, Masatoshi Saruwatari, NTT Optical Network Systems Laboratories, Japan. Recent advances in all-optical time-domain signal processing technologies are reviewed focusing on their performances and applications to 100 Gbit/s optical TDM transmission. (p. 36)

2:00pm (Invited)

UMC2 • Ultrafast wavelength conversion and switching by four-wave-mixing in semiconductor laser amplifiers, R. Ludwig, W. Pieper, R. Schnabel, H. G. Weber, Heinrich Hertz Institut Berlin, Germany. Experiments based on femtosecond gain-dynamics in SLA are reported: wideband wavelength conversion, fast switching for demultiplexing, and compensation of pulse distortions by optical phase conjugation. (p. 39)

2:30pm

UMC3 • Picosecond all-optical switching of a quantum well etalon using spin-polarization relaxation and electron tunneling, Yuji Nishikawa, Atsushi Tackeuchi, Satoshi Nakamura, Shunichi Muto, Naoki Yokoyama, Fujitsu Laboratories Ltd., Japan. With the use of the spin-polarization relaxation in a quantum well etalon, optical full switching is achieved with a decay time of 7 ps. (p. 42)

BALLROOM FOYER

2:45pm-3:15pm

Refreshment Break

BALLROOMS VI-VIII

3:15pm-5:00pm

UMD, High-Speed Testing

Chi-Hsiang Lee, University of Maryland, Presider

3:15pm (Invited)

UMD1 • Electro-optic testing of ultrafast electronic and optoelectronic devices, Tadao Nagatsuma, NTT LSI Laboratories, Japan. This paper describes the recent development in electro-optic measurement techniques for characterization and diagnosis of ultrafast electronic/optoelectronic devices and their application results. (p. 46)

3:45pm

UMD2 • Electro-optic sampling of picosecond photoresponse of epitaxial $\text{YBa}_2\text{Cu}_3\text{O}_{7-\delta}$ thin films, Frank A. Hegmann, Steven H. Moffat, Robert A. Hughes, John S. Preston, McMaster Univ., Canada; Douglas Jacobs-Perkins, Chia-Chi Wang, Thomas Y. Hsiang, Roman Sobolewski, Univ. Rochester. Photoresponse transients with widths as short as 2 ps are observed for the first time from superconducting $\text{YBa}_2\text{Cu}_3\text{O}_{7-\delta}$ transmission line structures using electro-optic sampling techniques. (p. 49)

4:00pm

UMD3 • Optoelectronic phase tracking and electro-optic sampling of free-running microwave signals up to 20 GHz in a laser-diode-based system, Gong-Ru Lin, Ci-Ling Pan, National Chiao Tung Univ., China; Hsiao-Hua Wu, Tunghai Univ. China. A laser-diode-based system is developed for optoelectronic phase-tracking and sampling of free-running microwave signals up to 20 GHz. (p. 52)

4:15pm

UMD4 • Airbridges for slotline mode suppression in terahertz coplanar waveguide, N. de B. Baynes, M. M. Ahmed, J. R. A. Cleaver, Univ. Cambridge, UK; J. Allam, K. Ogawa, Hitachi Europe Ltd., UK. Airbridges microfabricated using electron beams were shown to suppress slotline modes in coplanar waveguides for bandwidths approaching 1 THz, with minimal parasitic effects on propagating pulses. (p. 55)

4:30pm

UMD5 • First direct observation of single-flux-quantum pulses, Douglas Jacobs-Perkins, Marc Currie, Chia-Chi Wang, Roman Sobolewski, Marc J. Feldman, Thomas Y. Hsiang, Univ. Rochester. A cryogenic, electro-optic sampler provides the first experimental measurement of the temporal evolution of single-flux-quantum voltage pulses having 0.67 mV height and 3.2 ps width. (p. 58)

4:45pm

UMD6 • Optoelectronic characterization of RTDs, T. Nagatsuma, N. Shimizu, T. Waho, M. Shinagawa, NTT LSI Laboratories, Japan. Optoelectronic techniques are described for accurately measuring the switching time of ultrafast resonant tunneling diodes (RTDs). Their application to InGaAs/AlAs RTDs is also presented. (p. 61)

BALLROOMS VI-VIII

5:00pm-6:00pm

Postdeadline Paper Session

6:00pm-7:30pm

Conference Reception

BALLROOMS VI-VIII

8:15am-10:00am

UTuA • Ultrafast SourcesGadi Eisenstein, *Technion Israel Institute of Technology, Israel, Presider*

8:15am (Invited)

UTuA1 • Short-pulse optical power supplies for ultrafast optoelectronics applications, W. H. Knox, *AT&T Bell Laboratories*. We discuss recent developments in compact sources of ultrashort optical pulses and discuss the implications for high-speed and low-speed optoelectronic systems. (p. 66)

8:45am

UTuA2 • Ultrafast semiconductor laser diode seeded Cr:LiSAF regenerative amplifier system, Peter J. Delfyett, S. Grantham, K. Gabel, A. Yusim, S. Gee, M. Richardson, *Univ. Central Florida*; G. Alphonse, J. Connolly, *David Sarnoff Research Center*. An ultrafast semiconductor laser has been used to seed a flashlamp-pumped Cr:LiSAF regenerative amplifier system, producing subpicosecond pulses with millijoule pulse energy. This system has the potential to eliminate argon-pumped-based ultrafast laser systems. (p. 69)

9:00am

UTuA3 • Wavelength division multiplexing with femtosecond pulses, E. A. De Souza, M. C. Nuss, W. H. Knox, D. A. B. Miller, *AT&T Bell Laboratories*. The 3.7-THz spectral bandwidth of a single 85-fs laser source is used to demonstrate 16-channel wavelength division multiplexing with a linear modulator array. (p. 74)

9:15am

UTuA4 • Determination of linear and nonlinear chirp parameters of gain-switched diode laser pulse using short time Fourier transform, H. Takeshita, M. Tsuchiya, T. Kamiya, *Univ. Tokyo, Japan*. We present a novel approach to determine linear and nonlinear chirp parameters using spectrally resolved streak camera images and best fit procedure with short time Fourier transform scheme. (p. 77)

9:30am

UTuA5 • Carrier dynamics of gain-coupled and index-coupled InGaAs/InGaAlAs quantum well DFB lasers, J. Kovac, H. Schmidt, C. Kaden, H. P. Gauggel, V. Hofsäß, J. Kuhn, H. Schweizer, *Univ. Stuttgart, Germany*; A. Hase, H. Künzel, *Heinrich-Hertz-Institut Berlin GmbH, Germany*; H. Hillmer, *Deutsche Bundespost Telekom, Germany*. Dynamics of gain- and index-coupled distributed feedback (DFB) lasers has been investigated. Variation of the laser emission energy by detuning the DFB grating periods yields a change of the modulation pulse widths from 53 to 4.5 ps. (p. 80)

9:45am

UTuA6 • Ultrafast low-temperature-grown-GaAs photomixers, K. A. McIntosh, E. R. Brown, K. B. Nichols, O. B. McMahon, K. M. Molvar, W. F. DiNatale, T. M. Lyszczarz, *MIT Lincoln Laboratory*. Abstract not available. (p. 83)

BALLROOMS IV-V

10:00am-10:30am

Coffee Break

BALLROOMS VI-VIII

10:30am-12:00m

UTuB • High-Speed Communication SystemsJohn E. Bowers, *University of California-Santa Barbara, Presider*

10:30am (Invited)

UTuB1 • Fast SiGe-heterobipolar transistors for communication systems, Andreas Schüppen, *Daimler Benz AG, Germany*. SiGe-HBTs were investigated with respect to wireless communication systems. f_T and f_{max} values of 116 GHz and 120 GHz, respectively, and a noise figure of 0.9 dB with 6dB associated gain at 10 GHz were obtained. (p. 88)

11:00am (Invited)

UTuB2 • 20 Gbit/s optical transmission systems with monolithic IC technologies, Tetsuyuki Suzuki, *NEC Corp., Japan*. Si-ICs with SiGe-base, and AlGaAs/GaAs-HBT ICs with hetero guard-ring structure have been developed for 20-Gbit/s optical transmission systems. A fully-regenerating 20-Gbit/s optical repeater with the ICs have been successfully demonstrated. (p. 91)

11:30am (Invited)

UTuB3 • Diode multiplexer/demultiplexer ICs for 100 Gbit/s fiber-optic transmission, R. Pulella, U. Bhattacharya, S. T. Allen, M. J. W. Rodwell, *UC-Santa Barbara*. We report diode integrated circuits for multiplexing and demultiplexing at 100 Gbit/s. The ICs consist of an array of four sample-and-hold gates driven by nonlinear-transmission-line (NLTL) strobe generators. Initial measurements with 104 Gbit/s operation are demonstrated. (p. 94)

12:00m-1:30pm

Lunch Break

BALLROOMS VI-VIII

1:30pm-3:15pm

UTuC • High-Frequency Electronics: Devices and ApplicationsLoi Nguyen, *Hughes Research Laboratories, Presider*

1:30pm (Invited)

UTuC1 • Device and system technologies for microwave wireless applications, Y. K. Chen, R. Hamm, D. Humphrey, R. Kopf, J. Kuo, J. Lin, J. Lothian, R. Malik, F. Ren, R. Ryan, A. Tate, J. Weiner, D. Sivco, A. Cho, *AT&T Bell Laboratories*. In the past decade, the improvement in the integration level and production yield of the III-V devices and ICs has bred a new generation of front-end MMICs and baseband signal processing ICs for high-speed multimedia transmission. The impact of these high speed devices on the high-speed microwave communication link is addressed. (p. 98)

2:00pm (Invited)

UTuC2 • Opportunities of Si USLI Technology for GH applications, Jack Y.-C. Sun, *IBM Research Division and Microelectronics Division*. The opportunities and challenges of Si-based ULSI technologies for high-speed low-power data processing and wireless communication applications will be addressed with special emphasis on bulk Si, SOI, and SiGe CMOS and bipolar devices. (p. 99)

2:30pm

UTuC3 • Schottky-collector heterojunction bipolar transistors: device scaling laws for f_{\max} beyond 500 GHz, U. Bhattacharya, M. J. Mondry, G. Hurtz, I. Tan, R. Pullela, M. Reddy, J. Guthrie, M. J. W. Rodwell, J. E. Bowers, *UC-Santa Barbara*. We propose the Schottky-collector heterojunction bipolar transistor. By scaling to submicron dimensions, f_{\max} should exceed 500 GHz. (p. 102)

2:45pm

UTuC4 • Monolithic integration of low-temperature-grown GaAs and high-mobility 2DEG for ultrafast photonic circuits, J. Allam, K. Ogawa, A. P. Heberle, *Hitachi Cambridge Laboratory, UK*; N. de B. Baynes, J. R. A. Cleaver, *Univ. Cambridge, UK*; T. Mishima, I. Ohbu, *Hitachi Ltd., Japan*. A two-dimensional electron gas (2DEG) with high mobility was grown on a low-temperature GaAs layer with ≈ 0.5 ps carrier lifetime, for ultrafast photonic circuit applications. (p. 105)

3:00pm

UTuC5 • Manufacturable 200-GHz, low noise $P^+ \text{-GaInAs/N-AlInAs/GaInAs}$ JHEMT technology, J. B. Shealy, U. K. Mishra, *UC-Santa Barbara*; T. Y. Liu, M. A. Thompson, L. D. Nguyen, *Hughes Research Laboratories*. High-frequency, low-noise junction-modulated high-electron-mobility transistor (HEMT) technology is demonstrated with uniform threshold voltage characteristics. Submicrometer gatelength devices yielded high gain and state-of-the-art noise performance. (p. 108)

BALLROOMS IV-V

3:15pm-3:45pm

Refreshment Break (Poster Preview)

BALLROOMS VI-VIII

3:45pm-5:30pm

UTuD • Terahertz DynamicsDan Grischkowsky, *Oklahoma State University, Presider*

3:45pm (Invited)

UTuD1 • Probing terahertz dynamics in semiconductor nanostructures with the UCSB free-electron lasers, S. James Allen, *UC-Santa Barbara*. Terahertz relaxation in resonant tunneling diodes and photon assisted tunneling in multi-quantum well superlattices are explored with the UCSB free-electron lasers. (p. 112)

4:15pm (Invited)

UTuD2 • Bloch oscillations in GaAs/AlGaAs superlattices following excitation of continuum states: physics and application perspectives, H. G. Roskos, C. Waschke, P. Leisching, H. Kurz, *Rheinisch-Westfälische Technische Hochschule (RWTH) Aachen, Germany*; K. Köhler, *Fraunhofer-Institut für Angewandte Festkörperphysik, Germany*. Terahertz emission by Bloch oscillations following optical excitation of continuum states suggests conservation of intraband-phase coherence during scattering. Implications for the realization of superradiant emitters are discussed. (p. 115)

4:45pm

UTuD3 • Terahertz spectroscopy of a mesoscopic tunnel barrier, C. Karadi, S. Jauhar, L. P. Kouwenhoven, K. Wald, J. Orenstein, P. L. McEuen, *UC-Berkeley*; Y. Nagamune, J. Motohisa, H. Sakaki, *Univ. Tokyo, Japan*. We report measurements of the induced current across a mesoscopic tunnel barrier by terahertz pulses as a function of frequency, barrier height, and magnetic field. (p. 118)

5:00pm

UTuD4 • Micromachined three-dimensional photonic bandgap crystals, E. Özbay, G. Tuttle, *Iowa State Univ.* Using micromachined silicon and alumina wafers, we have fabricated and tested three-dimensional photonic bandgap crystals and defect structures at millimeter-wave frequencies. (p. 121)

5:15pm

UTuD5 • Measurement and analysis of THz radiation from bulk semiconductors, L. Ming, G. A. Wagoner, X.-C. Zhang, *Rensselaer Polytechnic Institute*; M. Alexander, *USAF Rome Laboratory*. Both the amplitude and phase of forward and backward THz radiation have been measured and calculated for the optically generated electrical transient parallel and perpendicular to the semiconductor surface. (p. 124)

BALLROOMS IV-V

5:30pm-6:30pm

UTuE • Poster Session

UTuE1 • Electro-optic probes: high-permittivity crystals vs. low-permittivity polymers, H.-J. Cheng, J. F. Whitaker, K. H. Herrick, N. Dib, L. P. B. Katehi, *Univ. Michigan*; J.-L. Coutaz, *Univ. Savoie, France*. We investigate through experiments and simulations the drawbacks of high-permittivity LiTaO_3 electro-optic probes and the potential benefits of low-permittivity electro-optic-polymer probes. (p. 128)

UTuE2 • Picosecond pulse generation by edge illumination of Si and InP photoconductive switches, Marc Currie, Chia-Chi Wang, Roman Sobolewski, Thomas Y. Hsiang, *Univ. Rochester*. We demonstrate edge illumination as a material-independent, pulse-generation method, producing 1.1-ps pulses on silicon and 0.55-ps pulses on indium phosphide. (p. 131)

UTuE3 • Paper withdrawn.

UTuE4 • Impact ionization in wide-band-gap materials under high-field, D. Du, X. Liu, J. Squier, G. Mourou, *Univ. Michigan*. The impact ionization parameters of SiO_2 and MgF_2 have been measured up to 280 MV/cm, for the first time to our knowledge, by utilizing femtosecond laser pulses. (p. 135)

UTuE5 • Step function photoconductive signal generation in integrated coplanar test fixtures, A. Zeng, M. K. Jackson, *Univ. British Columbia, Canada*; M. Van Hove, W. De Raedt, *Interuniversity Microelectronics Center, Belgium*. Measurement of photoconductive generation in monolithically integrated test fixtures shows that the step-like response is determined by rapid field screening followed by slower charge collection. (p. 138)

UTuE6 • Ultrafast carrier relaxation in semi-insulating GaAs implanted with arsenic ions (GaAs:As), Gong-Ru Lin, Feruz Ganikhanov, Wen-Chung Chen, C.-S. Chang, Ci-Ling Pan, *National Chiao Tung Univ., China*. The carrier relaxation dynamics of semi-insulating GaAs substrates implanted with arsenic ions of different dosages between 10^{13} and 10^{16} ions \cdot cm $^{-2}$ have been investigated. Carrier lifetime as short as 160 fs was observed. (p. 141)

UTuE7 • All-silicon, ultrafast, integrable optoelectronic interface, Chia-Chi Wang, Marc Currie, Thomas Y. Hsiang, *Univ. Rochester*. An all-silicon, ultrafast, integrable optoelectronic interface is proposed. The operational speed is expected to be 60 Gbit/s. (p. 144)

UTuE8 • Fast vertical silicon photodetectors with buried CoSi $_2$ contact, H. G. Roskos, J. P. Hermanns, E. Stein von Kamienski, H. Kurz, *Rheinisch-Westfälische Technische Hochschule (RWTH) Aachen, Germany*; F. Rüders, O. Hollricher, C. Buchal, S. Mantl, *Forschungszentrum Jülich, Germany*. We report on realization and characterization of ultrafast vertical Si photodiodes with buried CoSi $_2$ electrode. (p. 147)

UTuE9 • Diffraction effects in spatial and spectral properties of THz radiation from bulk GaAs excited by ultrashort pulses, N. Sarukura, Z. Liu, Y. Segawa, *The Institute of Physical and Chemical Research (RIKEN), Japan*; S. Koshihara, *Tokyo Institute of Technology, Japan*; K. Shimoyama, Y. Kondo, Y. Shibata, T. Takahashi, S. Hasebe, M. Ikezawa, *Tohoku Univ., Japan*. Diffraction effects are observed in the spectral shape and beam divergence of THz radiation from GaAs excited by ultrashort pulses with different spot sizes. (p. 150)

UTuE10 • Ultrafast characterization of parasitics in in-plane-gate field-effect transistors, K. Ogawa, J. Allam, J. J. Baumberg, *Hitachi Europe Ltd. UK*; N. de B. Baynes J. R. A. Cleaver, *Univ. Cambridge, UK*; T. Mishima, I. Ohbu, *Hitachi Ltd., Japan*. The parasitic gate-drain capacitance of in-plane-gate field-effect transistors was measured by ultrafast electrooptic sampling of displacement currents induced in the drain. (p. 153)

UTuE11 • Picosecond photoconductive sampling with nanosecond carrier lifetimes using an integrated inductive loop, Andrew C. Davidson, Frank W. Wise, Richard C. Compton, *Cornell Univ.* By electromagnetically coupling the time derivative of a signal to a separate circuit, photoconductive sampling with picosecond resolution is demonstrated on long-lifetime material. (p. 156)

UTuE12 • Measurement of intensity-modulated signal generated by a two-wavelength laser diode array up to 7 THz, Ci-Ling Pan, Chi-Luen Wang, *National Chiao Tung Univ., China*. We report detection of modulation signal on an optical carrier up to 7 THz, generated by a novel dual-wavelength grating-loaded laser diode array. (p. 159)

UTuE13 • Dependence of large signal response on the transverse mode structure in vertical-cavity lasers, H. Deng, K. L. Huffaker, J. Shin, D. G. Deppe, *Univ. Texas at Austin*. An interdependence between the temporal response and the transverse mode structure of vertical-cavity surface-emitting lasers is experimentally demonstrated. (p. 162)

BALLROOMS VI-VIII

8:30am-10:00am

JWA • Nanometer ProbingGerard A. Mourou, *University of Michigan, Presider*

8:30am (Invited)

JWA1 • Applications of scanning force microscopy for voltage measurements with high spatial and temporal resolutions, Francis Ho, A. Samson Hou, Bettina A. Nechay, David M. Bloom, *Stanford Univ.* We report on scanning force microscopy measurements with picosecond, and potentially sub-picosecond, temporal resolution by utilizing nonlinear tip-to-sample interactions. (p. 166)

9:00am

JWA2 • Ultrafast near-field optical probing, Jason B. Stark, Richart E. Slusher, *AT&T Bell Laboratories*; Umar Mohideen, *UC-Riverside*. We use broadband pulses to image the carrier dynamics of semiconductor microstructures on a submicron spatial scale, with a time resolution of 60 fs. (p. 169)

9:15am

JWA3 • Laser-diode-based scanning force microscope and ultrafast sampling probe, John Nees, Douglas Craig, *Univ. Michigan*; Soichi Hama, Shinichi Wakana, *Fujitsu Laboratories Ltd., Japan*. A laser diode is used to sample waveforms on high-speed devices using a highly sensitive photoconductive gate integrated into a scanning force microscope probe. (p. 172)

9:30am

JWA4 • STOE: scanning tunneling optoelectronic microscope, Koichiro Takeuchi, Akira Mizuhara, *Teratec Corp., Japan*. An STM was applied to high-speed sampling measurement using a special probe with a 1.8-ps photoconductive semiconductor switch made of low-temperature GaAs. (p. 175)

9:45am

JWA5 • High-frequency on-wafer testing with freely positionable silicon-on-sapphire photoconductive probes, T. Pfeifer, H.-M. Heiliger, H. G. Roskos, H. Kurz, *Rheinisch-Westfälische Technische Hochschule (RWTH) Aachen, Germany*. Freely positionable photoconductive probes based on silicon-on-sapphire are characterized as both generators and detectors of picosecond electric transients. (p. 178)

BALLROOMS IV-V

10:00am-10:30am

Coffee Break

BALLROOMS VI-VIII

10:30am-12:00m

JWB • Quantum DevicesJürgen Köhl, *Max Planck Institute, Germany, Presider*

10:30am (Invited)

JWB1 • Ultrafast all-optical switch with switch-off time unlimited by carrier lifetime, K. Tajima, S. Nakamura, *NEC Corp., Japan*. Experimental results are presented on a modified Mach-Zehnder type all-optical switch. Faster than 8 ps full-switching has been achieved and 1 ps switching at a very high repetition rate is theoretically predicted. (p. 182)

11:00am (Invited)

JWB2 • Quantum cascade lasers, F. Capasso, J. Faist, *AT&T Bell Laboratories*. Quantum cascade lasers based on diagonal and vertical intersubband transitions are discussed. Pulsed operation at 100 K with $J_h = 3 \text{ kA/cm}^2$, 60 mW peak power and a slope efficiency of 300 mW/A has been achieved. (p. 184)

11:30am

JWB3 • Scaling of Stark-shifted nonlinearities in MQW structures, A. N. Cartwright, X. R. Huang, Arthur L. Smirl, *Univ. Iowa*. Simple rules of scaling the per-carrier nonlinearity in Stark-shifted systems with well number, electric field, amplitude and width of the excitonic transition are demonstrated by measuring this quantity as a function of temperature, bias, and materials system for several multiple quantum well (MQW) structures. (p. 187)

11:45am

JWB4 • Dynamic Wannier-Stark effect and superradiance switching in semiconductor superlattices, J. B. Khurgin, S.-J. Lee, *Johns Hopkins Univ.*; N. M. Lawandy, *Brown Univ.* Two novel effects associated with transition from localized to extended states in semiconductor superlattices are introduced. Possible applications in the light sources and detectors are considered. (p. 190)

BALLROOMS VI-VIII

12:00m-12:10pm

UEO Closing Remarks and QOE Opening Remarks

Monday, March 13, 1995

High-Speed Devices and Circuits

UMA 8:30 am-10:00 am
Ballrooms VI-VIII

T.C.L.G. Sollner, *Presider*
Massachusetts Institute of Technology

Trends in Ultra fast Optoelectronics

Radhakrishnan Nagarajan and John E. Bowers

Department of Electrical and Computer Engineering

University of California, Santa Barbara, CA 93106. Tel: (805) 893 3918

The highest aggregate data transmission rate in optical fiber communication systems is rapidly approaching 200 GBit/s [1]. It was not too long ago when a 2.5 GBit/s system was considered to be novel. There are number of reasons for this rapid advance. One is the maturity of the optical processing elements based on the ultrafast fiber and semiconductor nonlinearities, second is the Erbium doped fiber amplifier technology, and third is the advancements in the high speed optoelectronic components. Here, we will review recent advances in this area.

Ultra high speed data transmission systems come in many varieties. First is the conventional electronic time division multiplexing (ETDM) where the high speed data stream is assembled electronically and then modulated onto an optical carrier either by directly driving a high speed laser or using an external modulator. Directly modulated laser data links operating at speeds up to 20 GBit/s have been demonstrated [2]. The second favored method is the wavelength division multiplexing (WDM) where optical carriers at several wavelengths are used to carry high speed data. Each wavelength channel has an individual laser transmitter. Although each transmitter may not have to be fast, aggregate rates of up to 160 GBit/s have been demonstrated using 8 wavelength channels each operating at 20 GBit/s [1]. The third method that has been successfully exploited in recent days is the use of optical time division multiplexing (OTDM), where the optical carrier (usually pulsed laser sources) are first modulated with data and subsequently multiplexed by delaying and summing the various data streams with respect to one another. These data streams can be optically demultiplexed and the high speed clock recovery can also be done optically. OTDM links operating at 100 GBit/s [3] have been demonstrated and multiplexers and demultiplexers up to 160 GBit/s [4]. Recent measurements of pulse jitter indicate that OTDM is possible to 1 TBit/s with 10^{-9} BER [5]. Both WDM and OTDM do not have to have very high speed optoelectronic components for their implementation while the ETDM relies heavily on the advancements in this area for its implementation. Lets examine the current level of maturity of these components.

Semiconductor Lasers and Modulators

High speed lasers and modulators are the basic components required to generate the optical data stream. The fastest lasers have -3 dB modulation bandwidth of about 33 GHz and the fastest modulators about 44 GHz. The modulators also have the advantage of generating low distortion optical pulses with minimum chirp. Their main disadvantages are high insertion loss (≈ 6 dB)

and large drive voltages (≈ 10 V) required at very high speeds. The high speed lasers have an advantage in this respect that they can be efficiently modulated at low drive currents (≈ 50 mA).

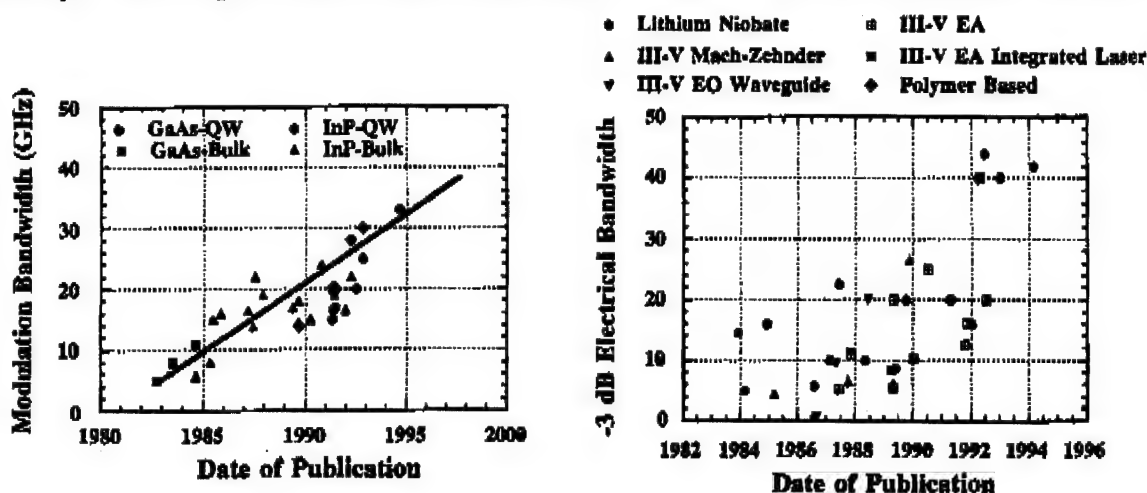


Fig. 1 The trend in bandwidth of directly modulated lasers and external modulators with year of publication.

Even higher bit rates in the modulator can be achieved for by using pulsed laser sources. These systems tend to be of the return-to-zero type optical format [3].

Photodetectors

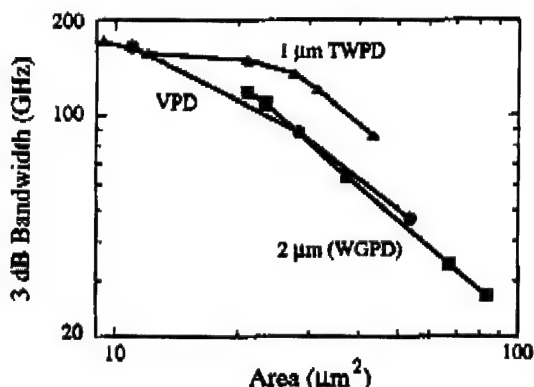


Fig. 2. 3-dB electrical bandwidths of various size in-plane and vertically-illuminated photodetectors from the same wafer.

The other requirement for ultrafast links is the high speed photodetector. The largest bandwidth reported in photodetectors for use at 1.55 μm wavelength is 110 GHz [6,7]. The largest modulation bandwidth reported in any p-i-n type photodetector is 172 GHz with an external quantum efficiency of 42% (Fig. 2). This device uses a traveling wave structure to separately optimize the speed of operation and responsivity [8]. Using p-i-n photodetectors and traveling wave amplifiers, optical receivers with 30 GHz bandwidth have been demonstrated [10].

Demultiplexers and Clock Recovery Circuits

At the receiver the high speed optical data has to be converted to some manageable low speed electronic form for further processing and use (at least for the time being!). For these one needs some form of demultiplexing the data and also clock recovery for data retiming and extraction. These functions used to be the domain of electronic components but at increasingly

increasingly higher speeds these are being done by optical nonlinear elements [10,11]. Electronics components based on the nonlinear shock line technology for use at these high bit rates are also underway [12].

Summary

Lets look at the requirements for a 160 GBit/s optical communication link and see what technologies are present and what needs to be developed.

Requirements	Status
Optical Pulsewidths < 2 ps	●
Optical Soliton Peak Power > 500 mW	●
Data Multiplexing - Optical	●
- Electronic	●
Direct Modulation	○
External Modulators - Bandwidth \approx 160 GHz	●
- Low Drive Voltages \approx 10 V	●/○
Modulator Driver Circuits - Risettime \approx 5 ps	●
- Voltage Swing \approx 10V	●
Optical Amplifiers	●
Photodetectors - Bandwidth > 80 GHz	●
Front End Amplifiers - 0.5 GHz < BW < 80 GHz	●
Data Demultiplexing - Optical	●
- Electronic	●
Clock Recovery - Optical	●
- Electronic	●
Fiber Dispersion Management	●

● - Possible or Has been demonstrated ● - Maybe ○ - Not Possible

This work was funded by DARPA, Rome Laboratories (Hanscom AFB).

References

1. A. H. Gnauck, et al., *Electronics Letters* 30(15), 1241 (Jul 1994).
2. D. Mathoorasing, et al., *Electronics Letters* 30(6), 507 (Mar 1994).
3. S. Kawanishi, et al., *Electronics Letters* 29(12), 1075 (Jun 1993).
4. K. Suzuki, et al., *Electronics Letters* 30(18), 1501 (Sep 1994).
5. P. Blixt, and J. E. Bowers, *IEEE Photonics Technology Letters*, to be published (Jan. 1995).
6. Y. G. Wey, et al., *IEEE Photon. Technol. Lett.* 5, 1310 (1993).
7. K. Kato, et al., *IEEE Photon. Technol. Lett.* 6(6), 719 (Jun. 1994).
8. K. S. Giboney, et al., *52nd Annual Device Research Conf.*, paper VIA-9 (Jun. 1994).
9. A. K. Peterson, et al., *Conference on Optical Fiber Communication (OFC) '95*.
10. R. J. Manning et al., *Electronics Letters* 30(10), 787 (May 1994).
11. I. Glesk, et al., *Electronics Letters* 30, 339 and 917 (May 1994).
12. Refer to R. Pallela, et al., invited paper at this Conference (1995).

Diode Laser Structures for High-Speed Direct Modulation and Monolithic Multi-Wavelength Transmitter OEIC's

J.D. Ralston*, S. Bürkner, W. Bronner, J. Hornung, S. Weisser,

E.C. Larkins, R.E. Sah, J. Rosenzweig, and J. Fleissner,

Fraunhofer-Institut für Angewandte Festkörperphysik, Tullastrasse 72,

D-79108 Freiburg, Germany

Tel. (+49) 761-5159-340 FAX (+49) 761-5159-400

*Present Address: SDL, Inc., 80 Rose Orchard Way, San Jose, CA 95134-1365

Tel. 408-943-9411 FAX 408-943-1070

The successful application of direct laser modulation for very-high-speed digital transmission or microwave/millimeter-wave analog optical links requires: reductions in the drive currents required to achieve high modulation bandwidths, increases in the maximum intrinsic modulation bandwidths, reductions in laser chirp under high-speed direct modulation, and high-speed laser structures which can be monolithically integrated with high-speed transistors. Due to the maturity of GaAs transistor and circuit fabrication technologies, we have pursued the development of GaAs-based MQW lasers which address all of the above requirements. In addition, we have demonstrated the feasibility of utilizing the impurity-free interdiffusion (IFID) process to fabricate multi-wavelength, high-speed, pseudomorphic laser arrays; such components promise substantial increases in both single-fiber transmission capacity and network flexibility via wavelength division multiplexing (WDM).

By adding both p-doping and/or strained $\text{In}_{0.35}\text{Ga}_{0.65}\text{As}/\text{GaAs}$ MQW's in the laser active region [1], we have achieved both very efficient high-speed direct modulation ($f_{3\text{dB}}=24$ GHz at a DC bias current of only 25 mA) and, as shown in Fig. 1, a record direct modulation bandwidth of 33 GHz [2] at a wavelength of $\sim 1.09 \mu\text{m}$. In addition, the strained p-doped lasers show a factor of 2 reduction in the linewidth enhancement factor, α , compared with that of unstrained, undoped GaAs/AlGaAs MQW lasers [3]. These modifications are expected to lead to reduced chirp under high-speed direct modulation. The above devices utilize a vertically-compact epilayer design [1] embedded in a dry-etched, short-cavity, coplanar ridge-waveguide (RWG) structure [2], as shown in Fig. 2. The laser mirrors are etched using a $\text{Cl}_2 + \text{BCl}_3$ chemically-assisted ion-beam etching (CAIBE) process [4] which relaxes several constraints previously reported in the dry-etching of $\text{Al}_x\text{Ga}_{1-x}\text{As}$ -containing optoelectronic device structures.

This laser design has been further incorporated into a complete technological process for the monolithic integration [5,6] of GaAs MQW lasers and HEMT-based laser-driver circuits capable of operation at data rates up to 20 Gb/s [7]. Fig. 3 shows the high-speed ridge-waveguide laser geometry used in the monolithic transmitter

OEIC's, with a side-feed, air-bridged coplanar contact geometry and CAIBE-etched mirrors. Fig. 4 shows a chip photograph of a monolithic 10-element linear array of independently addressable GaAs/AlGaAs MQW lasers and driver circuits.

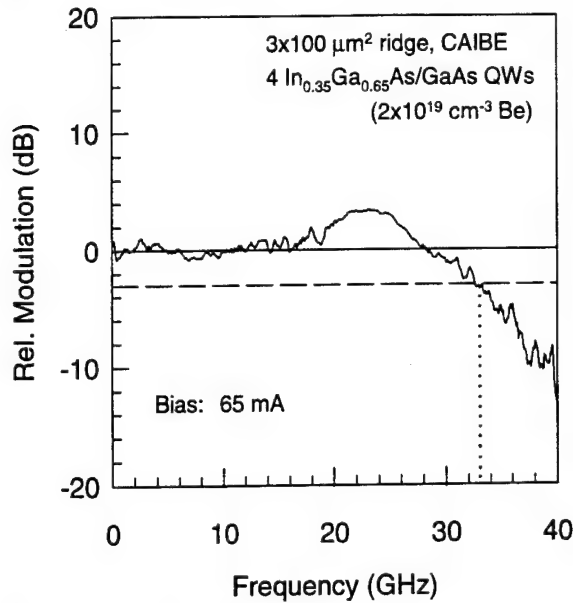


Fig. 1 33 GHz direct modulation of short-cavity InGaAs/GaAs MQW laser.

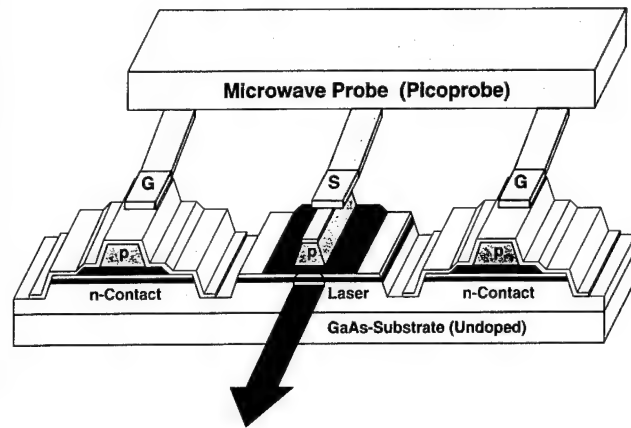


Fig. 2 Schematic layout of coplanar, triple-mesa, ridge-waveguide laser geometry used for high-speed direct modulation measurements.

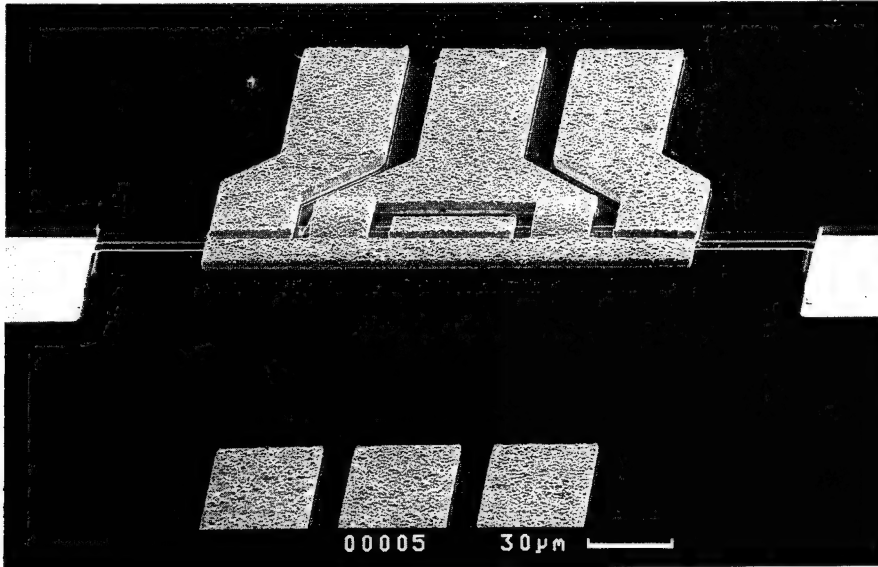


Fig. 3 Electron micrograph showing high-speed ridge-waveguide laser geometry utilized for laser/HEMT integration in monolithic transmitter OEIC's.

Finally, using the IFID process, wavelength shifts of at least 32 nm (34 meV) have been achieved *with no strain relaxation* and while maintaining the high-speed modulation properties of the pseudomorphic InGaAs/GaAs MQW lasers [8]. Fig. 5 compares the lasing wavelengths of as-grown and partially-interdiffused devices fabricated from the same epitaxial wafer, containing 4 undoped $\text{In}_{0.35}\text{Ga}_{0.65}\text{As}/\text{GaAs}$ MQW's in the active region. As shown in Fig. 6, the wavelength-shifted devices achieve $f_{3\text{dB}} = 26$ GHz at a DC bias of only 50 mA.

The above fabrication processes, device structures, and integration schemes provide the technological foundation for monolithic, multi-wavelength, GaAs-based

transmitter OEIC's in which each element is capable of low-bias-current direct modulation at bandwidths exceeding 20 GHz.

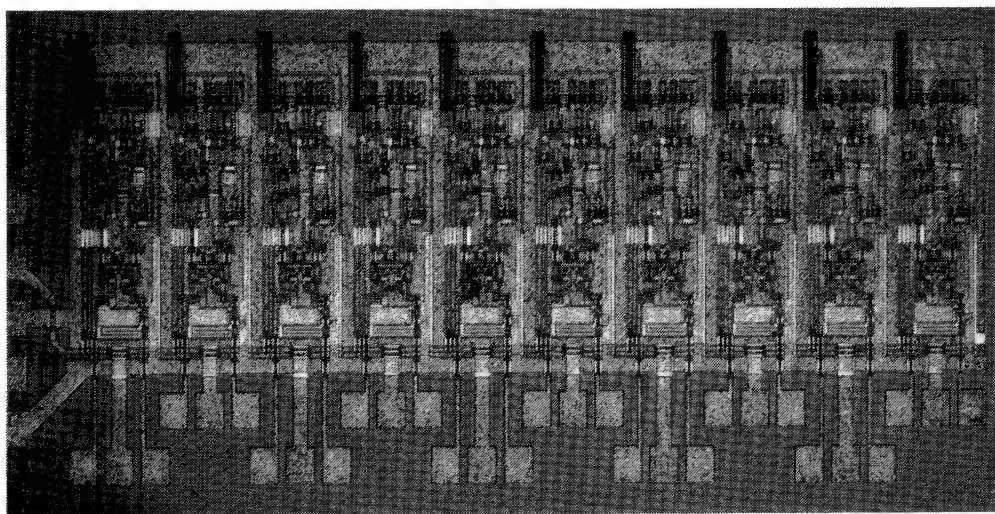


Fig. 4 Monolithic transmitter OEIC containing a linear array of 10 GaAs MQW lasers and HEMT driver circuits.

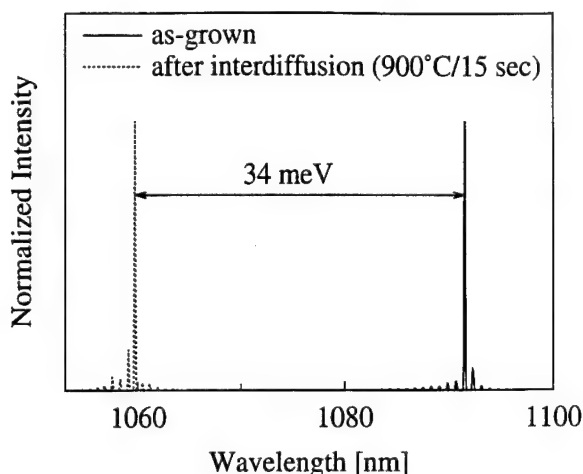


Fig. 5 Lasing spectra of as-grown and partially-interdiffused InGaAs/GaAs MQW lasers fabricated from the same epitaxial wafer.

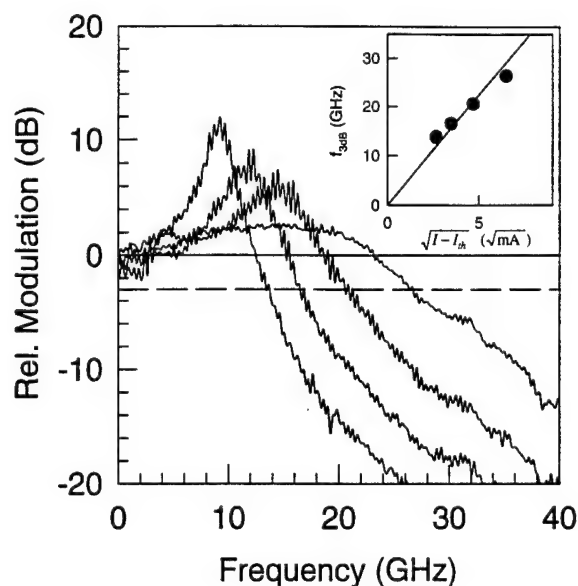


Fig. 6 Direct modulation response of wavelength-shifted $3 \times 100 \mu\text{m}^2$ InGaAs/GaAs ridge-waveguide laser at DC bias currents of 15, 20, 30 and 50 mA.

- [1] J.D. Ralston et al, *IEEE J. Quantum Electron.* **29**, 1648-1659 (1993).
- [2] J.D. Ralston et al, *IEEE Photon. Technol. Lett.* **6**, 1076-1079 (1994).
- [3] A. Schönfelder et al, *IEEE Photon. Technol. Lett.* **6**, 891-893 (1994).
- [4] J.D. Ralston et al, *III-V's Review* **7**, 51-55 (1994).
- [5] J. Hornung et al, *Electron. Lett.* **29**, 1694-1696 (1993).
- [6] J.D. Ralston et al, *1994 CLEO Technical Digest*, 275-276 (1994).
- [7] Z.-G. Wang et al, *IEEE J. Sol. State. Circuits* **28**, 829-834 (1993).
- [8] S. Bürkner et al, submitted for publication.

Submicron Schottky-Collector AlAs/InGaAs/InP Resonant Tunnel Diodes

M. Reddy*, M.J. Mondry*, S.C. Martin†, R.E. Muller†,
R.P. Smith†, M.J.W. Rodwell*, D.H. Chow‡ and J.N. Schulman ‡

Introduction

Resonant tunnel diodes (RTD) are currently the widest bandwidth semiconductor devices [1, 2], useful for high frequency oscillators and picosecond pulse generators. 712GHz oscillators [2] and 1.7ps pulse generators [3] fabricated with $\sim 1.0THz$ bandwidth InAs/AlSb RTDs, are some examples of high speed RTD applications. Here, we report the fabrication, DC, and microwave characteristics of AlAs/In_{0.53}Ga_{0.47}As/InP Schottky-collector resonant tunnel diodes (SRTDs) with deep submicron Schottky collectors and an estimated maximum frequency of oscillation $f_{max} = 2.2THz$. Monolithic integration of several SRTDs into sub-millimeter wave quasi optical oscillator arrays and for traveling wave deep sub-picosecond pulse generators is feasible with this device technology.

Schottky-Collector RTDs

RTD bandwidths are currently limited by parasitic resistance from the ohmic contacts. In Schottky-collector RTDs, the ohmic-contacted collector of a conventional RTD is replaced with a direct Schottky contact to the space-charge layer (Fig. 1a,b), eliminating the top contact series resistance [4]. The remaining series resistance components are minimized by scaling the Schottky-collector to deep submicron dimensions. This reduced series resistance leads to an increased maximum frequency of oscillation, f_{max} . 0.1 μm AlAs/GaAs SRTD's have

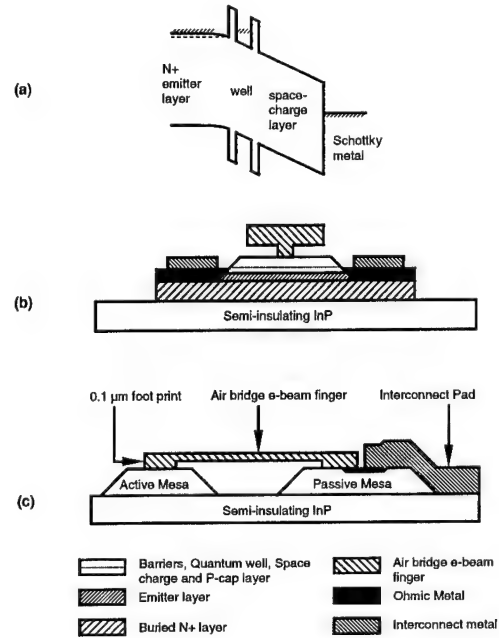


Figure 1: (a) Band diagram, (b) and (c) Perpendicular cross sections of a submicron SRTD

been fabricated with an estimated $f_{max} = 900GHz$ [5]. AlAs/In_{0.53}Ga_{0.47}As/InP SRTDs should yield further increases in f_{max} owing to the superior material properties of this system [6].

RTD electrical characteristics when biased in the negative-differential-resistance (NDR) region [1] are represented by the parasitic series resistance, R_s , the space charge layer capacitance, C , the negative resistance, R_n , and a quantum well inductance, L_{qw} (inset of Fig.2). $L_{qw} = -\tau_{qw}R_n$ (negative in the NDR region), where τ_{qw} is the electron lifetime in the quantum well. $f_{max} = \omega_{max}/2\pi$, is the frequency at which the network's admittance, $Y(\omega)$ has a zero real component. Inclusive of the quantum well lifetime τ_{qw} , the expression for calculating

*Department of Electrical and Computer Engineering, University of California, Santa Barbara, CA 93106. 805-893-8044, 805-893-3262 FAX

†Center for Space Microelectronics Technology, Jet Propulsion Laboratory, California Institute of Technology, 4800 Oak Grove Drive, Pasadena, CA 91109. 818-354-4424, 818-393-4540 FAX

‡Hughes Research Laboratories, Malibu, CA 90265. 310-317-5330, 310-317-5483 FAX

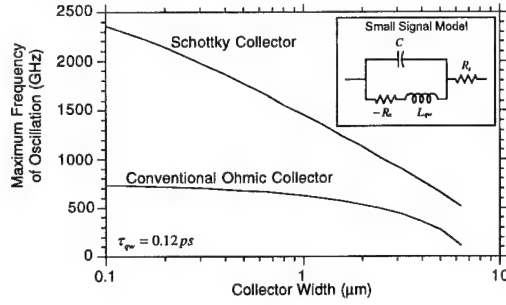


Figure 2: f_{max} comparison of a conventional RTD and a Schottky-Collector RTD, inclusive of the effects of τ_{qw} .

f_{max} is $Re\{Y(\omega = \omega_{max}) = 0\}$, where

$$\begin{aligned}
 Re[Y(\omega)] = & \left(\omega^4 \tau_{qw}^2 C^2 R_n^2 R_s - R_n + R_s \right. \\
 & \left. + \omega^2 (C^2 R_n^2 R_s + 2\tau_{qw} C R_n R_s) \right) \\
 & \times \left(\omega^4 \tau_{qw}^2 C^2 R_n^2 R_s^2 - 2R_n R_s + R_n^2 + R_s^2 \right. \\
 & \left. + \omega^2 (C^2 R_n^2 R_s^2 + 2\tau_{qw} C R_n R_s^2 + \tau_{qw}^2 R_n^2) \right)^{-1}
 \end{aligned} \quad (1)$$

Improvements in f_{max} are obtained by decreasing R_s , $R_n C$ and τ_{qw} . Thin barriers result in both small τ_{qw} and a high current density which reduces $R_n C$. Reduction in τ_{qw} and $R_n C$ through the use of very thin barriers is ultimately limited by degradation in the current peak to valley ratio (PVR) and by high device power dissipation. R_s is reduced by a Schottky collector of submicron width and f_{max} increased (Fig. 2). Compared to $0.1 \mu m$ AlAs/GaAs SRTDs [4], AlAs/ $In_{0.53}Ga_{0.47}As$ /InP SRTDs have slightly smaller τ_{qw} and substantially smaller R_s and $R_n C$ and should attain higher f_{max} .

Fabrication

Molecular beam epitaxial growth of the RTD layer structure started with the nucleation of a $1.0 \mu m$, $1.0 \times 10^{19}/cm^3$, Si doped, $In_{0.53}Ga_{0.47}As$ buried N+ contact layer to the [100] InP substrate at a $540^\circ C$ substrate temperature. This was followed by a $50 nm$, $1.0 \times 10^{18}/cm^3$, Si doped, $In_{0.53}Ga_{0.47}As$ emitter and a $10 nm$, undoped, $In_{0.53}Ga_{0.47}As$ spacer layer. The last $10 nm$ of the emitter and the entire spacer layer were grown at $320^\circ C$ substrate temperature to minimize out diffusion of Si

dopants into the double barrier structure consisting of $1.4 nm$ or $1.7 nm$ (5 or 6 monolayers), undoped AlAs barriers and $4.1 nm$, undoped, $In_{0.53}Ga_{0.47}As$ quantum well. Growth interruptions were used before and after the low temperature growth to stabilize the substrate temperature. The rest of the structure grown at $510^\circ C$ consisted of a $25 nm$, undoped, $In_{0.53}Ga_{0.47}As$ space-charge layer and $10 nm$, $5 \times 10^{18}/cm^3$, Be doped, $In_{0.53}Ga_{0.47}As$ P-cap layer.

Due to the approximately $0.1 eV - 0.3 eV$ potential barrier at the air-semiconductor interface there is significant free charge in the space charge region of the uncontacted regions surrounding the Schottky collector. Parasitic surface leakage currents will arise if this sheet charge is significant. Assuming a $0.2 eV$ potential barrier at the air-semiconductor interface, the calculated free charge density is $\sim 10^{11}/cm^2$ without the P-cap and is reduced to $\sim 10^9/cm^2$ with the P-cap. The P-cap layer, an extension of the space charge region, is fully depleted. Within the SRTD, the fully depleted P-cap increases the forward voltage by $0.4 V$. This increased forward voltage can be eliminated by a self-aligned recess etch through the P-cap before deposition of Schottky metal. Experiments with P-cap recess etch were abandoned due to difficulties in controlling the etch uniformity in very small area devices. The total space charge layer thickness is $35 nm$, which minimizes the space-charge transit time.

Ohmic contacts to the N+ layer were formed with a recess etch, a self-aligned AuGe/Ni/Au liftoff and a subsequent alloy. Airbridge Schottky collector contacts were defined using an interrupted footprint e-beam process [7]. With this process, the contact area is defined exclusively by e-beam lithography, and diodes with contact area as small as $0.05 \mu m^2 - 0.4 \mu m^2$ have been fabricated. The devices were mesa isolated using a $H_3PO_4 : H_2O_2 : H_2O$ etch. Ti/Pt/Au interconnect metal was deposited, which provided contacts to the tops of the both the active and passive mesas (Fig. 1b,c). Fig. 3 shows a scanning electron microscope (SEM) micrograph of a fabricated $0.1 \times 1.0 \mu m^2$ SRTD. Sub-micron SRTDs with 5 and 6 monolayer (ML) barriers were fabricated using this process.

Measurements

Due to the fringing of the electric field under the Schottky contact, the effective collector width is

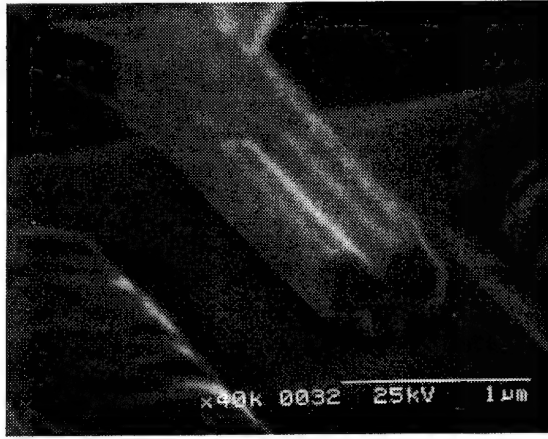


Figure 3: SEM of a $0.1 \mu\text{m} \times 1.0 \mu\text{m}$ AlAs/In_{0.53}Ga_{0.47}As/InP SRTD.

$0.2 \mu\text{m}$ [5]. The devices were laid out with contact pads for 50Ω microwave wafer probes. In all measurements the devices were biased through a network which provides a 50Ω source impedance over at least DC-65 GHz bandwidth, so accurate DC measurements could be made even in the NDR region for devices with $|R_n| \geq 100 \Omega$. The stabilized DC, I-V characteristics of a 5 ML barrier SRTD is shown in Fig. 4. The 6ML SRTD has an effective area of $0.8 \mu\text{m}^2$, with a peak current density of $2 \times 10^5 \text{ A/cm}^2$ at 1.03 V , a PVR of 2.15 and a peak negative conductance of $-7.9 \text{ mS}/\mu\text{m}^2$. The 5ML SRTD has an effective area of $0.4 \mu\text{m}^2$, with a peak current density of $5 \times 10^5 \text{ A/cm}^2$ at 0.95 V , a PVR of 1.7 and a peak negative conductance of $-19 \text{ mS}/\mu\text{m}^2$. Despite these high current densities, the devices did not burn out because of the thin space charge region and the small junction area. Quantum well lifetimes τ_{qw} were computed as 0.12 ps and 0.28 ps for the 5 and 6 ML samples respectively using the model described in [6]. From the measured $2.2 \Omega - \mu\text{m}$ bulk resistivity and the measured $6.5 \Omega - \mu\text{m}$ contact resistance, $R_s = 2.2 \Omega - \mu\text{m}^2$ is computed. A $3.0 fF/\mu\text{m}^2$ capacitance per unit area is extracted from microwave S-parameter measurements. From these measurements $f_{max} = 1.2 \text{ THz}$ for the 6ML sample and $f_{max} = 2.2 \text{ THz}$ for the 5ML sample as calculated by Eqn. 1. Given the measurement frequency limit imposed by existing instruments, f_{max} can be experimentally verified only by building sub-mm-wave oscillators; fabrication of monolithic sub-mm wave oscillators and traveling wave deep subpicosecond pulse generators using AlAs/In_{0.53}Ga_{0.47}As/InP SRTDs is currently being pursued.

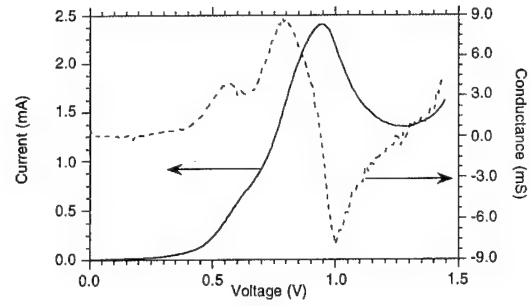


Figure 4: Stabilized DC measurements of a $0.4 \mu\text{m}^2$, 5 ML SRTD.

The work at U.C.S.B. was supported by ONR under contract # N00014-93-1-0378, NSF/PYI, and a JPL President's Fund. The work at JPL was performed by the Center for Space Microelectronics Technology, Jet Propulsion Laboratory, California Institute of Technology, and was sponsored by the National Aeronautics and Space Administration, Office of Advanced Concepts and Technology, and by the Innovative Science and Technology Office of BMDO through an agreement with NASA.

References

- [1] E.R. Brown, J.R. Soderstrom, C.D. Parker, L.J. Mahoney, K.M. Molvar, and T.C. McGill, *Appl. Phys. Lett.*, 58, 2291 (1991).
- [2] E.R. Brown, T.C.L.G. Sollner, C.D. Parker, W.D. Goodhue, and C.L. Chen, *Appl. Phys. Lett.*, 55, 1777 (1989).
- [3] E. Ozbay, D.M. Bloom, D.H. Chow, and J.N. Schulman, *IEEE Electron Dev. Lett.* 14, 400 (1993).
- [4] Y. Konishi, S.T. Allen, M. Reddy, M.J.W. Rodwell, R.P. Smith and J. Liu, *Solid-State Electronics*, 36, 1673 (1993).
- [5] R.P. Smith, S.T. Allen, M. Reddy, S.C. Martin, J. Liu, R.E. Muller, and M.J.W. Rodwell, *IEEE Electron Dev. Lett.*, 15, 295 (1994).
- [6] D.H. Chow, J.N. Schulman, E. Ozbay, and D.M. Bloom, *Appl. Phys. Lett.*, 6, 1685 (1992).
- [7] R.E. Muller, S.C. Martin, R.P. Smith, S.T. Allen, M. Reddy and M.J.W. Rodwell, The 38th International Symposium on Electron, Ion and Photon Beams, New Orleans, Louisiana, June 1994; *J. Vac. Sci. Technol. B* (to be published);

Ultra-High-Speed Superconductor Digital Circuits

V.K. Semenov

Department of Physics, SUNY, Stony Brook, NY 11794-3800

phone: (516) 632-8931; fax: (516) 632-8774

Josephson junction integrated circuits using Rapid Single-Flux-Quantum (RSFQ) logic are capable of performing logic operations at ultrahigh clock frequencies in excess of 100 GHz [1]. In this report I will describe recent progress in design, fabrication, and testing of several circuits of this family.

Currently two different niobium-trilayer technologies are available for fabrication of RSFQ circuits; each technology may be characterized by either the Josephson junction critical current density or size of a Josephson junction. One of these technologies, with moderate current density (1 kA/cm^2) and relatively large ($3.5 \text{ }\mu\text{m}$) Josephson junctions is commercially available from HYPRES, Inc. [2] and is convenient for fabrication of relatively complex circuits. A more advanced technology with higher critical current density (10 kA/cm^2) and smaller ($1.5 \text{ }\mu\text{m}^2$) junctions is now under development at SUNY [3]; up to now it has been used for fabrication of a few simple circuits.

Several integrated circuits of the modest integration scale (with up to 1000 Josephson junctions), including a frequency multiplier with the output frequency up to 90 GHz, pattern generator with upper frequency up to 85 GHz, 8-bit multiplier with the upper frequency of 6.3 GHz, and several shift registers have been successfully characterized at high frequencies, while several other circuits (including 4-bit decoder and 4+4-bit decimation filter) have tested at low frequencies. Development of the first complete RSFQ system (16-bit A/D converter with estimated 10 MHz signal bandwidth), a dense SFQ memory, and several other promising circuits, is under way.

The first circuit fabricated using the $1.5\text{-}\mu\text{m}^2$ technology (consisting of an SFQ pulse train generator and toggle flip-flop) has been tested successfully at the pulse train frequencies of up to 360 GHz, in a qualitative agreement with results of numerical simulations. To our knowledge, the maximum frequency of operation for this circuit is considerably higher than those reported previously for any digital device. A comprehensive account of design, performance, and possible applications of the RSFQ circuits will be presented at the meeting.

The work was supported by DoD's University Research Initiative under AFOSR Grant #F49620-92-J-0508.

1. K.K. Likharev and V.K. Semenov, IEEE Trans Appl. Supercon. vol. 1, p. 3, 1991.
2. Design Rules, available in HYPRES, Inc., 175 Clearbrook Road, Elmsford, NY 10523, phone (914) 592-1190.
3. P. Bunyk *et al.* "Ultra-High-Speed Rapid Single-Flux-Quantum Digital Circuits using a Planarized-Niobium-Trilayer Josephson Junction Technology", submitted to Appl. Phys. Lett.

Monday, March 13, 1995

Ultrafast Carrier Dynamics and Transport

UMB 10:30 am-12:15 pm
Ballrooms VI-VIII

Hiroyuki Sakaki, *Presider*
University of Tokyo, Japan

Identifying the Distinct Phases of Carrier Transport in Semiconductors with 10 fs Resolution

B. B. Hu, E. A. de Souza, W. H. Knox, J. E. Cunningham, and M. C. Nuss
 AT&T Bell Laboratories, 101 Crawfords Corner Road, Holmdel, NJ 07733-3030
 Tel. 908-949-4925, FAX: 908-949-2473

The rapid advance of femtosecond laser technology has offered superior time resolution for studying transient carrier transport phenomena, and many studies of these transport processes have been performed [1]. In order of time scale, carrier transport process can be divided into four distinct stages: In the first stage, when a biased semiconductor is excited by an ultrashort light pulse, an instantaneous polarization of the photojected electron-hole pairs is created [2-4]. In the second stage, carriers undergo ballistic acceleration without scattering by the electric field for times shorter than the mean free scattering time ($\sim 10^{-13}$ s). In the third stage, as scattering processes set in, the acceleration of the carriers stops, and the velocity reaches a maximum. Velocity-overshoot occurs for materials such as GaAs, when hot electrons are scattered into satellite L, X valleys with lower mobility. In the fourth stage, the velocity is maintained at a lower level in steady-state drift. These regimes, while easily defined, have not been clearly separated to date because scattering times limit the ballistic regime to ~ 50 fs for typical conditions.

Here, we present a study of carrier transport after injection of electron-hole pairs using a novel THz technique with 10 fs time resolution. By detecting the change of the dc field, we clearly separate the instantaneous polarization and carrier transport in the time domain. In addition, we show directly that within the first roughly 70 fs the electrons and holes are accelerated ballistically, and that the average drift distance increases quadratically in time. At later times, we observe that the

electron drift velocity reaches a maximum, and then relaxes down to a steady state value.

Our experimental technique is to inject electron-hole pairs with a 10 fs optical pulse into the field region of a large-aperture GaAs Schottky diode. As long as the change in electric field is small, it can be approximated by: $\Delta E_{dc}(t) = -[P_{in}(t) + Nex(t)]/\epsilon$, where $P_{in}(t)$ is the instantaneous e-h polarization, N is the photocarrier density, $x(t)$ the average displacement between electrons and holes at time t , e the dielectric constant, and e the electron charge. The relative change in THz energy $W(t)$ emitted from the second pulse is given by:

$$\frac{\Delta W}{W} = \frac{2\Delta E_{dc}}{E_{dc}} = -\frac{2}{E_{dc}\epsilon} \cdot [P_{in}(t) + Nex(t)]$$

Hence, by monitoring the change in THz energy as a function of time, we directly map

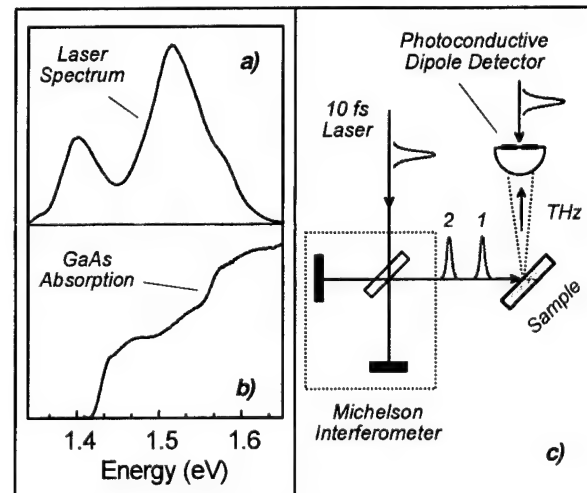


Fig. 1 a) Spectrum of the laser pulse. b) GaAs absorption spectrum. c) Schematic of the experimental setup

out the transport movement of the carriers generated by the prepulse.

Figure 1 a, b, and c show the laser spectrum, GaAs absorption spectrum and the schematic experimental setup, respectively. The optical source is a self-focusing-mode-locked Ti:Sapphire laser pumped by a cw-Argon ion laser [5]. It produces optical pulses with a duration of 10 fs at a repetition rate of 82 MHz. The laser beam is delivered into a Michelson interferometer. The pair of pulses from the Michelson interferometer is weakly focused and strikes the sample at an incident angle of 60 degrees, resulting in a carrier density of around 10^{15} cm^{-3} for a beam size of $0.5 \times 0.5 \text{ mm}^2$ on the sample. One pulse (p2) is chopped, and only the THz signal generated by p2 is detected, while the other pulse merely injects carriers. The THz signal is collected by a $50 \mu\text{m}$ photoconductive dipole antenna with a silicon hyperhemispherical substrate lens attached [6]. The THz energy $W(t)$ is computed by squaring and time-integrating each THz waveform.

Both a bulk GaAs sample and a MQW sample are used in our experiments. For the bulk sample, the intrinsic region consists of a $1.7 \mu\text{m}$ GaAs layer sandwiched by 3500 \AA $\text{Al}_{0.5}\text{Ga}_{0.5}\text{As}$ layers. The sample is capped with 100 \AA GaAs, and finally, a 50 \AA Ti film is deposited. A large and uniform electric field in the intrinsic region can be achieved by applying a reverse bias voltage between the semi-transparent metal film and the heavily doped substrate. The MQW sample is similar to the bulk sample with the $1.7 \mu\text{m}$ GaAs layer replaced by 100 periods of GaAs/ $\text{Al}_{0.32}\text{Ga}_{0.68}\text{As}$ ($120 \text{ \AA}/150 \text{ \AA}$). For comparison, we also design a Si p-i-n diode for the experiment. It has a n^+ -doped top layer of 500 \AA , an intrinsic region of $7 \mu\text{m}$ on a p^+ substrate.

Figure 2 shows results from the three samples. The solid lines are numerical fits to the experimental curves. The left vertical axis is

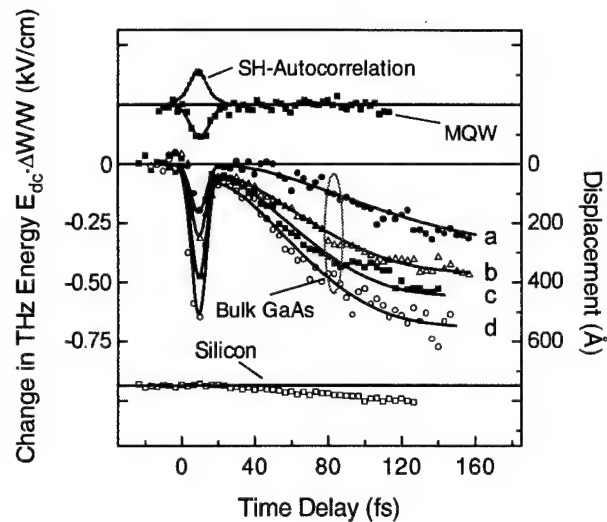


Fig. 2 THz energy and e-h pair displacement as a function of time after injection of carriers by the prepulse. a: 15.8 kV/cm , b: 17.8 kV/cm , c: 20 kV/cm , and d: 23 kV/cm .

the field-normalized change in THz energy $(\Delta W/W) \cdot E_{dc}$ from the second pulse, while the right vertical axis shows the average displacement. For reference, we also plot the second harmonic autocorrelation of the optical pulse. We also repeat the measurement for GaAs at different crystal orientations by rotating its azimuth angle (not shown). No crystal orientation dependence is observed, indicating that the bulk $\chi^{(2)}$ effect is negligible in our experiments.

The fast dip observed in the MQW and GaAs samples is clearly the instantaneous electron-hole polarization, since it is the only contribution to the THz signal in the MQW sample [4], while in the bulk sample the carriers can hardly move any distance during the first 10 fs. For an indirect bandgap material such as Si, optical creation of an electron-hole pair is achieved through incoherent random optical phonon scattering which destroys the coherence between the electrons and holes. As a result, we do not observe the instantaneous polarization in the silicon sample (lower trace in Fig. 2). In our experiments, the width of the dip is comparable to the optical pulse duration, showing that the speed of the polari-

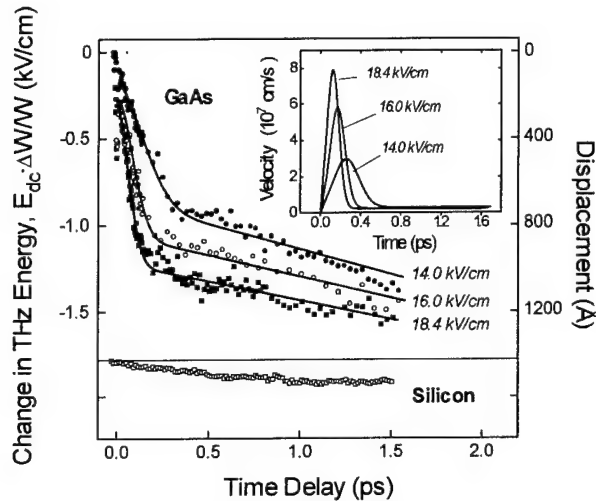


Fig. 3 THz energy as a function of time for GaAs on a longer time scale. Inset: time derivative of the solid fits to the data.

zation of electron-hole pairs is limited only by the optical pulse.

The subsequent increase of the electron-hole displacement in the bulk GaAs and silicon samples represents the field screening due to the space charge field set up by electrons and holes as they separate. At early times, we expect that the carriers are accelerated ballistically in the electric field. This is illustrated in Fig. 2 as the average displacement in the first 70 fs can be fitted by a quadratic time dependence. By fitting the experimental curves with $eE_{dc}t^2/2m^*$, we obtain an average reduced effective mass for the electron-hole pair of $0.043 m_0$, where m_0 is the electron mass.

Figure 3 shows the results from the bulk GaAs sample and the Si sample on a longer time scale. The solid lines are numerical fits to the experimental data. By taking the time derivative of the solid lines, we can obtain the time dependence of the relative electron-hole drift velocity (inset in Fig. 3.). For a field of 18.4 kV/cm, we observe that the drift velocity reaches its maximum overshoot value in about

100 fs, then relaxes down to its steady value in about 200 fs. The time scale we observed here is much shorter than that in previous Monte-Carlo simulation [7]. Also, the amount of the overshoot observed is roughly twice as large as theoretically estimated. This discrepancy between our results and previous Monte-Carlo simulations warrants a critical examination of our understanding of current transport on a 10 fs time scale.

In summary, for the first time, we clearly separate the instantaneous polarization from the carrier transport. Furthermore, we show that electron and holes are ballistically accelerated by the field within the first 70 fs. At later times, we observe that the drift velocity overshoots its steady state value in roughly 200 fs. Our experiments thus clearly reveal the distinct stages of carrier transport in semiconductors.

- [1] see for example: "Hot Carriers in Semiconductor Nanostructures," ed. J. Shah, Academic Press, Boston (1992)
- [2] S. L. Chuang, S. Schmitt-Rink, B. I. Greene, P. N. Saeta, and A. F. J. Levi, *Phys. Rev. Lett.* vol. 68, 102 (1992).
- [3] A. V. Kuznetsov, and C. J. Stranton, *Phys. Rev. B*, vol. 8, 10828 (1993)
- [4] P. C. M. Planken, M. C. Nuss, W. H. Knox, D. A. B. Miller, and K. W. Goossen, *Appl. Phys. Lett.* vol. 61, 2009, (1992).
- [5] Melanie T. Asaki, Chung-Po Huang, Dennis Garvey, Jianping Zhou, Henry C. Kapteyn, and Margrate M. Murnane, *Opt. Lett.* vol. 18, 977 (1993).
- [6] P. R. Smith, D. H. Auston, and M. C. Nuss, *IEEE J. Quantum Electron.* QE-24, 255 (1988).
- [7] G. M. Wysin, D. L. Smith, and A. Re-dondo, *Phys. Rev. B*, vol. 12514, (1988).

Coherent Charge Oscillations in Bulk GaAs

Arthur L. Smirl, W. Sha, and Shekhar. Patkar

Laboratory for Photonics and Quantum Electronics, 100 IATL, University of Iowa, Iowa City, IA 52242

Tel: (319) 335-3460 Fax: (319) 335-3462

and W. F. Tseng

National Institute of Standards and Technology, Gaithersburg, MD 20899

Recently, transistor-like three terminal (launcher-base-detector) devices with base regions of dimensions comparable to (or less than) typical mean free path lengths have been used to study transport in the near ballistic regime,^{1,2} and femtosecond techniques with temporal resolutions less than the mean scattering times have been used to investigate velocity overshoot³ and the nearly ballistic acceleration of electrons^{4,5}. In addition, coherent oscillatory electronic wavepackets have been observed in coupled quantum-wells⁶, and Bloch oscillations have been observed in superlattices^{7,8}. Here, we report the first direct observation of coherent charge oscillations in a bulk semiconductor in the presence of a constant built-in field, and we confirm that these oscillations are the result of ballistic charge transport by separately demonstrating that they occur on a time scale short compared to the measured dephasing time.

In these experiments, electrons and holes are suddenly generated into bulk material in the presence of a constant field. For times short compared to the mean scattering time, the electrons and holes are initially accelerated in opposite directions by the presence of the constant field. As they move apart, a space-charge field develops as the result of the Coulomb attraction between the oppositely charged species. This restoring force causes the plasma to coherently oscillate until collisions dampen the oscillations. We emphasize that the motion observed here is over a small region of the Brillouin zone near the band edge and that the oscillations are produced by the restoring space-charge field. This is in direct contrast to Bloch oscillations that are observed in minibands, where charge motion is over the entire miniband and where the oscillations are caused by Bragg reflections at the Brillouin zone edge.

Our measurements were performed at 80 K in a GaAs vertical p-i-n structure with a 3.5 kV/cm built-in field and a 400 nm-thick intrinsic region using the geometry shown in Fig. 1. The electrons and holes were photo-generated in the intrinsic region by a 100 fs pump pulse tuned to the GaAs band edge. The ballistic charge oscillations were then monitored with a time delayed probe by measuring the change in the near-band-edge electro-absorption as these oscillations screened the built-in p-i-n field. A few representative traces of the time-derivative of the change in transmission induced by these oscillations are

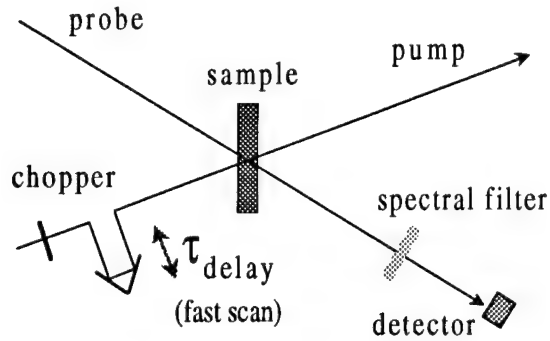


Fig. 1. Experimental geometry for monitoring the band edge electro-absorption in a GaAs p-i-n.

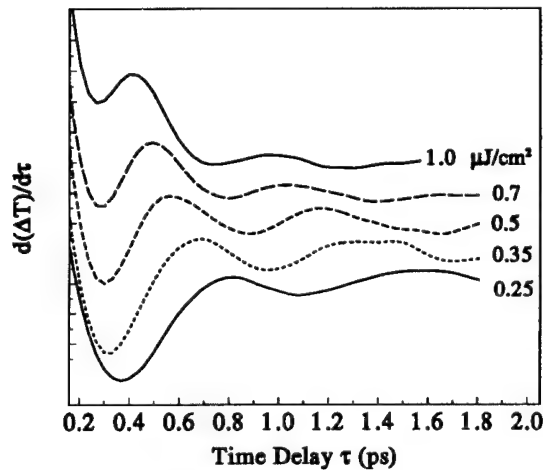


Fig. 2. The time derivative of the change in electro-absorption versus pump-probe time delay for several fluences.

shown in Fig. 2. Several features are worth noting. First, notice that clear oscillations are observed over a range of fluences. These oscillations decay in a time period of a few hundred femtoseconds, consistent with the expected mean time between collisions at this temperature in GaAs. Finally, the frequency of oscillation clearly increases with increasing fluence. In fact, by verifying that the optical absorption was linear over this range of fluences, we were able to estimate the carrier densities and to demonstrate that the measured frequencies had a square-root dependence on the carrier density and that the measured frequencies deviated from the calculated plasma oscillation frequencies (given by $\omega_p^2 = ne^2/\epsilon m^*$, where ω_p is the plasma frequency, n is the carrier density, e the electronic charge, ϵ the dielectric constant and m^* the effective mass) by less than 25% for the entire fluence range. Also, from a simple coherent plasma model, we estimate the oscillation amplitude and the maximum kinetic energy gained in these experiments. The results (not shown) indicate that, for low fluences, the carriers move ~ 100 nm and gain more than 10 meV in energy before collisions disrupt their motion.

To verify that our oscillations were indeed the result of coherent charge motion, we also measured the carrier dephasing in an electric-field-free sample under otherwise identical conditions using transient degenerate four-wave-mixing techniques. The results are shown in Fig. 3 for selected fluences. Notice that the dephasing times extracted from the four-wave-mixing signals are consistent with the decays of the oscillations shown in Fig. 1. Finally, to exclude the possibility that the oscillations are the result of intervalley scattering between the Γ and L valleys, we note that the maximum energy gained per carrier is

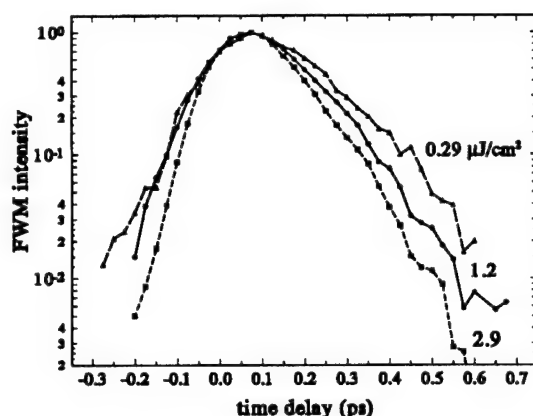


Fig. 3. The time-integrated degenerate-four-wave signal in an electric-field-free bulk GaAs sample for selected pump fluences.

of 15 meV, which is much lower than the ~300 meV needed for intervalley transfer (and for Gunn oscillations).

Consequently, we have verified that we have directly observed, for the first time, coherent plasma oscillations of electrons and holes in a bulk semiconductors and that the charge oscillations occur in the ballistic transport regime on a subpicosecond time scale.

References:

1. A. F. J. Levi, J. R. Hayes, and R. Bhat, *Appl. Phys. Lett.* **48**, 1609 (1985).
2. M. Heiblum, M. I. Nathan, D. C. Thomas, and C. M. Knoedler, *Phys. Rev. Lett.* **55**, 2200 (1985)
3. K. E. Meyer, M. Passot, and G. Mourou, *Appl. Phys. Lett.* **53**, 2254 (1988).
4. W. Sha, T. B. Norris, W. J. Schaff, and K. E. Meyer, *Phys. Rev. Lett.* **67**, 2553 (1991).
5. B. B. Hu, E. A. DeSouza, W. H. Knox, M. C. Nuss and J. E. Cunningham, *Proceedings of Ultrafast Phenomena IX*, paper PD12 Dana Point, CA, May 1994.
6. K. Leo, J. Shah, T. C. Damen, A. Schulze, T. Meier, S. Schmitt-Rink, P. Thomas, E. O. Göbel, S. L. Chuang, M. S. C. Luo, W. Schäfer, K. Köhler and P. Ganser, *IEEE, J. Quant. Elect.* **28**, 2498 (1992).
7. T. Dekorsy, P. Leisching, K. Köhler, and H. Kurz, *Phys. Rev. B* **50**, 8106 (1994), and references therein.
8. J. Feldmann, K. Leo, J. Shah, D. A. B. Miller, J. E. Cunningham, T. Meir, G. von Plessen, A. Schulze, P. Thomas, and S. Schmitt-Rink, *Phys. Rev. B* **46**, 7252 (1992).

How Do Carrier-carrier Interactions in GaAs Depend on the Carrier Distribution?

J. A. Kash

IBM Research Division

Room 29-149, Thomas J. Watson Research Center
Yorktown Heights, New York, 10598 USA

Telephone (914) 945-1448; FAX (914) 945-2141; email kash@watson.ibm.com

Carrier-carrier interactions play an important role in determining the performance of fast electronic and optoelectronic devices. They are also very difficult to model, especially when the carrier distributions are far from equilibrium. The difficulties arise primarily from an inability to treat collective effects such as screening and the formation of plasmons, which play a key role in carrier-carrier scattering processes in semiconductors.¹⁻⁴ These effects should be influenced by the energy distribution of the carriers.¹ As a simple illustration of how the carrier distribution affects the scattering, a hot plasma has been predicted to provide weaker screening than a cold plasma.⁵ In recent publications,^{6, 7} it was suggested that coherence effects on carrier-carrier interactions should be included when the carriers are generated by subpicosecond laser pulses. Experimentally, there has not yet been a direct quantitative comparison of carrier-carrier scattering rates from electron-hole (e-h) plasmas which have the same density but very different energy distributions, although both thermal⁸ and non-thermal^{9, 10} carrier distributions have been separately studied.

In the experiments reported here, carrier-carrier scattering is compared between distributions that are very different energetically, yet of the same density. In particular, scattering is compared between the carrier distribution that occurs during a 150 fsec optical pulse, and the distribution that is created by a pulse of the same fluence but 100 times longer in duration. The 150 fsec pulse produces a "hot" nonequilibrium distribution of carriers with a large average energy. The longer pulse creates a "cold" thermal distribution ($T \approx 100\text{K}$) of much lower average energy. The key experimental result reported here is that the energy loss rate due to carrier-carrier scattering during the 150 fsec pulse is found to be several times stronger than that seen with the longer pulse. This observation is in accord with the weaker screening expected from a "hot" carrier distribution.

The experimental technique used here to observe carrier-carrier scattering uses the luminescence generated by nonequilibrium electrons recombining at neutral acceptors (hot (e, Λ^0) luminescence).^{8, 11} A single laser pulse was used to both create the plasma and excite the hot luminescence. Laser pulses centered at 1.691 eV were generated by a cw modelocked Ti:Sapphire laser (Spectra Physics Tsunami). The pulses as generated were nearly transform limited 125 fsec pulses (sech² shape assumed) with a spectral width of 11 meV, at a repetition rate of 82 MHz. A prism filter was used to spectrally narrow the pulses to 9 meV, broadening them temporally to 150 fsec. Pulses of about 15 psec were generated by narrowing the 150 fsec

pulses to a 4 meV spectral width, and then passing these pulses through a 4-pass dispersive grating delay line. The fsec or psec pulses were then focussed onto the sample at normal incidence, with the laser electric field polarized along a {100} crystal axis. The sample was a 1 μm thick layer of GaAs, Be-doped at $8 \times 10^{16} \text{ cm}^{-3}$, MBE-grown on a [100] GaAs substrate. The sample temperature was about 8K. Only the luminescence polarized perpendicularly to the laser was collected, filtered, dispersed, and detected by a triple monochromator and cooled CCD. The carrier density generated by each pulse was determined from the pulse fluence at the sample (maximum of 0.3 nJoules), the spot size (about 120 μm .), and the absorption depth (0.7 μm .), and should only be taken as an estimate, since the luminescence from the entire focal spot was collected. Because of the relatively long absorption depth and large spot size of the laser, carrier diffusion and surface recombination during the laser pulses can be ignored.

Figure 1 shows a comparison between the hot luminescence spectra as excited by fsec and psec laser pulses. The spectra are scaled so that, if the luminescence was linear in laser power, (a) and (b), and (c) and (d), would be identical. Clearly the pairs are not identical; the differences are due to carrier-carrier scattering. For laser powers below 10 mW (injected carrier density of about $2 \times 10^{16} \text{ cm}^{-3}$), the integrated area under the hot (e, Λ^0) luminescence peaks are linear with laser power, so carrier-carrier scattering is unimportant. At the higher power, the intensity of the peaks is reduced as carrier-carrier interactions become important. Comparing Figs. 1(a) and 1(c), it is apparent that the reduction is more significant for the fsec laser pulses than for the psec pulses. Straightforward analysis shows that the electron-plasma energy loss rate at the high density is about 2 to 4 times greater for the fsec pulses than for the same carrier density injected by the psec pulses. This is a significant difference, and is a clear demonstration of the weaker screening of the nonequilibrium plasma. The increased energy loss rate for the nonequilibrium plasma is roughly what one would expect for negligible screening.

The linewidth of the highest energy peak of hot (e, Λ^0) luminescence under fsec pulse excitation has also been studied. Rossi et al.⁶ have predicted that coherence effects cause a dramatic broadening of this linewidth when the injected carrier density exceeds about 10^{16} cm^{-3} . Here, no broadening effects were observed as the carrier density was varied from about 10^{15} cm^{-3} to $2 \times 10^{16} \text{ cm}^{-3}$. At the higher densities, there is a significant background of band-to-band luminescence underlying the hot (e, Λ^0) luminescence.¹² Since this background grows superlinearly with injected carrier density, it was not possible to make a meaningful measurement of the linewidth at still higher densities. However, the data does show that such coherence effects, if they exist, are smaller than the conventional contributions to the linewidth, and will be hard to observe. (Conventional contributions to the linewidth include inhomogeneous contributions from the width of the acceptor level and the valence band warping,^{13, 14} and homogeneous terms related to the inelastic lifetime of the electron in its nonequilibrium state and also the hole which is created at the same time.)

In conclusion, it has been shown that a hot electron loses energy to a nonequilibrium "hot" plasma at a rate several times that for a thermalized "cold" plasma of lower average energy, probably because of reduced screening for the hot plasma. This reduced scattering needs to be properly accounted for in modeling any device or physical effect in which a nonequilibrium or very hot carrier distribution is present.

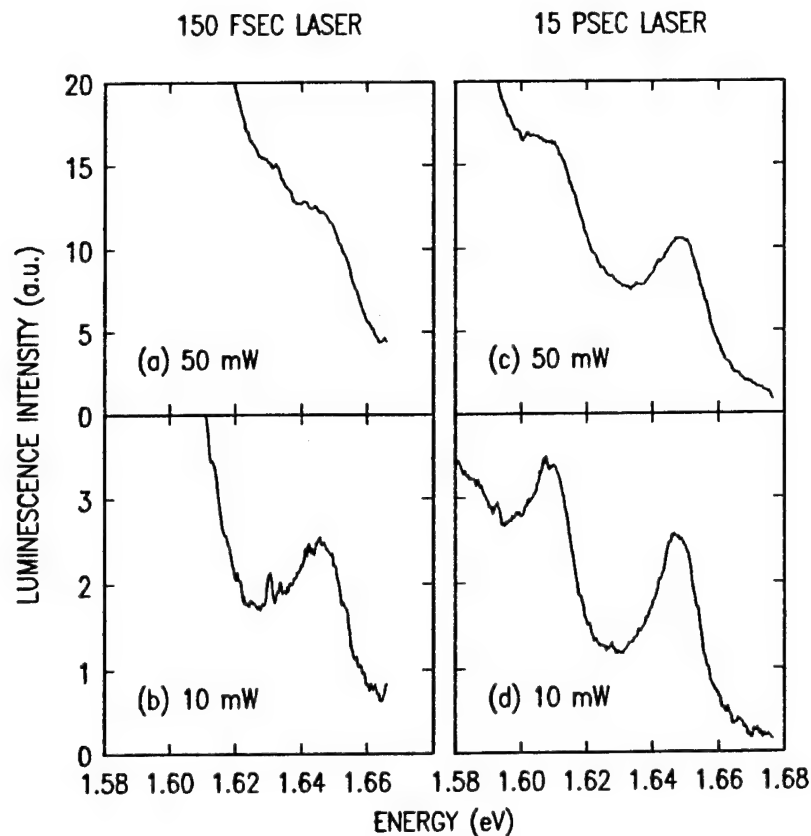


Figure 1. Hot luminescence in GaAs:Be for laser excitation with (a and b) a 150 fsec pulse, and with (c and d) a pulse of about 15 psec. A laser power of 10 mW corresponds to an injected carrier density of about $2 \times 10^{16} \text{ cm}^{-3}$.

REFERENCES

- 1 D. C. Scott, R. Binder and S. W. Koch, Phys. Rev. Lett. **69**, 347 (1992).
- 2 J. F. Young and P. J. Kelly, Phys. Rev. B **47**, 6316 (1993).
- 3 L. Rota, P. Lugli, T. Elsaesser and J. Shah, Phys. Rev. B **47**, 4226 (1993).
- 4 J. H. Collet, Phys. Rev. B **47**, 10279 (1993).
- 5 S. S. Jha, J. A. Kash and J. C. Tsang, Phys. Rev. B **34**, 5498 (1986).
- 6 F. Rossi, S. Haas and T. Kuhn, Phys. Rev. Lett. **72**, 152 (1994).
- 7 A. Leitenstorfer, A. Lohner, T. Elsaesser, S. Haas, F. Rossi, T. Kuhn, W. Klein, G. Boehm, G. Traenkle and G. Weimann, Phys. Rev. Lett. **73**, 1687 (1994).
- 8 J. A. Kash, Phys. Rev. B **48**, 18336 (1993).
- 9 Y. Kostoulas, T. Gong and P. M. Fauchet, Semicond. Sci. Technol. **9**, 462 (1994).
- 10 K. W. Sun, M. G. Kane and S. A. Lyon, Europhys. Lett. **26**, 123 (1994).
- 11 B. P. Zakharchenya, D. N. Mirlin, V. I. Perel and I. I. Reshina, Sov. Phys. Usp. **25**, 143 (1982).
- 12 J. C. Tsang and J. A. Kash, Phys. Rev. B **34**, 6003 (1986).
- 13 G. Fasol, W. Hackenberg, H. P. Hughes, K. Ploog, E. Bauser and H. Kano, Phys. Rev. B **41**, 1461 (1990).
- 14 J. A. Kash, M. Zachau, M. A. Tischler and U. Ekenberg, Phys. Rev. Lett. **69**, 2260 (1992).

Ultrafast hole tunneling in GaInAs/AlInAs asymmetric double quantum wells

S. Ten, M.F.Krol⁽¹⁾, B.P.McGinnis, M.J. Hayduk⁽¹⁾,
G. Khitrova and N. Peyghambarian

Optical Sciences Center, University of Arizona, Tucson, AZ, 85721

Tel. (602) 621-2989, Fax (602) 621-9610

⁽¹⁾ *Rome Laboratory Photonics Center, Griffiss Air Force Base, New York, 13441*

Tel. (315) 330-4456, Fax (315) 330-7901

Absorption and refractive index nonlinearities in semiconductor heterostructures due to real carrier generation are large, but the relatively long recovery time (~ 1 ns) represents a major problem for fast device applications. There have been many attempts to reduce the recovery time by optimizing the design of heterostructures. For example, in structures such as asymmetric double quantum wells (ADCWs) which consist of different size quantum wells coupled by a thin barrier, the recovery time of the narrow well excitonic absorption is controlled by carrier tunneling from the narrow well to the wide well. It was demonstrated that tunneling of electrons indeed results in fast absorption recovery, however slow heavy hole tunneling makes it incomplete [1]. Fast electron tunneling is controlled by longitudinal optical (LO) phonon scattering when the energy separation between the lowest electronic subbands in the narrow and wide well is larger than the LO phonon energy. Hole tunneling is slow because the separation between the hole subbands is usually smaller than the LO phonon energy and the heavy hole wavefunctions are more localized due to their larger effective mass. However, resonances between hole subbands efficiently accelerate hole tunneling [2].

In this paper we report fast and complete recovery of excitonic absorption in GaInAs/AlInAs ADQWs. We investigated structures which were grown lattice matched by molecular beam epitaxy on undoped (100) InP substrates. Each structure consisted of 30 periods of 40 Å Ga_{0.47}In_{0.53}As narrow well/ L_b Å Al_{0.48}In_{0.52}As tunnel barrier/ 60 Å Ga_{0.47}In_{0.53}As wide well/ 150 Å Al_{0.48}In_{0.52}As barrier, where L_b is the thickness of the tunnel barrier and was 27 and 37 Å in our experiment. The widths of the narrow and wide well were designed such that at 77 K the narrow and wide well excitonic absorption peaks were at 1230 and 1340 nm, respectively.

Time resolved transmission changes in the 1220-1300 nm spectral range were investigated using a tunable pump-probe setup. A Kerr Lens Modelocked Ti:Sapphire laser generated a 100 MHz train of 100 fs pulses at 850 nm which were used to generate carriers in the ADQW samples and to time resolve the probe transmission. A CW Cr:Forsterite laser provided a probe tunable between 1220 nm and 1300 nm. Time resolution of 100 fs was achieved by mixing the transmitted probe with the reference pulses from the Ti:Sapphire laser. The upconverted signal was filtered with a monochromator and detected by a

photomultiplier. The probe was tuned to the heavy hole exciton peak of the narrow well, thus allowing observation of changes in the narrow well carrier population.

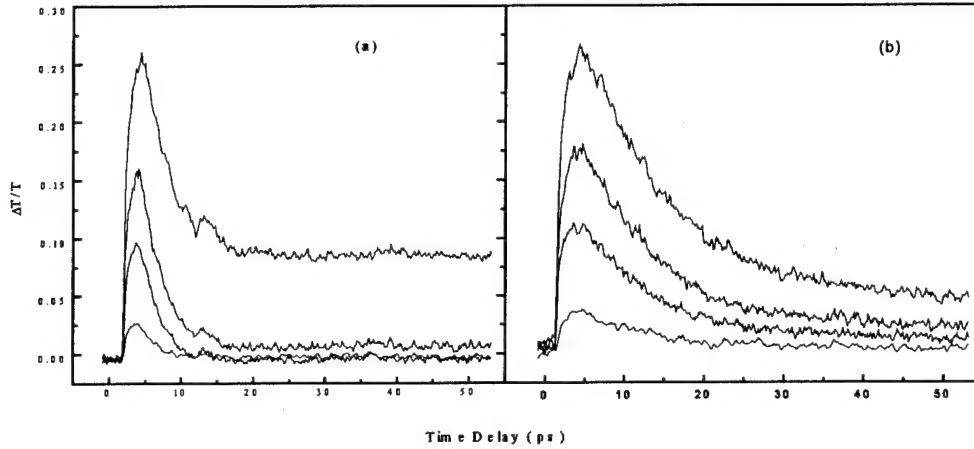


Fig. 1. Time-resolved differential transmission data for the samples 40/27/60 (a) and 40/37/60 (b) at different carrier densities - 1.4×10^{11} , 5.6×10^{11} , 1.1×10^{12} and $2.3 \times 10^{12} \text{ cm}^{-2}$.

The heavy hole excitonic absorption dynamics at 77 K are shown in Fig. 1 for samples with barrier widths of $L_b=27 \text{ \AA}$ (a) and $L_b=37 \text{ \AA}$ (b) at different carrier densities. At low carrier densities the excitonic absorption recovers completely with a single time constant of 2.4 ps for $L_b=27 \text{ \AA}$ and 11.5 ps for $L_b=37 \text{ \AA}$. At high carrier densities a long lasting component is present in the absorption dynamics. The experimental data shown here are very different from previous transmission studies of tunneling in GaAs/GaAlAs ADQWs, where two time constants were observed at low carrier densities. To elucidate the mechanism of absorption recovery we calculated electron tunneling times determined by LO phonon emission, using the formalism developed by Price[3] and taking into account bandfilling effects for electrons in the wide well. Calculated tunneling times match those observed in the experiment for different barriers and carrier densities. Thus we conclude that the recovery of narrow well absorption is controlled by LO phonon assisted electron tunneling. The same mechanism is not allowed for heavy hole tunneling since the separation between the highest subbands in the narrow and wide well is less than the LO phonon energy ($\hbar\Omega=33.2 \text{ meV}$), and acoustic phonon scattering would result in a long lasting component in the differential transmission, which was not observed at low carrier density in our experiment.

Explanation of the absorption dynamics relies on hole bandstructure, wavefunction localization and excitation conditions in our experiment. We calculated the hole dispersion in our ADQWs from 4×4 the Luttinger hamiltonian using the procedure outlined in [4] (see Fig.2 (a)). Bands are labeled according to their character and localization at the Γ point. Carriers were generated in the first

subband of the narrow well (HH^{N}_1) with momenta $k \approx 0.065 \text{ \AA}^{-1}$. There are no resonances between any hole subbands in our ADQWs.

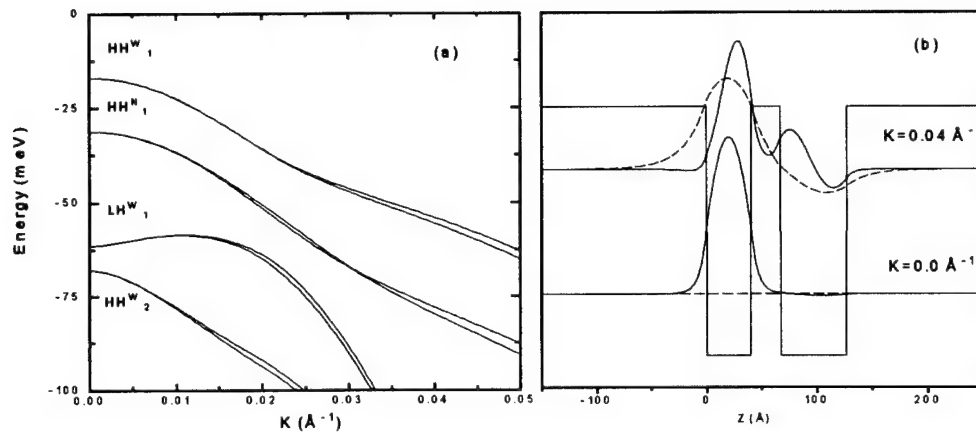


Fig. 2. Bandstructure of the 40/27/60 ADQW (a) and narrow well heavy hole wavefunctions at different in-plane momentum (solid line represents $J_z = 3/2$ component, dashed - $J_z = 1/2$) (b)

However hole wavefunctions are very delocalized because of bandmixing. Two wavefunctions corresponding to different momenta are shown in Fig.2(b) for HH^{N}_1 subband. Away from the Γ point bandmixing increases the delocalization of the $J_z = \pm 3/2, \pm 1/2$ wavefunction components. Thus, hole tunneling from HH^{N}_1 subband becomes very fast at $k \neq 0$. For example, when alloy scattering is considered, we estimate hole tunneling times to be subpicosecond.

Generation of holes in HH^{N}_1 with high momenta leads to the tunneling of holes to HH^{W}_1 on subpicosecond time scale before reaching the bottom of HH^{N}_1 subband. Therefore, at low carrier density holes do not appear in the bottom of HH^{N}_1 and the changes in the heavy hole excitonic absorption are controlled only by electron dynamics. However, at high carrier densities bandfilling of HH^{W}_1 results in the relaxation of holes to the bottom of HH^{N}_1 generating the long lasting component in the differential transmission shown in Fig.1.

References:

- 1) S. Muto, T. Inata, A. Tackeuchi, Y. Sugiyama and T. Fujii, *Appl. Phys. Lett.* 58 (21), 2393 (1991).
- 2) R. Ferreira and G. Bastard, *Europhys. Lett.*, 10 (3), 279 (1989).
- 3) P. J. Price, *Annals of Phys.* 133, 217 (1981).
- 4) G. Bastard, *Wave Mechanics Applied to Semiconductor Heterostructures*, Halsted Press, 101 (1988).

Hole Relaxation in p-type InGaAs/AlGaAs Quantum Wells Observed by Ultrafast Mid-Infrared Spectroscopy

Z. Xu and P. M. Fauchet

Department of Electrical Engineering, University of Rochester, Rochester, NY 14627

C. W. Rella, B. A. Richman, H. A. Schwettman

*Stanford Picosecond FEL Center, W. W. Hansen Experimental Physics Laboratory,
Stanford University, Stanford, CA 94305*

G. W. Wicks

The Institute of Optics, University of Rochester, Rochester, NY 14627

The mechanism of intersubband relaxation in quantum wells (QWs) is very important from a fundamental physics perspective and for device applications. Measurements performed by infrared bleaching [1-3] and anti-Stokes Raman scattering [4] techniques in n-type QWs have revealed a relaxation time ranging from less than 1 ps to 10 ps when the well is narrow enough to make the intersubband transition energy larger than the LO phonon energy. The differences amongst the experimental results and between theory [5] and experiments can be traced to different experimental conditions (e.g., the carrier density) and to the influence of inter-valley scattering, LO-phonon screening and hot phonons. In p-type quantum wells, the relaxation time is expected to be shorter for several reasons: the density of state is larger and the bandstructure and the scattering mechanisms are different. A determination of the cooling rate for holes performed by time resolved photoluminescence yielded a relaxation time of 1 ps [6]. However, these measurements are not direct since both electrons and holes were present. A direct determination requires that no electrons be photogenerated. Here, we report the first direct measurement of the relaxation time of holes in p-type quantum wells by the pump-probe technique using ~ 1 ps pulses generated by a mid-infrared free electron laser.

The samples used in our experiments were strained quantum wells grown by molecular beam epitaxy (MBE). Because of the significant lattice mismatch between InGaAs and AlGaAs, a 2 micron thick buffer layer, in which the indium concentration varied linearly from 0 to 30%, was grown between the QW layer and the GaAs substrate in order to obtain high quality samples. The QW layer consists of 50 $\text{In}_{0.5}\text{Ga}_{0.5}\text{As}/\text{Al}_{0.5}\text{Ga}_{0.5}\text{As}$ periods. The $\text{In}_{0.5}\text{Ga}_{0.5}\text{As}$ well was 4 nm wide and the $\text{Al}_{0.5}\text{Ga}_{0.5}\text{As}$ barrier was 8 nm wide. Thin 5.7 Å thick GaAs smoothing layers were added at the interfaces for optimal growth. Two samples were grown; one in which the whole quantum well layer was doped by Be and another one which was undoped to provide a good reference in the linear absorption measurement. The dopant concentration is 10^{19} cm^{-3} and the sheet density is thus $1.2 \times 10^{13} \text{ cm}^{-2}$ if all the carriers are transferred to the wells.

The room temperature FTIR spectrum shown in Figure 1 shows an absorption peak at $5.25 \mu\text{m}$ (220 meV) with a full width at half maximum (FWHM) of 50 meV. The absorption peak is one order of magnitude wider than in n-type quantum wells. The major reason for this difference is the very large intrinsic state broadening in the valence band, which is due to hole-hole scattering and is expected to produce a width of 20 to 30 meV [7]. We attribute the

absorption peak of Figure 1 to the heavy hole to light hole transition as indicated in the inset. We calculate that the strain induced energy splitting between the heavy hole state and the light hole state is $\Delta = 150$ meV, while the quantum confinement induced energy splitting is 90 meV at $k = 0$. As a result the total energy difference between the heavy hole and light hole state is estimated to be 240 meV, which is consistent with what we observe in the absorption spectrum (220 meV).

We performed equal-wavelength pump-probe measurements at room temperature near 5 μm using the Stanford picosecond free electron laser (FEL). The output of FEL was a macropulse train with a repetition rate of 10 Hz and a macropulse duration of 3 ms. Each macropulse was made of a micropulse train with individual pulses separated by 85 ns and of a duration that is less than 1 ps. The laser was tunable from 4 to 6 μm while the pulsewidth (FWHM) obtained from autocorrelation measurements remained 0.7 to 1 ps, assuming a Gaussian pulseshape. A single pulse selection technique was used to reduce the thermal effects during the experiments. The peak intensity of the pump pulse on the sample was varied from 0.3 to 10 GW/cm^2 .

The change of transmission measured at 5.05 μm with a pump intensity of 2.5 GW/cm^2 is shown in Figure 2 on a logarithmic scale. Following the treatment of Ref. 8, the data has been analyzed using the population equations for a two-level system with the relaxation time τ being the only variable. The fits correspond to a relaxation time of 1 ps, 1.5 ps and 2 ps. Similar experiments have been performed throughout the broad absorption line and as a function of excitation level. Figure 3 shows the maximum induced transmission as a function of the relative intensity. The solid line is a best fit assuming a homogeneously broadened two-level system with a saturation intensity of 3.2 GW/cm^2 . This saturation intensity is significantly higher than in n-type quantum wells [1], in part because the absorption cross section for our p-type sample is 1 order of magnitude smaller than in n-type quantum wells. In general, the relaxation time increases with increasing excitation level, typically from ~ 1 ps to ~ 2 ps. As is expected from a homogeneously broadened system, the relaxation time appears to be wavelength independent within the accuracy of our measurements.

In the conduction band, polar LO-phonon scattering is the most relevant relaxation mechanism for both intersubband relaxation and intrasubband relaxation. In the valence band, the phonons and the holes can interact through the optical deformation potential, which is more efficient and less easily screened than the Frohlich interaction. As a result, the scattering time in the valence band is expected to be shorter than that in the conduction band. The relaxation time observed in our experiments is longer than 1 ps and therefore it is not likely to reflect the *initial intersubband* scattering event (dwell time) [9]. What is measured is the *intrasubband cooling* of the hot holes. The holes in the excited subband (light hole subband) are scattered to the heavy hole subband through optical deformation potential scattering. The intrasubband cooling then takes place by phonon emission on a 1 ps time scale. The actual situation is more complicated since hole-hole scattering is efficient and thus the hot holes can cool down quickly by giving energy to the cold hole reservoir. However, since the excited hole population is a significant fraction of the total hole population during all our measurements, this process may have only a limited contribution. The slight increase of the relaxation time at higher excitation intensity may indicate that hot-phonon reabsorption plays a role. We will present a detailed analysis of these different factors.

In conclusion, we report the first measurement of the intravalence band relaxation in p-type quantum wells by the infrared bleaching technique. A relaxation time of ~ 1.5 ps was observed. We attribute this relaxation time to the intrasubband cooling of the hot holes through optical deformation potential scattering. We acknowledge support from the US Office of Naval Research through contracts N00014-92-J-4063 and N00014-91-C-0170.

References

1. A. Seilmeier et al, *Phys. Rev. Lett.* **59**, 1345 (1987)
2. F. H. Julien et al, *Appl. Phys. Lett.* **53**, 116 (1988)
3. T. Elsaesser et al, *Appl. Phys. Lett.* **45**, 256 (1989)
4. M. C. Tatham, J. R. Ryan, and C. T. Foxon, *Phys. Rev. Lett.* **63**, 1637 (1989)
5. B. K. Ridley, *Phys. Rev.* **B39**, 5282 (1989)
6. J. N. Sweetser et al, *Appl. Phys. Lett.* **63**, 3461 (1993)
7. M. Asada, *IEEE J. Quantum Electron.* **QE-25**, 2019 (1989)
8. B. N. Murdin et al, *Semicond. Sci. Technol.* **9**, 1554 (1994)
9. J. F. Young, T. Gong, P. M. Fauchet, and P. J. Kelly, *Phys. Rev.* **B50**, 2208 (1994)

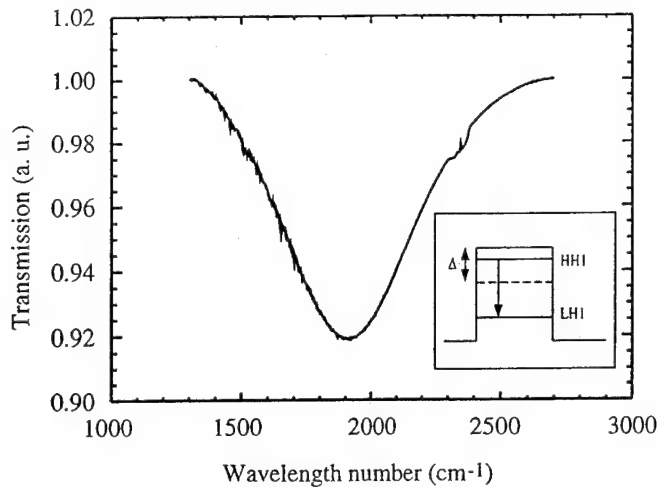


Figure 1. Infrared absorption of the QW sample. The strong absorption is due to the heavy hole 1 to light hole 1 transition as indicated in the inset. Δ is the strain induced energy splitting.

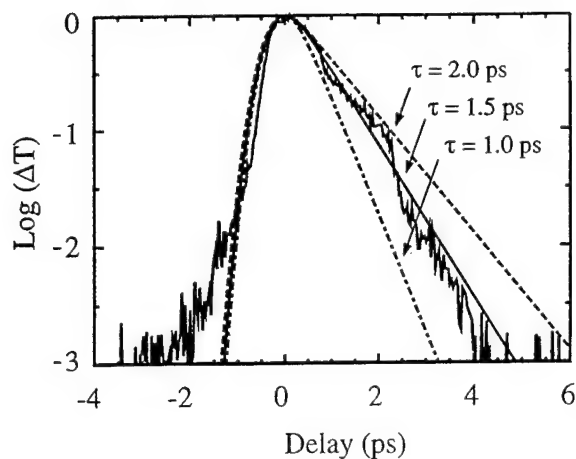


Figure 2. Pump induced transmission change of the probe beam for a pump intensity of 2.5 GW/cm² measured at 5.05 μ m as a function of the delay time, on a logarithmic scale. The fits assume an exponential relaxation of 1 ps, 1.5 ps and 2 ps.

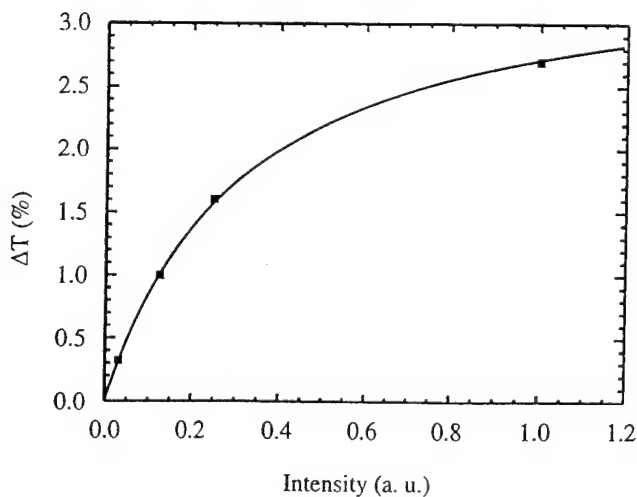


Figure 3. Peak value of the pump induced transmission change of the probe beam as a function of pump intensity. The solid line corresponds to the best fit with a saturation intensity of 3.2 GW/cm² and a complete bleaching producing a change in transmission of 3.6%.

Time-Resolved Photocarrier Decay For Mid-Infrared Materials With Excitation Correlation

Alan Kost, Linda West, T. C. Hasenberg, and D. H. Chow

Hughes Research Laboratories, 3011 Malibu Canyon Rd., Malibu, CA 90265
Tel. 310-317-5280, FAX 310-317-5483, E-Mail (Internet) akost@msmail4.hac.com

Perhaps the most frequently used approach to measuring electron-hole recombination rates in semiconductors is to examine photoluminescence decay. If the luminescence is at a wavelength of 1.5 μm or shorter, decay can be measured with picosecond time resolution using a streak camera, photodiode, or photon counting apparatus. Time-resolving photoluminescence in the mid-infrared is problematic because of the lack of fast photodiodes or suitable photocathodes for these wavelengths. Excitation correlation (EC) is an alternative to time-resolved luminescence that requires only slow photodetectors.¹⁻³ Previously, EC has been used to measure carrier decay for materials emitting in the visible and near infrared. Here we extend the technique to the mid-infrared. We describe numerical calculations to derive Shockley-Read, radiative, and Auger coefficients.

With EC, samples are excited by two short optical pulses separated in time by a variable amount τ . Figure 1a illustrates the case where excitation pulses are separated by a long time τ_1 so that there is no temporal overlap between photocarrier populations. The corresponding time integrated photoluminescence $I(\tau_1)$ is shown in Figure 1b. Figure 1c illustrates the case where excitation pulses are separated by a shorter time τ_2 so that photocarrier populations overlap. In general, luminescence is a nonlinear function of photocarrier density. This means that the level $I(\tau_2)$ (Figure 1d) is not generally equal to $I(\tau_1)$. Values for recombination constants are inferred from $I(\tau)$ with a fitting procedure described below.

The experimental set-up is shown in Figure 2. A modelocked Ti:Sapphire laser produces optical pulses ≈ 200 fs long at a repetition rate of 69 MHz. The output of the Ti:Sapphire laser is split into two beams of roughly equal average power. One beam follows a path of fixed length before it is focused onto the sample. The 2nd beam follows a path of variable length and is focused onto the same location on the sample. Photoluminescence is collected with a CaF_2 lens and imaged onto a cooled InSb photodiode for detection to at least 5 μm . Optical beams are chopped at frequencies of $5\nu_0$ and $6\nu_0$ respectively and a lock-in amplifier is used to detect the signal at the sum frequency of $11\nu_0$. This signal is proportional to the change in the integrated photoluminescence from overlapping populations making the measurement background free. The time resolution of the system is 200 fs - limited by the optical pulse duration.

To demonstrate EC for mid-infrared materials we examined a multiple quantum well (MQW) structure with $\text{Ga}_{0.75}\text{In}_{0.25}\text{Sb}/\text{InAs}$ Type II superlattices for the wells. These superlattices are of interest for a variety of infrared applications including detectors and lasers.⁴ The quantum well barriers are $\text{Al}_{0.2}\text{Ga}_{0.8}\text{Sb}$ and a top cladding layer is $\text{AlAs}_{0.08}\text{Sb}_{0.92}$. The upper clad is transparent to the 784 nm light from the Ti:Sapphire laser so that excitation generates electron-hole pairs in the MQW. Luminescence is at 3.2 μm for a temperature of 80K.

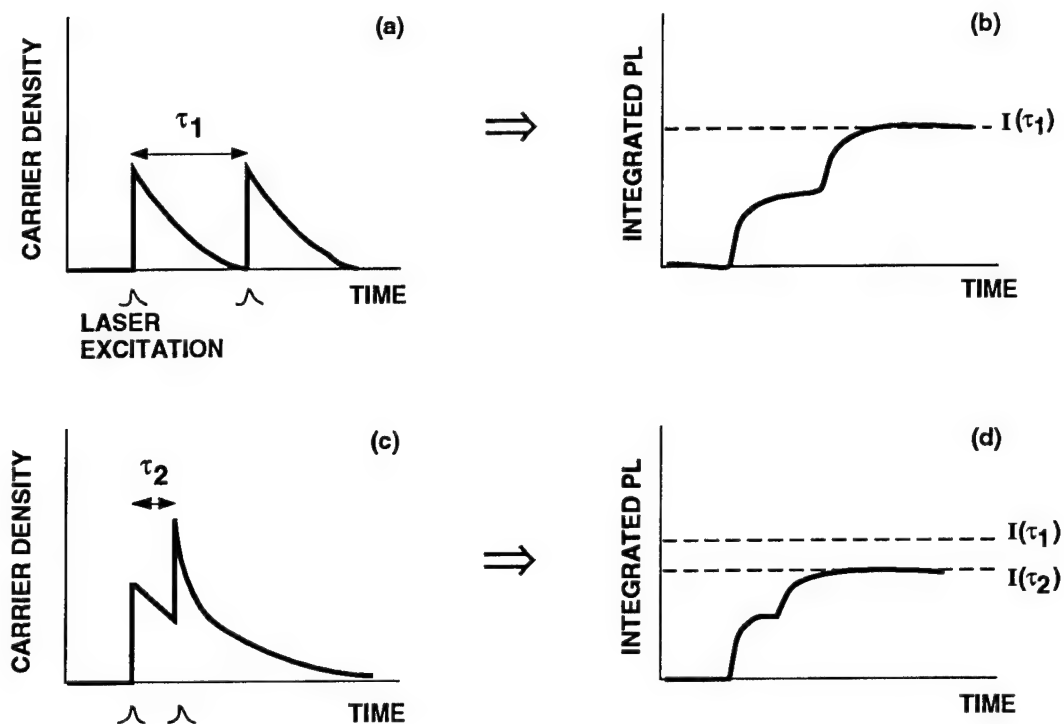


Figure 1. Overlapping populations modify the time-integrated photoluminescence.

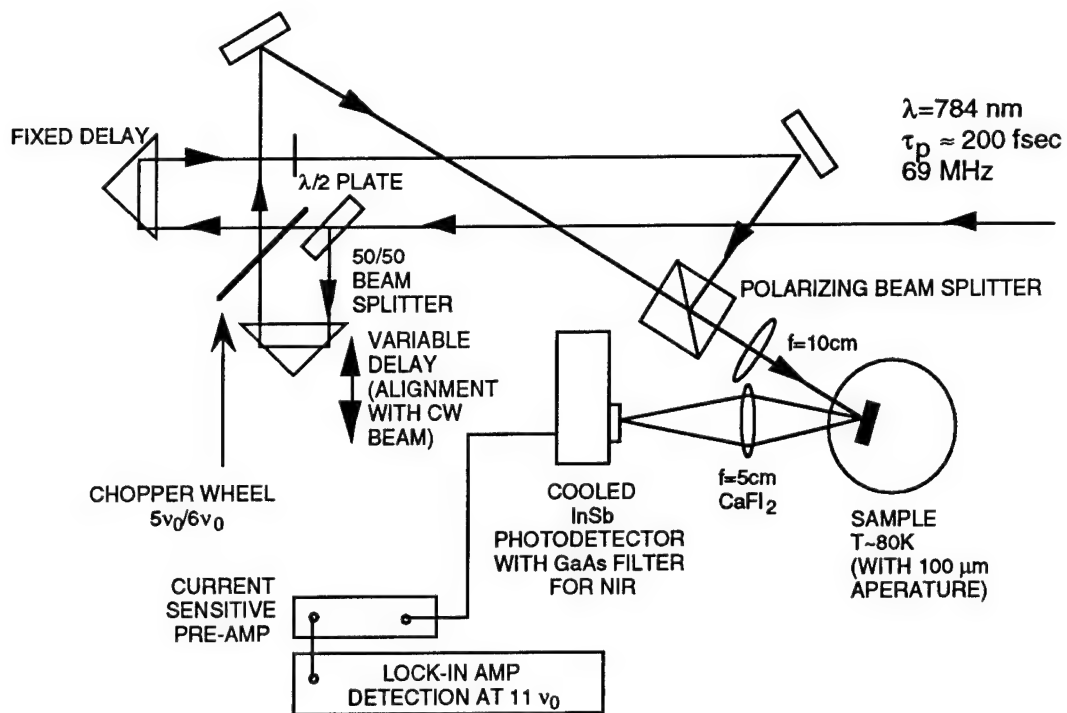


Figure 2. Experimental set-up to measure photocarrier decay by excitation correlation.

Figure 3 shows the correlation signal for the MQW. The average power in the excitation beams was 45 mW focused to a 40 μm diameter spot ($1/e$ diameter in intensity) so that the incident photon flux was $2 \times 10^{14} \text{ cm}^{-2}$ per pulse. Almost all of the incident photons are absorbed in the highly absorbing, 0.97 μm thick MQW region but the precise distribution of photocarriers in the wells is not known. If the photogenerated electron-hole pairs are distributed uniformly in just the first four quantum wells, the density is $2 \times 10^{19} \text{ cm}^{-3}$ in the wells. To obtain Shockley-Read, radiative, and Auger recombination rates, the data were fit using a numerical model taking the photocarrier decay to be $dn/dt = -c_1n - c_2n^2 - c_3n^3$ with c_1 , c_2 , and c_3 as adjustable parameters. The best fit was found for $c_2 = c_3 = 0$ and $c_1 = 0.7 \text{ ns}^{-1}$ which implies that the carrier decay is exponential with a time constant of 1.4 ns.

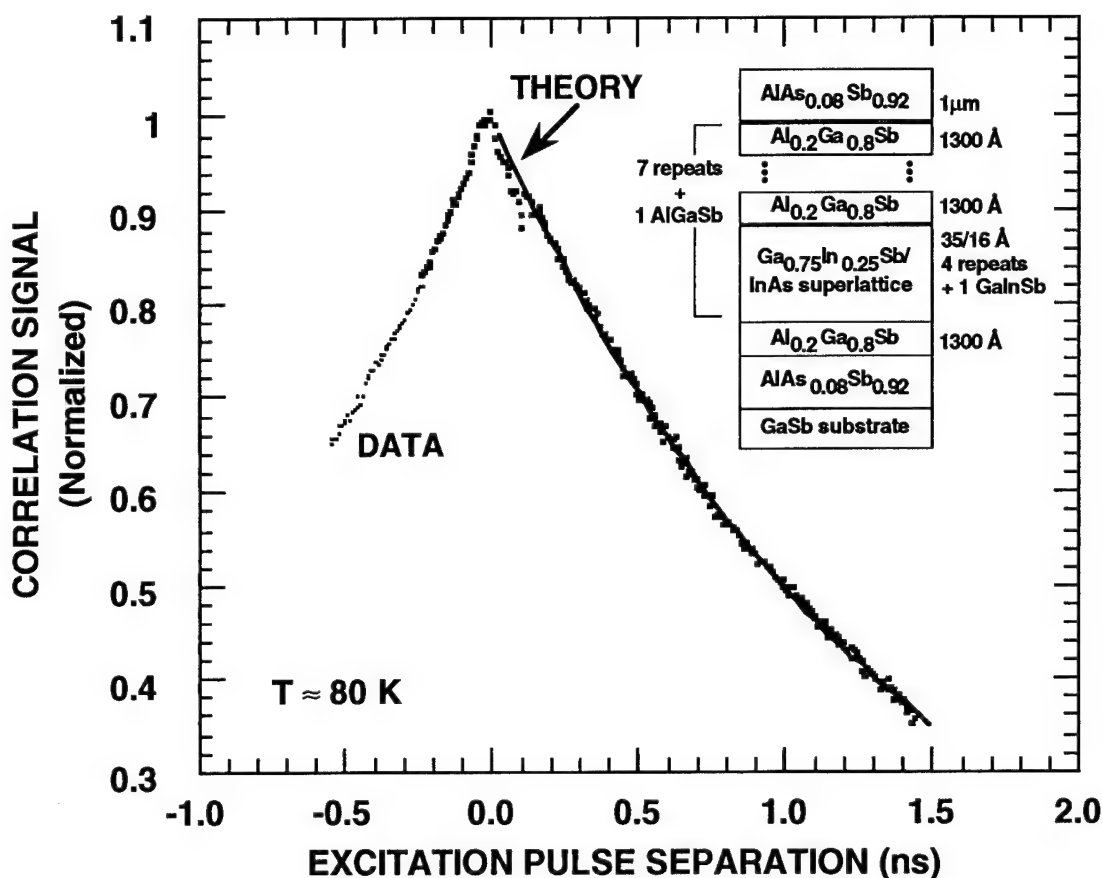


Figure 3. The excitation correlation and best fit to the data.

This work was supported in part by Air Force Phillips Laboratory contract F29601-93-C-0037.

REFERENCES:

1. D. Rosen, A. G. Doukas, Y. Budansky, A. Katz, and R. R. Alfano, Appl. Phys. Lett. **39**, 935 (1981).
2. M. Jorgensen and J. M. Hvan, Appl. Phys. Lett. **43**, 460 (1983).
3. M. B. Johnson, T. C. McGill, and A. T. Hunter, J. Appl. Phys. **63**, (1988).
4. D. H. Chow, R. H. Miles, J. N. Schulman, D. A. Collins, and T. C. McGill, Semicon. Sci. Technol. **6**, C47 (1991).

Arsenic-Ion-Implanted GaAs as an Ultrafast Photoconductor

H.H. Wang and J. F. Whitaker

Center for Ultrafast Optical Science, University of Michigan, Ann Arbor, MI 48109-2099
Tel: 313-763-4875; FAX: 313-763-4876

H. Fujioka

Dept. of Material Science & Mineral Eng., Univ. of California-Berkeley, Berkeley, CA 94720
Tel.: 510-642-0205; FAX: 510-642-9164

Z. Liliental-Weber

Lawrence Berkeley Laboratory, Berkeley, CA 94720
Tel.: 510-486-6276; Fax: 510-486-4995

It is now well known that low-temperature-MBE-grown GaAs (LT-GaAs) has a photoexcited carrier lifetime that is subpicosecond – or at most a few picoseconds – and, when annealed, outstanding properties in terms of photodetection and gating (*i.e.*, high resistivity, high breakdown voltage, and reasonable mobility) [1]. The unique behavior of LT-GaAs has even led to the creation of commercial detector and sampling gate applications based on these materials. However, due to the MBE growth process, LT-GaAs, is a relatively expensive material compared with conventional, LEC, undoped GaAs. Moreover, because of the low-temperature growth, LT-GaAs properties are highly dependent on the MBE conditions (*e.g.*, beam equivalent pressure, temperature calibration, *etc.*) and thus tend to vary from wafer to wafer, especially for different MBE machines. Furthermore, for the fabrication of MESFET-based, high-speed photoreceivers, low-temperature growth is not convenient due to circuit requirements for a *localized* photoconductive active area (with a high crystal quality and high mobility maintained in the rest of the device).

A potential alternative to LT-GaAs is arsenic-ion-implanted GaAs, not only because it uses a process which is compatible with conventional device fabrication, but also because its preparation cost is much cheaper. The material itself has a number of properties similar to those of LT-GaAs. For instance, it is non-stoichiometric (and As-rich) within the projection range of the implantation, and As-implanted GaAs that has been annealed has been found to contain As-precipitates inside the GaAs matrix [2]. We have measured, for the first time, the ultrafast photoconductive response for As-implanted GaAs, and also determined that the material has a mobility and breakdown-voltage behavior that is similar to LT-GaAs photoconductors. Resistivity, though less than that of LT-GaAs by nearly a factor of 10, has been found to be adequate for optoelectronic applications. In addition, we have also studied the persistent photoconductive response of the material – represented by tails on waveforms optoelectronically-switched with 100-fs laser pulses – versus dc voltage bias.

The substrates employed in the ion-implantation were LEC, undoped GaAs wafers with resistivity of about 1×10^7 ohm-cm. Arsenic atoms were implanted in the wafers with kinetic energy of 200 KeV and a dose of either 10^{15} or 10^{16} cm⁻². After implantation, wafers were broken into several pieces in order to anneal samples at different temperatures and for varying times. The most widely studied set of samples were annealed at $T_A = 200, 250,$ and 300°C for 1 hour each, and at 600°C for 15 s, 2 min and 20 min.

Transient reflectivity measurements were performed in a standard pump-probe configuration with 100-fs Ti:sapphire laser pulses at 850 nm in order to investigate which annealing conditions created materials with a fast carrier response. From the optical measurements, we have found that when $T_A \leq 300^\circ\text{C}$, the GaAs appears to remain in a polycrystalline or amorphous state even for long anneal times. However, if the sample was annealed above 600°C , the optical response was typical of a more monocrystalline sample. The

annealing time then became very critical, since the material needed to have a high enough defect density to provide ultrafast recombination, but also a low enough active defect density for the GaAs to have high resistivity and mobility. A range of carrier lifetimes were observed, although many of the samples exhibited subpicosecond response components (Fig. 1). As a result, several of the samples have been fabricated with simple detector patterns in order to measure dark resistance and photoconductive switching response.

The sheet resistance was measured for four of the samples implanted with an As dose of 10^{16} cm^{-2} . The unannealed sample, along with the one annealed at low temperature, had a very low resistivity, implying that defect densities were so high that hopping conduction dominated the dark current. However, an increase of almost four orders of magnitude in resistivity was achieved once the sample was annealed at 600°C for only 15 seconds. Therefore, the last two samples, which contain As precipitates, likely have a GaAs matrix that is nearly recrystallized, and they could also be used to measure photoconductive lifetimes.

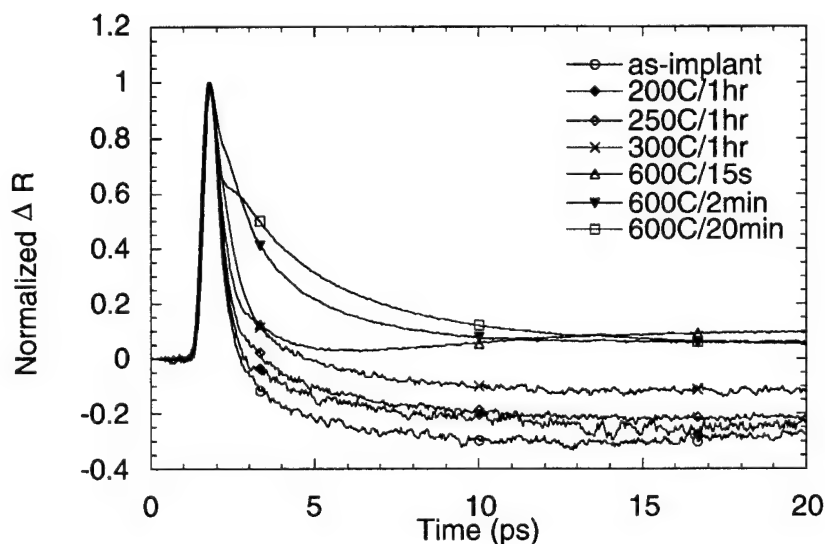


Fig. 1 Transient reflectivity for As-implanted GaAs under different annealing conditions. Symbols are markers.

The photoconductive switching characterization was performed by shorting a dc-biased coplanar stripline (CPS) with the 100-fs laser pulses. A standard electro-optic sampling experiment using a LiTaO₃ probe was conducted to measure the material detector response [3]. The photoconductive gap had a 20- μm separation, and the dc bias on the detector was 5 V. Figure 2 shows the photoconductive response of the implanted GaAs annealed at 600°C for 15s. The full-width-half-maximum (FWHM) of the detector response was 1.23 ps, and the $1/e$ fall time was 0.64 ps. The switching efficiency, which is proportional to the responsivity, was $\sim 2\%$, comparable to that of typical LT-GaAs layers and with approximately the same speed. Other GaAs wafers implanted with different doses and annealed at high temperature also displayed a similar, picosecond lifetime as in Fig. 2.

Another critical factor affecting the speed and practicality of these and any detectors is the bias-dependent tail effect. This has already been investigated for LT-GaAs photodetectors, where for growth conditions optimized for ultrafast response ($T_{\text{growth}} \sim 200^\circ\text{C}$, $T_A \sim 600^\circ\text{C}$ *in situ* for 10 min) it has been found that significant tails do not appear until bias voltages reach many tens of volts [4]. Here we have also observed the bias-dependent tail effect for As-implanted GaAs photodetectors, but for much lower bias voltages. As shown in Fig. 3, a persistent response is observed immediately as bias is increased above $V_b = 5 \text{ V}$. When V_b was increased to greater than 20 V, a secondary component of photocurrent significantly increased, lasting for about 100 to 150 ps. The effect of this persistent tail currently prevents the As-

implanted GaAs photodetectors from operating at high bias, but it may be possible to engineer implanted materials to avoid this effect. More comprehensive modelling of LT- and As-implanted GaAs is underway to determine the cause of the tails in the materials, although the observation of tails in the response of LT-GaAs which has been grown at higher temperatures (and thus has fewer defects) suggests a saturation of trapping states. Gallium-related or other defects that exist in As-implanted GaAs, but not in LT-GaAs, may also be responsible, perhaps contributing to the re-emission of trapped carriers and the tail response.

In summary, we have measured the first ultrafast photoconductive response of arsenic-implanted GaAs. With a picosecond lifetime, this material has the potential to be an attractive substitute for LT-GaAs in optoelectronic applications due to its low fabrication cost. We have also investigated bias-dependent tail effects in the photoconductive response of the material and plan to conduct further work to understand and diminish the persistent photocurrent.

References:

- [1] see J.F. Whitaker, *Mat. Sci. Eng.* **B22**, 61 (1993) and references therein.
- [2] A Claverie, F. Namavar, Z. Liliental-Weber, *Appl. Phys. Lett.* **62**, 1271 (1993).
- [3] J.A. Valdmanis, G.A. Mourou, *IEEE J. Quantum Electron.* **QE-22**, 69 (1986).
- [4] M. Frankel, *et al.*, *IEEE Trans. Electron Devices* **37**, 2493 (1990).

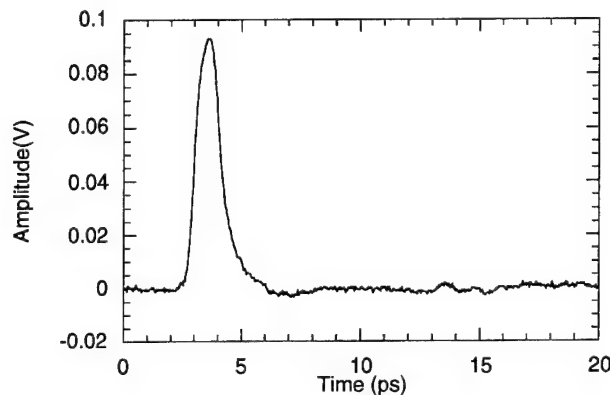


Fig. 2 Picosecond photoconductive response of As-implanted GaAs.

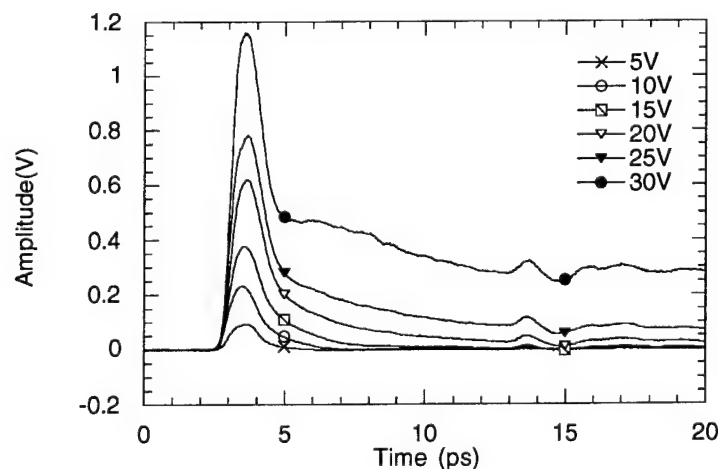


Fig. 3 Bias dependence of the photoconductive response of As-implanted GaAs. Symbols are markers.

Monday, March 13, 1995

All-Optical Switching

UMC 1:30 pm-2:45 pm
Ballrooms VI-VIII

Jay M. Wiesenfeld, *Presider*
AT&T Bell Laboratories

All-Optical Signal Processing Technology in 100 Gbit/s Optical TDM Transmission

Masatoshi Saruwatari

NTT Optical Network Systems Laboratories

1-2356 Take, Yokosuka-shi, Kanagawa, 238-03 Japan

Tel: +81-468-59-3042, Fax: +81-468-59-3396

The coming broadband network (B-ISDN) era will require ultrahigh speed technologies not only for transmission lines, but also for transmission nodes. The goal is to handle signal rates of more than 100-Gbit/s, so that vast amounts of information including data and pictures, can be provided to many subscribers through optical fiber cables. To this end, all-optical time-domain signal processing technologies are being studied for realizing ultrahigh-bit-rate optical time-division-multiplexing (TDM) transmission systems. They include high-speed picosecond optical pulse generation, all-optical multi/demultiplexing (MUX/DEMUX) and optical timing extraction techniques. Here, recent advances in these essential technologies and applications to 100Gbit/s optical TDM transmission will be described together with major issues and future prospects.

In order to achieve very high-speed optical TDM transmission, it is essential for optical pulse sources to generate transform-limited (TL) picosecond pulses, namely, < 5 ps chirpless pulses at repetition-rates ranging from 5 to 20 GHz. In addition, tunable and controllable repetition rates are required to permit synchronization with other signals.

Harmonic mode-locking of Er-doped fiber (EDF) lasers is promising because it offers pure TL picosecond pulses and tunable repetition rates and wavelength. By using a single-polarization cavity, a stable 3.3ps TL pulse with a 0.33 time-bandwidth product was obtained up to 20 GHz without any bit-error [1]. Also, a wavelength tunability over 7nm was confirmed to optimize transmission characteristics. Recently, supercontinuum (SC) pulse generation in dispersion-shifted fiber [2] was demonstrated with EDF laser pumping. This is a novel optical source applicable for TDM/WDM systems as well as subpicosecond pulse generators. This is because less than 1-ps pulses at arbitrary wavelengths can be attained by merely filtering the SC spectrum. Recent 100Gbit/s TDM transmission experiments have been conducted using these pulse generation techniques.

All-optical demultiplexers (DEMUXs) are key devices for developing optical TDM transmission systems. To apply the DEMUXs to real communication systems, the following requirements must be satisfied; fast and stable bit-error-free operation, low control power suitability for LD or Er-laser pumping, polarization independent (PI) operation, synchronization to received high-speed signals, and cascability for multi-output operation.

So far, error-free DEMEX operation pumped by LD or Er-lasers has been conducted with various methods such as four-wave-mixing (FWM) switches using long fibers [3] or LDAs [4] as well as loop mirror switches using fibers (NOLM) [5] or LDAs (TOAD)[6]. Polarization independent (PI) operation was also realized at up to 100 Gbit/s using a cross-spliced polarization-preserving fiber NOLM switch [7] or a FWM fiber switch having a polarization rotating mirror structure [8]. Recently, 100 Gbit/s error-free operation has been demonstrated with a very compact LDA-FWM switch [9], and 160 Gbit/s with a TOAD switch [10]. Moreover, novel four-output 100Gbit/s demultiplexing based on multi-channel FWM [11] has been successfully conducted by applying a linearly-chirped square pump pulse generated from SC pulses.

Timing extraction, which extracts the timed clock from the received optical signals, is one of the key functions for constructing high-speed optical TDM transmission systems. Requirements for optical timing extraction include ultrafast operation, low phase noise of less than 1 ps RMS jitter, high sensitivity and polarization independence.

To date, various timing extraction techniques based on fast photonics have been studied. They are classified into three approaches: optical tank circuit [12], injection locking [13], and phase-lock loop (PLL) circuits using a LD amplifier as a fast phase detector [14]. The PLL has the advantage of permitting, in principle, complete retiming with no phase-error.

Operation speed of the PLL is determined by the response of the phase detector used. By using all-optical gain modulation in LD amplifiers, a 6.3-GHz retimed signal has been recovered using a residual 6.3-GHz component in a 100-Gbit/s optical TDM signal [15]. Recently, a prescaler PLL circuit [16,17] was reported where the prescaled frequency clock of 6.3GHz, 1/16th of 100-GHz, was directly extracted from the complete 100 Gbit/s signal without 6.3GHz component. This utilizes the harmonic frequency components that the short optical clock possesses and the high speed four-wave-mixing process in the LDA instead of gain-saturation. [With this method, the prescaled frequency clock of 6.3GHz can be extracted from randomly modulated 100 Gbit/s and 200 Gbit/s signals.]

100-Gbit/s optical TDM transmission systems will utilize the above technologies as shown in Fig.1. They include a wavelength-tunable mode-locked Er fiber laser, a 16:1 MUX made with a silica-based planar light-wave circuit (PLC), a timing extraction phase-locked loop (PLL) using a traveling-wave laser-diode amplifier (TW-LDA) as a phase detector, and an all-optical DEMUX using a polarization-maintaining 3-km fiber loop or a TW-LDA as the nonlinear (Kerr effect or four-wave-mixing) materials. The Er laser provides stable 6.3-GHz, 3.5-ps transform-limited (TL) pulses for external modulation, and the PLC-MUX stably multiplexes the 6.3-Gbit/s baseline signal into a 100 Gbit/s test signal. The PLL circuit extracts a 6.3-GHz prescaled clock from the received 100-Gbit/s signal, and the all-optical DEMUX demultiplexes the 100-Gbit/s TDM signal into the original 6.3-Gbit/s signal.

With these techniques, a 100-Gbit/s optical TDM signal, 16 x 6.3-Gbit/s, was successfully transmitted 200-km without any bit error through five fibers connected via four in-line Er-doped fiber amplifiers. These new technologies have the potential to achieve more than 100-Gbit/s transmission over longer distances and will play a major role in establishing tera-bit communication networks.

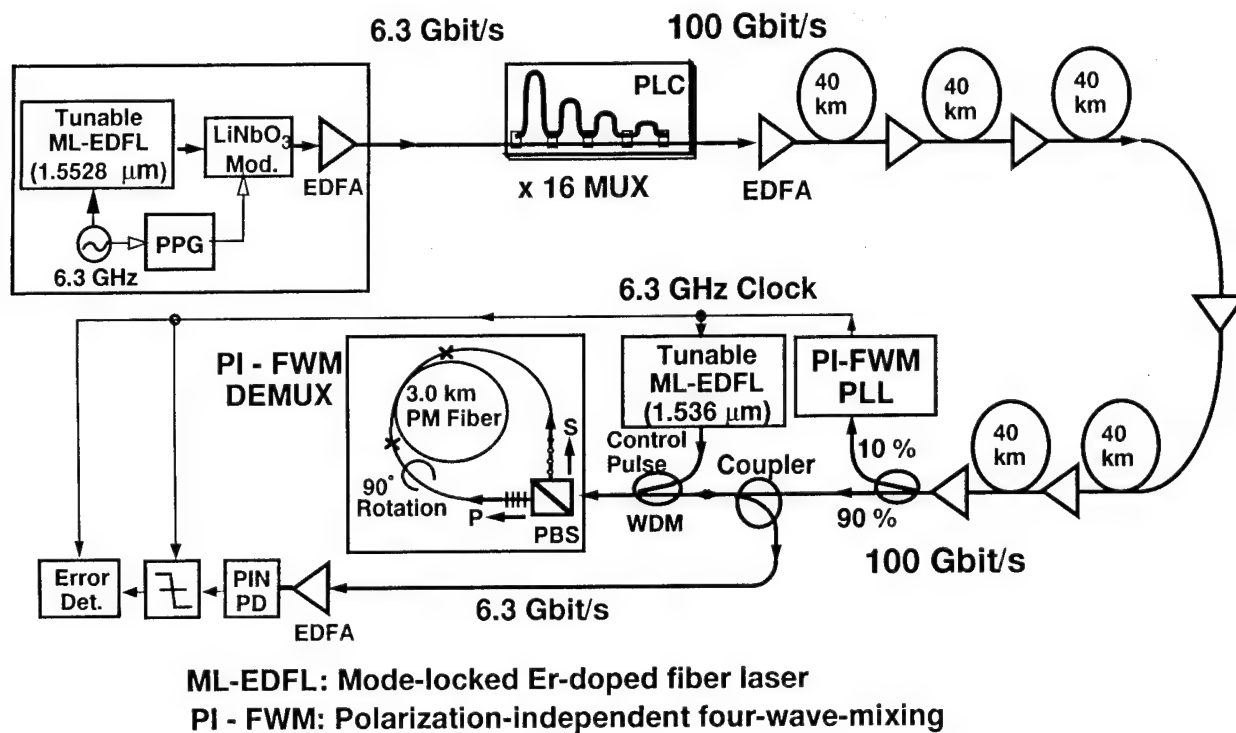


Fig.1. Experimental setup for 100 Gbit/s, 200 km Optical TDM Transmission

References

- [1] H. Takara, S. Kawanishi, and M. Saruwatari, Electron. Lett., **29**, 1149(1993); **30**, 1143(1994).
- [2] T.Morioka, S.Kawanishi, K.Mori, and M.Saruwatari, Electron. Lett., **30**, 790(1994), **30**, 1166(1994).
- [3] P. A. Andrekson et. al., Electron. Lett., **27**, 922(1991).
- [4] R. Ludwig and G. Laybon, Tech.Digest of ECOC'93, ThP12.2(1993).
- [5] P. A. Andrekson et al., Tech.Digest of OFC'92, PDp. 8, 1992.
- [6] A.D.Ellis and D.M. Spirit, Electron. Lett., **30**, 72(1994).
- [7] K. Uchiyama, S.Kawanishi, H.Takara, T.Morioka, and M.Saruwatari, Elect. Lett., **30**, 873(1994).
- [8] T.Morioka, S. Kawanishi, K. Uchiyama, H.Takara, and M. Saruwatari, Elect. Lett., **30**, 591(1994).
- [9] S.Kawanishi, T.Morioka, O.Kamatani, H.Takara, J.M.Jacob and M. Saruwatari, Elect. Lett., **30**, 981(1994).
- [10] K.Suzuki, K.Iwatsuki, S.Nishi and M.Saruwatari, Elect. Lett., **30**, 660(1994).
- [11] T.Morioka, S.Kawanishi, H.Takara, K.Mori and M. Saruwatari, Tech. Digest of ECOC'94, Mo.B.4.4, Firenze(1994.9).
- [12] M. Jinno and T. Matsumoto, IEEE J. of Quant. Elect., **28**, 895(1992).
- [13] P. E. Barnsley et al., IEEE Photonics Technol. Lett., **4**, 83(1992)/ As et al., Elect.Lett., **29**, 141(1993)/ A. Ehrhardt, et al., ECOC'93, ThP 12.9(1993).
- [14] S. Kawanishi and M. Saruwatari, Tech. Dig. ECOC'89, Mob4-5(1989)/ K. Takayama et al., IEEE Photon.Technol.Lett., **4**, 99(1992).
- [15] S. Kawanishi, H. Takara, K. Uchiyama, M. Saruwatari, and T. Kitoh, Electron. Lett., **29**, 2211(1993).
- [16] O.Kamatani, S.Kawanishi and M.Saruwatari, Electron. Lett., **30**, 807(1994).
- [17] S. Kawanishi, T. Morioka, O. Kamatani, H. Takara, and M. Saruwatari, Electron. Lett., **30**, 800(1994).

Ultrafast Wavelength Conversion and Switching by Four-wave-mixing in Semiconductor Laser Amplifiers

R. Ludwig, W. Pieper, R. Schnabel, H.G. Weber
 Heinrich-Hertz-Institut für Nachrichtentechnik Berlin GmbH
 Einsteinufer 37, 10587 Berlin, GERMANY
 Phone: +49 30 31002-446, Fax: -241, e-mail: LUDWIG@HHI.DE

Semiconductor laser amplifiers (SLA) will play an important role as functional devices for optical signal processing. The main advantages of these devices are optical gain, compactness and the potential for opto-electronic integration. Applications of the SLA, in which the operation speed is restricted by the free carrier lifetime to less than about 10 GHz are studied extensively [1]. In this paper we report on applications of the SLA, in which the operation speed is determined by intraband dynamic (spectral hole burning, dynamic carrier heating) with characteristic times in the femtosecond range. The following experiments are considered: wavelength- or frequency-conversion of optical data signals, operation as demultiplexer or all-optical AND-gate, and finally operation as optical-phase conjugator for compensating deterministic pulse distortions caused by linear fiber dispersion and nonlinear self-phase modulation on the fiber. All experiments reported here have in common, that they use four-wave mixing (FWM) based on the ultrafast gain dynamics in SLA which promises data rates in excess of 100Gbit/s.

Fig. 1 depicts a typical FWM-spectrum. Two light waves (output powers P_0 and P_1) coupled into a SLA cause modulation of gain and refractive index at the beat frequency (the frequency spacing Δf) between the two incident light waves. For small frequency spacings ($\Delta f < 10$ GHz) the physical mechanism behind FWM is predominantly carrier density modulation at the beat frequency Δf . For large frequency spacings ($\Delta f > 10$ GHz), the efficiency for carrier density modulation decreases strongly and modulation of the carrier distribution (e.g. spectral hole burning and carrier heating) becomes important [2]. The gain and refractive index modulations generate two new light waves, (output powers P_{-1} and P_2) which are frequency shifted from the two input waves by the beat frequency Δf . If one of the two input waves is modulated (e.g. the wave corresponding to P_1), one of the newly generated waves (P_{-1}) represents a frequency shifted and phase conjugated replica of this data signal. The frequency conversion range may extend over the entire gain curve of the SLA. The maximum frequency shift obtained in our experiments was $2\Delta f = 15\text{THz} = 120\text{ nm}$.

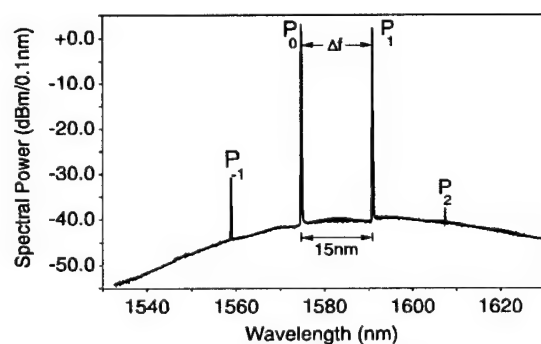


Fig. 1: Four-Wave-Mixing Spectrum

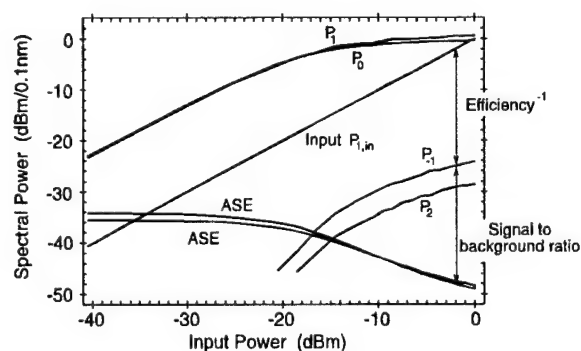


Fig. 2: Dependence of the components in the FWM-spectrum on the input power

Fig. 2 depicts the output powers P_{-1} , P_0 , P_1 , P_2 and the ASE-powers at the wavelengths (λ_{-1} , λ_2) corresponding to the P_{-1} and P_2 -signals versus the input power $P_{1,in}$. In this experiment, both input waves were cw-waves with the same input powers. The resolution of the optical spectrum analyzer is 0.1 nm. Indicated

in this figure is also the FWM-efficiency, i.e. the ratio $P_{-1}/P_{1,in}$ and the signal to background ratio $SBR = P_{-1}/ASE(\lambda_{-1})$. It is evident from the results in Fig. 2, that the FWM-efficiency has a maximum between -15 and -10 dBm input power and decreases for higher input powers. On the other hand, the signal to background ratio reveals a steady increase with increasing input power. Several groups performed studies on the FWM-efficiency /3, 4/ and on the SBR /5/. In a system application the SBR is related to the signal to noise ratio which determines the quality of the transmission system. Fig. 3 depicts bit error rate (BER) measurements of a 5 Gbit/s data signal for 3 different SBR-values. The experimental results reveal that $SBR > 20$ dB is required for a satisfactory transmission quality at 5 Gbit/s.

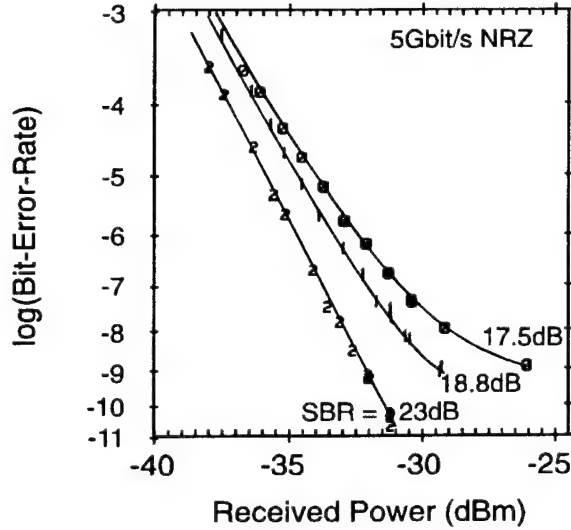


Fig. 3: Bit error rate measurements

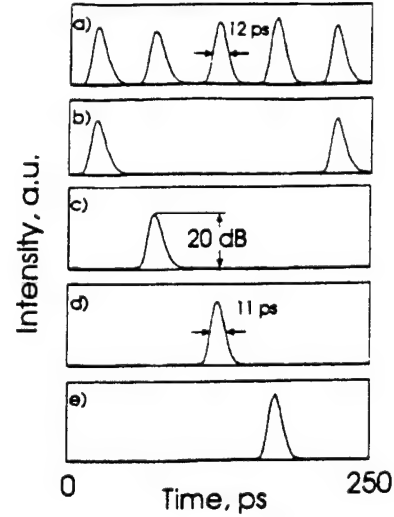


Fig. 4: Streak camera measurement of a 20 GHz pulse train, and four demultiplexed 5 GHz pulse trains

Based on the above described FWM-scheme several wavelength or frequency conversion experiments have been reported: 25 nm wavelength conversion of a train of 30 ps pulses /6, 7/, 20 nm wavelength conversion of a 622 Mbit/s data signal /5/, 15 nm wavelength conversion of a 18 Gbit/s data signal /8/ and 4 nm frequency conversion for various high bit rate data signals /9/. In all these experiments the signal was converted to a shorter wavelength. With optical pulses for both input signals and with one of the newly generated FWM-components selected by an optical filter, this schema was also used as optical demultiplexer or AND-gate. A 3 GHz pulse train was demultiplexed to 1 GHz /8/, and a 20 Gbit/s /10/ and a 100 Gbit/s /11/ data signal were demultiplexed. We describe the 20 Gbit/s demultiplexing experiment in more detail. BER-measurements revealed error free transmission. The bit rate was only limited by the available pulse width of the signal pulses. The low frequency carrier density dynamics in the SLA caused an intersymbol interference which gives raise to a power penalty. By an appropriate feed forward of the injection current into the SLA this penalty was reduced to 2dB and moreover the demultiplexing efficiency was increased. Fig. 4 depicts Streak camera measurements of a 20 GHz pulse train (a) and four (b, c, d, e) demultiplexed 5 GHz pulse trains. The extinction ratio was > 20 dB.

As indicated above, the newly generated FWM-components are not only frequency shifted but also phase conjugated replica of the input data signal. This property of the FWM-scheme was used in transmission experiments (midway spectral inversion) to compensate for signal deformations due to chromatic dispersion of the fiber /12/ and due to fiber nonlinearity /13/.

The above described FWM-scheme has the disadvantage, that both light signals at the SLA input need to have the same state of polarisation. There are however other schemes [14, 15], which for instance enable polarisation independent frequency conversion. In Ref. [14] an experiment was reported with polarisation independent frequency conversion of a 10-channel OFDM signal with a channel spacing of 9 GHz, a modulation rate of 140 Mbit/s per channel and the corresponding overall signal bandwidth of 90 GHz. BER-measurements on the 275 GHz frequency shifted OFDM-signal revealed no severe system degradation due to polarisation fluctuation or cross talk.

Ultrafast four-wave mixing in semiconductor laser amplifiers offers several attractive applications. The examples reported here include wavelength conversion, demultiplexing and optical phase conjugation. The technique has the potential for use with bit rates in excess of 100 Gbit/s. Moreover, as this technique is based on semiconductor devices, it has the potential for monolithic integration on InP to provide compact and reliable components.

References

- /1/ H.G.Weber, G. Großkopf, R. Ludwig, E. Patzak, R. Schnabel: ECOC/IOOC'91, Paris, paper MoC2.1
- /2/ L.F. Tiemeijer: Appl.Phys.Lett., 1991, Vol.59, No.5, pp. 499-501
- /3/ A. D'Ottavi, E. Iannone, A. Mecozzi, S. Scotti, P. Spano, R. Dall'Ara, G. Guekos, J. Eckner: ECOC'94, Florence, Vol.2, pp.737-740
- /4/ J. Zhou, N. Park, J.W. Dawson, K.J. Vahala, M.A. Newkirk, B.I. Miller: Appl. Phys. Lett. 1993, Vol.63, No.9, pp.1179-1181
- /5/ M.C. Tatham, G. Sherlock: in Integrated Photonics Research, Palm Springs, 1993, Tech. Dig. PD1
- /6/ R. Schnabel, W. Pieper, R. Ludwig, H.G. Weber: in Photonics in Switching, Palm Springs, 1993, Tech. Dig. PD1
- /7/ R. Schnabel, W. Pieper, R. Ludwig, H.G. Weber: Electron. Lett., 1993, Vol. 29, No. 9, pp. 821-822
- /8/ R. Schnabel, W. Pieper, A. Ehrhardt, M. Eiselt, H.G. Weber: Electron. Lett., 1993, Vol. 29, No.23, pp. 2047-2048
- /9/ R. Ludwig, G. Raybon: Electron.Lett., 1994, Vol.30, No.4, pp.338-339
- /10/ R. Ludwig, G. Raybon: ECOC'93, Montreux, paper ThP 12.2
- /11/ S. Kawanishi, T. Morioka, O. Kawatari, H. Takara, J.M. Jacob, M. Sarawatari: Electron. Lett., 1994, Vol.30, No.12, pp.981-982
- /12/ M.C. Tatham, G. Sherlock, L.D. Westbrook: Electron. Lett., 1993, Vol.29, No.21, pp.1851-1852
- /13/ W. Pieper, C. Kurtzke, R. Schnabel, D. Breuer, R. Ludwig, H.G. Weber, K. Petermann: Electron. Lett., 1994, Vol.30, No.9, pp.724-726
- /14/ R. Schnabel, U. Hilbk, Th. Hermes, P. Meißner, C.v.Helmolt, K. Magari, F. Raub, W. Pieper, F.J. Westphal, R. Ludwig, L. Küller, H.G. Weber: IEEE Photon. Techn. Lett., 1994, Vol.6, No.1, pp.56-58
- /15/ R.M. Jopson, R.E. Tench: Electron. Lett., 1993, Vol.29, No.25, pp. 2216-2217

Picosecond All-Optical Switching of a Quantum Well Etalon Using Spin-Polarization Relaxation and Electron Tunneling

Yuji Nishikawa, Atsushi Tackeuchi, Satoshi Nakamura, Shunichi Muto,
and Naoki Yokoyama

Fujitsu Laboratories Ltd.,

10-1 Morinosato-Wakamiya, Atsugi, Kanagawa 243-01, Japan

TEL +81(462)48-3111, FAX +81(462)48-5193

Recently strong emphasis is put on searching for a large and fast nonlinear optical material to realize all-optical switching. In fact, ultrafast optical switching is expected to be very important in future ultra-high bit rate optical network in such a role as an interface between electronic circuits and optical systems. The multiple quantum well (MQW) structure has attracted much attention due to its remarkably large optical nonlinearity in excitonic absorption bleaching. However, absorption recovery in MQWs takes tens of nanoseconds due to the restriction by the recombination lifetime. This recovery time is too slow in comparison with electronic devices. We observed a picosecond absorption recovery of circularly polarized light due to electron spin relaxation in GaAs/AlGaAs MQW.¹⁾ We showed that the absorption recovered to the half of the original value at 16 ps at room temperature.¹⁾ Recently, Kawazoe et al. obtained picosecond polarization full switching in AlGaAs/AlAs MQW using spin relaxation. They used the absorption change and obtained a full switching signal by electrically subtracting the signals of the right and the left polarized light.²⁾ In this paper, we demonstrate the optical gate operation of a quantum well etalon using its refractive index change due to spin relaxation and the electron tunneling. The use of the refractive index change enabled us to demonstrate an all-optical gate operation using a simple method of the optical subtraction between the signals of the right and the left polarized light.

By matching the wavelength of the circularly polarized pump to the e1-hh1 transition energy in quantum wells, we can excite the fully spin-polarized electrons from the heavy hole level. After spin relaxation, populations of up- and down-spin carriers are equal. Optical gate operation of the etalon is realized by the spin-dependent shift of the Fabry-Perot (FP) peak. Up-spin-aligned carriers shift only the FP peak of the left circularly polarized light, leaving the FP peak of the right circularly polarized light unchanged. Similarly to the absorption change, these two FP peaks reach the same position after spin relaxation. Therefore, when we observe the

difference between the left and the right circularly polarized components of the probe beam, we can obtain the picosecond full switching signal caused by spin relaxation.

The structure used for this experiment was a type-II tunneling bi-quantum well (TBQ) as shown in Fig. 1.³⁾ The merit of the use of the type-II TBQ instead of MQW is the controllability of the recovery time from the absorption and refractive index changes using the electron tunneling. The type-II TBQ etalon used here consists of 97 periods of type-II TBQs with 2.8-nm GaAs quantum wells, 7.1-nm AlAs wells and 1.7-nm Al_{0.51}Ga_{0.49}As barriers sandwiched by AlAs/Al_{0.25}Ga_{0.75}As (64.2 nm/54.4 nm) distributed Bragg reflectors (DBR), 14 periods for the back mirror and 9 periods for the front mirror. We found an e1-hh1 excitonic peak in the GaAs wells at 744.0 nm and a Fabry-Perot (FP) peak at 753.6 nm with a 3-nm full width at half maximum.

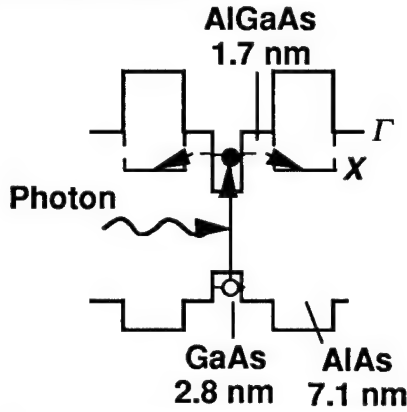


Figure 1. The schematic band diagram of the type-II TBQ structure.

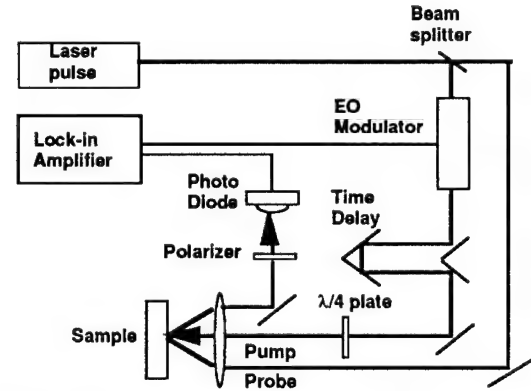


Figure 2. Experimental setup with the optical differential method to demonstrate the polarization switching. The direction of the polarizer was set perpendicular to the polarization of the probe beam.

We performed time-resolved pump-probe measurements shown in Fig. 2. The time resolution of our setup is about 5 ps. We tuned the pump and probe wavelengths to the linear part of the FP peak of the reflection spectrum of the etalon, which means the pumping on the foot of the e1-hh1 excitonic peak. A quarter-wave plate makes the left circularly polarized pump beam, while the probe beam is a linearly polarized light. The direction of the polarizer is set perpendicular to the polarization of the initial probe beam to obtain the polarization switching signal.

The linearly polarized light consists of equal amounts of the right and the left circularly polarized light. Then, the intensity, I_{perp} , of the output-light which is perpendicular to the polarization of the probe beam can be described as:

$$I_{\text{perp}} = \frac{1}{2} [(E + \sqrt{2}\Delta_+)(E + \sqrt{2}\Delta_-) \{1 - \cos(\phi_+ - \phi_-)\} + (\Delta_+ - \Delta_-)^2] \\ \propto (N_+ - N_-)^2$$

where E is the electric field of the initial linearly polarized probe and ϕ_+ (ϕ_-) and Δ_+ (Δ_-) are the phase and electric field change of the left (right) circularly polarized component of the probe beam and N_+ (N_-) is a density of spin-up (down) electrons. We neglect the effects of hole-spin polarization, since it decays in less than a picosecond. When a polarizer is set perpendicular to the polarization of the probe beam, the switching signal with a decay time of $(2/T_t + 4/T_s)^{-1}$ is expected, where T_t and T_s are the decay times by the electron tunneling and spin relaxation, respectively. This method provides us with a simple all-optical switching setup.

Figure 3 shows an all-optical gate operation of the etalon using spin relaxation at room temperature. The pump pulse energy was $48 \text{ fJ}/\mu\text{m}^2$. With the time resolution of about 5 ps, the decay time of 7 ps was achieved. The experimental decay is consistent with the expected value of 4 ps calculated by $(2/T_t + 4/T_s)^{-1}$ as the combination of spin relaxation ($T_s \sim 32 \text{ ps}$ ¹⁾) and the Γ -X tunneling of electrons ($T_t = 17 \text{ ps}$ ³⁾).

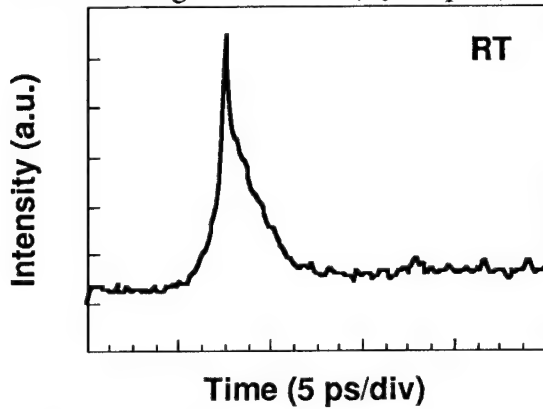


Figure 3. All-optical switching signal of the type-II TBQ etalon for the pump pulse energy of $48 \text{ fJ}/\mu\text{m}^2$ at room temperature.

We emphasize that the new setup needs only two additional optical parts, *i.e.*, a quarter-wave plate and a polarizer compared to the conventional all-optical switching setup. We also note that our system has a potential for high repetition operation²⁾, since switching signal obtained by a differential method remains the same as long as we operate it in regions where the optical nonlinearity is proportional to the pump energy.

To summarize, the all-optical gate operation of a type-II TBQ etalon was demonstrated using the spin relaxation. A simple optical differential method was also demonstrated for this measurement. The decay time of 7 ps was obtained by the combination of the tunneling effect and spin relaxation.

- 1) A. Tackeuchi, S. Muto, T. Inata and T. Fujii, Appl. Phys. Lett. 56, 2213 (1990).
- 2) T. Kawazoe, T. Mishina and Y. Masumoto, Jpn. J. Appl. Phys. 32, L1756 (1993).
- 3) A. Tackeuchi, T. Inata, Y. Nakata, S. Nakamura, Y. Sugiyama and S. Muto, Appl. Phys. Lett. 61, 1892 (1992).

Monday, March 13, 1995

High-Speed Testing

UMD 3:15 pm-5:00 pm
Ballrooms VI-VIII

Chi-Hsiang Lee, *Presider*
University of Maryland

Electro-Optic Testing of Ultrafast Electronic and Optoelectronic Devices

Tadao Nagatsuma

NTT LSI Laboratories,
3-1 Morinosato Wakamiya, Atsugi, Kanagawa 243-01, Japan
Tel. +81 462 40 2252, Fax. +81 462 40 4219

Rapid progress in the speed of semiconductor devices and integrated circuits has been creating a great need for new testing tools which have a capability of subpicosecond temporal resolution. Since early 1980s, ultrafast lasers and optoelectronic technologies have spawned a variety of novel measurement techniques whose bandwidth approaches the terahertz regime. One of the most promising optical techniques to meet this demand is electro-optic sampling (EOS) [1]-[4]. In the past 10 years, the EOS technique has become a laboratory standard. It will now move from in-house technique to widespread engineering use. In this paper, we review recent developments in electro-optic measurement techniques for characterization and diagnosis of ultrafast electronic and photonic devices and report application results.

The excellent practicability of the EOS technique arises from its simple measurement principle, i.e., optical intensity modulation using electro-optic or Pockels effect. Recent pulse generation technology based on semiconductor laser diodes, such as mode-locked diode-pumped Nd:YLF lasers, gain switched diode lasers and fiber ring lasers, has demonstrated the success of this technique around the world. Figure 1 shows a wingless 350 fs from a soliton pulse generator. All we have to do is just turn on some switches for the laser diode driver and the optical

amplifier. The most common system embodiments of the EOS technique are internal-node IC testing (Fig. 2(a)), and impulse response measurement of devices and ICs (Fig. 2(b)).

The internal-node-waveform probe is a powerful tool for finding a failure portion in ultrahigh-speed ICs due, for example, to unexpected geometrical parasitics when the IC clock frequency increases. Internal-node voltage signals in a 20-Gbit/s digital IC are traced in detail using an automated on-wafer IC probing system based on the external EOS [5] as shown in Fig. 3. Gate D2 was found to critically determine performance limits; the output waveform (node (E)) is close to a malfunction due to clock noise crosstalk and insufficient voltage swing.

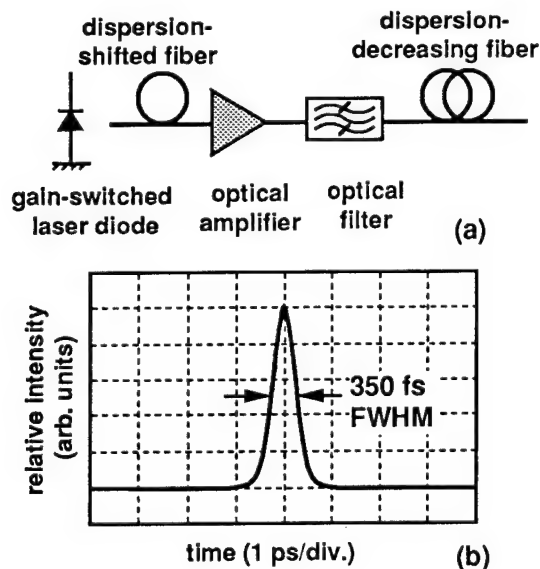


Fig. 1 (a) Block diagram of a soliton pulse generator. (b) Autocorrelation trace.

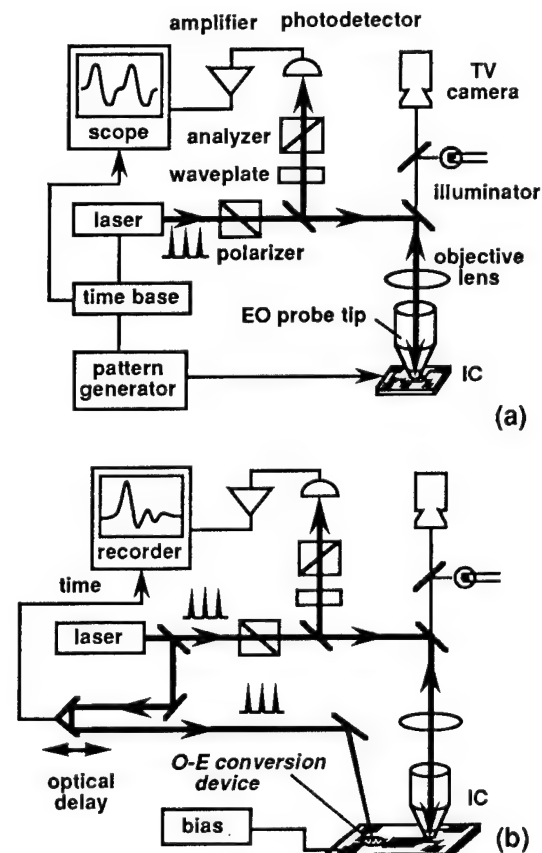


Fig. 2 Typical EOS system setup. (a) Internal-node probing system. (b) Pulse response measurement system.

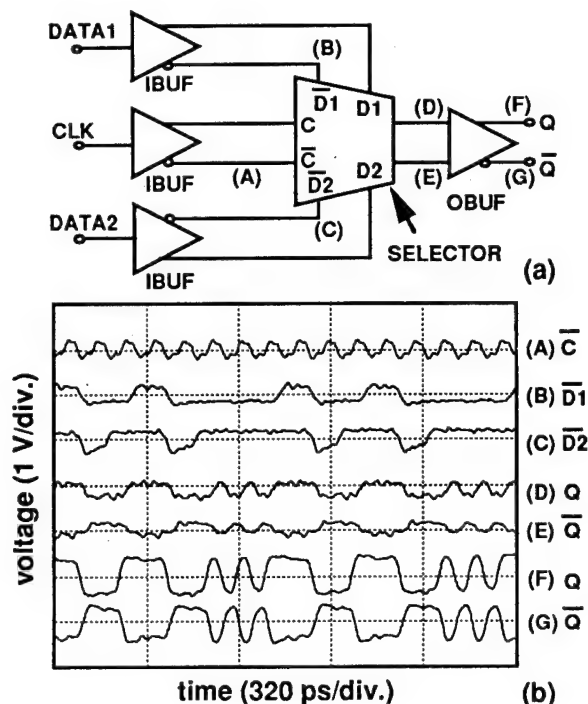


Fig. 3 Detailed waveform probing in GaAs HBT selector IC (@20 Gbit/s).

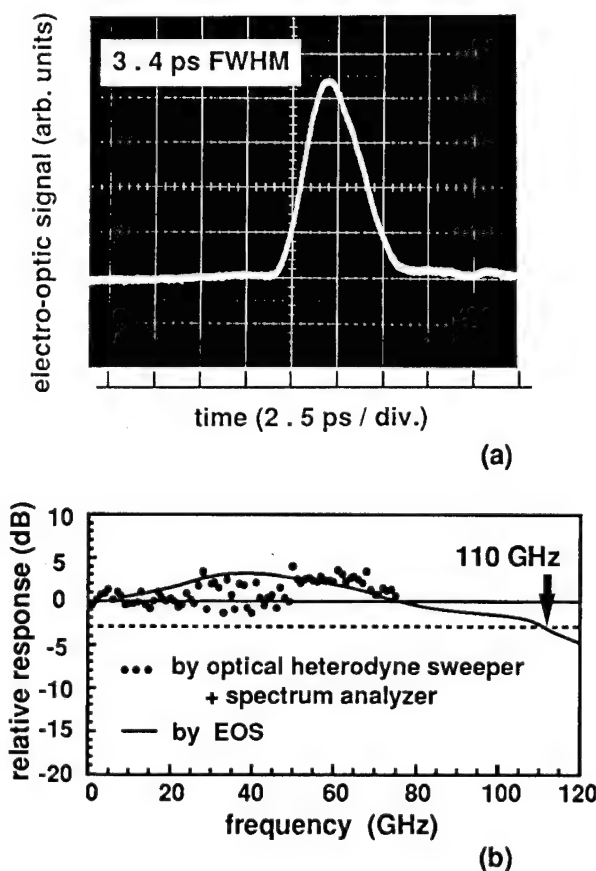


Fig. 4 Time (a) and frequency (b) characteristics of waveguide-type p-i-n photodiode (@1.55 μm).

Pulse response characterization of devices has been intensively studied using optical triggering and probing schemes. This offers jitter-free measurement. This scheme can be applied to time-domain network analysis for measuring S-parameters [6]. Two kinds of ultrafast photonic devices are characterized using the 1.55- μm soliton pulse generator of Fig. 1. The first example is a novel p-i-n photodiode with a multi-mode waveguide and mushroom structure devised to achieve both high efficiency and large bandwidth (Fig. 4) [7]. By a Fourier transformation of the time-domain response, the frequency response of the photodiode can be plotted by comparing the result obtained with the conventional network analyzer whose upper frequency limit is 75 GHz. Another example is a photoconductive AND gate for an ultrafast demultiplexer circuit made with low-temperature grown InGaAs/InAlAs MSM photodetectors (Fig. 5) [8]. The circuit has a differential configuration to increase the contrast ratio, avoiding the signal feedthrough problem. The expected operation of signal cancellation in the picosecond regime is confirmed by internally probing the circuit when it was triggered by the soliton pulse. (only PD1 was illuminated.) The switching speed of resonant tunneling diodes is also measured with the optical triggering and probing schemes. Detailed results are presented at this meeting.

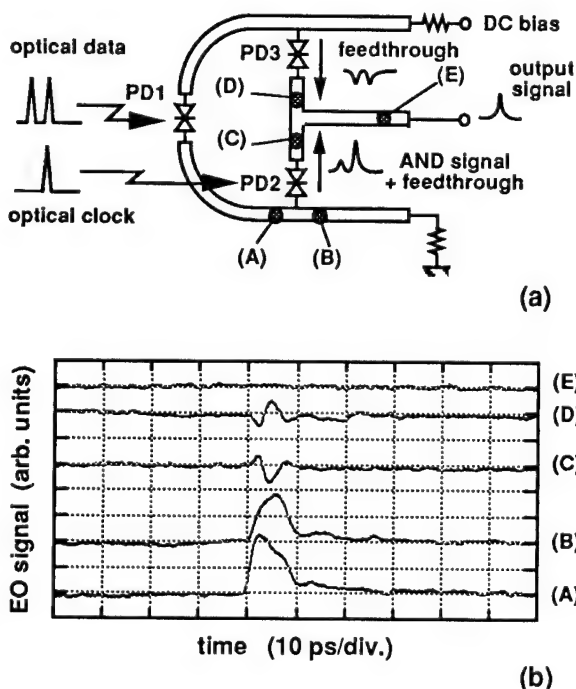


Fig. 5 Operation diagnosis of a photoconductive AND gate. (a) Circuit configuration. (b) Measured pulse-response waveforms.

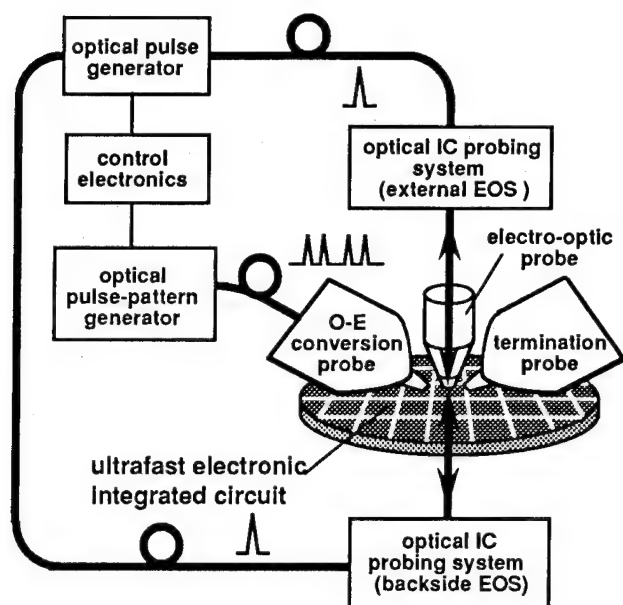


Fig. 6 Block diagram of an optoelectronic on-wafer IC characterization system.

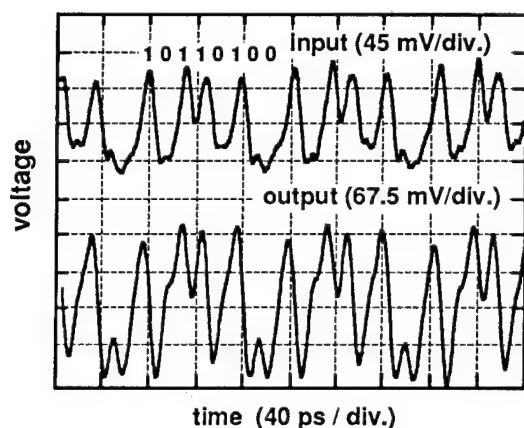


Fig. 7 Measured pulse-pattern response of the HEMT amplifier IC (@64 Gbit/s).

With the increase of IC clock rates, the lack of high-frequency pulse-pattern generators (PPGs) to drive ICs has become a serious problem. The speed of electronic PPGs commercially available is limited to below 15 Gbit/s. Thus, new optoelectronic techniques for characterizing ultrahigh-bit-rate ICs have been developed. The concept of the new optoelectronic testing is shown in Fig. 6. An optical pulse-pattern signal generator and an ultrafast optical-to-electrical (O-E) conversion probe are combined with EOS-based probing techniques[9,10]. The optical PPG can generate pulse-pattern signals at an ultrahigh bit rate and is tunable from 10 to 72 Gbit/s in return to zero (RZ) mode. These optical signals are delivered to the

O-E conversion probe through low-dispersion optical fibers, and the high frequency electrical pulse-pattern signal is generated very near the IC under test. This system was used for on-wafer large signal characterization of an ultrawide-band HEMT amplifier. Figure 7 shows the pulse-pattern response measured by applying a 64-Gbit/s RZ pulse pattern signal to the amplifier. The measured output waveforms are distorted at the rising and falling edges. The measured gain is 7 dB, which is 1.5 dB smaller than that obtained with a network analyzer due to saturation. The distortion and saturation characteristics are important from a practical viewpoint, and are not measurable with purely electronic conventional instruments at rates of over 20 Gbit/s.

In addition to device testing and characterizations described above, new application areas have been emerging, such as radiation pattern analysis of an MMIC antenna [11] and a handy high-impedance probe for multi-gigahertz printed circuit boards and modules [12].

In conclusion, we have described recent developments in electro-optic testing technologies and their application to state-of-the-art devices and ICs. The combination of electrical and optical technologies for signal generation, control and detection will play an increasingly important role not only in measurement but also in signal processing. This will allow us to break through the frequency limit of electronics.

Acknowledgments: The author would like to acknowledge the contributions of Mitsuru Shinagawa, Makoto Yaita, Taiichi Otsuji, Kazutoshi Kato, Naofumi Shimizu, Mikio Yoneyama, and Ryo Takahashi.

REFERENCES

- [1] K. J. Weingarten, M. J. W. Rodwell, and D. M. Bloom, *IEEE J. Quantum Electron.*, 24, 198 (1988).
- [2] J. A. Valdmanis, *Semiconductors and Semimetals*, 28, Academic Press, 135 (1990).
- [3] J. M. Wiesenfeld and R. K. Jain, *ibid.*, 221 (1990).
- [4] T. Nagatsuma, *IEICE Trans. Electron.*, E76-C, 55 (1993).
- [5] T. Nagatsuma, M. Shinagawa, M. Yaita, and K. Takeya, *Proc. 1994 IEEE Instru. Meas. Tech. Conf.(IMTC'94)*, THPM 10-4, 1476 (1994).
- [6] M. Y. Frankel, J. F. Whitaker, G. A. Mourou, and J. A. Valdmanis, *Solid-State Electron.*, 35, 325 (1992).
- [7] K. Kato, A. Kozen, Y. Muramoto, Y. Itaya, T. Nagatsuma, and M. Yaita, *IEEE Photon. Technol. Lett.*, 6, 719 (1994).
- [8] M. Yoneyama, T. Shibata, E. Sano, Y. Kawamura, R. Takahashi, T. Enoki, T. Nagatsuma, and M. Yaita, to be presented at OFC'95, ThK4, San Diego.
- [9] T. Otsuji, K. Kato, T. Nagatsuma, and M. Yoneyama, *Proc. 1994 LEOS Annual Meeting*, UO5.3.
- [10] T. Nagatsuma, T. Otsuji, N. Shimizu, M. Yaita, K. Kato, and M. Shinagawa, *Proc. 1994 IEEE Topical Meeting on Optical Microwave Interactions*, DI2, 7 (1994).
- [11] Y. Imaizumi, M. Shimizu, H. Kamitsuna, and H. Ogawa, *Proc. 1994 IEICE Spring Conf.*, SC-1-8, 2-777 (1994).
- [12] M. Shinagawa and T. Nagatsuma, to be presented at 1995 Instru. Meas. Tech. Conf. (IMTC'95), Boston.

Electro-optic sampling of picosecond photoresponse of epitaxial $\text{YBa}_2\text{Cu}_3\text{O}_{7-\delta}$ thin films

Frank A. Hegmann, Steven H. Moffat, Robert A. Hughes, and John S. Preston
Department of Physics and Astronomy and Department of Engineering Physics
McMaster University

Hamilton, Ontario, Canada L8S 4M1
Phone: (905) 525-9140 x24929 or x27294
Fax: (905) 527-8409

Douglas Jacobs-Perkins, Chia-Chi Wang, Thomas Y. Hsiang, and Roman Sobolewski
Laboratory for Laser Energetics and Department of Electrical Engineering
University of Rochester

250 East River Road
Rochester, NY 14623-1299
Phone: (716) 275-4709
Fax: (716) 273-1014

The origin of the fast photoresponse observed below T_C from current-biased $\text{YBa}_2\text{Cu}_3\text{O}_{7-\delta}$ (YBCO) superconducting thin films has been a source of controversy for several years now.¹⁻⁶ The photoresponse signals have been attributed to either bolometric (thermal or equilibrium) or nonbolometric (nonthermal or nonequilibrium) mechanisms. A variety of nonbolometric mechanisms have been proposed to explain the fast transients, such as nonequilibrium electron heating¹ and nonequilibrium-induced changes in the kinetic inductance of the YBCO bridge.^{2,3,6} For laser pulses with durations greater than 5 ps, a kinetic inductance model based on equilibrium or thermal changes in the temperature of the bridge has been proposed.^{4,5}

Studying the fast photoresponse of high- T_C thin films may reveal important information on scattering and recombination processes. Pump-probe experiments on YBCO films have reported picosecond and subpicosecond time constants,^{7,8} but interpretation of the results are still controversial mainly due to uncertainty in the band structure of YBCO. Performing photoresponse experiments with current-biased samples may provide more direct information on nonequilibrium processes, but the bandwidth of the oscilloscopes used in these experiments is usually the limiting factor in the temporal resolution of the electrical transient. Fast photoresponse signals with widths ranging from 16 ps to 40 ps have been reported recently using fast oscilloscopes.^{3,5,6} Electro-optic sampling offers improved time resolution in the subpicosecond regime, and has been used to study superconducting electronics and pulse propagation on transmission lines.^{9,10} Recently, electro-optic sampling has been used to show that laser-induced switching of Pb films from the superconducting to the normal state occurs in less than 1 ps.¹¹ To our knowledge, the experiments described in this paper are the first electro-optic measurements of photoresponse transients from a high- T_C thin film. We have observed transients

with widths as short as 2 ps (with no slow component afterwards), which is the fastest photoresponse signal reported to date from a YBCO thin film.

The YBCO films were deposited epitaxially by laser ablation onto LaAlO_3 substrates, and then patterned into a coplanar transmission line structure terminated by a bridge 20 μm wide and 100 μm long.⁵ The transition temperature T_c of the film was 88 K, and the critical current density at 77 K was about 10^6 A/cm². The samples were mounted in vacuum on a cold finger cooled with liquid nitrogen (77 K). A LiTaO_3 crystal for electro-optic sampling was placed over the coplanar transmission line about 100 μm from the end of the bridge. The bridge was illuminated by 150 fs, 790 nm pulses from a mode-locked Ti:sapphire laser with a repetition rate of 76 MHz. The average beam power incident on the bridge was about 2 mW, and a spot size of 15 μm gave a fluence of about 20 $\mu\text{J}/\text{cm}^2$.

Figure 1(a) shows a fast photoresponse signal with a width of 2 ps from a 100 nm YBCO film. As the bias current is increased, as shown in Fig. 1(b), the amplitude of the fast transient increases and a slow tail appears with a decay just under 10 ps. At larger bias currents, as in Fig. 1(c), the amplitude and decay time of the tail become larger.

We believe that the fast response seen in Fig. 1(a) arises from a change in kinetic inductance of the bridge induced by the laser pulse. The duration of the transient suggests that net pair-breaking in YBCO occurs within 2 ps after the incident laser pulse. We are currently performing additional experiments to investigate the exact nature of the fast response and slower tail. The fast response shown here also makes YBCO thin films useful as high-speed photodetectors operating above 100 GHz.

References

1. A. D. Semenov, I. G. Goghidze, G. N. Gol'tsmann, A. V. Sergeev, and E. M. Gershenzon, *Appl. Phys. Lett.* **63**, 681 (1993).
2. N. Bluzer, *Phys. Rev. B* **44**, 10222 (1991). N. Bluzer, *J. Appl. Phys.* **71**, 1336 (1992). N. Bluzer, *IEEE Trans. Appl. Supercond.* **3**, 2869 (1993).
3. A. Ghis, S. Pfister, J. C. Villegier, M. Nail, and J. P. Maneval, *IEEE Trans. Appl. Supercond.* **3**, 2136 (1993).
4. F. A. Hegmann and J. S. Preston, *Phys. Rev. B* **48**, 16023 (1993).
5. F. A. Hegmann, R. A. Hughes, and J. S. Preston, *Appl. Phys. Lett.* **64**, 3172 (1994).
6. M. A. Heusinger, A. D. Semenov, R. S. Nebosis, Y. P. Gousev, and K. F. Renk, submitted to *IEEE Trans. Appl. Supercond.*, Oct. 16, 1994.
7. S. G. Han, Z. V. Hardeny, K. S. Wong, O. G. Symko, and G. Koren, *Phys. Rev. Lett.* **65**, 2708 (1990).
8. T. Gong, L. X. Zheng, W. Xiong, W. Kula, Y. Kostoulas, R. Sobolewski, and P. M. Fauchet, *Phys. Rev. B* **47**, 14495 (1993).
9. M. Currie, C.-C. Wang, D. Jacobs-Perkins, R. Sobolewski, and T. Y. Hsiang, submitted to *IEEE Trans. Appl. Supercond.*, Oct. 16, 1994.
10. S. Alexandrou, R. Sobolewski, and T. Y. Hsiang, *IEEE J. Quantum Electron.* **28**, 2325 (1992).
11. X. H. Hu, T. Juhasz, and W. E. Bron, *Appl. Phys. Lett.* **59**, 3333 (1991).

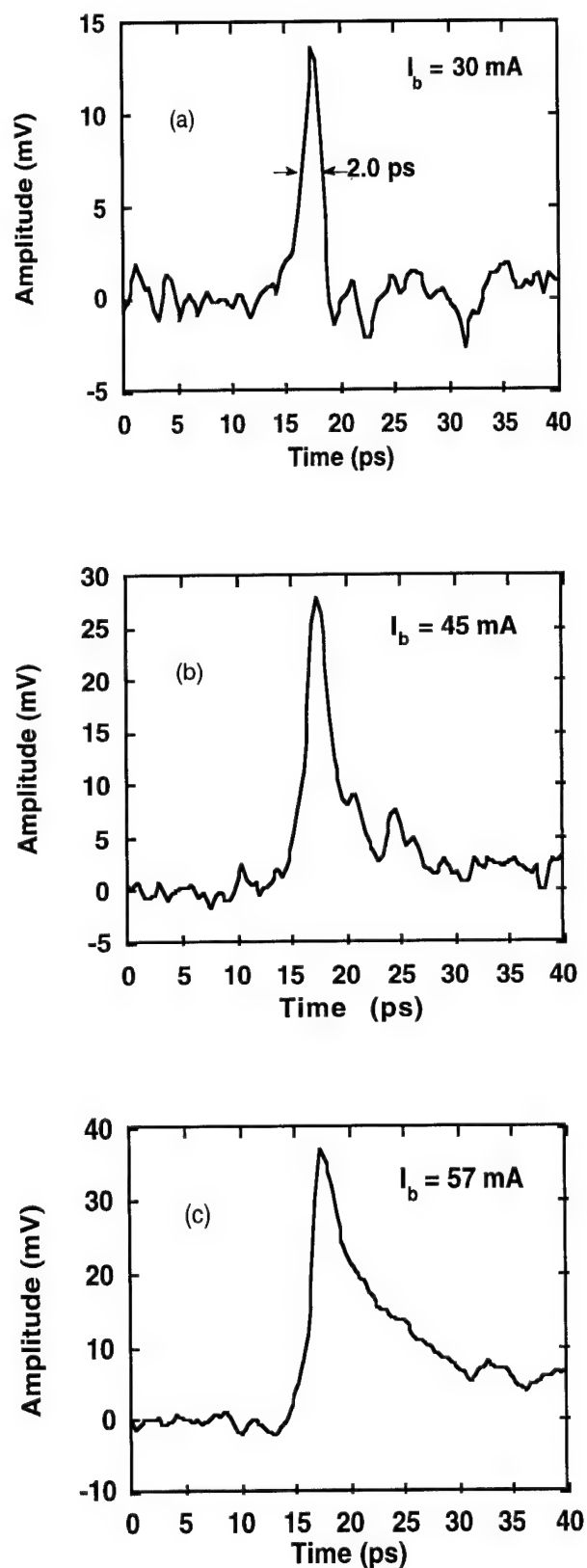


Fig. 1. Photoresponse signals seen from a 100-nm YBCO film at bias currents of (a) 30 mA, (b) 45 mA, and (c) 57 mA. The width of the fast transient in (a) is 2 ps. Notice the slower tail developing after the fast transient in (b) and (c). The bridge was 20 μm wide and had a length of 100 μm . The sample was cooled to 77 K using liquid nitrogen. Sampling of the transient was performed at a distance roughly 200 μm from the excitation pulse.

Optoelectronic Phase Tracking and Electro-Optic Sampling of Free-running Microwave Signals up to 20 GHz in a Laser-Diode-Based System

Gong-Ru Lin and Ci-Ling Pan

Institute of Electro-optical Engineering, National Chiao Tung University

Hsinchu, Taiwan 300, R.O.C.

Fax: 886-35-716631, E-mail: clpan@cc.nctu.edu.tw

Hsiao-Hua Wu

Department of Physics, Tunghai University,

Taichung, Taiwan 407, R.O.C.

Recently, several optoelectronic phase lock schemes have been demonstrated to meet the demand of synchronizing the target voltage-controlled-oscillator to the harmonics of optical probing pulses [1-4]. In reality, the microwave signal under test might be free-running and originated from a monolithic microwave integrated circuit (MMIC). In this work, we demonstrate optoelectronic phase tracking and electro-optic sampling of the microwave signal from a free-running oscillator. Gain-switched semiconductor lasers are employed. This system has potential applications for on-wafer testing of MMIC's.

The experimental apparatus consists of an optoelectronic phase lock loop (OEPLL) [5] and an electro-optic (EO) sampler as shown in Fig. 1. A sweep oscillator (HP8350B) operating over a range of 0.01 to 20 GHz simulates as a free-running oscillator on a MMIC. The frequency variation of the sweep oscillator output with time is roughly a few hundred kHz in a 10-min period. In the OEPLL, a gain-switched laser diode (LD1, $\lambda=0.8\ \mu\text{m}$) generates a train of 50-ps pulses at an average power of 0.3 mW. It is focused on the gap of a GaAs photoconductive switch. The microwave signal at frequency f_m biasing the switch is mixed at the switch with the harmonics of the optical pulse train and produces a desired intermediate frequency (IF) signal through a low pass amplifier. This IF signal is then used as the external reference source of the lock-in amplifier for electro-optic sampling. An error signal obtained by comparing phase of the IF signal to a reference is sent to a voltage-controlled oscillator (VCO, HP8640B) via a loop filter. The repetition frequency of LD1 is controlled by the VCO. When the phase-tracking condition is achieved, the frequency of the VCO should be $f_o = (f_m \pm f_{IF})/N$, where f_m is the microwave frequency and N is an integer. Another InGaAsP/InP laser diode (LD2, $\lambda = 1.3\ \mu\text{m}$) for reflective-mode electrooptic sampling is gain-switched by the same VCO as used in the OEPLL and producing an optical pulse train with an average power and pulse width of about 1 mW and 40 ps, respectively. The microwave signal from the HP8350B is sampled by first mixing with the harmonics of the laser pulse from LD2 and down converts to the IF signal in a GaAs microstrip transmission line. One interesting feature of the present system is that the optical delay line is located in the OEPLL system. As a result, the fluctuation of the EO signal due to positioning of the probing beam ($\lambda=1.3\ \mu\text{m}$) is significantly reduced. The phase and the amplitude of the microwave signal is measured using a low frequency lock-in amplifier with the external reference frequency provided the OEPLL. A stable phase and amplitude signal can thus be observed on the lock-in amplifier when the phase of the microwave signal has been tracked by the VCO.

A low-frequency oscilloscope is then used to display the signals from the reference IF source, and the waveform of the microwave signal via a low frequency replica. The time base of the oscilloscope is triggered by the reference IF. If phase tracking is achieved, clean waveforms from these signals can be observed. In this work, the phase of a free-running microwave signal up to 20 GHz has been successfully tracked by tuning the repetition frequency of the LD1. The tracking range of the OEPLL is 100 kHz. The key component which allows phase tracking of the VCO to the free-running microwave

signal is the laser activated photoconductive harmonic mixer (PCHM) biased with the microwave signal. The conversion loss of the PCHM from the microwave input signal (RF) at 500 MHz down to the IF output signal at 100 kHz is measured to be 38.5 dB. The root mean square (RMS) noise density of the IF signal under the same condition is $0.42 \mu\text{V}/\sqrt{\text{Hz}}$. At 20 GHz, the conversion loss increases to 69 dB. This is a result of bandwidth limitation imposed by both the laser pulses and the photoconductive response.

In the electro-optic sampler, the downconverted IF signal from the electro-optic sampler at 100 kHz is 0.765 mV in response to a microwave signal power of 4 dBm at 500 MHz. This corresponds to a throughput from RF to IF of -62 dB. The IF signal decreases as the frequency of the microwave signal increases. This can be explained by the bandwidth limitation imposed by the laser pulses. To improve the signal-to-noise ratio, a bandpass filter of which the center frequency can auto-track that of the reference input is utilized. The passband (between 70% pass points) of the filter is chosen to be 1/5 that of the center frequency. With the filter operational, the rms noise density for the IF signal drops to $1.6 \mu\text{V}/\sqrt{\text{Hz}}$. A gain-variable amplification stage follows the filter before the IF signals is fed to the phase detector (PD).

Figure 2 illustrates typical down-converted electro-optic sampled waveform of the free-running microwave signal at 20 GHz. The sideband power spectrum for the VCO has also been monitored as one increases the frequency of the free-running microwave signals. This is shown in Fig. 3. The signal-sideband phase noise density of the phase-locked VCO at 500 MHz is about -70 dBc/Hz at a frequency offset of 5 kHz. It decreases to be -85 dBc/Hz for the microwave signal near the 40th harmonics, or 20 GHz. It is apparent that the phase locking performance of this system improved as the microwave frequency increases. In summary, phase-tracking of free-running microwave signals can be accomplished without requiring any electrical contacts between the microwave test circuit and other components of the sampling system in the present scheme. This is advantageous to previously reported electro-optic sampling systems which employ conventional electronic or optoelectronic phase-locking techniques. It is thus particularly suitable for measurement of circuits with free-running internal oscillators.

References

- [1] M. G. Li, E. A. Chauchard, C. H. Lee, and H. -L. A. Hung, IEEE Tran. Microwave Theory Tech. **38**, 1924, (1990).
- [2] H. H. Wu, C. -S. Chang, and C. -L. Pan, Electron. Lett. **27**, 1622, (1991).
- [3] C. -L. Pan, K. Y. Tang, and H. H. Wu, IEEE Microwave and Guided Wave Lett. **3**, 113, (1993).
- [4] C. -L. Pan, G. R. Lin, D. Y. Chyou, IEEE Microwave and Guided Wave Lett. **4**, 115, (1994).
- [5] C. -L. Pan and H. H. Wu, IEEE Photon. Technol. Lett. **4**, 1298, (1992).

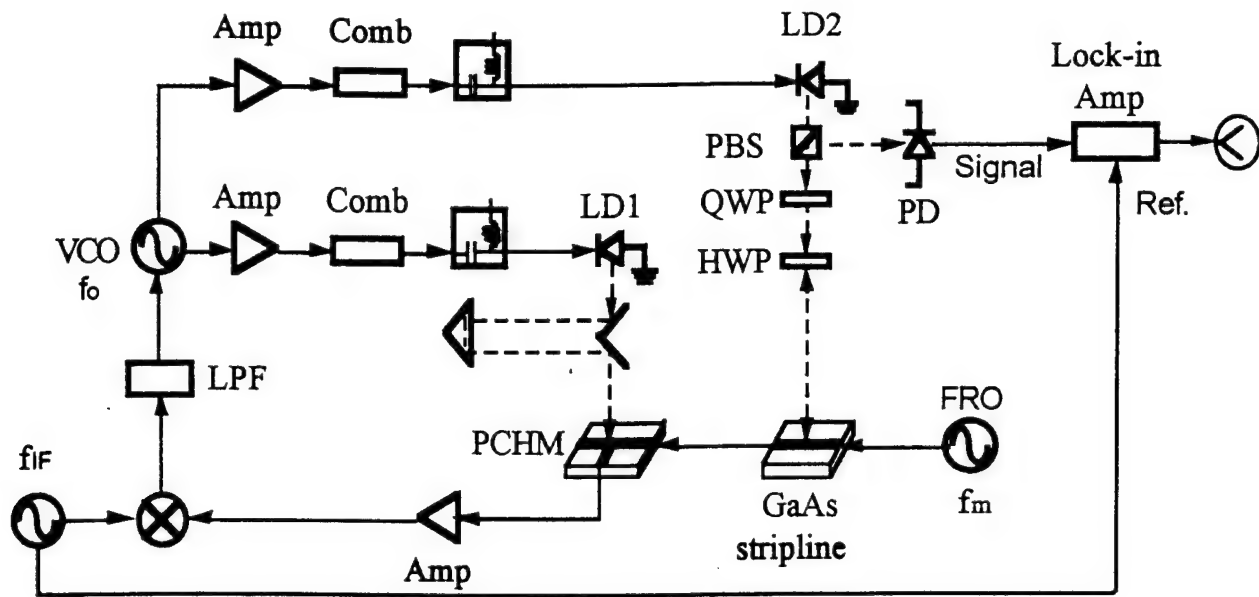


Fig.1 Schematic diagram of the experimental apparatus. PBS: polarized beam splitter, QWP: quarter wave plate, HWP: half wave plate, LPF: loop filter, FRO: free-running oscillator.

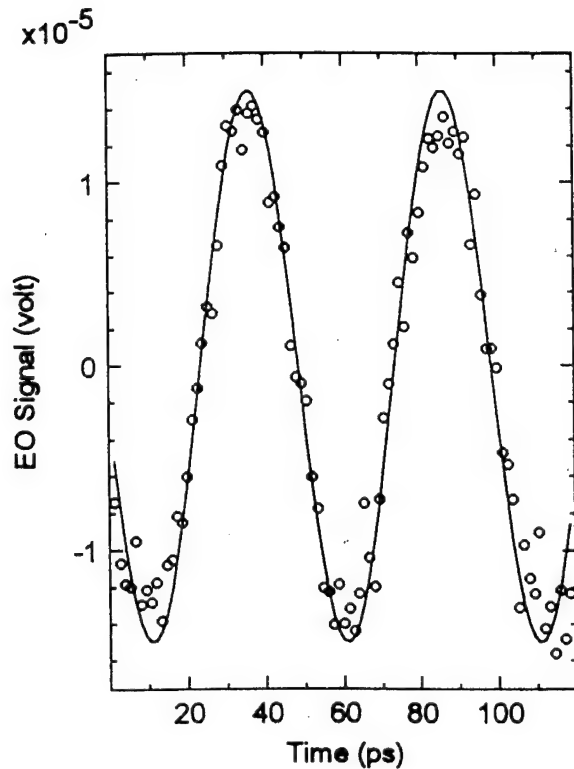


Fig.2 Downconverted electrooptic sampled waveform of the microwave signal at 20 GHz.

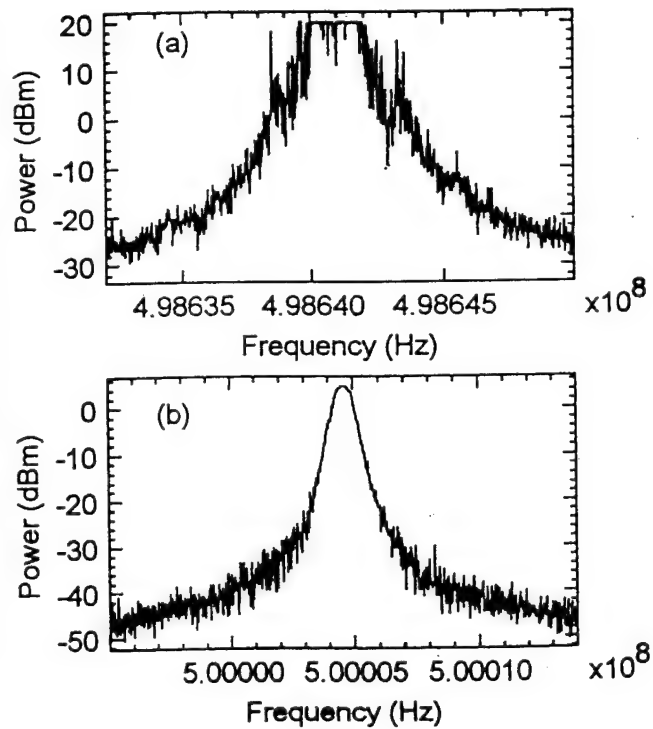


Fig.3 Power spectrum of the VCO phase-locked to free-running microwave clock signals at (a) 500 MHz and (b) 20 GHz.

Airbridges for slotline mode suppression in THz coplanar waveguide

N. de B. Baynes*, J. Allam[†], K. Ogawa[†], M.M. Ahmed* and J.R.A. Cleaver*

**Microelectronics Research Centre, University of Cambridge*

[†]Hitachi Cambridge Laboratory, Hitachi Europe Ltd.

Cavendish Laboratory, Madingley Road, Cambridge CB3 0HE, U.K.

Tel. (44) 223 467944 Fax. (44) 223 467942

Coplanar waveguides (CPW) are attractive transmission lines for monolithic microwave integrated circuits due to low dispersion and easy integration with planar devices. Due to the presence of two ground planes, both the quasi-TEM symmetric CPW mode and non-TEM asymmetric slotline mode can propagate, as shown in figure 1. To suppress the unwanted slotline mode, airbridges are used¹ to connect the ground planes on either side of the central conductor at discontinuities in the waveguide which would mix the modes. The use of airbridges in microwave circuits is well-established, and they have been studied^{2,3} both experimentally and numerically at frequencies up to ≈ 100 GHz. Recently, coplanar transmission lines and waveguides with bandwidths up to ≈ 1 THz have been demonstrated.⁴ In this paper, we study the generation of mixed modes on CPW and their suppression by airbridge structures, using electro-optic sampling of picosecond pulses generated by ultrafast photoconductive switches.

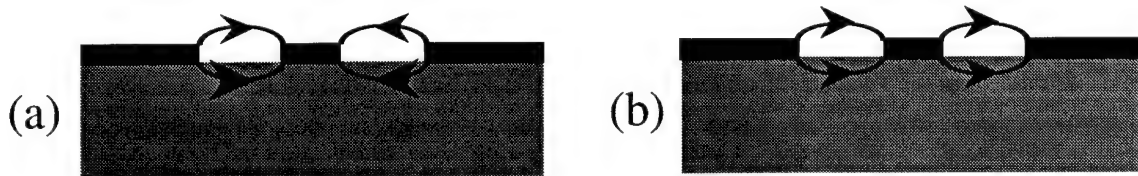


Figure 1. (a) Symmetric (CPW) mode and (b) asymmetric (slotline) mode in coplanar waveguide.

Coplanar waveguides with central conductor width of $20\text{ }\mu\text{m}$ and separation between ground planes of $10\text{ }\mu\text{m}$ were formed on low-temperature GaAs.⁵ Interdigitated photoconductive switches with $1\text{ }\mu\text{m}$ fingers and gaps were fabricated. The switches were biased by additional CPW structures, so that in the absence of the airbridges, the ground planes were not connected in the region of the switches (see figures 2 and 3).

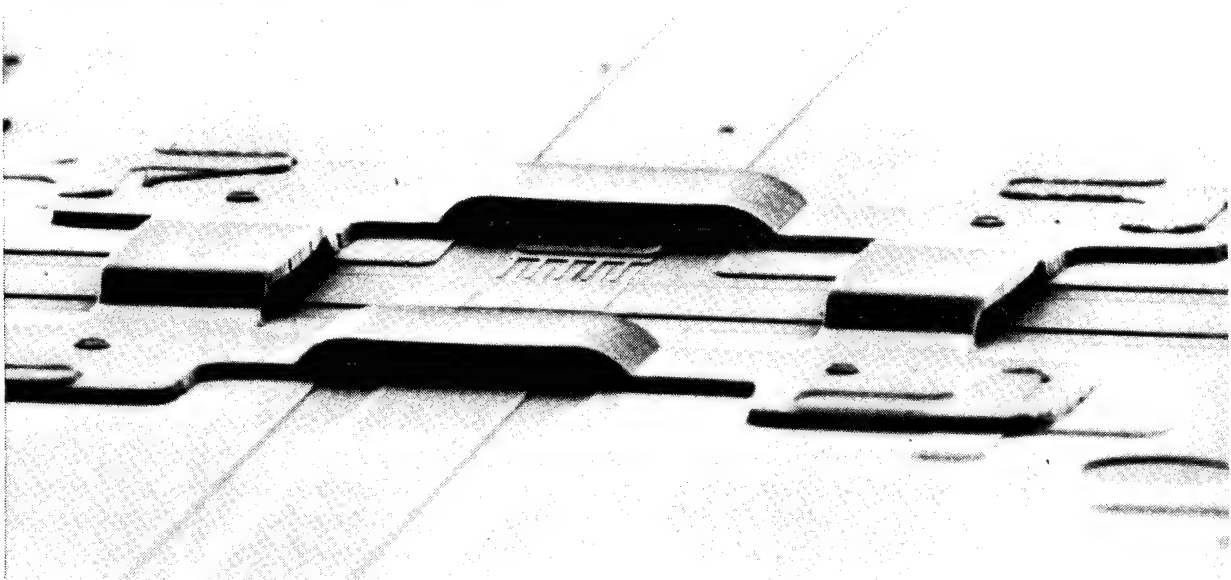


Figure 2. SEM micrograph of airbridges on CPW.

Electron-beam techniques allow fabrication of airbridges with large clearance over the substrate and well-controlled cross-section (and hence high mechanical strength and low electrical resistance).⁶ The two-stage resist process employs linear grading of the electron beam dose and reflow at 120 °C to control the resist profile. Metallisation consisted of 20 nm NiCr, 1.6 μm Ag and 100 nm Au. The bridges were 20 μm wide with a span of 50 μm . The clearance between center conductor and airbridge was $\approx 4 \mu\text{m}$. A scanning electron micrograph of one of the airbridge structures, together with CPW and switches, is shown in figure 2.

The pulse propagating in the CPW was measured using electro-optic sampling, with an external electro-optic probe tip positioned at varying distance from the generating photoconductive switch. The electric field across both gaps of the CPW was measured; i.e. on the same and the opposite side as the photoconductive switch as shown in figure 3. The measured pulse for the CPW without airbridges is shown in figure 4. The electric field in each of the gaps differs by a factor of ≈ 2 , and this difference persists over several mm. Structure associated with the symmetric and asymmetric modes is clearly seen in the pulses.

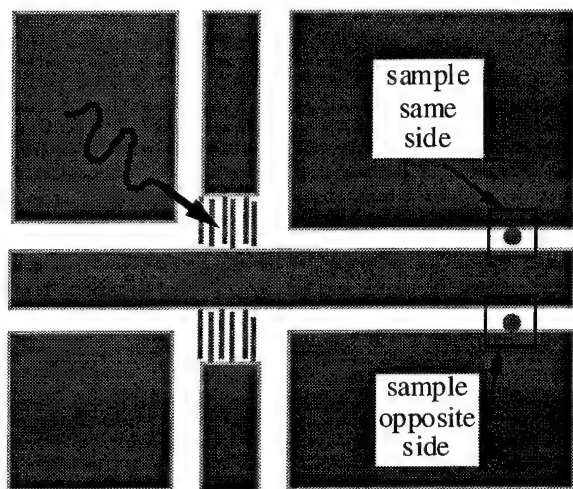


Figure 3. Illumination and sampling position in CPW

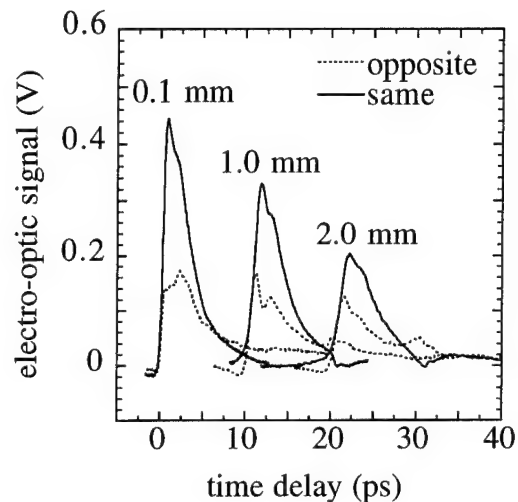


Figure 4. Pulse propagating in CPW due to illumination of one of the photoconductive switches.

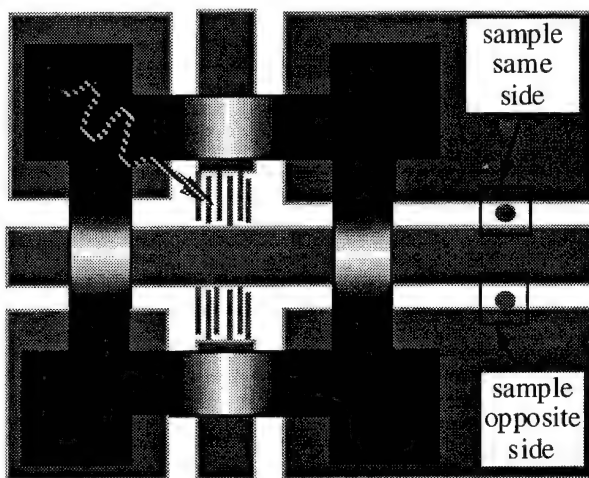


Figure 5. Illumination and sampling position in CPW with airbridges.

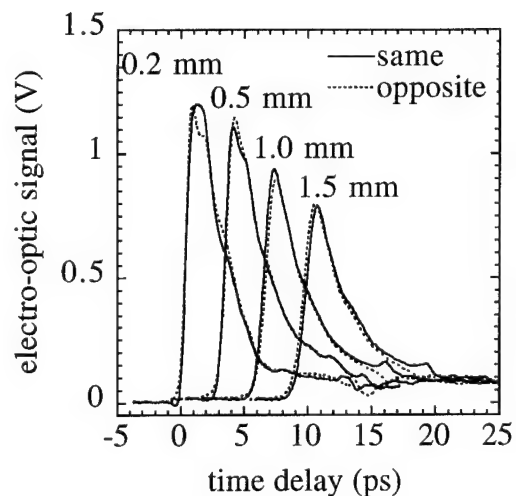


Figure 6. Pulse propagating in CPW with airbridges linking ground plane in vicinity of generating switch.

Figure 6 shows the pulse propagating in the CPW with airbridges, in the geometry shown in figure 5. The electric field measured in each of the gaps is almost identical, apart from a small difference at the shortest propagation times which may be associated with the finite distance between the switch and the airbridges. This indicates that picosecond pulses can be launched on CPW and propagated in the quasi-TEM mode. Pulse broadening is dominated by radiation due to the mismatch between the dielectric constants of the semiconductor substrate and air superstrate.

The airbridges present impedance discontinuities which may cause parasitic effects depending on the location and size. The effect of the discontinuity on a propagating pulse was measured in the reflectance geometry shown in figure 7, and the pulses incident on and reflected from the airbridge are shown in figure 8. The reflected pulses are indicated by the arrows. The magnitude of the reflection is small (approximately 2 % of the incident pulse) and is approximately consistent with the reflection expected from the parallel-plate capacitor formed between the center conductor and the overlapping region of the airbridge.

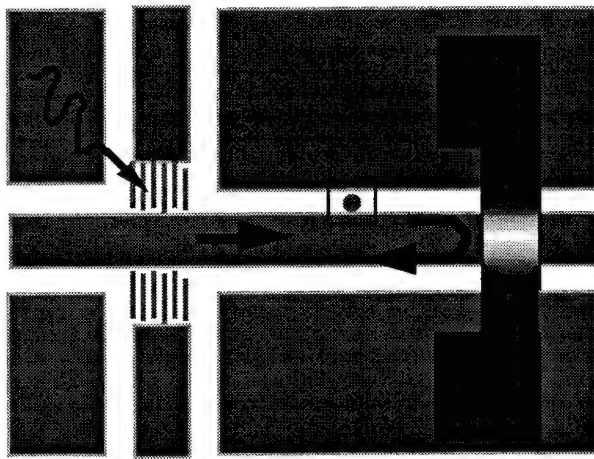


Figure 7. Measurement of reflectance from parasitics associated with an airbridge.

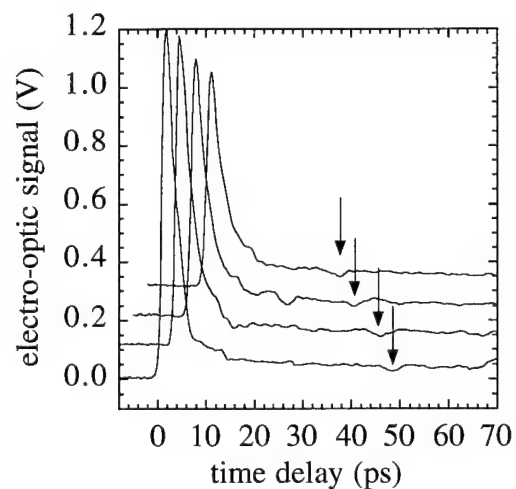


Figure 8. Pulse incident on and reflected from airbridge structure. Successive traces (offset for clarity) represent different positions of probe. Arrows indicate reflections due to airbridge.

In conclusion, picosecond pulses can be generated on CPW and propagated in the quasi-TEM mode if the slotline modes are suppressed using airbridges. Parasitic effects of the airbridge on pulse propagation are small. The airbridges are mechanically strong and reliable.

References

- ¹N.H. Koster, S. Koblowski, R. Bertenburg, S. Heinen, and I. Wolf, Proc. 19th European Microwave Conf., pp.666 - 671 (1989).
- ²H. Jin and R. Vahldieck, IEEE MTT-S Digest, pp.207 - 210 (1992).
- ³N.I. Dib, P.B. Katehi and G.E. Ponchak, IEEE MTT-S Digest, pp.469 - 472 (1991).
- ⁴M.Y. Frankel, S. Gupta, J.A. Valdmanis and G.A. Mourou, IEEE Trans. Microwave Theory Tech. 39, 910 (1991).
- ⁵J. Allam, K. Ogawa, J. White, N. de B. Baynes, J.R.A. Cleaver, I. Ohbu, T. Tanoue and T. Mishima, *OSA Proceedings on Ultrafast Electronics and Optoelectronics*, 1993, (J. Shah and U. Mishra, eds.) Vol. 14, p. 197.
- ⁶R.G. Woodham, R.M. Jones, D.G. Hasko, J.R.A. Cleaver and H. Ahmed, *Microelectronic Engineering* 17, pp. 563 - 566 (1992).

First Direct Observation of Single-Flux-Quantum Pulses

Douglas Jacobs-Perkins, Marc Currie, Chia-Chi Wang, Roman Sobolewski,
Marc J. Feldman, and Thomas Y. Hsiang;

LABORATORY FOR LASER ENERGETICS and
DEPARTMENT OF ELECTRICAL ENGINEERING
University of Rochester
Rochester, NY 14623-1299 USA
phone: (716) 275-4709
fax: (716) 275-5960

We report the first direct and nonintrusive measurement of single-flux-quantum (SFQ) pulses propagating on a superconducting microstrip line. We present and discuss experimental results obtained with reflective electro-optic (EO) sampling.

The superconducting SFQ pulse is the basic information “bit” of several new families of digital logic. SFQ logic promises digital, large-scale, integrated-circuit clock rates of hundreds of GHz, much faster and with much lower power dissipation than semiconductor technologies.¹

An SFQ voltage pulse is generated when a quantum of magnetic flux passes through a Josephson junction. The pulse area is quantized: the time integral of the voltage is exactly equal to $h/2e$, which is 2.07 mV•ps. This pulse exceeds traditional measurement resolution-bandwidth limitations, and until now, the temporal evolution of an SFQ pulse has never been experimentally measured. Nevertheless, SFQ pulses are commonly generated, processed, and detected in many different digital and analog superconducting circuits.

We have experimentally measured the temporal evolution of superconducting SFQ pulses using a cryogenic reflective EO sampling system. Single-pulse height was measured to be 0.67 mV high by 3.2 ps wide. The time integral of multiple voltage pulses was consistently an integer multiple of flux quantum, $h/2e$. The sampling system has ~200-fs time resolution and, with averaging, achieved noise levels below 70 μ V rms.

The SFQ pulses were generated by using a planar interdigitated Nb/Si/Nb metal-semiconductor-metal photodiode² as an optoelectronic switch on a superconducting microstrip line. The diode produces a sawtooth-like pulse with subpicosecond rise time. Diode recovery time is of the order of tens of picoseconds. Pulse height is adjustable, determined by the amount of laser radiation applied. The diode drives a Josephson transmission line (JTL) “pulse shaper” consisting of two Nb/AlO_x/Nb Josephson junctions. The resulting SFQ pulses were launched onto another superconducting microstrip and were detected noninvasively by electro-optically sampling the microstrip fringing field.

SFQ circuits typically use microstrip-line interconnects that restrict most of the signal energy between the strip line and ground plane. This makes nonintrusive measurement of the fringing fields from the interconnects^{3,4} very difficult. At the University of Rochester⁵ early use of EO sampling to measure the response of Josephson junctions to picosecond transients was

partially successful: The junction turn-on delay and rise time were accurately determined, but Josephson oscillations were not conclusively resolved.

Our EO sampling system⁵ is modified for measurement of devices located in a cryogenic dewar. A lithium tantalite crystal is bonded to the device under test. A Ti:sapphire laser with ~150-fs pulses is used for pulse excitation and sampling. The excitation beam is frequency doubled to pass through the crystal to activate the MSM diode. The 800-nm sampling beam passes through the EO crystal and is reflected at the chip surface by a dielectric coating.

Extensive signal averaging is required to obtain the submillivolt sensitivity needed to detect the fringing field produced by the microstrip line. We restrict our observations window to 50 ps, corresponding to an experiment duration of about 10 min.

Figure 1 shows a sequence of our measured results. In Fig. 1(a), the diode responds to the light excitation within a fraction of a picosecond and recovers to its nonconducting state in 26 ps. Figure 1(b) shows the two-junction JTL response when the light intensity is just enough to produce a single SFQ pulse, with an observed width of 3.2 ps and maximum height of 0.67 mV. When light intensity is increased, multiple flux quanta are generated. Figure 1(c) shows an example of three generated SFQ pulses, with the first two closely placed and the third entering about 6 ps after the second.

Figure 1(b) shows that, for the first time, an isolated SFQ pulse has been directly identified by time-domain measurements. Time integration of this pulse is shown as the dotted line in Fig. 1(b). The integrated value of 2.1 mV-ps corresponds to the value of one flux quantum, $h/2e$. Similarly, the result in Fig. 1(c) is integrated and shown to contain three discrete flux quanta. It is interesting to note that, aside from magnetic-field quantization and microwave-induced step measurements, *our results can be viewed as a third confirmation of the paired-charge quantization in superconductors.*

An immediate application of our system is in the time-domain design verification of SFQ circuits. Single logic blocks can be activated with the pulse, and their functional delay times and response times can be measured with picosecond accuracy. Interconnect dispersion characteristics can also be easily measured up to a terahertz. Multiple switching pulses can also be provided for testing circuits requiring multiple inputs.

In conclusion, we have demonstrated one method of optoelectronically creating and detecting an SFQ pulse with subpicosecond and submillivolt resolution. The pulse was generated using a two-junction Josephson pulse shaper fed by a Nb-Si-Nb MSM photodiode. The pulse measured with a cryogenic EO sampling system had a 0.67-mV amplitude and a 3.2-ps width. The calculated pulse integral of 2.1 mV-ps verifies that the measured signal was indeed an SFQ pulse.

This research is supported by University Research Initiative at the University of Rochester sponsored by the Army Research Office grant No. DAAL03-92-G-0112. C.-C. Wang acknowledges support from the Frank Horton Graduate Fellowship Program.

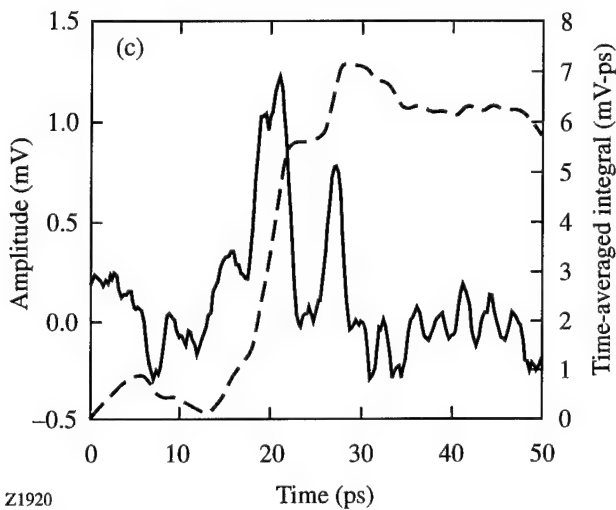
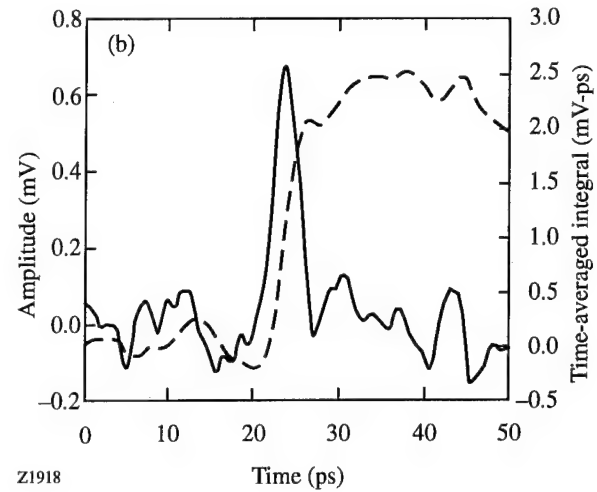
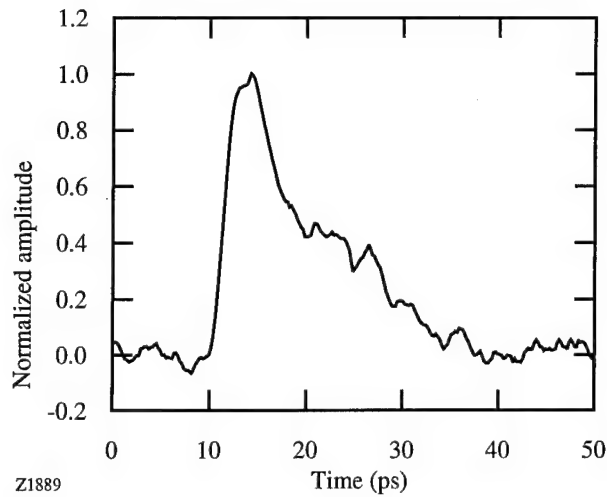


Fig. 1 (a) Response of Nb/Si/Nb MSM photodiode. Pulse amplitude is determined by illumination intensity.
 (b) Response at output of JTL, when output from photodiode is just enough to produce a single SFQ pulse, indicated by time-averaged integral of $\sim 2\text{mV}\cdot\text{ps}$.
 (c) Response at output of JTL, when output from photodiode is increased enough to produce three SFQ pulses, indicated by time-averaged integral of $\sim 6\text{mV}\cdot\text{ps}$.

REFERENCES

1. K. K. Likharev and V. K. Semanov, *IEEE Trans. Appl. Superconduct.* **1**, 3 (1991).
2. C.-C. Wang, S. Alexandrou, D. Jacobs-Perkins, and T. Y. Hsiang, *Appl. Phys. Lett.* **64**, 3578 (1994).
3. U. D. Keil and D. R. Dykaar, *Appl. Phys. Lett.* **61**, 1504 (1992).
4. S. Alexandrou, C.-C. Wang, R. Sobolewski, and T. Y. Hsiang, *IEEE J. Quantum Electron.* **30**, 1332 (1994).
5. D. R. Dykaar, R. Sobolewski, and T. Y. Hsiang, *IEEE Trans. Magn.* **25**, 1392 (1989).

Optoelectronic Characterization of Resonant Tunneling Diodes

T. Nagatsuma, N. Shimizu, T. Waho, and M. Shinagawa

NTT LSI Laboratories,

3-1 Morinosato Wakamiya, Atsugi, Kanagawa 243-01, Japan

Tel. +81 462 40 2252, Fax. +81 462 40 4219

Resonant tunneling diodes (RTD's) have been intensively studied for their application to ultrahigh-speed/frequency circuit components such as oscillators [1], triggering devices [2], and pulse generators [3]. Switching time from peak to valley in the negative resistance region is one of their important characteristics from a practical viewpoint as well as being of physical interest[4]-[9]. Since the RTD's switching time has already outpaced the capability of electronic sampling oscilloscopes (7-ps resolution) to measure it, an electro-optic sampling (EOS) technique has been commonly used.

Two types of EOS-based methods have been reported for measuring RTD's switching time. One is the optical triggering scheme. In this, an ultrafast photoconductive switch was wire-bonded to the RTD chip to trigger the device, and the response was measured by using a hybrid EO modulator [6] or a superstrate EO modulator [7]. Although this scheme is principally jitter-free, the signal-to-noise ratio (S/N) of measured waveforms was not sufficient to deduce accurately a 10-90% transition time due to excess laser noise. In addition, the obtained switching time was much shorter than theoretically estimated because the experiment may have been done under overdrive conditions [6]. The other method is the radio-frequency (RF) synchronization scheme. The RTD was driven by a sinusoidal signal from a synthesizer electrically synchronized to the repetition rate of the laser source, and the voltage step pulse-forming structure was measured by direct or external EOS [8],[9]. This method yielded switching times consistent with estimated ones. The effects, if any, of timing jitter of the laser and the

synthesizer remain unknown factors in determining the switching time when this reaches an order of 1 ps.

This paper introduces a new, practical scheme to accurately measure the switching time of ultrafast RTD's. Figure 1 shows the experimental setup. The pulse laser source used was an extremely low-noise, stable soliton pulse generator producing wingless pulses of less than 400-fs width at 1.55 μm [10]. The laser beam was divided into two beams: one triggering an 18-GHz photodiode followed by an attenuator, pulse amplifier and low-pass filter, and the other synchronously sampling the RTD response to the triggering pulse. There was virtually no jitter. One of the differences between this scheme and conventional optical triggering was that the magnitude and slew rate of the drive signal could be optimized by using the attenuator and the filter to switch the RTD's under practical operating conditions, thus avoiding overdrive. Another important feature was that the photodiode bias voltage was electrically modulated with a 100%-modulation depth to allow a narrow-band lock-in detection. In contrast to the usual mechanical choppers inserted in front of the photodiode, phase stability of the reference signal was greatly improved. Consequently, at least a 10-dB enhancement in the S/N ratio was achieved. An external on-wafer EOS system with a highly-sensitive CdTe probe tip was employed to probe the RTD response. The probing point could be placed very close to the RTD to eliminate the dispersion of the electrical signal travelling along the 50- Ω transmission line. Additionally, the repetition rate and the duty factor of the triggering signal was 500 MHz and less than 10%, respectively. This

reduced the power dissipation of the RTD below that of the RF synchronization scheme. This feature will be useful for measuring ultrafast RTD's having higher peak current density, because possible device-heating problems can be avoided.

This measurement setup was used to measure the switching time of RTD's in the InGaAs/AlAs material system, which is one of the most promising systems for integrated-circuit application with respect to speed and voltage swing availability. The

RTD was fabricated at the center conductors sandwiched between the 50- Ω transmission lines. Detail of the device fabrication will be reported elsewhere. As shown in Fig. 2, a 100-ps wide electrical pulse with a 1.26-V_p amplitude (a) was applied to the RTD, and the pulse-forming response (b) was then measured. Barrier thickness, well thickness, emitter size, and peak current density of the measured RTD were 2.0 nm, 4.1 nm, $2 \times 5 \mu\text{m}^2$ and $1.2 \times 10^5 \text{ A/cm}^2$, respectively.

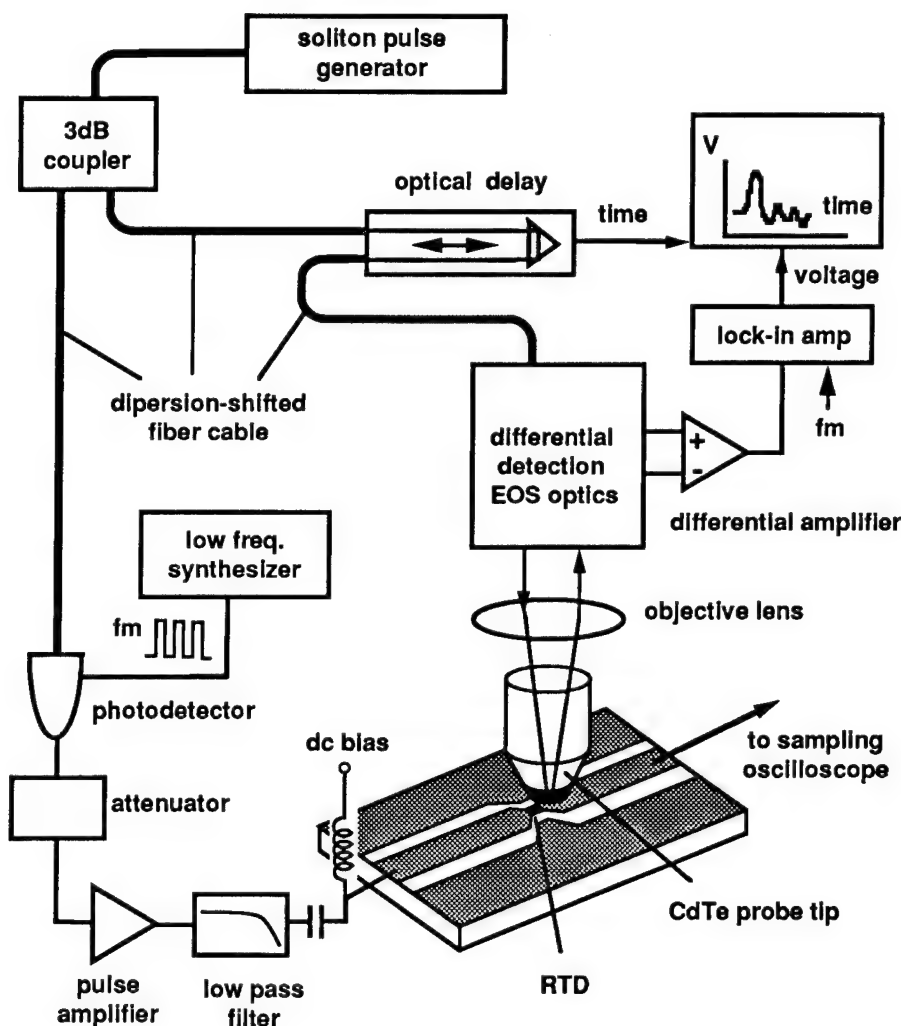


Fig. 1. Setup for measuring the switching time of ultrafast RTD's. To ensure good measurement reproducibility while eliminating the need for optical alignment as much as possible, optical components are connected by using low dispersion optical fiber cables.

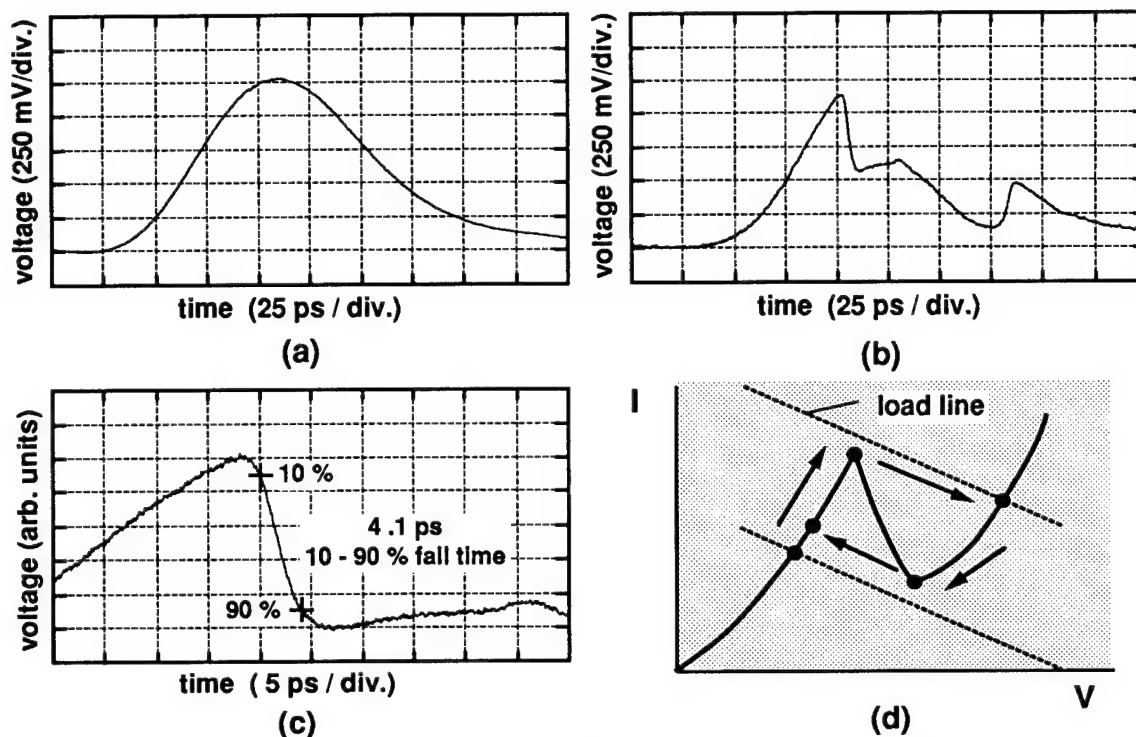


Fig. 2. Measured waveforms of InGaAs/AlAs RTD's. (a) drive pulse, (b) overall RTD response, (c) peak-to-valley transition, (d) schematic switching trajectory in the I-V curve.

The obtained S/N ratio was at least 50 dB for the 1 Vp-p signal. Changes in waveform against repetitive measurement were within the noise level. The waveform structure agreed well with Whitaker's analytic representation [6]. Thus, both peak-to-valley and valley-to-peak transitions occurred at rising and falling edges of the drive pulse. The transition from peak to valley points was precisely measured as shown in Fig. 2(c). The 10-90 % fall time was as small as 4.1 ps, which appears to be shortest ever measured in InGaAs/AlAs RTD's. Other devices with the same device parameters on the wafer were shown to have almost the same switching time. This value was consistent with the theoretical switching time of $4RC$ (about 4.8 ps), where R and C are the average negative resistance and the device capacitance, respectively [4]. By increasing the peak current density while reducing the barrier thickness, the switching time of the InGaAs/AlAs RTD's may be shown to be decreased further in the near future.

In conclusion, we have presented a practical method for accurately characterizing the switching properties of RTD's. This method is effective for ultrafast RTD's having high peak current densities, such as

those found in InGaAs/AlAs and InAs/AlSb material systems.

References

- [1] E. R. Brown, T. C. L. G. Sollner, C. D. Parker, W. D. Goodhue, and C. L. Chen, *Appl. Phys. Lett.*, 55, 1777 (1989).
- [2] E. Özbay, and D. M. Bloom, *IEEE Electron Device Lett.*, 12, 480 (1991)
- [3] R. Y. Yu, Y. Konishi, S. T. Allen, M. Reddy, M. J. W. Rodwell, *IEEE Micro. Guided Wave Lett.*, 4, 220 (1994).
- [4] S. K. Diamond, E. Ozbay, M. J. W. Rodwell, D. M. Bloom, Y. C. Pao, and J. S. Harris, *Appl. Phys. Lett.*, 54, 153 (1989).
- [5] E. R. Brown, C. D. Parker, A. R. Cawala, M. J. Manfra, T. C. L. G. Sollner, C. L. Chen, S. W. Pang, and K. M. Malvar, *Proc. SPIE*, 1288, 122 (1990).
- [6] J. F. Whitaker, G. A. Mourou, T. C. L. G. Sollner, and W. D. Goodhue, *Appl. Phys. Lett.*, 53, 385 (1989).
- [7] A. Takeuchi, T. Inata, S. Muto, and E. Miyauchi, *Jpn. J. Appl. Phys.*, 28, L750 (1989).
- [8] E. Özbay, D. M. Bloom, and S. K. Diamond, *Electron. Lett.*, 26, 1046 (1990).
- [9] K. W. Chang and W. V. Sorin, *Tech. Dig. Ultrafast Electronics & Optoelectronics, MC4-1*, 33 (1993).
- [10] T. Nagatsuma, M. Yaita, M. Shinagawa, K. Kato, A. Kozen, K. Iwatsuki, K. Suzuki, *Electron. Lett.*, 30, 814 (1994).

Tuesday, March 14, 1995

Ultrafast Sources

UTuA 8:15 am-10:00 am
Ballrooms VI-VIII

Gadi Eisenstein, *Presider*
Technion Israel Institute of Technology, Israel

Short Pulse Optical Power Supplies for Optoelectronics Applications

W. H. Knox

4B-415 AT&T Bell Laboratories, 101 Crawfords Corner Road Holmdel, NJ 07733

(908) 949-0958 ; (908) 949-2473 (fax) ; 8fs@spin.att.com

Research in the field of high speed optoelectronics has resulted in a number of possible applications that could have impact in the "real-world". At present, however, commercially available ultrashort pulse optical sources are generally expensive and bulky, and have large electrical power and cooling service requirements. This limits present applications of ultrafast technology to primarily scientific markets. In order to widen the impact of these technologies, new sources have to be developed that are commensurate with a wider range of applications within large markets. For many applications, it would also help if they could be made to resemble electrical power supplies. Figure 1 shows an application for ultrafast optoelectronics that nicely illustrates the problem: optical clock distribution. In the implementation of complex multi-processor systems with clock rates in excess of 500 MHz, it is likely that optics can provide systems advantages in low-jitter and low-drift clock synchronization.

Electronics designers take for granted the existence of electrical power supplies when

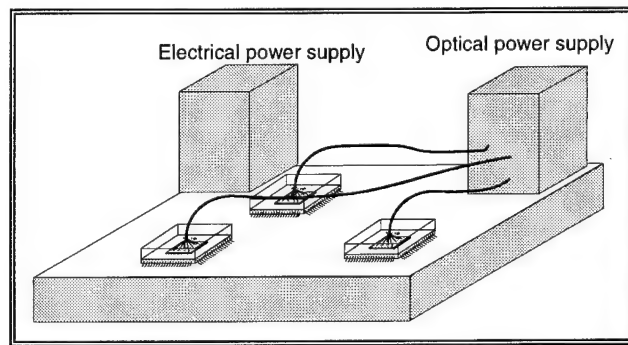


Figure 1. Example of high speed optoelectronics application requiring a "real-world" short pulse optical source.

designing such systems. It is clear that if short-pulse optical power supplies existed in

such a form, it would be very much more likely that they would be used in the "real-world".

A number of approaches are currently being investigated with the goal of achieving the required combination of parameters such as compactness, pulsewidth, fiber-coupled average power, wavelength, efficiency and environmental stability. Figure 2

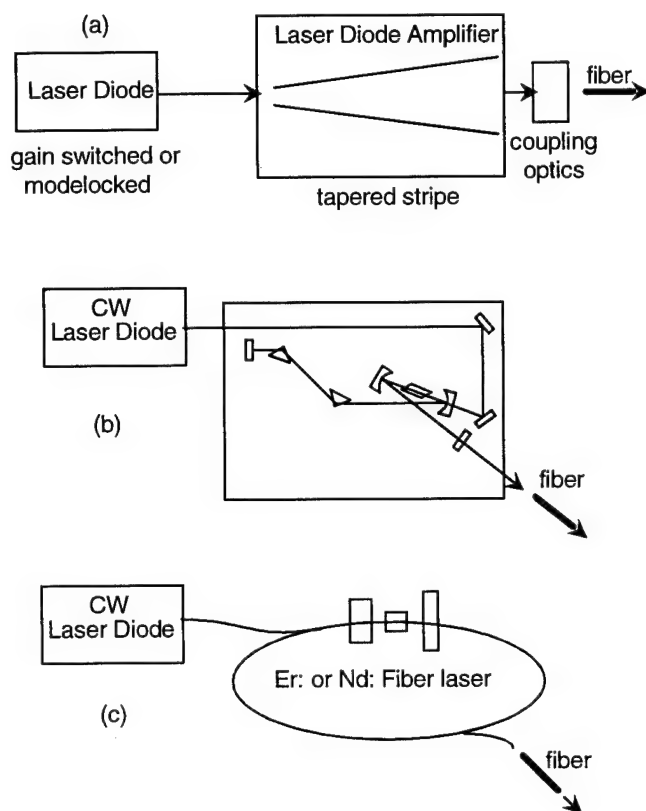


Figure 2. Approaches to the compact short pulse optical power supply.

summarizes the three major approaches. Figure 2a shows an approach wherein a laser diode is either gain-switched or modelocked, then amplified before coupling to a fiber. Figure 2b shows the diode-pumped solid state laser approach, and Figure 2c shows the diode-pumped fiber laser approach. It is commonly thought that any such source could only be made from laser diodes, since they are the most compact optical sources yet developed, however the combined requirements of high average power, short pulsewidth

and single-mode fiber-coupling are difficult to achieve with all-diode systems. We will discuss this problem.

There have been recent laboratory advances in all-solid-state ultrafast lasers in the direction of increased compactness and lower power requirements. Although several research groups are working in this area, big laser companies do not appear to be moving aggressively in this direction. Part of the problem is illustrated in Figure 3. In the absence of "real-world" sources, the emergence of "real-world" applications will be slow. On the other hand, in the absence of applications that address large markets, companies will be reluctant to pour money into development of such sources.

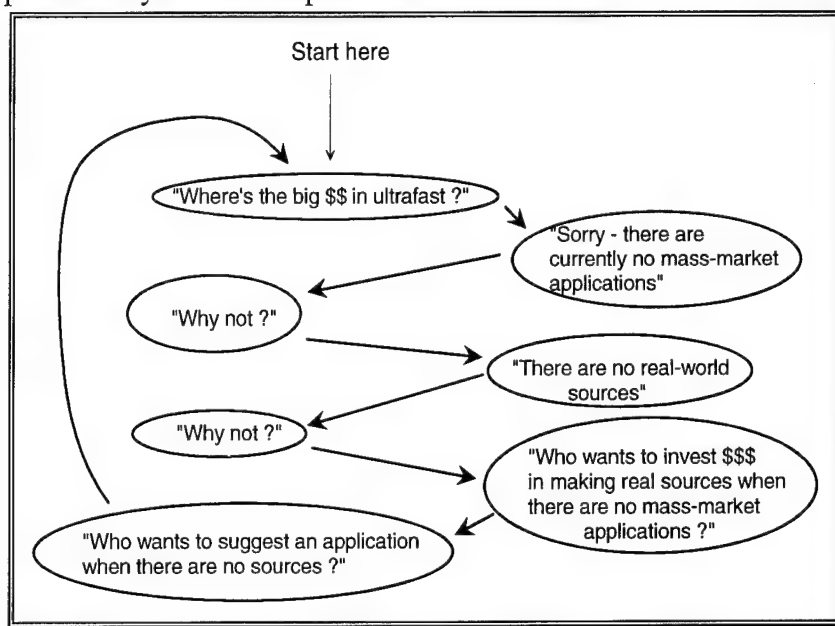


Figure 3. The Ultrafast "Catch-22"

In this presentation, we will discuss the general requirements for ultrafast optical power supplies. We will also point out that many applications for ultrafast technology, (and perhaps the most important from a market point of view) actually are not what are generally thought of as high speed applications, although they require high speed technology.

Ultrafast Semiconductor Laser Diode Seeded Cr:LiSAF Regenerative Amplifier System

Peter J. Delfyett, S. Grantham, K. Gabel, A. Yusim, S. Gee, M. Richardson

Center for Research and Education in Optics and Lasers (CREOL)

Department of Electrical and Computer Engineering

Department of Physics

University of Central Florida

Orlando, Florida 32826

(407) 658-6812

delfyett@faculty.creol.ucf.edu

G. Alphonse, J. Connolly

David Sarnoff Research Center

Princeton, New Jersey 08543

Compact and efficient sources of ultrashort, high power optical pulses will play an important role in novel technologies ranging from x-ray generation for photolithography, high spatial resolution medical imaging, and high speed measurement and characterization systems. In this talk, we present the first results, to our knowledge, of an ultrafast semiconductor laser diode system which is used as a seed source for a flashlamp pumped Cr:LiSAF regenerative amplifier system.

The experimental setup is illustrated in Fig. 1. Ultrashort optical pulses are generated from a hybrid modelocked external cavity semiconductor diode laser system. The system is capable of generating optical pulses with temporal durations of 200 femtoseconds in duration with pulse energies on the order of 30-35 picojoules [1]. The system consists of a GaAs/AlGaAs semiconductor traveling wave optical

amplifier in an external cavity with a GaAs/AlGaAs multiple quantum well rear reflector which serves as a saturable absorber. The external cavity diode laser is excited with both d.c. currents and ~ 1 watt of r.f. current at a frequency of 274 MHz, corresponding to the longitudinal mode spacing of the external cavity, to achieve hybrid modelocking. The generated optical pulses are passed through an optical isolator and injected into a second semiconductor traveling wave optical amplifier to increase the optical pulse energy to ~ 75 picojoules. The pulses are then stretched to 120 picoseconds using a standard grating pulse stretcher and injected into another semiconductor optical amplifier to select every fifth pulse from the pulse train. This initial pulse slicing was performed prior to the main regenerative amplifier pulse slicer to reduce the diode laser system repetition rate to be compatible with the regenerative amplifier system pulse slicer. It should be noted that owing to the hybrid modelocked nature of the diode laser system, direct electrical triggering of the regenerative amplifier pulse slicer can be employed, avoiding the use of a fast photodetector to provide triggering pulses. The final pulse selection is performed by a standard Pockel's cell and injected into the regenerative amplifier which consists of a linear cavity configuration and a pulse slicer placed at the output coupler of the regenerative [2]. The single selected pulse is then directed to a pulse compressor and diagnostics.

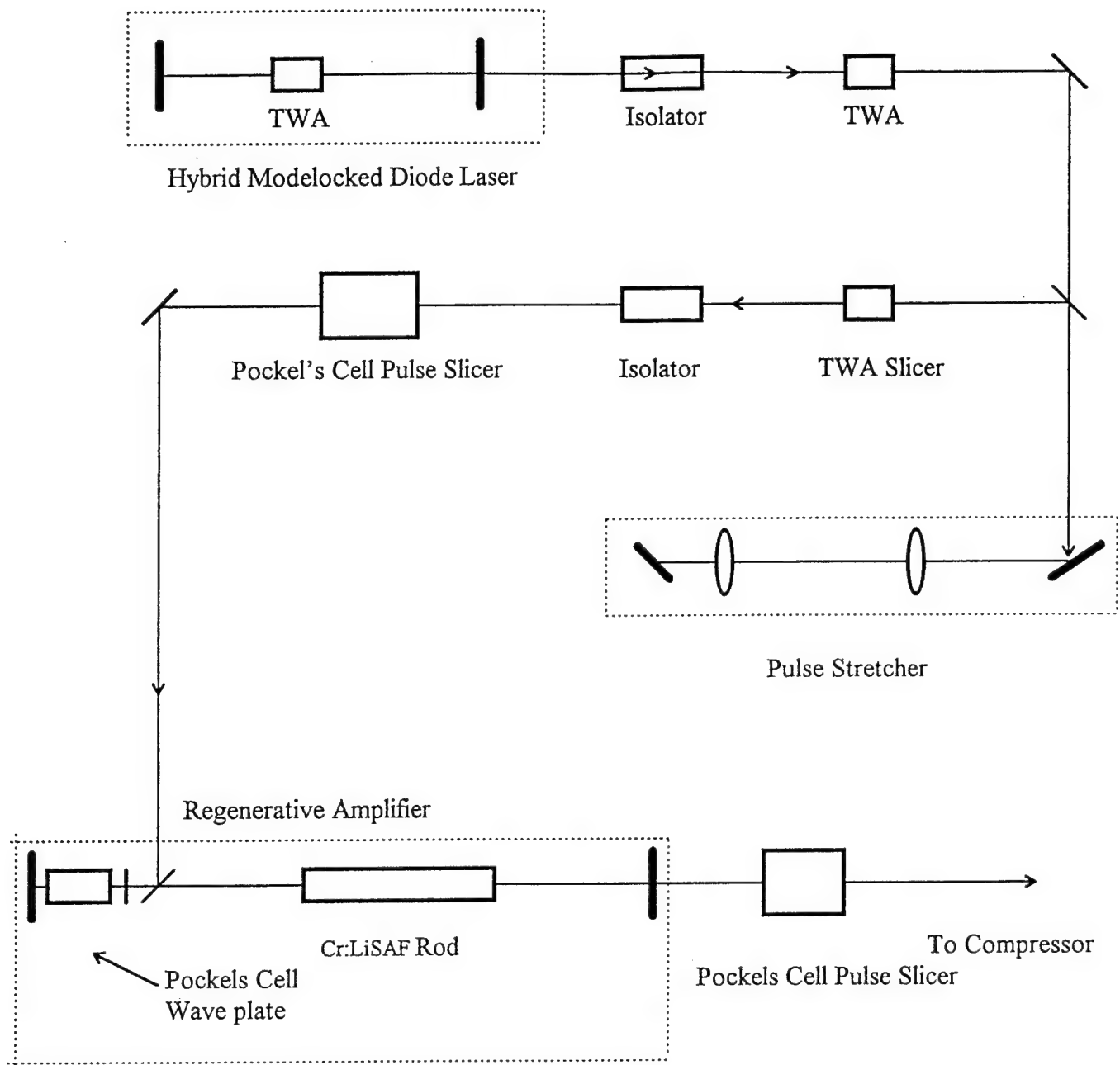
The amplified single pulse along with the rejected pulse train is shown in Fig. 2. These results were obtained by injecting ~ 40 picojoule pulses from the diode system into the regenerative amplifier. The rejected pulse train shows that ~ 55 round trips are required for the injected pulse to reach maximum gain. The single selected pulse energy was measured to be 1.25 mJ, representing a gain of over 30 million. The amplified single pulse spectrum is shown in Fig. 3, showing the injected diode laser wavelength at 841 nm, with the spontaneous emission peak of the Cr:LiSAF at 848 nm. Gain narrowing of approximately a factor of 2 is experienced in the amplification process owing to the large gain factor.

In conclusion, we have demonstrated the first experiments, to our knowledge, of a femtosecond diode laser system seeding a flashlamp pumped Cr:LiSAF regenerative amplifier system, producing

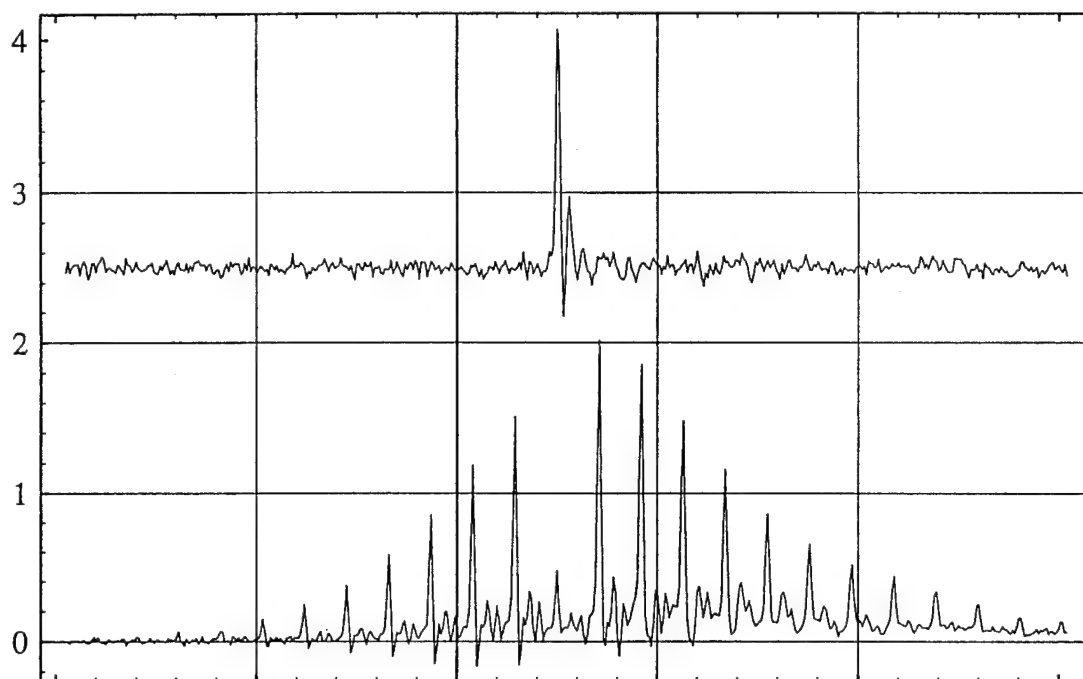
subpicosecond optical pulses with millijoule pulse energies. This laser system has the potential to replace ion laser based ultrafast, high power laser systems.

References

- [1] P. J. Delfyett, et al., IEEE Journ. Quant. Electr., 28, 2203, (1992).
- [2] P. Beaud, et al., Optics Comm, 95, 46, (1993).

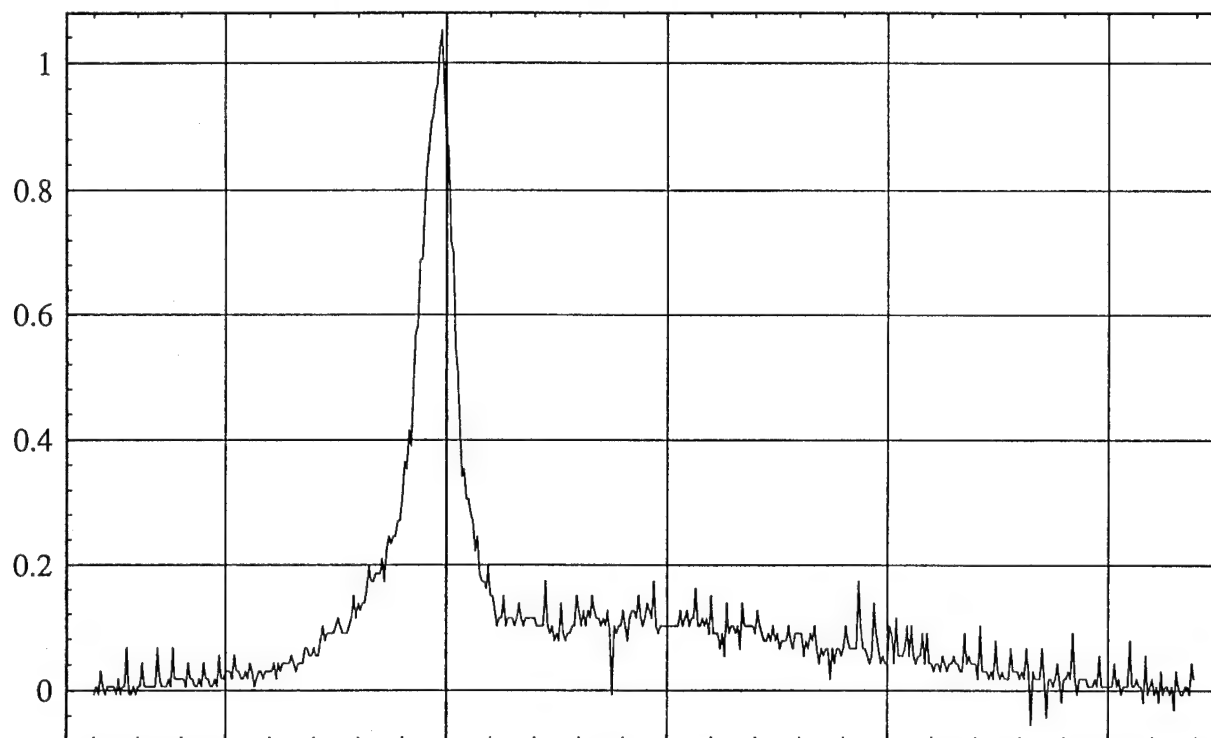


[1] Schematic of the experimental setup. TWA: Semiconductor Traveling Wave Optical Amplifier



Time (50 ns/div)

[2] Oscilloscope trace of the selected single pulse and the rejected pulse train.



Wavelength (10 nm/div)

[3] Optical spectrum showing the amplified injected diode laser signal.

Wavelength Division Multiplexing with Femtosecond Pulses

E. A. De Souza, M. C. Nuss, W. H. Knox, and D. A. B. Miller

AT&T Bell Laboratories, 101 Crawfords Corner Road, Holmdel NJ 07733

Phone: (908) 949-0238; FAX: (908) 949-2473

Ultrashort laser pulses have always had a central place in the study of high-speed phenomena as well as in applications involving very high data rates. Here, we present an application of femtosecond laser pulses that is not directly related to high speed, but rather makes use of the large spectral bandwidth of short pulses. Conventionally, wavelength-division-multiplexed (WDM) systems utilize a separate laser for each WDM channel. For systems with many channels the wavelength of each laser then needs to be controlled and stabilized individually to assure that the emission wavelength coincides with the pre-assigned WDM channels. This need for multiple, frequency-stabilized sources is a considerable problem for any WDM systems.

Our approach overcomes this problem by use of a single femtosecond laser source with a broadband spectrum covering all WDM channels simultaneously. For example, a 100 fs laser pulse has 3 THz spectral bandwidth, enough for 30 channels spaced at 100 GHz. The spectrum of the femtosecond pulse is "sliced" by a passive filter in order to define the WDM channels. Each one of these WDM channels is modulated by a linear modulator array at the repetition rate of the laser.

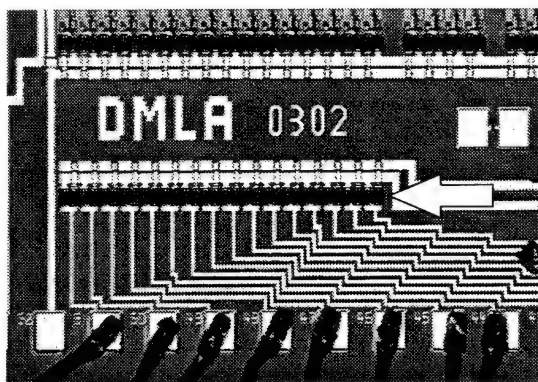
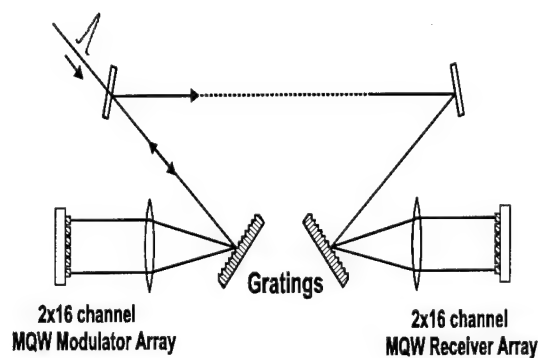


Fig. 1. Left: Experimental apparatus to implement femtosecond WDM at 850 nm. Right: Linear 16 channel reflection-mode modulator array.

The experimental setup used in our femtosecond WDM experiment is shown in figure 1. The transmitter consists of a 1200-line/mm diffraction grating placed one focal length in front of a $f=50\text{ mm}$ laser diode collimating lens (Melles-Griot 06 GLC 006) and a 16-channel reflection-mode modulator array placed at the focus of the lens. The receiver side has a similar configuration with the modulator array replaced by a detector array. The femtosecond pulse from a self-focusing modelocked Ti:Sapphire laser with 9 nm (3.7 THz) spectral bandwidth centered at 850 nm is spectrally and spatially dispersed by the diffraction grating and focused onto the linear modulator array by the collimating lens. The spectral dispersion of the apparatus is given by $dx/d\lambda = f/(d \cdot \cos\theta)$, where f , d and θ are the focal length of the collimating lens, grating

period, and the diffracted angle, respectively. For our setup, $dx/d\lambda = 120 \mu\text{m}/\text{nm}$. The beam is focused to approximately $10 \mu\text{m}$ vertically on the modulator array and the spectrum is spread out to roughly 1 mm , which is a little longer than the total length of the modulator array.

Figure 1 (right) shows a photograph of the 16 channel reflection-mode modulator array used in our experiment. It consists of 32 multiple quantum well (MQW) diodes working in pairs in a differential mode. Each modulator has two MQW diodes in series biased at approximately 8.4 V . The data signal is injected at the midpoint between the diodes and swings between zero and approximately 7 V . The size of each quantum well diode is $20 \times 20 \mu\text{m}$ with $5 \mu\text{m}$ spacing. This linear array also works as a passive filter which defines the 16 WDM channels on the spectrum of the femtosecond pulse. Each channel has approximately 115 GHz (0.28 nm) channel bandwidth defined by the $20 \mu\text{m}$ width of the MQW diode. On the modulator, each channel is modulated individually and reflected back along the input path. The modulated signals are recollimated spectrally and spatially by the lens and grating, picked off by a beam splitter, and transmitted to the receiver setup through a fiber or in free space.

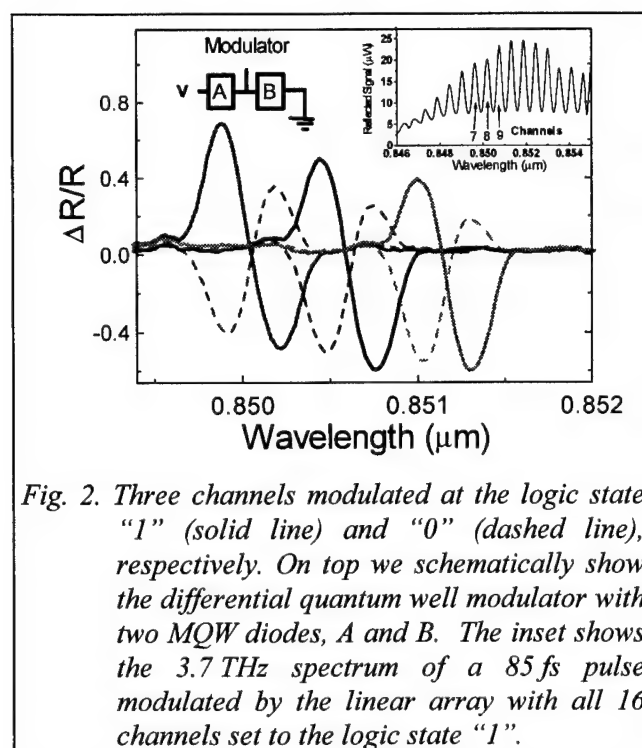


Fig. 2. Three channels modulated at the logic state "1" (solid line) and "0" (dashed line), respectively. On top we schematically show the differential quantum well modulator with two MQW diodes, A and B. The inset shows the 3.7 THz spectrum of a 85 fs pulse modulated by the linear array with all 16 channels set to the logic state "1".

Figure 2 shows the spectrum of the light reflected back from the modulator array. It shows the reflectivity change for three channels (7, 8, and 9) modulated at different logic states "1" (solid line) and "0" (dashed line). The logic signals are encoded differentially, with the reflectivity of the left MQW diode (A) enhanced compared to the one on the right (B) for a logic "1", and vice versa for a "0". Because the modulator array is not mechanically pixelated, the optical crosstalk between adjacent channels is approximately -5 dB . However, we have shown that pixelation leads to a 30 dB reduction in optical crosstalk.

The system performance is demonstrated by modulating a single channel at the repetition rate of the laser (approximately 82 Mbit/s) and transmitting the information in free space to a single-ended APD receiver. The result is shown in Fig. 3. The NRZ modulation signal is shown on top. The optical power incident on the modulator is approximately $100 \mu\text{W}$. The received signal is shown at the bottom of Fig. 3. The modulation of the pulse train is clearly visible with contrast ratio of $3:1$. This low contrast ratio results from the single-ended detection and can be improved by using a differential receiver.

Even with the rather low contrast ratio, figure 4 shows an open eye pattern indicating error-free operation at 82 Mbit/s for $100 \mu\text{W}$ optical power incident on the modulator. In fact, the bit-error-rate (BER) at any power level is entirely limited by receiver noise in our experiment.

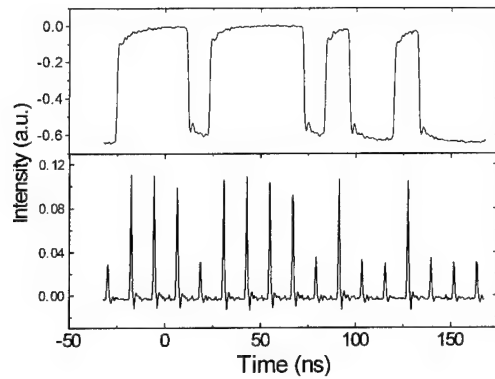


Fig. 3. Single channel transmission using NRZ format at 82 Mbit/s. On top the input signal on the modulator is shown, while the bottom shows the received signal.

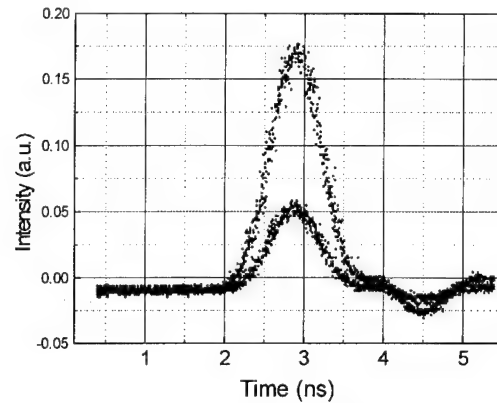


Fig. 4. Eye diagram at 82 Mbit/s operation with a single-ended receiver.

In conclusion, we demonstrate femtosecond wavelength division multiplexing that uses a single source to generate all WDM channels simultaneously rather than requiring one laser per channel. Experiments are under way to demonstrate this principle with a femtosecond source at $1.5\ \mu\text{m}$ [2] and using integrated InP gratings and modulators [3].

References

- [1] T. K. Woodward et al., Phot. Techn. Lett. **4**, 614 (1992).
- [2] K. Tamura, C. R. Doerr, L. E. Nelson, H. A. Haus, and E. P. Ippen, Opt. Lett. **19**, 46 (1994).
- [3] M. Zirngibl, C. H. Joyner, Electron. Lett. **30**, 701 (1994).

Determination of Linear and Nonlinear Chirp Parameters of Gain-Switched Diode Laser Pulse Using Short Time Fourier Transform

H. Takeshita, M. Tsuchiya and T. Kamiya

Department of Electronic Engineering, University of Tokyo

7-3-1 Hongo, Tokyo 113, Japan; Tel: +81-3-3812-2111 (ext. 6679) Fax: +81-3-3818-5706

I. Introduction

For future ultra high speed fiber optic telecommunication¹ and/or very fast industrial measurements², one need compact, stable and reliable sources of pico and subpicosecond optical pulses. The gain-switching operation of semiconductor distributed feedback (DFB) laser diode (LD) is advantageous to other pulse generation methods due to the controllability of pulse intervals in a wide range. However, improvement of its performance is required in such aspects as shorter pulse duration, larger pulse energy, higher repetition rate, lower timing jitters, and precise control of those. As for the reduction of pulse width, a fiber optic compression scheme^{3,4} was proved to be effective, in which original pulses of a few tens picosecond are compressed into the subpicosecond range by a transmission through a linear dispersion fiber and a so-called soliton fiber. Linear down chirp of gain-switched DFB-LD pulse is essential in the former and a nonlinear effect of fiber in the latter. One should note here that for the control of compressed pulse quality it is important to make the chirp of original pulse properly fitted to length, dispersion and nonlinearity of fiber system, and also to keep the nonlinear chirp as small as possible. Therefore, it is necessary to establish an experimental method for precise chirp measurement⁵⁻⁷ as well as to clarify its dependence on conditions of LD operation.

We present in this paper a novel systematic approach to evaluate linear and nonlinear chirp parameters C_1 and C_2 based both on the spectrally resolved streak camera images and on the best fit procedure using short time Fourier transform (STFT)^{8,9}, with which the time-frequency uncertainty relationship is consistently treated. This method is rather simple and sensitive. In addition, we show that knowledge of device parameter dependence of chirp parameters thus derived helped optimizing the fiber optic pulse compression.

II. Chirp Parameter Determination Procedure

First, we describe a measurement with a grating monochromator and a streak camera for obtaining both temporally and spectrally resolved image of a chirped pulse:

$$f(t) = f_0(t) \exp[j\omega_c t + j\phi(t)]. \quad (1)$$

In the above equation, f_0 is the slowly varying envelope, $\phi(t)$ the time dependent phase and ω_c the center angular frequency. We express the chirp $\Delta\lambda(t)$ taking account of C_1 and C_2 as

$$\Delta\lambda(t) = -\frac{2\pi c}{\omega_c^2} \frac{d\phi}{dt} = C_1(t - t_0) + C_2(t - t_0)^2, \quad (2)$$

where c is the velocity of light, and $f_0(t)$ gets maximum at $t = t_0$. We assume here that the spatial pulse cross section at the grating is given by a Gaussian function $\exp[-2\ln 2(x/X)^2]$, where x is the distance from the beam center and X the beam radius. The diffraction theory shows that the pulse at the exit of monochromator is expressed by

$$V(t', \omega) = \int_{-\infty}^{\infty} f(t) g(t - t') \exp(-j\omega t) dt, \quad (3)$$

$$g(t) = \exp[-2\ln 2(t/T_M)^2], \quad (4)$$

$$T_M = 2\pi X/\omega d, \quad (5)$$

where d is the pitch of grating, and the temporal broadening T_M is introduced originating from the finite spatial broadening X at the grating. Equation 3 is the same formula as that of STFT with $g(t)$ as a window function. The spectrally resolved streak camera image $W_{SC}(\tau, \omega)$ is given by a convolution of $|V|^2$ and the temporal impulse response $h(t)$ of the streak camera:

$$W_{SC}(\tau, \omega) = \int_{-\infty}^{\infty} |V(t', \omega)|^2 h(t' - \tau) dt', \quad (6)$$

$$h(t) = \exp[-4\ln 2(t/T_{SC})^2]. \quad (7)$$

Note that it is impossible to derive C_1 and C_2 directly by the inverse STFT of an experimentally measured image because only intensity profile is detected by a streak camera.

Instead, we utilize an alternative approach. In Fig. 1, a temporal intensity profile $A(t)$ derived in a separate measurement only with the streak camera is shown. A trial function $f_i(t)$ is prepared using $A(t)$ as

$$f_i(t) = A(t) \exp[j\omega_c t + j\phi_i(t)]. \quad (8)$$

Here, ϕ_i is the phase derived by putting a trial set of C_1 and C_2 into Eq. 2. From Eqs. 3 - 8, a streak image is numerically generated. By comparing it with the experimental result and varying C_1 and C_2 so that the deviation between those is minimized, C_1 and C_2 are eventually determined for the best fitted image. The procedure of this STFT approach is schematically shown in Fig. 2.

III. Experiment and Discussion

We prepared the experimental setup mentioned above, which consists of a 250 mm monochromator and a streak camera (Hamamatsu Photonics C1587), and measured spectrally resolved streak camera images of pulses from a gain-switched DFB-LD with a center wavelength λ_c of 1.556 μm and threshold current of 8 mA. Current pulses of 130 ps, which were generated with a 100 MHz

frequency synthesizer, an electrical amplifier of 50 dB gain and a comb generator, were fed to the LD with DC bias current I_b . Temperature θ of LD was controlled by a Peltier cooler.

The streak camera was operated in the synchronous scanning mode. Since the quantum efficiency of photo-emitted electrons in 1.5 μm range is quite low, integration of signals for 3 minutes was necessary to get enough signal-to-noise ratio. Its timing jitters were negligible in comparison with its own temporal resolution T_{SC} of 15 ps, which was measured with subpicosecond optical pulses in a separate measurement. The pitch d of grating in the monochromator is 600 groove/mm.

In order to make the nonlinear chirp appear clearly, we optimized a ratio of the wavelength resolution $\Delta\lambda_M$ to the temporal one T_M so that the streak camera image is tilted with an angle around 45 degree. The adjustment was done by varying X through a change in the input slit width of monochromator. $\Delta\lambda_M$ of 0.6 nm was typical at 1.556 μm , which was checked with a CW light from the DFB-LD, and corresponding T_M is 13 ps. In addition, we inserted 1:4 magnification optics between the monochromator and the streak camera.

Typical spectrally resolved streak camera image is shown in Fig. 3 (a), which was taken under a condition that the output power P_{RF} of synthesizer was -13.3 dBm, $I_b = 0$ mA and $\theta = 18$ C. Following the procedure described in the previous section, an image was numerically generated (Fig. 3 (b)). Those two images are apparently in a good agreement with each other indicating that the STFT approach is effective. The chirp characteristics thus evaluated are plotted in Fig. 1.

Furthermore, we systematically measured the streak camera images under a variety of conditions and determined sets of C_1 and C_2 . Figures 4 show dependence of C_1 and C_2 on P_{RF} (a), I_b (b) and θ (c). Gray zones in Figs. 4 indicate an optimum C_1 value for the linear compression scheme using a 1 km fiber with normal dispersion of -16 ps/km/nm at 1.55 μm ^{3,4}. It is clearly shown that both C_1 and C_2 are sensitive most to P_{RF} in the three parameters, and hence the control of P_{RF} is a very important issue. For the best P_{RF} (= -13.3 dBm), C_1 is almost independent either of I_b or θ . On the other hand, $|C_2|$ increases as I_b increases or as θ gets out of the range of 13 - 23 C. Actually, linearly compressed pulse was shortest (~ 4 ps in full width at half maximum of autocorrelation trace) under the condition that $P_{RF} = -13.3$ dBm, $I_b = 0$ mA and $\theta = 18$ C, and was broadened outside the above temperature range. Therefore, one should conclude that, for this particular DFB-LD, I_b should be zero and θ should be kept in such range while P_{RF} should be tuned to be optimum.

In addition, those pulses were compressed further by the adiabatic compression scheme using an Er-doped fiber amplifier and an anomalous

dispersion fiber. Dependence of pulse qualities at the final stage of compression on the driving conditions was studied in a similar manner. However, since the optical power of launched pulse is another important parameter, the optimization is more complicated than the case of linear dispersion fiber. The details of results will be reported elsewhere.

IV. Summary

A novel systematic approach to determine linear and nonlinear chirp parameters is presented, which is based both on the spectrally resolved streak camera images and on the best fit procedure using STFT. We have successfully determined C_1 and C_2 , and demonstrated that this approach is useful in the optimization of picosecond pulse generation by a gain-switched laser diode and fiber optic compression scheme.

The authors would like to express a sincere gratitude to Mr. T. Urakami, Mr. H. Takahashi, and Dr. Y. Tsuchiya of Hamamatsu Photonics for their corporation in the measurement. They thank Dr. Y. Ogawa of Oki Electric for the supply of DFB-LD.

References

1. S. Kawanishi, H. Takara, K. Uchiyama, T. Kitoh and M. Saruwatari: "100 Gb/s, 50 km Optical Transmission Employing All-Optical Multi / Demultiplexing and PLL Timing Extraction", OFC'93 Post Deadline Paper, PD2 (1993).
2. J. A. Valdmanis "1 THz-Bandwidth Prober for High-Speed Devices and Integrated Circuits", Electron. Lett. **23**, 1308-1310.
3. J. T. Ong, R. Takahashi, M. Tsuchiya, S. H. Wong, R. Sahara, Y. Ogawa and T. Kamiya: "Subpicosecond Soliton Compression of Gain Switched Diode Laser Pulses Using An Erbium-doped Fiber Amplifier", IEEE J. Quantum Electron. **29**, 1701-1707 (1993).
4. R. Sahara, H. Takeshita, K. Miwa, M. Tsuchiya and T. Kamiya: "Electrooptic Sampling Evaluation of 1.5 μm Optoelectronic Devices by Soliton Compressed Semiconductor Laser Pulses", to be published in IEEE J. Quantum Electron.
5. K. Naganuma, K. Mogi and H. Yamada, "General Method for Ultrashort Light Pulse Chirp Measurement", IEEE J. Quantum Electron. **25**, 1225-1233 (1989).
6. R. Trebino and D. J. Kane: "Using Phase Retrieval to Measure the Intensity and Phase of Ultrashort Pulses: Frequency-Resolved Optical Gating", J. Opt. Soc. Am. A **10**, 1101-1111 (1993).
7. T. Morioka and M. Saruwatari: "Demonstration of Chirping Manipulation of Laser-Diode Chirped Optical Pulses Utilizing Cross-Phase Modulation in Optical Fibers", Electron. Lett. **25**, 646-648 (1989).
8. A. N. Akansu and R. A. Haddad, "Multiresolution Signal Decomposition.", Chapter 5 (Academic Press, Inc., New York, 1992)
9. C. Hirlimann, M. May and J. F. Morhange, "Analyse en ondelettes d'impulsions ultracourtes", Ann. Phys. Colloq. **2**, Suppl. 16, 181-182 (1991)

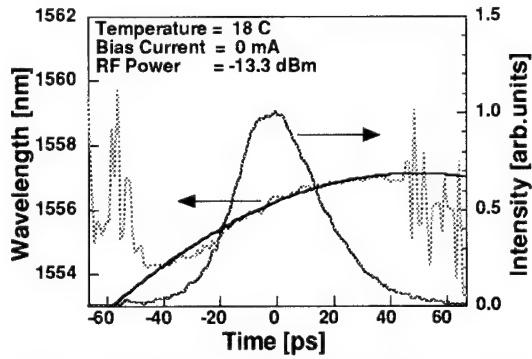


Fig. 1 Transient intensity profile of a gain-switched pulse is plotted with its chirping characteristics derived by the STFT approach. Gray line shows ridge wavelength of corresponding measured image.

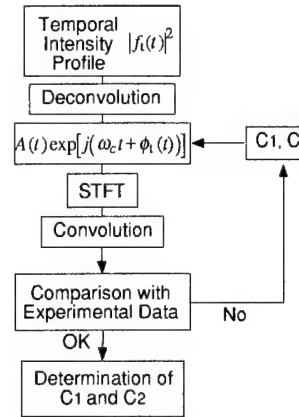


Fig. 2 Flow chart of the STFT approach for the determination of linear and nonlinear chirp parameters C_1 and C_2 .

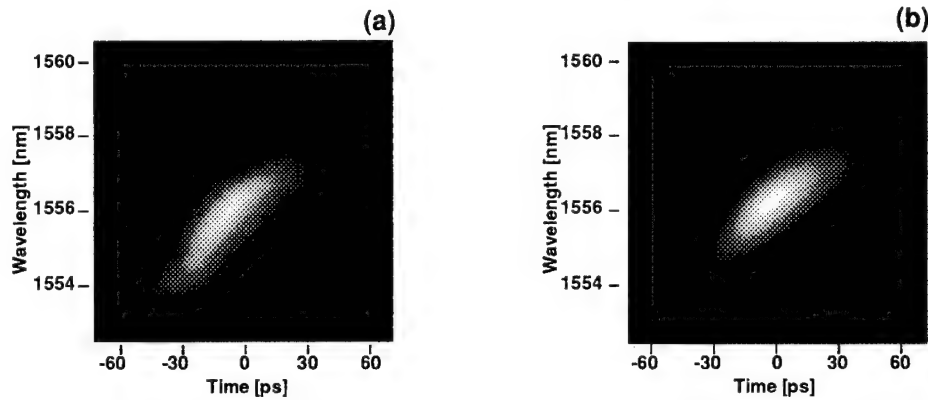


Fig. 3 Temporally and spectrally resolved image of a gain-switched diode laser pulse measured with a grating monochromator and a streak camera (a), and corresponding image generated numerically by the STFT approach (b).

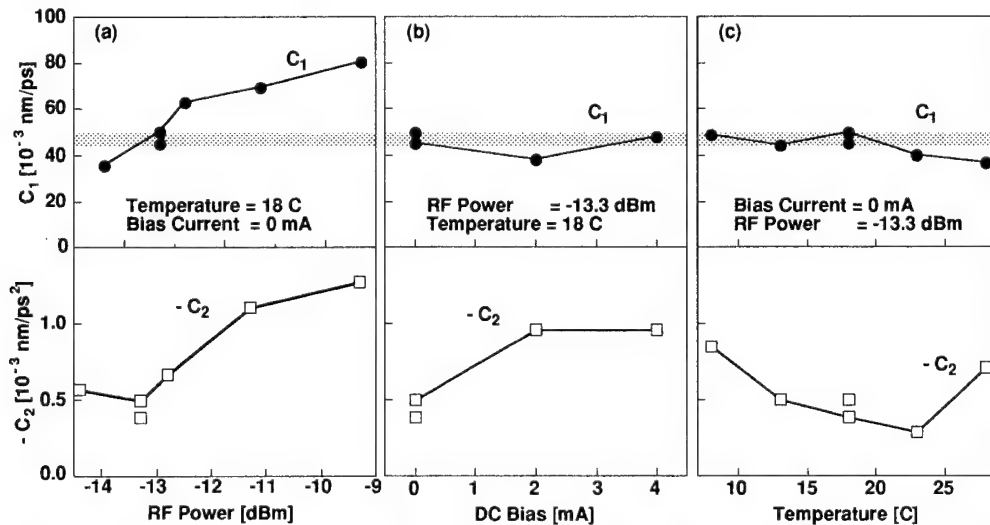


Fig. 4 Dependence of linear and nonlinear chirp parameters C_1 and C_2 on conditions of LD operation: RF power of frequency synthesizer (a), DC bias current (b) and temperature of LD (c). Gray zones indicate optimum C_1 value for the linear compression scheme using a 1 km fiber with normal dispersion of -16 ps/km/nm at 1.55 nm.

Carrier dynamics of gain-coupled and index-coupled InGaAs/InGaAlAs quantum well distributed feedback lasers

J. Kovač, C. Kaden, V. Hofsäß, H. Schmidt, H. P. Gauggel, J. Kuhn, H. Schweizer
 4. Physikalisches Institut, Universität Stuttgart, Pfaffenwaldring 57
 D-70550 Stuttgart, Germany
 Tel.: 49-711-685-4961, Fax: 49-711-685-5097

A. Hase, H. Künzel
 Heinrich-Hertz-Institut Berlin GmbH, Einsteinufer 37
 D-10587 Berlin, Germany

H. Hillmer
 Deutsche Bundespost Telekom, Forschungsinstitut, P.O.Box 100003
 D-64176 Darmstadt, Germany

Picosecond pulse generation in semiconductor lasers is indispensable for ultrafast optical information processing systems. For the application in high data-rate systems based on optical fiber transmission links single mode lasers with high modulation response are necessary. Very promising are gain-coupled (GC) distributed feedback (DFB) lasers, which should remain in stable single mode operation even at high modulation rates /1/.

On the other hand reliable device technologies are important to meet the requirements of reproducibility at low costs. To realize long wavelength 1.3 μm GC DFB lasers we developed a fully planar technology of masked implantation enhanced intermixing (MIEI) /2/ based on high quality InGaAs/InGaAlAs quantum well structures /3/. A gain-coupled device is obtained by periodic band structure variation along the resonator. Therefore local segments are shadowed by a sub-micron grating Au-mask /4/. Subsequent implantation and thermal annealing processes result in Al and Ga interdiffusion in the implanted regions of the active layers leading to periodic lateral band gap variations and thus periodic gain shifts.

The analysis of gain shift was accomplished by realization and comparison of conventionally fabricated index-coupled (IC) DFB lasers with and without homogeneous implantation enhanced intermixing (IEI) /5/ of the active region.

The control of the different technology steps was carried out by photo-luminescence and time-resolved spectroscopy. The energy position and the amplitude of optical gain were determined as a function of the implantation dose. For a variation of the implantation dose up to $3 \cdot 10^{13} \text{ cm}^{-2}$ we obtained a gain shift to higher energies up to 30 meV, indicated by the comparison of the low temperature amplified spontaneous emission spectra of quantum well structures with and without the process of IEI in fig. 1.

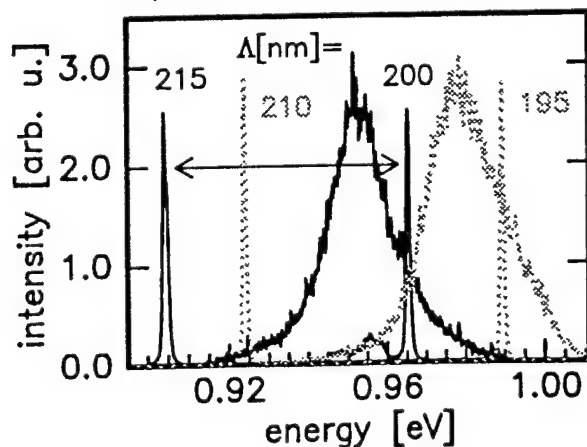


Fig. 1 Amplified spontaneous emission spectra and IC DFB laser spectra of non-implanted structures (full line) and IEI structures implanted with an Ar^+ dose of $3 \cdot 10^{13} \text{ cm}^{-2}$ (dotted line). The arrow between the DFB lasers with different grating periods Δ indicates the low and high energy end of the gain region of the non-implanted sample.

Realization of DFB lasers with a large range of different DFB grating periods opened the analysis of band structure dependent carrier dynamics and of the effect of gain shift in IC and MIEI GC DFB lasers. According to the Bragg-condition non-implanted IC DFB lasers require grating periods Λ from 200 nm to 215 nm (see horizontal arrow in fig. 1). Due to the gain shift IEI IC DFB lasers require grating periods from 195 nm to 210 nm and MIEI GC DFB lasers (not shown in fig. 1 for the sake of clarity) from 190 nm to 202.5 nm.

The investigation of fast carrier dynamics in these devices was performed by a gain-switching method in conjunction with the technique of light frequency up-conversion /6/ (time resolution about 2 ps); this technique simultaneously yields a high spectral resolution, which enables the observation of the transient laser mode behavior.

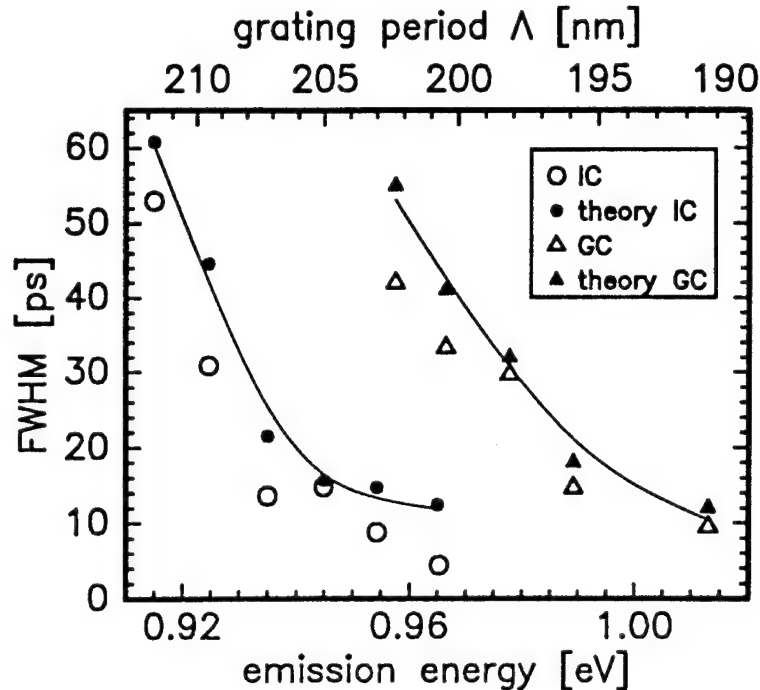


Fig. 2 Experimental FWHM values for MIEI GC (open triangles) and IC (open circles) lasers versus emission energy of the DFB lasers. To extract exclusively band structure effects and to avoid non-radiative recombination processes measurements were performed at $T = 2K$.

Solid symbols are calculated values obtained from laser rate equations. (The solid lines serve as a guide for the eye).

In fig. 2 the pulse response of MIEI GC and non-implanted IC DFB lasers on a 2 ps excitation pulse is plotted versus the emission energy (open symbols). On the top axis the corresponding grating period is depicted. Three interesting features can be observed. i) The pulse response for both coupling types becomes faster with higher emission energy, i. e. with decreasing grating period. ii) Modulation bandwidth of GC DFB lasers is rigidly shifted to higher emission energy compared to IC DFB lasers due to the spectral gain shift induced by MIEI. iii) The maximum modulation speed of MIEI GC lasers is comparable with speed of IC lasers in agreement with theory /7/.

The full widths at half maxima (FWHMs) of the IC DFB lasers decrease from 53 ps at an emission energy of 915.0 meV down to 4.5 ps at 965.3 meV, while for MIEI GC DFB lasers this decrease amounts from 42 ps (957.6 meV) to 9.5 (1013.0 meV). These energy dependent pulse widths are in agreement with theoretical analysis based on coupled light and carrier rate equations /8/. In conjunction with line shape analysis of the spontaneous emission at laser thresholds of the different DFB lasers an ab initio parameter free calculation is performed, considering the band structure dependent differential gain $dg/dn(E)$. Increasing dg/dn values with increasing emission energy result in faster modulation speed as shown in fig. 2 by the calculated solid symbols.

- 1 Y.Nakano, Y.Luo, K.Tada; Appl. Phys. Lett. **55**, 1606, (1989).
- 2 A.Hase, C.Kaden, J.Kovač, V.Hofsäβ, H.Künzel, H.Schweizer; 6th International Conference on InP and Related Materials, IEEE Catalog # 94CH 3369-6 Library of Congress # 94-61270, pp. 163, Santa Barbara 1994.
- 3 H.Künzel, J.Böttcher, A.Hase, V.Hofsäβ, C.Kaden, H.Schweizer; to be published in J. of Crystal Growth.
- 4 C.Kaden, H.Gräbeldinger, H.P.Gauggel, V.Hofsäβ, A.Hase, A.Menschig, H.Schweizer, R.Zengerle, H.J.Brückner; Microelectronic Eng. **ME-23**, 469, (1994).
- 5 H.Leier, A.Forchel, G.Hörcher, J.Hommel, S.Bayer, H.Rothfritz, G.Weimann, W.Schlapp; J. Appl. Phys. **67** (4), 1805, (1990).
- 6 J. Shah; IEEE J. of Quantum Electron., **QE-24**, pp. 276-288, (1988).
- 7 L.M.Zhang, J.E.Carroll; IEEE Photonics Technology Letters, Vol. **5**, 506, (1993).
- 8 K.Y.Lau, A.Yariv; in Semiconductor and Semimetals, edited by W.T.Tsang, (Academic Press, Inc., 1985), Vol. 22, Part B, pp. 69-152.

ULTRAFAST LOW-TEMPERATURE-GROWN-GaAs PHOTOMIXERS*

K. A. McIntosh, E. R. Brown, K. B. Nichols, O. B. McMahon, K.M. Molvar,
W.F. DiNatale, and T.M. Lyszczarz

Lincoln Laboratory, Massachusetts Institute of Technology
Lexington, Massachusetts 02173-9108

Various ultrafast electronic and optoelectronic devices have been developed as sources for the terahertz spectral region. Most of these sources exhibit relatively low power spectral density. This can be due to their inherently broadband nature, as with ultrafast switches pumped with subpicosecond optical pulses [1], or to their low conversion efficiencies, as with optical three-wave mixing [2]. Optical heterodyne conversion, or photomixing, has recently been explored as a technique for the production of coherent radiation at terahertz frequencies [3]. In order to produce useful levels of power in this frequency range a photomixer must exhibit high responsivities, be robust under optical pumping, and be capable of ultrafast operation. Low-temperature-grown (LTG) GaAs photomixers have demonstrated all of these properties and should be useful for applications such as ultra-wideband sweep oscillators and tunable local oscillators. This paper will discuss the latest LTG-GaAs photomixer devices, showing twenty times more output power at 3 THz than earlier devices [4].

The two photomixer structures used for these measurements were fabricated on a 1.5 micron thick LTG-GaAs layer grown by molecular beam epitaxy at 200 °C on a semi-insulating GaAs substrate. Interdigitated metal electrodes 0.2 microns wide with a 2.0 micron period were fabricated by electron beam lithography at the driving point of a 3-turn self-complementary spiral antenna on the top surface of the LTG-GaAs. Mixer 1 had a 20 x 20 micron electrode area with a 20 micron interconnect to the spiral and was designed for operation to roughly 1 THz. Mixer 2 incorporated an 8 x 8 micron electrode area connected directly to a spiral antenna designed to operate up to 4 THz. These structures are shown in Figures 1 and 2. Optical pumping of the photomixer is accomplished with two Ti:Al₂O₃ lasers, one a standing wave cavity and one a ring cavity, whose output beams are spatially combined in a single-mode fiber-optic combiner and focused onto the interdigitated electrode region. The standing-wave laser is kept at a fixed frequency, while the frequency of the ring laser is tuned to vary the difference frequency. Difference frequency radiation propagates through a silicon hyper-hemispherical lens mounted on the back surface of the semi-insulating GaAs substrate and is focused with a TPX lens onto a composite silicon bolometer.

The high frequency behavior of these devices is controlled by two time constants, one related to the photocarrier lifetime and the other to the product of the electrode capacitance and the antenna radiation resistance ($\approx 72 \text{ ohm}$). Time resolved reflectivity measurements on the LTG-GaAs show the photocarrier lifetimes to be approximately 0.27 ps , resulting in a lifetime-limited 3-dB-down frequency of 590 GHz . The calculated electrode capacitances are 3.0 fF and 0.47 fF for Mixers 1 and 2, respectively, resulting in RC-limited 3-dB-down frequencies of 730 GHz and 4.7 THz . The measured bandwidth curves for Mixers 1 and 2 are shown in Fig. 3. The output power is relatively flat with frequency up to 300 GHz for both mixers, but beyond 500 GHz Mixer 1 rolls off at approximately 12 dB/octave while Mixer 2 rolls off at approximately 6 dB/octave . This is the expected behavior since the lower capacitance Mixer 2 should be limited only by photocarrier lifetime in the frequency range measured. Twenty times greater output power is measured for Mixer 2 than for Mixer 1 at 3 THz due to the lower capacitance of Mixer 2.

To the best of our knowledge, the LTG-GaAs photomixer is the most broadly tunable coherent source demonstrated in this frequency region. As such it is already finding widespread use for molecular spectroscopy, solid-state device characterization, component diagnostics, and frequency metrology.

- [1] A.S. Weiling, B.B. Hu, N.M. Froberg, and D.H. Auston, *Appl. Phys. Lett.* **64**, 137 (1994).
- [2] Y.R. Shen, *The Principles of Nonlinear Optics* (Wiley, New York, 1984), Chap.8.
- [3] E.R. Brown, K.A. McIntosh, K.B. Nichols, M.J. Manfra, and C.L. Dennis, *Proc. SPIE* **2145**, 200 (1994).
- [4] K.A. McIntosh, E.R. Brown, K.B. Nichols, M.J. Manfra, and C.L. Dennis, 52nd Device Research Conference, Paper IIIB-1, (1994)

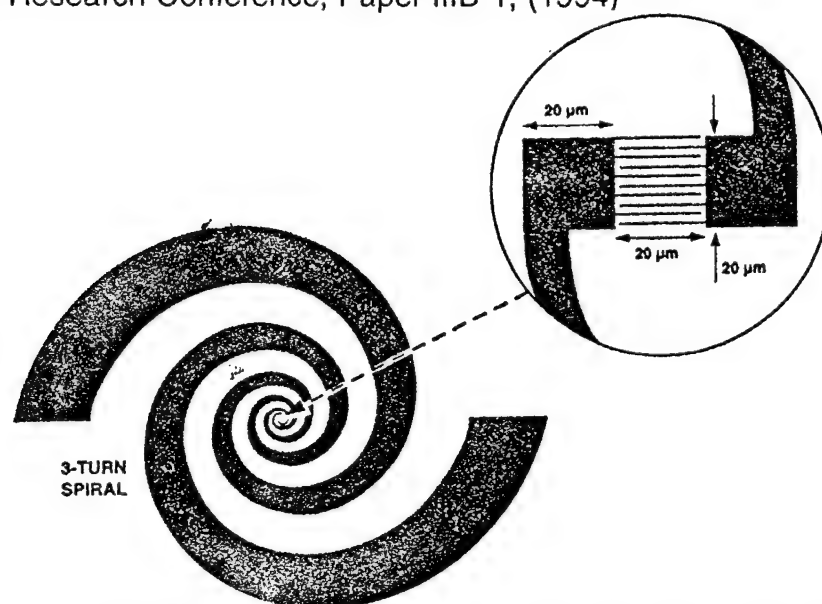


Figure 1 Illustration of Mixer 1 showing interdigitated electrodes with interconnect to three-turn self-complementary spiral antenna.

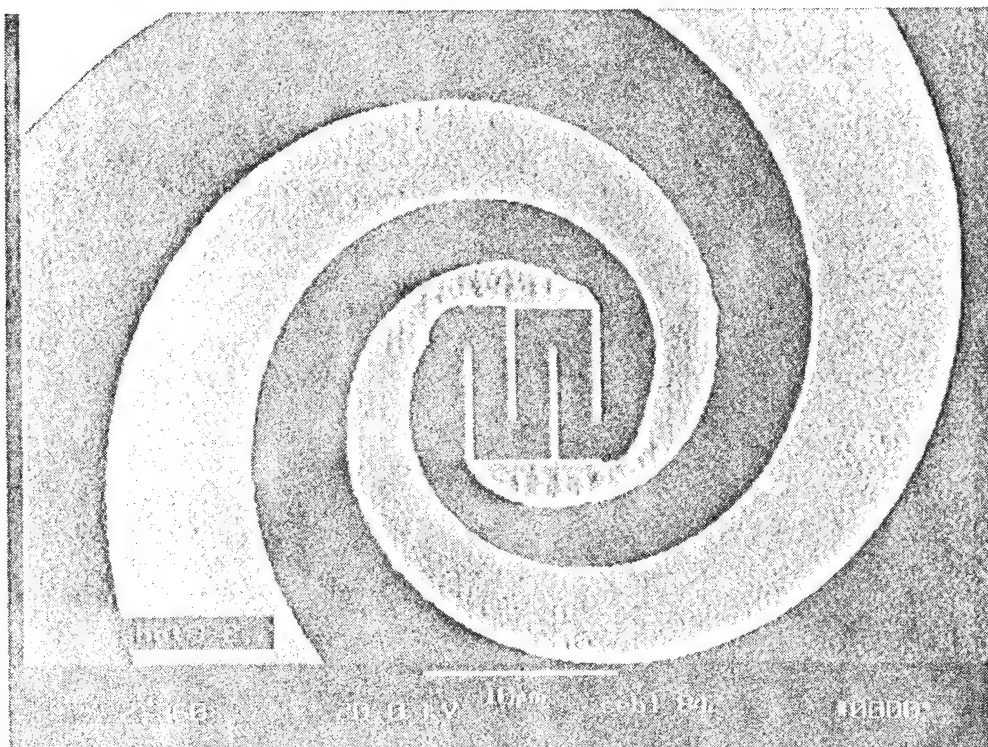


Figure 2 Scanning electron micrograph of central region of Mixer 2.

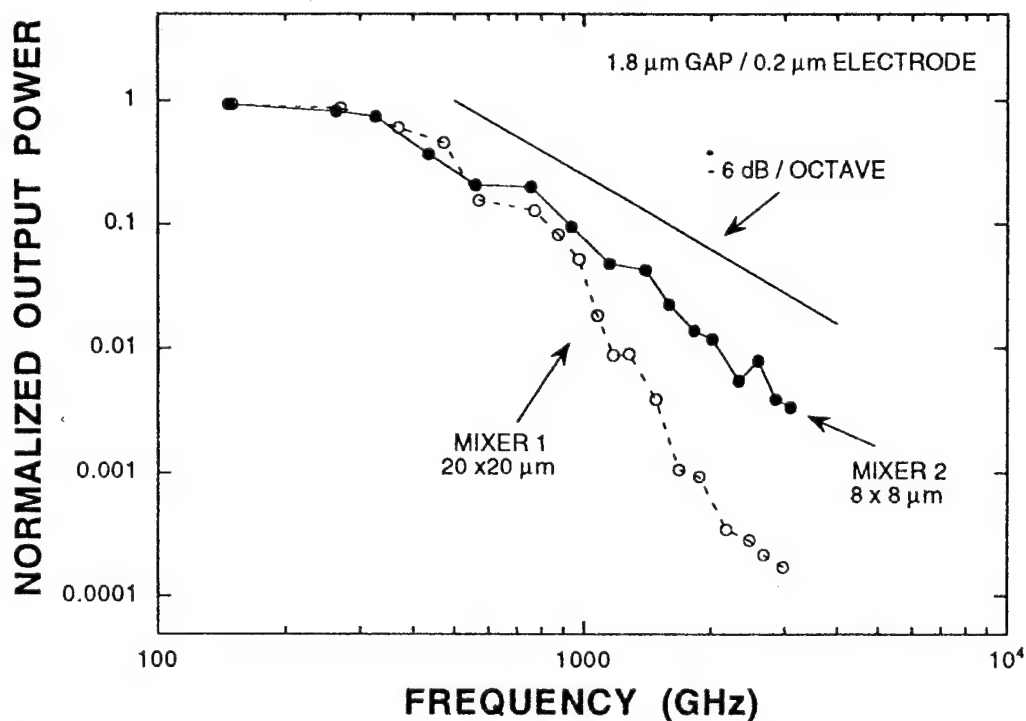


Figure 3 Measured output power from Mixer 1 and Mixer 2 showing the lifetime-limited rolloff in Mixer 2 and the combined lifetime and RC-limited rolloff in Mixer 1.

Tuesday, March 14, 1995

High-Speed Communication Systems

UTuB 10:30 am-12:00 m
Ballrooms VI-VIII

John E. Bowers, *Presider*
University of California-Santa Barbara

Fast SiGe-Heterobipolar Transistors for Communication Systems

A. Schüppen

Daimler Benz AG, Research Center Ulm, D-89013 Ulm, Germany
Tel.: +49-731-5052052, Fax: +49-731-5054102

Introduction

Today's and future wireless communication systems, e.g. mobile phones and wireless LANs, require transistors with improved high frequency and low noise performance. At the moment the frequencies for these applications are in the 0.9 – 2.4 GHz range, but due to the steadily growing data flow and the required faster transfer speeds the frequency range of communication systems will be extended to 10 or 20 GHz in the near future. Homo silicon device circuits seem to be restricted to below 2 GHz. Hence, SiGe-HBTs could fill the gap between 2 GHz mass market and above 12 GHz niche applications. SiGe-HBTs offer the potential of increased performance in both low power low noise front-ends, and in high frequency power amplifiers up to 20 GHz. The increasing interest in SiGe-HBTs is a result of their excellent RF performance with recently reported record f_T and f_{max} values up to 120 GHz [1,2,3], noise figures of 0.9 dB at 10 GHz [4], and a low noise corner frequency of 300 Hz [5]. In addition, SiGe-HBT fabrication is compatible to standard silicon bipolar and CMOS technology.

ECL ring oscillators with SiGe-HBTs have reached 19ps switching time [6]. A hybrid K-band DRO [7] exhibited a RF power of 8.5 dBm at 23 GHz with a phase noise of -92 dBc(1Hz) at 100 kHz off carrier. An X-band VCO tunable from 8.2 – 12 GHz with 10 dBm RF output power and a phase noise of 80 dBc (100kHz/1Hz) has been reported [8]. Mixed analog and digital applications of SiGe-HBTs were demonstrated by a 1 GHz 12 bit digital to analog converter [9] and a 16 Gbit/s multiplexer [10]. With respect to power amplification multi emitter finger SiGe-HBTs reached 20 dB power gain at 10 GHz with $10 \times 10 \times 1 \mu\text{m}^2$ emitter fingers and a predicted RF output power of 2 W/mm [1].

DC Performance

Double mesa type [11] and passivated SiGe-HBTs [12] were investigated. The double mesa type transistor has the advantage of an easy and fast fabrication technology, but they are not passivated. The essential technological step is a groove etch which separates the active transistor from the contact pads. The Gummel plot in Fig.1a for a unpassivated transistor with large emitter area ($1.6 \times 10^{-3} \text{ cm}^2$) shows an approximately ideal behaviour and a current gain of up to 770, indicating low defect densities in the MBE layers.

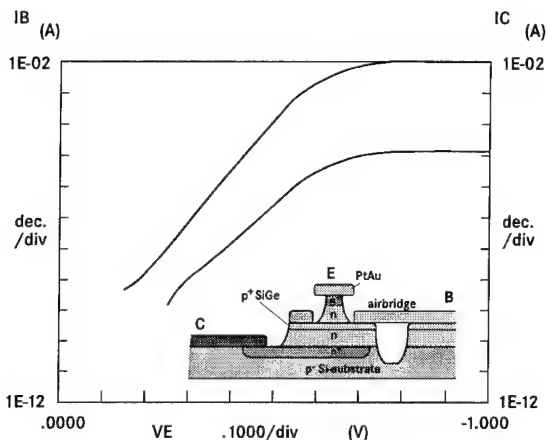


Fig.1a: Gummel plot of a double mesa SiGe-HBT: $A_E = 1.6 \times 10^{-3} \text{ cm}^2$, $\beta_{max} = 770$

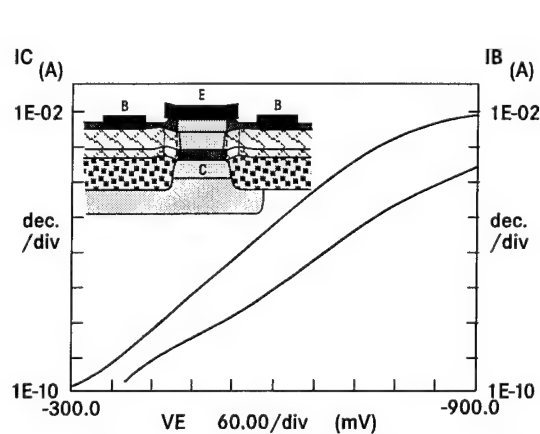


Fig.1b: Gummel plot of a differential SiGe-HBT: $A_E = 1.5 \times 10^{-3} \text{ cm}^2$, $\beta_{max} = 100$

The so called differential SiGe-HBT (Fig.1b) is a completely passivated transistor with reduced parasitic collector base area. The device layers were grown by MBE on SiO_2 patterned Si wafers. The monocrystalline epi-layers inside the SiO_2 windows are used for the active transistor region, whereas the boron doped polycrystalline Si and SiGe on top of the surrounding oxide serves as the base interconnect. More technological details can be found in [11,12].

RF Performance

a) High unity-current-gain frequency f_T

The transit frequency can be written as a sum of base, collector and emitter transit times and the corresponding charging times [11]. However, for short collectors and high current densities the base transit time becomes the essential part of the total transit time. Hence, a short base with box shaped germanium and boron profile increases f_T as can be seen in Fig.2, where for two different doping concentration the unity-current-gain frequencies were calculated. The 1D-calculations take into consideration i) the geometric transistor layout, ii) the semiconductor, the contact, the spreading, and the lead resistances, and iii) the intrinsic and parasitic space charge capacitances. The logarithmic plot indicates a limit in transit frequency at about 120 GHz, because base thicknesses below 5 nm are not reasonable due to the

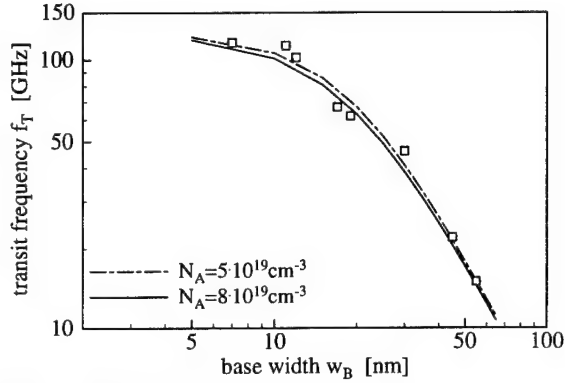


Fig.2: Measured and calculated f_T vs w_B , calculation: $C: 150\text{nm}/2 \times 10^{17}\text{cm}^{-3}$; $B: 30\% \text{ Ge}$; $E: 70\text{nm}/1 \times 10^{18}\text{cm}^{-3}$ $A_E = 2 \times 0.8 \times 8 \mu\text{m}^2$, $V_{CE} = 3\text{V}$, $\mu_n \approx 200\text{cm}^2/\text{Vs}$

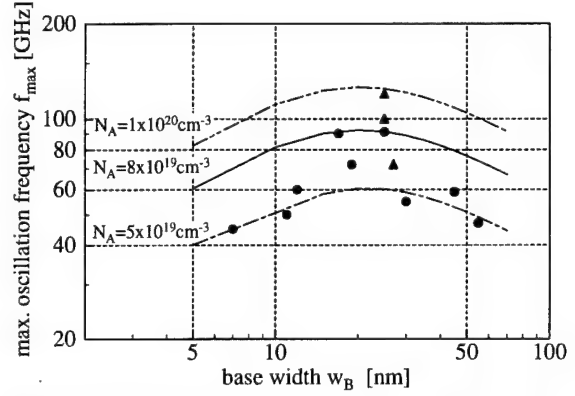


Fig.3: Measured and calculated f_{max} vs w_B , calculation parameter as Fig.2; (● double emitter finger HBTs, ▲ multi emitter finger SiGe HBTs)

inset of tunneling currents and the punch through effect. A further slight increase in f_T may be only possible by a lower base doping concentration and an additionally smaller emitter width or by using a drift field by a graded germanium and boron profile as suggest by the IBM group [2].

b) High maximum oscillation frequency f_{max}

For all electronic applications the maximum frequency of oscillation f_{max} is an important figure merit, which can be written as

$$f_{max} = \sqrt{\frac{f_T}{8\pi R_B C_{BC}}} \quad (1)$$

High f_{max} values demand high transit frequencies, low base resistances and low collector-base capacitances. However, f_T decreases quadratically with increasing base width w_B , whereas the base sheet resistance decreases linearly with rising base width. These dependencies on w_B yield a maximum in the f_{max} versus w_B plot, as depicted in Fig.3. In contrast to f_T , which is approximately independent of the base doping, there exists a strong correlation between the base doping concentration N_A (which is the parameter in Fig.3), and the f_{max} values. This is a result of the decreasing base sheet resistance with increasing base doping inspite of the nearly constant f_T values. For the parameter, chosen here, the f_{max} maximum can be found for doped SiGe base widths between 15 – 25 nm. The experimental data points spread regarding technological reasons. A further improvement of f_{max} can be achieved by reducing the collector base capacitance, i.e. by thicker and lower doped collector regions [1]. From small signal equivalent circuit parameters, which were obtained by S-parameter measurements, the normalized collector base capacitances c_{BC} for various collector designs were determined (Fig.4). As expected the f_{max} values increase for smaller c_{BC} values. The solid lines are calculations using the f_{max} -formula as mentioned above. The curve parameters of $f_T/R_B = 4(8) \text{ GHz}/\Omega$ take into account that both the transit frequencies and the base resistances depend on the base width. As expected, for a more thick low doped collector higher f_{max} values were obtained and the measured data fit between the two calculated curves.

Noise Performance

a) Low Frequency Noise

Another important figure of merit is the noise figure, which originates at lower frequencies from surface effects that give rise to a $1/f$ noise spectrum. For medium frequencies the noise figure becomes approximately constant and will be determined by the series resistances R_E , R_B and the current gain

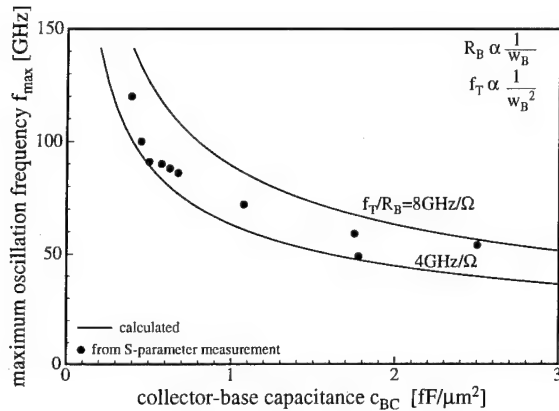


Fig.4: max. oscillation frequency vs collector-base capacitance normalized on the total collector-base area, parameter is the f_T/R_B ratio

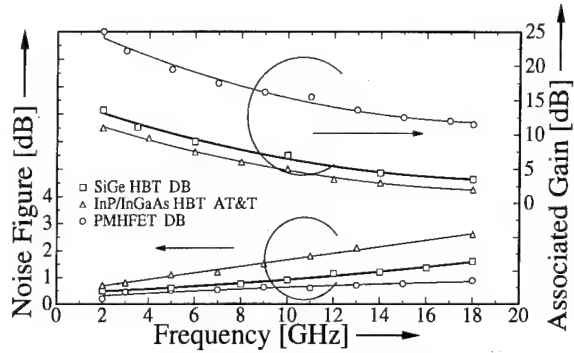


Fig.5: RF noise figures and associated gains vs frequency of a III-V HEMT, a III-V HBT and a SiGe-HBT

β . A measure between the two parts of the noise spectrum is the low noise corner frequency. Recently Harame et al. published a corner frequency of 300 Hz for SiGe-HBTs [5], which is an excellent value for high frequency bipolar transistors. Standard Si-BJT (BFR96) with a transit frequency of 12 GHz exhibits typically 1000 Hz, whereas Si-BJTs (AT42085) with $f_T = 40$ reaches only 10 kHz low noise corner frequency.

b) High Frequency Noise

At high frequencies the noise figure increases approximately with f^2 . The intrinsic noise source is mainly shot noise at the emitter and the collector barriers. For medium frequencies 0.1 - 2 GHz a high current gain is required to achieve low noise figures, whereas for higher frequencies a low base resistance and a short base transit time influences positively the noise behaviour. It is well known that HEMTs have the best high frequency noise performance as can be seen in Fig.5. However at frequencies up to 10 GHz SiGe-HBTs are only slightly worse than III-V HEMTs. It should be mentioned that the best SiGe-HBTs show noise figures of 0.5 dB at 2 GHz and 0.9 dB at 10 GHz, and an associated gain of 14 dB and 6 dB, respectively. III-V HBTs exhibit worse values. This might be explained by the additional spike-like barrier due to the conduction band offset, which is negligible in the Si-SiGe transition.

Conclusion

SiGe-HBTs are indeed promising devices for today's and future communication systems due to their outstanding RF and noise performances, i.e. cutoff frequencies above 100 GHz, a power gain of 20 dB at 10 GHz, a noise figure of 0.5 dB at 2 GHz, and a low-noise corner frequency of 300 Hz. Though most of the results stem from discrete devices SiGe is already going to be produced. In long term the SiGe hetero fieldeffect transistor (HFET) will become another candidate creating a new advanced generation in mainstream CMOS, s.c. SiGe Hetero CMOS (HCMOS). On the other hand, if optical applications, as Si/SiGe multi quantum well detectors and wave guides, will play an important role in future silicon technology is still an open question. However, "SiGe is just on an upswing" is a true statement.

References

- [1] A. Schüppen, A. Gruhle, U. Erben, H. Kibbel, U. König, *Tech. Dig. IEDM'94*, p. 377 (1994).
- [2] E.F. Crabbé, B.S. Meyerson, J.M.C. Stork, D. Harame, *Tech. Dig. IEDM 93*, p.83 (1993).
- [3] A. Schüppen, A. Gruhle, H. Kibbel, U. Erben, U. König, *Electron. Lett.*, **30**(14) p.1187 (1994).
- [4] H. Schumacher, U. Erben, A. Gruhle, *IEEE MTT-S Digest MTT-Symp. San Diego*, p.1167 (1994).
- [5] D.L. Harame, K. Schonenberg, M. Gilbert, D. Nguyen-Ngoc et al., *Tech. Dig. IEDM'94*, p.437 (1994).
- [6] F. Sato, T. Hashimoto, T. Tatsumi, H. Kitahata, T. Tashiro, *Tech. Dig. IEDM 92*, p. 397 (1992).
- [7] U. Gülich, A. Gruhle, J.F. Luy, *MIOP'93 Conf. Proc.*, p.146 (1993).
- [8] A. Gruhle, H. Kibbel, R. Speck, *Proc. EuMC Conf., Cannes 1994*, p. 648 (1994).
- [9] D.L. Harame, J.M.C. Stork, B.S. Meyerson, K.Y.-J. Hsu, J. Cotte, K.A. Jenkins, J.D. Cressler, P. Restle, E.F. Crabbé, *Tech. Dig. IEDM 93*, p. 71 (1993).
- [10] H.-U. Schreiber, J.N. Albers, B.G. Bosch, *Proc. Int. Semicon. Dev. Res. Symp. (ISDRS)*, p. 457 (1993).
- [11] A. Gruhle "SiGe-HBTs" in "Silicon-based Millimetre-wave devices" ed. by J.-F. Luy and P. Russer, Springer Verlag, Berlin, p.149 (1994).
- [12] A. Schüppen, U. König, A. Gruhle, H. Kibbel, U. Erben, *Proc. ESSDERC'94*, ed. C. Hill and P. Ashburn, p. 469 (1994).

20 Gbit/s Optical Transmission Systems with Monolithic IC Technologies

Tetsuyuki Suzaki

Opto-Electronics Research Laboratories, NEC Corporation
1-1, Miyazaki 4-Chome, Miyamae-ku, Kawasaki, Kanagawa 216, Japan

Tel. +81-44-856-2109 Fax +81-44-856-2222

email: suzaki@optsys.cl.nec.co.jp

1. INTRODUCTION

Rapid progress in multimedia communication requires large capacity optical transmission lines over 10 Gbit/s. One of the candidates considered for forthcoming high speed transmission systems is 20 Gb/s optical IM-DD transmission system. There have been several reports about IM-DD optical transmission experiments at 20 Gbit/s (1, 2, 3, 4). Monolithic integrated circuits are indispensable to turn such high speed optical transmission systems into practical application. The performance of various monolithic ICs for optical communications is summarized in Fig. 1. Si ICs are very attractive for realizing the high speed IM-DD systems up to 20 Gbit/s, because of their high uniformity and yield (5, 6, 7). The Si bipolar transistors, however, are not suited to fabricate circuits with high output voltage swing such as modulator driver, because of their breakdown voltage limitation. The compound devices, such as GaAs-HBTs, GaAs-MESFET and heterojunction FETs, have high cut-off frequency over 100 GHz (8, 9), so they are very effective to achieve the high speed ICs operating over 20 Gbit/s. They also have the advantage of utilizing microwave circuit technologies, which make it possible to design high frequency narrowband circuit, such as a clock amplifier at over 20 GHz.

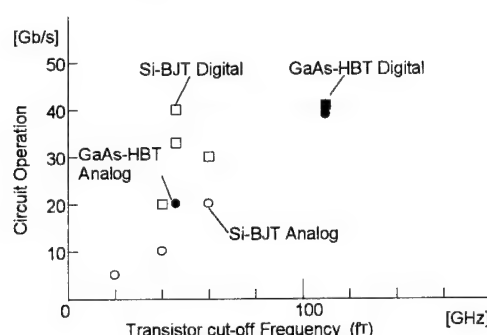


Fig. 1 Various IC Performance versus transistor cut-off frequencies (5, 6, 7, 8).

This paper describes the design and performance of several monolithic ICs for 20-Gbit/s optical transmission systems; Si-ICs with SiGe-base, and

AlGaAs/GaAs-HBT ICs with hetero guard-ring structure. A fully-regenerating 20-Gbit/s optical repeater with the ICs has been developed to confirm the feasibility of future high speed optical communication at 20 Gbit/s.

2. SiGe-BASE BIPOLAR TRANSISTOR ICs

Among the Si bipolar transistor, a Super Self-aligned Selectively grown SiGe Base (SSSB) bipolar transistor (7) is very attractive to realize high speed ICs. A graded SiGe base reduces the base transit time due to the presence of a drift field. Therefore, the SiGe-base bipolar transistor provides faster maximum cut-off frequency (f_T) than conventional Si bipolar transistors. To improve the high speed characteristics, a bonded Silicon On Insulator (SOI) technology is employed. The SSSB transistor achieves high f_T of 60 GHz. Using this transistor, several kinds of IC have been developed for 20 Gbit/s optical communication systems. Table 1 summarizes the operating speed or bandwidth of the ICs (6, 7, 12).

Table 1 Performance of developed SiGe-base transistor ICs (5,6)

Circuit	Operating Speed
Preamplifier	19.0 GHz
Gain Controllable Amp.	16.0 GHz
D-F/F	20 Gbit/s
Selector	30 Gbit/s
Decision	20 Gbit/s
Multiplier	20 GHz

3. AlGaAs/GaAs HBT ICs

(1) AlGaAs/GaAs HBT Process

The AlGaAs/GaAs HBT is one of the most powerful candidates for realizing high speed circuits operating at over 20-Gbit/s. HBT epitaxial wafers were prepared

by MOCVD, including C-doped uniform base layers. The HBTs and diodes were fabricated using the developed HBT self-aligned process, and adopting Pt-Ti-Pt-Au base metal structure. A hetero guard-ring structure is introduced to reduce the transistor variation. Load resistors were formed WSiN thin films. The transistors achieved good high frequency characteristics, as f_T of 45-GHz and f_{MAX} of 105-GHz.

(2) Preamplifier design

To realize a wide bandwidth amplifier over 10 GHz, it is very effective to apply microwave tuning techniques, such as open/short stubs, or line impedance optimization. Among these techniques, the peaking technique with an on-chip spiral inductance has been studied and applied for high speed MMICs. An example of an on-chip spiral inductor on GaAs substrate is shown in Fig. 2 (a). The width and space of the lines of the spiral inductor are 3 μm and 10 μm , respectively. Figure 2 (b) shows the simulation and measurement results of the inductors. The measured frequency response for these spiral inductors is represented with open circle and closed circle, which shows a good agreement with the simulated results up to 20 GHz.

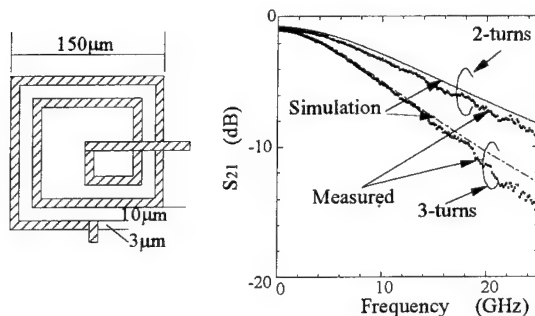


Fig. 2 On-Chip Spiral Inductor.
(a) Schematics (b) Frequency Response

Figure 3 shows a circuit diagram of the preamplifier IC using AlGaAs/GaAs HBTs (11). A transimpedance type circuit configuration is applied in order to realize a wide bandwidth. The spiral inductor is used for the inductive load in the first gain stage, and is remarkably effective to get large transimpedance bandwidth. To realize large dynamic range operation, an input offset control circuit is adopted, which allows a large input current up to 7.5 mA.

Figure 4 shows the transimpedance characteristics of the preamplifier IC. Without spiral inductor, 16.5 GHz bandwidth is obtained as shown by dashed line, while by introducing the spiral inductor, the band-

width was improved to 20.9 GHz with 40-dB Ω transimpedance gain.

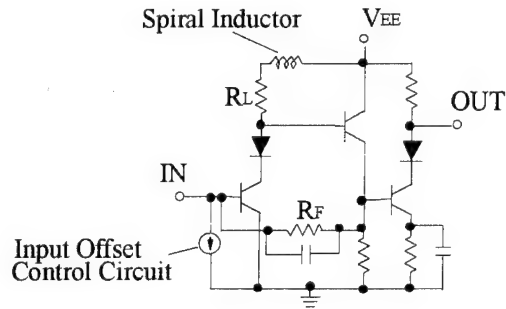


Fig. 3 AlGaAs/GaAs HBT preamplifier IC circuit diagram

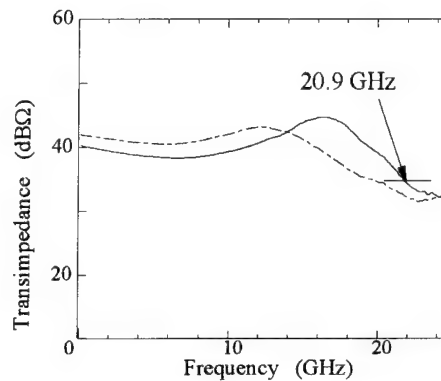


Fig. 4 AlGaAs/GaAs HBT preamplifier IC frequency response
solid line: with spiral inductor
dashed line: without spiral inductor

4. A FULLY-REGENERATING 20 Gbit/s OPTICAL REPEATER WITH MONOLITHIC ICs

(1) Repeater Configuration

A fully-regenerating 20 Gbit/s optical repeater based on the monolithic ICs has been developed (12). Figure 5 shows its schematic diagram. The repeater has 3R functions: reshaping, retiming, and regenerating at 20 Gbit/s. All circuits, except clock extraction and modulator driver, are realized with Si ICs.

(2) Optical Transmitter

In the optical transmitter, the 20 Gbit/s signals are generated from two 10 Gbit/s signals by bit multiplexing with a Si selector IC and a D-type Flip-flop (D-F/F) IC. Following the D-F/F IC, a modulator driver circuit with GaAs FETs amplifies signal voltage swing up to 7V_{p-p}, which is applied to a LiNbO₃ Mach-Zehnder optical

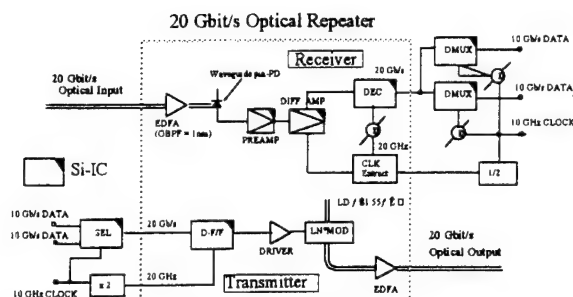


Fig. 5 A fully-regenerating 20 Gbit/s optical repeater.

modulator. The output light waveform from the transmitter is shown in Fig. 6 (a). Using 1.55- μ m wavelength light, a 12 dB extinction ratio is achieved with rise and fall times of 18 psec and 20 psec, respectively.

(3) Optical Receiver

A wide bandwidth front end module has been developed with a waveguide pin photodiode (pin-PD) and a Si pre-amplifier IC. The preamplifier IC with 300 Ω feedback resistance, achieves a 19.0 GHz bandwidth. The waveguide pin-PD exhibits an input capacitance as small as 45 fF and wide bandwidth over 40 GHz. The optical frequency response has a 16 GHz bandwidth and a 43 dB Ω transimpedance gain as shown in Fig. 6 (b).

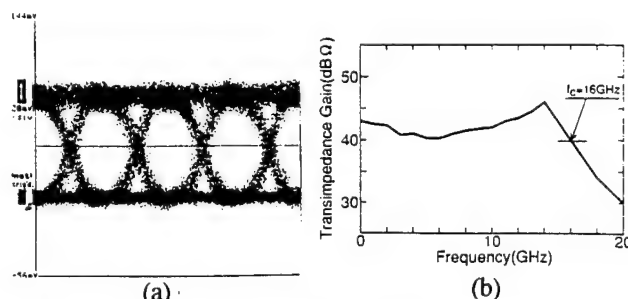


Fig. 6 20 Gbit/s optical repeater characteristics
(a) Optical output eye diagram
(b) Front end optical frequency response

Following the front end, a Si differential amplifier IC, with 16 GHz bandwidth and 10 dB gain, amplifies the signal and divides it to both a decision circuit and a 20 GHz clock extraction circuit. The decision circuit uses a Si D-F/F IC, which has a 250 mV_{p-p} input sensitivity and 180 degree clock phase margin at 20 Gbit/s. The clock extraction circuit is composed of GaAs FETs and a dielectric filter.

(4) System Performance

The optical receiver sensitivity measurement has been successfully carried out at a 20 Gbit/s data rate with the

repeater described above. After regenerating the data with the decision circuit, two Si D-F/F ICs demultiplexed the 20 Gbit/s data to two 10 Gbit/s data streams. Figure 7 shows the measured bit error rates for these two 10 Gbit/s channels with 2⁷-1 pseudorandom pattern. Receiver sensitivities for 10⁻⁹ of bit error rate were -23.0 dBm and -23.5 dBm for each channel.

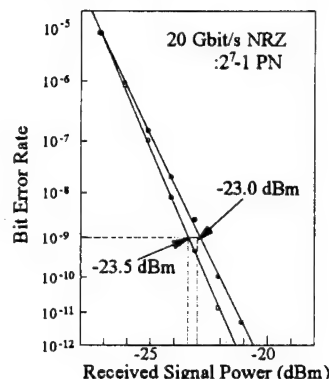


Fig. 7 Bit error rate characteristics at 20 Gbit/s

5. CONCLUSIONS

High-speed monolithic ICs have been developed for 20 Gbit/s optical communication systems. The SiGe-base bipolar transistors realize analog and digital ICs operating at 20 Gbit/s. The AlGaAs/GaAs HBT preamplifier IC shows the feasibility for high speed operation over 20 Gbit/s. A fully-regenerating optical repeater was successfully demonstrated with Si ICs and a waveguide pin-PD. These results pave the path towards next generation of optical communication systems handling 20 Gbit/s data stream.

REFERENCES

- [1] K. Hagimoto et al., in Proc. OFC'92, TuI3, San Jose.
- [2] K. Fukuchi et al., in Proc. ECOC'93, TuC4. 2, Montreux.
- [3] W. S. Lee et al., Electron. Lett. Vol. 30, No. 7, p. 584, 1994
- [4] T. Kataoka et al., Electron. Lett., Vol. 30, No. 9, p. 715, 1994.
- [5] A. Felder et al., in Proc. ISSCC'93, TP10.3, 1993.
- [6] M. Soda et al., in Proc. ISSCC'94, TP10.2, 1994.
- [7] T. Hashimoto et al., in Proc. BCTM'94, 10.3, 1994.
- [8] J. Akagi et al., in ISSCC'94 Tech. Digest, TP10.1, 1994.
- [9] T. Seshita, et al., in ISSCC'94 Tech. Digest, TP 10.3, 1994
- [10] F. Sato, et al., in IEDM Tech. Digest, pp. 397-400, 1992.
- [11] H. Tezuka, et al., in Proc. APMC'94, 37-4, 1994
- [12] H. Tezuka, et al., in Proc. ECOC'94 Post deadline, pp. 109-112, 1994

Diode Multiplexer/Demultiplexer IC's for 100 GB/s Fiber-Optic Transmission

R. Pullela, U. Bhattacharya, S. T. Allen *, M.J.W. Rodwell
Department of Electrical and Computer Engineering
University of California, Santa Barbara, CA 93106
805-893-8044, 805-893-3262 FAX

Introduction

Fiber-optic data transmission systems are evolving rapidly. 10 GB/s time-division-multiplexed (TDM) systems are approaching deployment, and there is extensive research on 40 GB/s transmission. Because of perceived limits to electronic component bandwidths, present research on 100 GB/s systems has focused on wavelength-division-multiplexing or TDM using optical switching.

Although a substantial challenge, 100 GB/s TDM fiber optic transmission is feasible using electronic amplification and multiplexing. Fig. 2 shows a receiver block diagram. For 100 GB/s, component bandwidths greater than ~ 60 –70 GHz are required. Most required components have been demonstrated, including 110 GHz-bandwidth, $1.3 \mu\text{m}$ photodetectors [1] and 70 GHz electrooptic modulators. We will report elsewhere [2] HEMT traveling-wave amplifiers with 98 GHz bandwidth. Optical fiber dispersion can be counteracted by dispersion compensation. Erbium-doped-fiber (EDFA) optical preamplifiers will provide adequate receiver sensitivity.

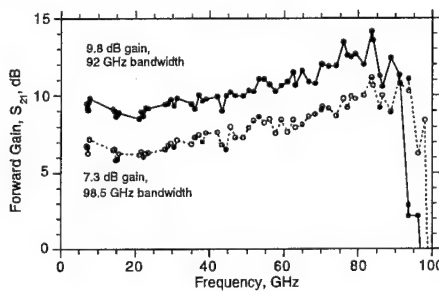


Figure 1: Capacitive division TWA.

100 GB/s multiplexer and demultiplexers are critical missing elements. 27 GB/s transistor mul-

*S.T. Allen is now with Cree Research Inc., 2810 Meridian Parkway, Suite 176, Durham, NC 27713

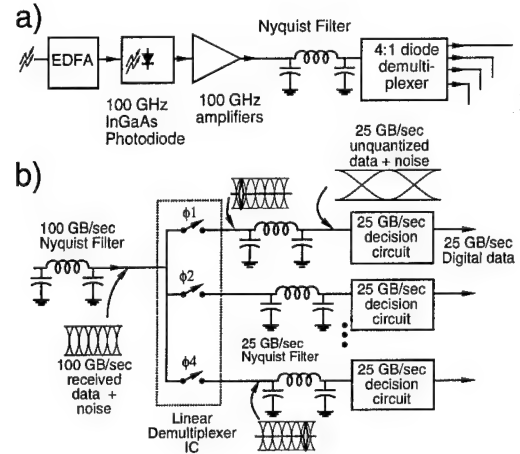


Figure 2: Block diagram of a 100 GB/s fiber-optic receiver (a), and of the diode demultiplexer (b).

tiplexers [3] should soon evolve to 40 GB/s rates, but multiplexing at 100 GB/s with present transistor technology appears to be difficult. Terahertz Schottky diode technology provides a solution. We have fabricated diode-based multiplexers and demultiplexers for 100 GB/s transmission. Here we report initial results.

System description

Block diagrams of the receiver and the diode demultiplexer are shown in fig. 2. The photodetector output is amplified by HEMT traveling wave amplifiers. The signal is passed through a 100 GB/s Nyquist filter (a ~ 50 GHz low-pass filter), to bandlimit noise. The signal is passed through a linear demultiplexer IC consisting of four synchronized sampling gates clocked by a 25 GHz, 4-phase clock ($\phi_1 - \phi_4$). The diode bridges generate four parallel analog sampled data streams. Each data stream is passed through a 25 GB/s Nyquist filter and ampli-

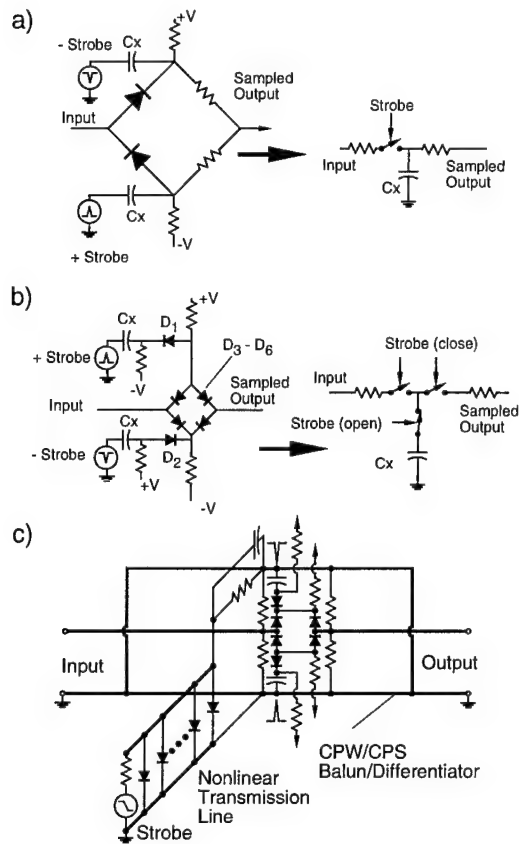


Figure 3: (a) 2-diode sampling bridge and simplified model showing the output RC charging network. (b) 6-diode switch and its simplified model. (c) one channel of four of the diode mux/demux IC

fier to a 25 GB/s transistor decision circuit, where the analog samples are restored to binary levels. A similar system is used for multiplexing.

Circuit design

The mux/demux requires an array of diode "sample-hold" (sample-and-Nyquist-filter) gates. A nonzero sampling aperture time τ is equivalent to a filter with transfer function $H(f) = (\pi f \tau)^{-1} \sin(\pi f \tau)$; this response is incorporated into the design of the 100 GB/s Nyquist filter. A 5 ps aperture time τ is thus readily tolerated. Diode sampling bridges gated by (diode) nonlinear transmission line (NLTL) pulse generators attain subpicosecond aperture times [4], [5], and have bandwidths far in excess of that required here. Such circuits must be modified before use in multiplexers.

Two-diode (and 4-diode) sampling bridges (fig.

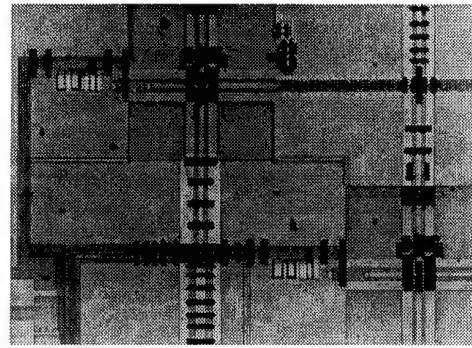


Figure 4: Photomicrograph of a section of the 4-channel demultiplexer IC

3a) used in microwave instruments contain a capacitor C_x which both couples the strobe pulse to the bridge and serves as the hold capacitor. The output circuit is loaded by a high resistance. While the bridge has a high *input* bandwidth, as needed for repetitive sampling in (e.g.) oscilloscopes, the capacitor's RC discharge time limits the sampled *output* bandwidth to at most a few MHz. >60 -70 GHz output bandwidth is required here.

Wide diode bridge output bandwidths are obtained through use of transistor or transformer strobe coupling networks, but such techniques are not scalable to 100 GB/s. In a six-diode NLTL-gated bridge (fig. 3b,c) the strobe pulse coupling capacitors C_x are switched out of the signal path during the sampling event. Combined with an 50Ω output circuit, the output bandwidth is increased $\sim 10^5 : 1$ over a 2-diode NLTL-gated bridge. Input and output bandwidths can be several hundred GHz. In the present design the 1.3 ps NLTL wavefront is converted into a 4 ps FWHM strobe impulse. Circuit simulations predict a 3–4 ps aperture time and a 110–150 GHz output bandwidth.

To avoid crosstalk between demultiplexed channels, the switch off-state transmission must be small. The diodes must therefore have high cut-off frequencies, small junction areas, and small pad parasitics. The bridge uses air-bridge-contacted Schottky diodes [5] of $2.25\mu\text{m}^2$ area and 2.5 THz cutoff frequency. On-wafer interference between the four 6V NLTL strobe (clock) signals and the ~ 100 mV data is a major difficulty. Clock interference is relevant only in the multiplexer; the spurious signals at 25, 50 and 75 GHz are beyond the bandwidth of the demultiplexer's Nyquist filters. In addition to fabrication of the full 4-channel mux/demux ICs, single-channel ICs (fig. 3c) were also fabricated. With each single-channel IC having only one NLTL clock line, and having a much more

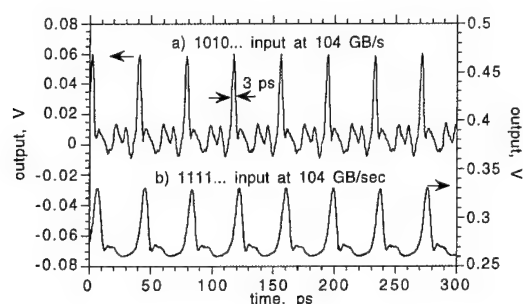


Figure 5: (a) 26 GB/s 1111... output of a single-channel IC for a 104 GB/s 1010... input, measured by an on-wafer sampling circuit, with clock interference nulled. (b) 26 GB/s 1111... output of a single-channel IC for a 104 GB/s 1111... input, measured by an active probe. Clock interference is *not* nulled.

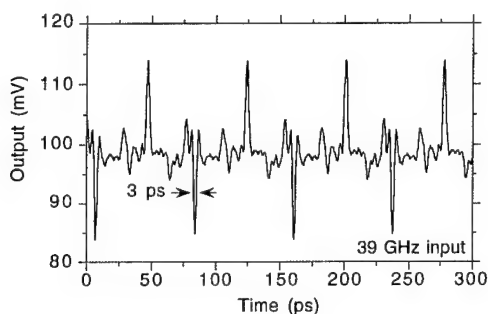


Figure 6: 1010... output pattern of the single-channel IC for a 39 GHz input.

compact layout than the 4-channel IC, interference is much less likely. To assemble a full multiplexer, four single-channel ICs must be connected in a hybrid assembly.

Results

Full testing of the demultiplexer requires generation of 100 GB/s pseudo-random bit streams (PRBS) generated by the 100 GB/s diode multiplexer. This has not yet been performed. For initial demultiplexer evaluation, sinusoidal input test signals are used. A 50 GHz sinusoid corresponds to a 1010... pattern at a 100 GB/s data rate, while 1111... and 0000... streams are emulated by positive and negative DC inputs. Available signal generators forced testing at 104 GB/s. Demultiplexer outputs are measured here with 2 tools. Some IC's were fabricated with integrated on-wafer sampling

circuits. While these provide wideband measurements, the close proximity of the sampling circuit to the multiplexer results in spurious coupling between the sampling circuit and the demultiplexer's strobe NLTL which must frequently be corrected numerically. To obtain measurement uncorrupted by clock coupling in the instrumentation, the demultiplexers are also tested by NLTL-based active probes [4]. Any remaining clock coupling observed is due to the (de)multiplexer itself. The active probes limit waveform measurements to ~ 3.5 ps resolution.

Fig. 5 shows demultiplexed 26 GB/s 1111... output patterns of a single-channel IC for 104 GB/s 1010... and 1111... input patterns. The latter measurement, taken by an active probe, indicated ~ -20 dB clock interference. The aperture time is 3 ps (fig. 5a), and the output bandwidth is 150 GHz. Fig. 6 shows the demultiplexer output at 39 GHz input, generating an alternating 1010... output. With the full 4-channel unit, clock coupling is observed, and pending mask redesign, the multiplexer must be constructed from the single-channel IC's.

Conclusions

Electronic components will permit 100 GB/s fiber data transmission, with diode integrated circuits used for multiplexing and demultiplexing. We have demonstrated first results with such diode ICs; the required bandwidths are readily attained. The 6-diode gates can also have impact on high-speed instrumentation applications requiring high output bandwidths, including harmonic mixers for spectrum analysis, bit-error-rate test sets, and multiplexed A-D converters.

This work was supported by the ARPA Thunder and Lightning program.

References

- [1] Y.-G. Wey, et. al., IEEE Photonics Tech. Lett., vol. 5, no. 11, Nov. 1993.
- [2] J. Pusi, et. al., submitted to 1995 IEEE Microwave and Millimeter-Wave Monolithic Circuits Symposium.
- [3] K. Runge, et. al., 1991 IEEE GaAs IC symposium, Monterey, CA, October 20-23.
- [4] M. Rodwell, et. al. IEEE Proceedings, Vol. 82, No. 7, July 1994, pp. 1037-1058.
- [5] S.T. Allen, et. al. 52nd annual IEEE Device Research Conference, Boulder, CO. June 1994.

Tuesday, March 14, 1995

High-Frequency Electronics: Devices and Applications

UTuC 1:30 pm-3:15 pm
Ballrooms VI-VIII

Loi Nguyen, *Presider*
Hughes Research Laboratories

Device and System Technologies for Microwave Wireless Applications

Y. K. Chen, R. Hamm, D. Humphrey, R. Kopf, J. Kuo, J. Lin, J. Lothian, R. Malik,
F. Ren, R. Ryan, A. Tate, J. Weiner, D. Sivco, M. Haner, and A. Cho
AT&T Bell Laboratories, Murray Hill, NJ 07974
Phone: (908)-582-7956, Fax: (908)-582-2451

The microwave components and subsystems have made significant progress in the past few years due to the advancement in the III-V compound semiconductor technologies. Commercial applications using microwave and millimeter-wave integrated circuits are rapidly expanding in the areas of direct broadcasting satellite (DBS), local multiple-point distribution systems (LMDS), and high speed wireless local area network (WLAN).

Because the bandwidth of the allocated frequency spectrum in the air is a precious commodity, sophisticated data compression and signal processing techniques are needed to transmit the broadband information reliably and efficiently. The improvement in the integration level and production yield of the III-V ICs also breeds a new generation of high-speed baseband signal processing ICs which make high data rate multimedia digital transmission more bandwidth-efficient. We have developed compound semiconductor HBTs and HEMTs at AT&T with cutoff frequencies exceeding 100 GHz.

In this talk, we will describe a prototype high speed digital microwave data link for optical fiber node. The impacts of these high speed devices on this microwave communication link will be addressed, and novel circuits using these devices will also be illustrated as well.

Opportunities of Si ULSI Technology for GHz Applications

Jack Y.C. Sun

Semiconductor Research and Development Center
IBM Microelectronics Division and Research Division
IBM Corp. Bldg. 630, M/S E40

1580 Rt. 52, Hopewell Junction, NY 12533-6531

Phone: (914) 892-2090, Fax: (914) 892-2155, e-mail: jyccsun@watson.ibm.com

The fast growing mixed-signal microcontroller and low power wireless communication markets provide tremendous opportunities for Si ULSI. Si CMOS ULSI offers low stand-by power and high integration level, which translates into improved performance, functionality, cost, reliability, and battery life. This paper will provide an overview of the potential to expand the core digital CMOS ULSI logic technology into GHz mixed-signal applications. The opportunities and challenges of SOI, bipolar, and SiGe HBT's will be discussed.

CMOS and SOI

Fig. 1 shows the scaling trend of bulk CMOS technology. At a given channel length, SOI may offer another 30-50% performance gain. Over 100 GHz cutoff frequency has been reported for sub-0.1 μm channel length bulk NFET's [1] as shown in Fig. 2. Very high transconductance (g_m) values can be achieved with scaled digital CMOS devices, though the output resistance (r_o) of these short and fast devices is limited by channel length modulation, DIBL, and substrate current induced body effect (Fig. 3). However, specially optimized analog FET devices with 10x better r_o and voltage gain than those digital devices can easily be integrated into a bulk digital process with minimum extra process complexity and cost. For example, an asymmetrically implanted DMOS device was used to improve r_o , substrate current, and hot carrier reliability for high voltage analog functions [2]. An ideal device structure to obtain high g_m while minimizing r_o reduction due to DIBL is the double-gate FET device where drain field lines are terminated at the top and bottom gates. Monte Carlo simulation of a 0.03 μm NFET with double gates [3] is shown in Fig. 4, where the voltage gain ($g_m r_o$) can still exceed 10 for such a short channel device.

SOI technology is particularly attractive for low voltage and low power applications due to its better subthreshold slope, low capacitance, low body effect (substrate sensitivity), low soft error rate, latch up immunity, and simpler fabrication process. With a high resistivity substrate, it is possible to decouple the interelectrode capacitances within active devices to reduce noise, and integrate low-loss micro-strip lines and high-Q passive elements for microwave analog circuits with high speed digital circuitry [4] on SOI. Although digital circuits may take advantage of the kink effect of a partially-depleted (PD) SOI devices to enhance the switching performance, fully depleted (FD) SOI devices without the kink effect are usually required for analog applications since the kink effect would severely degrade the output resistance and available gain. For mixed signal applications, it is possible to integrate digital and analog SOI devices on the same chip by using a common body film thickness and customizing the body doping profiles separately, i.e. low body doping is used for the FD-SOI analog device, and higher body doping is used for the digital device. Fig. 5 shows the design space for a 0.25 μm FD-SOI analog device with 7 nm gate oxide. Such fully-depleted 0.25 μm SOI and silicon-on-sapphire (SOS) devices have been fabricated and show excellent device characteristics (Fig. 6). Here I-V curves without self-heating are extracted by a novel pulsed measurement technique [5] and the drain currents are typically 30% higher than dc static curves at high power levels. It must be emphasized that the g_m and r_o values of SOI devices measured from dc static IV curves are erroneous due to self-heating effects. With this new pulse technique, accurate true IV curves and thermal equivalent circuits for digital and/or analog operation can be extracted directly. These SOI devices have measured f_T values higher than 17 GHz at 0.3 μm channel length, which makes it possible for a

high performance operational amplifier designed with 0.5 μm ground rules and 2 levels of metal to achieve 3.25 Ghz (simulated) unity gain bandwidth [6]. Despite some materials and processing challenges, there is renewed interest in SOS due to its advantages over regular SOI in terms of self-heating, noise, and backgate effects, as would a semi-insulating GaAs substrate offer.

One key challenge to low voltage low power mixed-signal designs is the *headroom* for analog circuits when the CMOS supply voltage is reduced below 2.5V. There are several options to address this issue, e.g., low- V_t (or zero V_t) load devices, separate V_{DD} 's for digital and analog blocks, etc.. Low V_t devices can be used to increase the headroom when one common V_{DD} is used for both the digital and analog circuits. In fact, even digital CMOS itself will need multiple V_t 's as V_{DD} scales below 2V, i.e., a low V_t to maintain an acceptable V_t/V_{DD} ratio (e.g., < 0.25) for the highest switching speed in critical delay paths, and a high V_t where necessary to minimize the standby power. On the other hand, if one uses a higher rail-to-rail voltage for the analog circuits, attention must be paid to the gate insulator integrity and reliability since high V_{GD} may exist across analog devices.

Si BJT and SiGe-base HBT

Bipolar devices offer higher g_m and better precision than MOS for analog applications. Multi-GHz Si BJT analog and communication circuits have been reported, e.g., 15.5 Ghz pre-amp [7], and 9 Ghz VCO circuits [8]. Extending the limits of Si BJT's, thin base SiGe bandgap engineering by UHV/CVD LTE techniques has pushed the f_T of SiGe NPN transistors to over 100 GHz, and PNP to over 50 GHz (Fig.7, 8). Very high beta- V_A values and low noise are possible at high speed for SiGe-base HBT's [9]. Recently, a 12-bit DAC with over 1 G sample/sec performance has been demonstrated using a self-aligned SiGe-base NPN HBT technology.[10] A 19 Ghz pre-amp using a gas-source selective MBE SiGe HBT technology was also reported [11].

Monolithic integration of >30 Ghz Si BJT and >50Ghz SiGe HBT with 0.25mm CMOS has been demonstrated [12], making them attractive for mixed-signal applications well into tens Ghz range, albeit at some additional cost. SiGe HBT will displace some of the high frequency analog applications which used to be the III-V territory. However, it will be quite a challenge to push SiGe HBT's well above 100 Ghz. Precise control of the SiGe heterojunction position and gradient as well as doping profiles are crucial to speed and linearity.

Conclusions

With giga-bit memory chips (density, bandwidth) and giga-hertz logic chips (processing horsepower) on the horizon, Si CMOS ULSI will be the foundation for high speed Ghz digital and mixed-signal applications. CMOS-only technology will likely dominate mixed signal IC's in the Ghz range and below, and SOI will provide additional performance and density boost, especially at low voltage and low power. Bipolar (Si or SiGe) analog blocks may be used as stand-alones or integrated with CMOS for 10-100 Ghz applications. Besides device optimization such as r_o and gate resistance improvement for CMOS and f_T - BV_{CEO} and beta- V_A improvement for bipolar, attention must be paid to other analog elements such as resistors, capacitors, and inductors, as well as device matching and noise reduction techniques.

References

- [1] Y. Taur, et. al., IEDM93, p.130.
- [2] L. Su, et. al., IEDM91, p.367.
- [3] D. Frank, et. al., IEDM92, p.553.
- [4] M. Hanes, et. al., IEEE EDL-14, p. 219, 1993.
- [5] K. Jenkins, J. Sun, J. Pelloie, 1994 IEEE SOI Conf. p. 121.
- [6] C. Hutchens, private communication.
- [7] H. Kitahata, et. al., BCTM92, p.155.
- [8] A. Pottbacker, et. al., JSSC-29, p.1572, 1994.
- [9] E. Crabbe, et. al., IEDM93, p.83.
- [10] D. Harame, et. al., IEDM93, p.874.
- [11] M. Soda, et.al., JSSC-29, p.1577, (1994)
- [12] D. Harame, et. al., IEDM92, p.19.

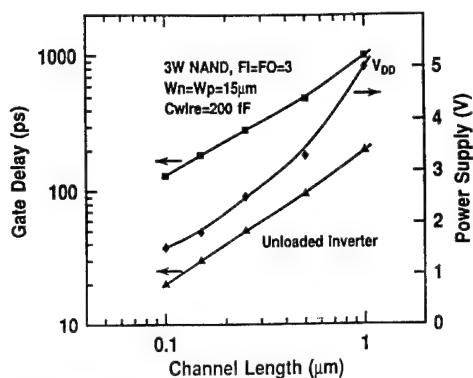


Fig. 1. Bulk CMOS scaling.

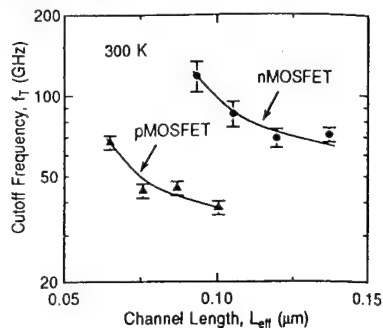
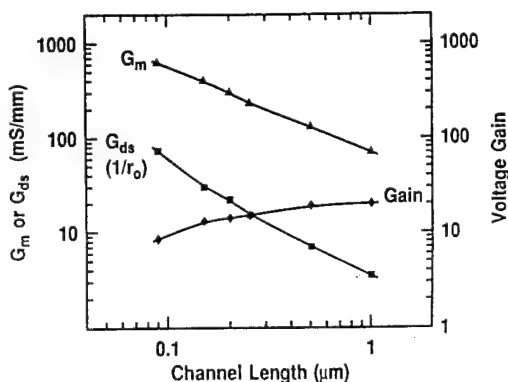
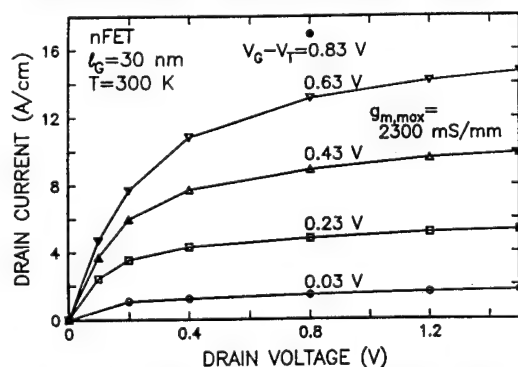
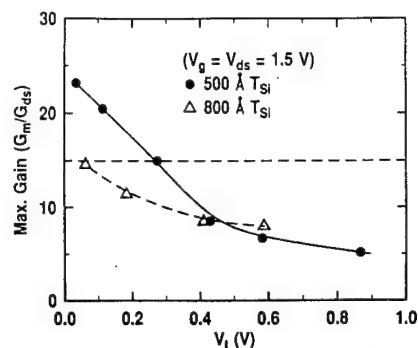
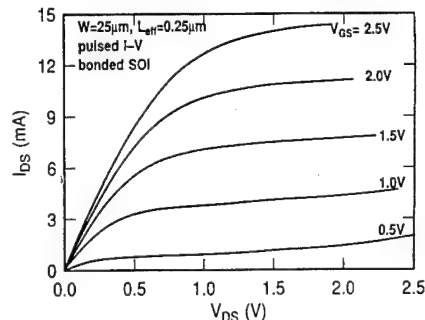
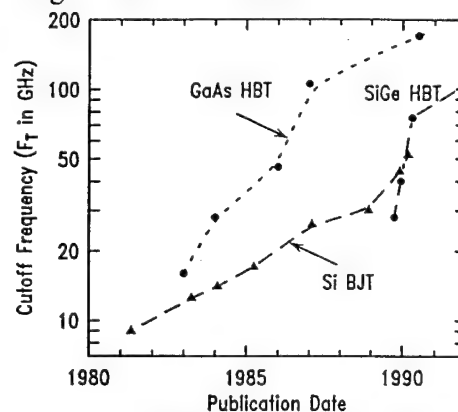
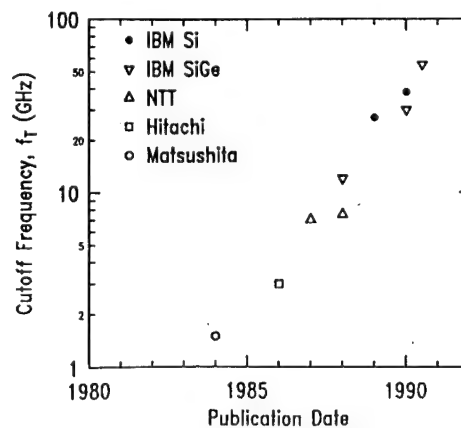
Fig. 2. f_T of $0.1\mu\text{m}$ NFET's and PFET's [1]Fig. 3. Nominal analog characteristics of digital nFET's at $V_G=V_D=0.5V_{DD}$. r_o , gain, and dynamic swing are higher at lower V_G .Fig. 4. Simulated $0.03\mu\text{m}$ double-gate NFET. [3]Fig. 5. $0.25\mu\text{m}$ FD-SOI design space.

Fig. 6. True I-V of an SOI NFET.

Fig. 7. f_T trend of Si and SiGe NPN.Fig. 8. f_T trend of Si and SiGe PNP.

Schottky-Collector Heterojunction Bipolar Transistors: Device Scaling Laws for f_{max} beyond 500 GHz

U. Bhattacharya, M. J. Mondry, G. Hurtz, I. Tan

R. Pullela, M. Reddy, J. Guthrie,

M. J. W. Rodwell, and J. E. Bowers

Department of Electrical and Computer Engineering

University of California, Santa Barbara, CA 93106

805-893-8044, 805-893-3262 FAX

Introduction

Heterojunction bipolar transistors (HBTs) have high transconductance and extremely reproducible DC parameters. These attributes make HBTs the device of choice for high-speed precision analog and mixed analog-digital circuits. HBT cutoff frequencies are however considerably below that of high-electron-mobility field-effect-transistors (HEMTs).

Scaling laws are central to high-frequency semiconductor device design. As the semiconductor layer thicknesses and Schottky contact widths of HEMTs and Schottky diodes are decreased, the device bandwidths increase. It is remarkable that power-gain cutoff frequencies f_{max} of normal HBTs do not significantly increase when the emitter dimensions are reduced below $\sim 2 \mu\text{m}$. Consequently, HBTs are not normally fabricated with deep sub-micron dimensions.

Here we propose the Schottky-collector heterojunction bipolar transistor (SCHBT), a modified HBT whose scaling properties should result in increased cutoff frequencies. The SCHBT is derived from our prior work on Schottky-collector resonant-tunnel-diodes (SRTDs) [1, 2, 3]. The SCHBT, like the SRTD, should obtain a large reduction in a resistance-capacitance time constant, hence a large increase in f_{max} , by extreme scaling through the use of a submicron Schottky collector contact.

f_{max} of the SCHBT increases as $\lambda^{-1/2}$, where λ is the process minimum feature size. An SCHBT processed at $\lambda = 0.2 \mu\text{m}$ should attain $f_{max} \sim 600$ GHz. While fabrication of a such a device will require development of sophisticated dry etching and passivation technologies, it will be difficult to obtain similar cutoff frequencies with the conventional HBT.

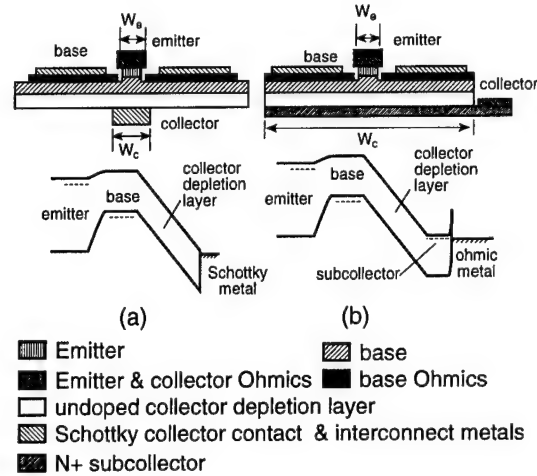


Figure 1: Layer structures and band diagrams comparing an SCHBT (a) to an HBT (b).

Scaling Laws

With the SCHBT (fig. 1), two features should result in increased bandwidth during scaling. First, an epitaxial transfer process step inverts the transistor epitaxial layers during processing, allowing fabrication of aligned emitter and collector contacts with small widths W_e and W_c . Second, use of a Schottky collector contact in preference to a normal N^+ semiconductor collector will permit scaling the collector contact to deep submicron dimensions. This scaling reduces $r_{bb}C_{cb}$, increasing f_{max} .

While the current-gain cutoff frequency $f_\tau = 1/2\pi(\tau_b + \tau_c)$ at high current densities depends only on the base and collector transit times $\tau_b \approx W_b^2/2D_n + W_b/v_{sat}$ and $\tau_c = W_c/2v_{sat}$, $f_{max} \approx \sqrt{f_\tau/8\pi r_{bb}C_{cb}}$ involves the base resistance r_{bb} and the collector-base capacitance C_{cb} . W_b is the base thickness, W_c the collector depletion layer thickness, and v_{sat} the electron velocity. Regardless of the value of f_τ , transistors cannot provide power

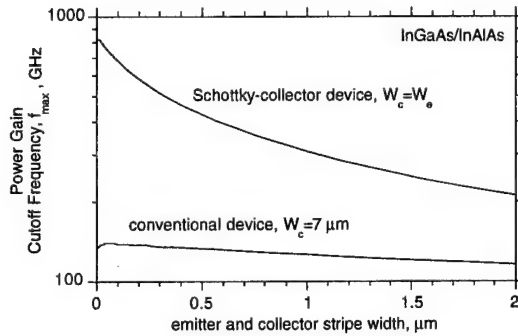


Figure 2: Calculated f_{max} of HBTs and SCHBTs versus emitter width W_e for InGaAs/InAlAs devices with $T_c = 2000 \text{ \AA}$, $T_b = 800 \text{ \AA}$, and material parameters taken from Hafizi et. al. [5]

gain above f_{max} .

In the normal HBT (fig. 1a) the collector junction width W_c is much larger than the emitter stripe width W_e , increasing C_{cb} and decreasing f_{max} . The collector-base capacitance $C_{cb} = \epsilon W_c / T_c$ is proportional to the collector width W_c but is independent of the emitter width. The base resistance, $r_{bb} = \sqrt{\rho_{bc}\rho_{bs}}/2l + W_e\rho_{bs}/12l$ is dominated by the base ohmic contact resistance term ($\sqrt{\rho_{bc}\rho_{bs}}/2l$) and is consequently independent of the emitter width for $W_e < 2 \mu\text{m}$. ρ_{bc} is the specific base contact resistivity, l the emitter stripe length, W_e the emitter width, $\rho_{bs} = \rho_b/T_b$ the base sheet resistivity, and ρ_b the base bulk resistivity. Since f_T and $r_{bb}C_{cb}$ are independent of the emitter width, so is f_{max} . For emitter stripe widths below $\sim 2 \mu\text{m}$, f_{max} does not improve.

In contrast, SCHBTs (fig.1b) have $W_c = W_e$. This results in a smaller C_{cb} and a significant increase in f_{max} . Inclusive of fringing fields, $C_{cb} \simeq \epsilon l(W_c + T_c)/T_c$. C_{cb} , proportional to the collector width, is proportional to the emitter width since the widths are now equal. The base resistance is still independent of W_e , and hence $r_{bb}C_{cb} \propto W_c + T_c$. Consequently, with T_c and T_b fixed, $f_{max} \propto (W_c + T_c)^{-1/2}$. Bandwidth increases as the inverse square root of the process minimum feature size.

The Schottky collector also eliminates the collector contact resistance r_c , but r_c has significant impact on HBT bandwidth only when $r_c C_{cb} \sim \tau_c$, e.g. for collector space-charge-thicknesses T_c below 1000 \AA . In InGaAs/InAlAs SCHBTs the contact is to InGaAs. Schottky contacts to N-InGaAs result in very leaky junctions due to the small 0.2 eV conduction-band barrier, but it is the large

0.5 eV valence-band barrier which is relevant here; on base/Schottky-collector junctions with $W_c = 2000 \text{ \AA}$, we measure $< 10 \text{ A/cm}^2$ leakage at 4 V reverse bias.

Fig. 2 compares calculated HBT and SCHBT cutoff frequencies versus W_e for InAlAs/InGaAs devices, using measured HBT parameters ($T_c = 2000 \text{ \AA}$, $T_b = 800 \text{ \AA}$, $\tau_b + \tau_c = 1.4 \text{ ps}$, $\rho_{bs} = 137 \Omega/\text{square}$, $\rho_{bc} = 70 \Omega - \mu\text{m}^2$) taken from Hafizi et. al. [4]. Use of Hafizi's parameters, with fixed base and collector thicknesses, in calculation of the SCHBT scaling properties is conservative, in that it is beneficial here to reduce T_c and T_b as W_e is reduced. Even assuming fixed T_c and T_b , very high SCHBT cutoff frequencies are projected (fig. 2).

There are limits to emitter and collector scaling. As the emitter width is reduced, its periphery-area ratio increases and the current gain β drops due to surface recombination at the emitter-base mesa edge. In AlGaAs/GaAs, HBTs have attained very low surface recombination rates through use of depleted AlGaAs surface passivation layers [5]. In InGaAs/InAlAs, reduction of β for narrow emitters is much less severe because of the material's lower surface recombination velocities. An efficient Schottky collector must be as wide as the emitter, and alignment tolerances must be accommodated. With a projection mask aligner, $0.5 \mu\text{m}$ features can be defined at $0.2 \mu\text{m}$ alignment tolerance, resulting in $W_e = 0.5 \mu\text{m}$, $W_c = 0.9 \mu\text{m}$, and $f_{max} = 330 \text{ GHz}$ is calculated (fig. 2). With electron-beam lithography and reactive ion etching, $W_e = W_c = 0.2 \mu\text{m}$ should be feasible, giving a projected 580 GHz f_{max} (fig. 2).

Fabrication

SCHBTs require processing of both sides of the transistor layers using epitaxial transfer (fig. 3) [6]. After a collector-up growth of the InAlAs/InGaAs HBT layers on a InP substrate, metal is deposited to form direct Schottky collector contacts to the undoped collector depletion layer. The wafer is then inverted and epoxied under vacuum to (e.g.) a GaAs substrate, whereupon the InP substrate is removed by an HCl selective etch. Alignment marks on the collector surface are then made visible using a recess etch. The remaining processes (emitter contact deposition, self-aligned base recess etch and base contact deposition, base mesa etch, and planarized emitter connections) then follow a normal HBT fabrication sequence [4].

There are two demanding steps in HBT fabri-

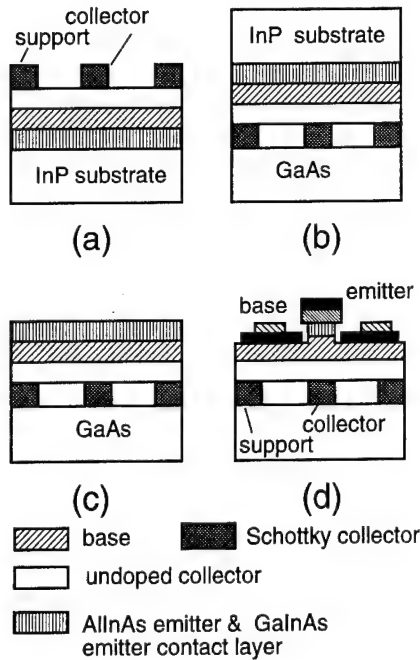


Figure 3: SCHBT fabrication process. Schottky collector contacts are deposited on MBE grown collector-up material (a). The wafer is inverted and epoxied under vacuum to a GaAs substrate (b). The InP substrate is removed by etching in HCl (c). Remaining process steps follow a normal HBT sequence (d).

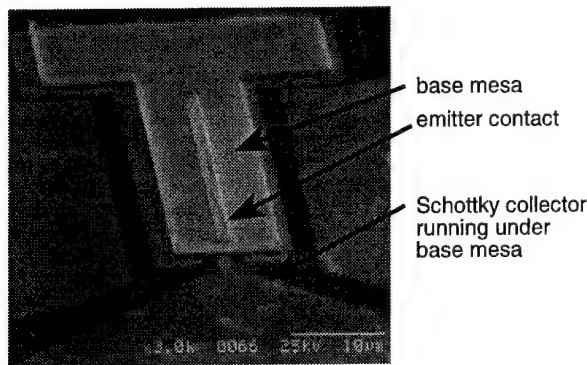


Figure 4: Electron micrograph of an SCHBT with $W_c = W_e = 1\mu\text{m}$ subsequent to epitaxial transfer, emitter and base ohmic contact deposition, and base mesa etching.

cation; MBE growth with accurate positioning of the base doping profile relative to the heterointerface, and control of the recess etch used in the self-aligned base process. SCHBT fabrication adds the additional step of epitaxial transfer [6]. These process steps can be integrated into a normal HBT process flow. We have performed extensive experiments on epitaxial transfer of HBT layers for SCHBT fabrication. Fig. 4 shows a sample with $W_c = W_e = 1\mu\text{m}$ after epitaxial transfer, the self-aligned emitter-base processes, and base mesa etching. The epoxy-bonded transferred epitaxial films are robust: experimental samples survive without degradation ohmic contact sintering (300°C), hot solvent cleaning, and the polyimide thermal curing cycles associated with the emitter planarization process.

Conclusions

Cutoff frequencies of heterojunction bipolar transistors do not increase as process dimensions are reduced below $1\mu\text{m}$. Schottky-collector HBTs should attain progressively increasing cutoff frequencies as the device dimensions are reduced. Successful realization of devices with cutoff frequencies above 500 GHz is dependent upon integration of an epitaxial transfer step into a normal HBT process, and development of dry etching and passivation technologies for fabrication of deep submicron emitters.

We acknowledge discussions with U. Mishra, W. Stanchina, P. Zampardi, and G. Sullivan. This work was supported by the AFOSR under grant F49620-92-J-0469.

References

- [1] Y. Konishi et. al., 1992 Engineering Foundation workshop on advanced heterostructure transistors, Kona, Hawaii, November.
- [2] Y. Konishi et. al., Solid-State Electronics, Vol. 36, No. 12, pp. 1673-1676, 1993
- [3] R.P. Smith et. al., IEEE Electron Device Letters, Vol. 15, No. 8, August 1994
- [4] M. Hafizi et. al., IEEE Trans. Elect. Dev., Vol. 40, No. 12, Dec. 1993.
- [5] C. Dai et. al., 1994 IEEE Device Research Conference, June 20-22, Boulder Co.
- [6] V. Abert-Engels et. al., 1994 IEEE Device Research Conference, June 20-22, Boulder Co

Monolithic integration of low-temperature-grown GaAs and high-mobility 2DEG for ultrafast photonic circuits

J. Allam, K. Ogawa and A.P. Heberle

*Hitachi Cambridge Laboratory, Hitachi Europe Ltd.,
Cavendish Laboratory, Madingley Road, Cambridge CB3 0HE, U.K..
Telephone: (44 223) 467944 Facsimile: (44 223) 467942*

N. de B. Baynes and J.R.A. Cleaver

*Microelectronics Research Centre, University of Cambridge,
Cavendish Laboratory, Madingley Road, Cambridge CB3 0HE, U.K..*

T. Mishima and I. Ohbu

*Central Research Laboratory, Hitachi Ltd.,
1-280, Higashi-koigakubo, Kokubunji-shi, Tokyo 185, Japan.*

GaAs grown at low substrate temperatures by molecular beam epitaxy (LT GaAs) and subsequently annealed exhibits properties attractive for photonic circuits incorporating ultrafast photodetectors and active devices such as FET's.¹ It is highly insulating, making it attractive as a buffer layer to suppress backgating in FET's,² and it exhibits sub-picosecond carrier lifetime³ making it highly suitable for ultrafast photoconductive switches.

Melloch et al.⁴ have reported a high mobility ($\mu \approx 2 \times 10^6 \text{ cm}^2 \text{V}^{-1} \text{s}^{-1}$) AlGaAs/GaAs two-dimensional electron gas (2DEG) grown on LT GaAs, but the carrier lifetime in the LT GaAs was not measured. We used a similar wafer (subsequently referred to as #1) to fabricate integrated photonic sampling circuits.⁵ The wafer consisted of 1 μm of LT GaAs grown at 250 °C on a semi-insulating substrate, followed by 2 μm of buffer layers and the 2DEG. Although the mobility of the 2DEG was not degraded by growth on the LT layer, the carrier lifetime was $\approx 40 \text{ ps}$, much longer than the sub-picosecond lifetime of optimised material³. The apparent position of the LT layer deduced from reflectance measurements on an etched sample was shifted from the position expected from growth specifications and transmission electron microscopy. This is due to forward diffusion⁶ of excess As during the long anneal in the growth of subsequent layers.

In this paper, we describe the design and characterisation of a wafer in which the properties of the LT GaAs layer were simultaneously optimised both as an ultrafast photoconductive layer and as a buffer layer for the growth of high mobility 2DEG. Arsenic diffusion was reduced by annealing of the LT layer prior to growth of the subsequent layers and by growing AlAs diffusion barriers above and below the LT layer.⁶ The growth temperature of the LT layer was lowered to 220 °C, and the buffer layer width reduced to decrease the overall annealing time. The layer structure is shown in Table I. Two layers (A and B) were grown under identical conditions.

In order to measure the carrier lifetime in the region of the LT GaAs layer, samples were etched using a combination of selective and timed etches to reveal the following layers: upper AlAs (position 1), upper temperature-graded layer (2), top of LT GaAs layer (3), middle of LT GaAs layer (4) and lower temperature-graded layer (5). The carrier lifetime was measured at room temperature by photoluminescence (PL) upconversion and by transient reflectance (TR). The PL data is shown in figure 1 (data from different positions are offset for clarity). The rise time of the PL intensity ($\tau_c \approx 100 \text{ fs}$) corresponds to the cooling of carriers from the non-equilibrium injected distribution. The fall time corresponds to the carrier lifetime (τ_r). Recombination in the substrate causes an additional slow component, which increases in intensity as the etched surface approaches the substrate. TR measurements at $\lambda \approx 860 \text{ nm}$ are shown in figure 2, and were fitted as the sum of two exponentials with time constants τ_c and τ_r . The carrier lifetime obtained from PL and TR measurements is shown in Table II. Good agreement is obtained between the two measurement methods and the two wafers. The response at positions 1 and 2 is identical since the AlAs layer is transparent at the measurement wavelength. In both samples, the carrier lifetime in

the LT GaAs (positions 3 and 4) is measured to be 0.4 - 0.5 ps, with a slightly longer lifetime in the temperature-graded region (position 2).

Thickness	Composition	n doping (cm ⁻³)	Temperature	Layer
10 nm	GaAs	10 ¹⁷		cap
45 nm	Al ₃ Ga ₇ As	1.3 x 10 ¹⁸	615 °C	donor layer
25 nm	Al ₃ Ga ₇ As	u.d.	615 °C	spacer layer
0.2 μm	GaAs	u.d.	600 °C	buffer 2
0.2 μm	GaAs	u.d.	600 °C	buffer 2
5 nm	Al ₃ Ga ₇ As	u.d.) 10 period
5 nm	GaAs) superlattice
0.1 μm	GaAs	u.d.	600 °C	buffer 1
Anneal at 600 °C for 10 minutes				
50 nm	AlAs	u.d.	600 °C	
0.1 μm	GaAs	u.d.	220 - 600 °C	temp. graded
1 μm	LT GaAs	u.d.	220 °C	photoconductor
0.1 μm	GaAs	u.d.	600 - 220 °C	temp. graded
50 nm	AlAs	u.d.	600 °C	
0.1 μm	GaAs	u.d.	600 °C	
substrate	(100) GaAs			

Table I. Specification of integrated LT GaAs / 2DEG wafer.

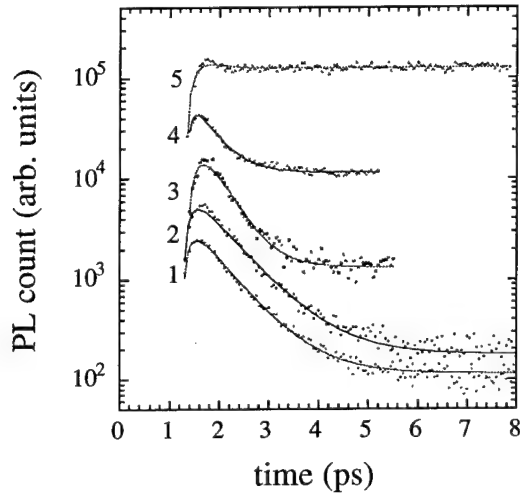


Figure 1. Time-resolved luminescence of wafer A.

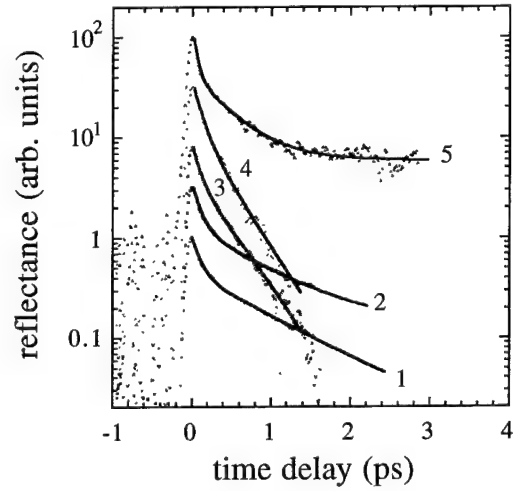


Figure 2. Transient reflectance of wafer A.

Wafer A			Wafer B		
Position	τ_r (ps)		Position	τ_r (ps)	
	PL	TR		PL	TR
1	0.70	0.99	1		1.72
2	0.70	0.85	2	1.25	
3	0.44	0.42	3	0.49	0.45
4	0.43	0.36	4	0.44	0.47
5		0.44	5	0.38	0.54

Table II. Carrier lifetimes from PL and transient reflectance.

The properties of the 2DEG were investigated by low-temperature magnetoresistance measurements. The sheet carrier concentration was determined both from the period of the Shubnikov - de Haas (SdH) oscillations and from the magnitude of the Hall resistance (R_H). Figure 3 shows clear oscillations in the longitudinal magnetoresistance. Carrier concentrations derived from SdH and from R_H were in good agreement. The sheet resistance (and hence mobility) was determined from van de Pauw measurements. Measurements were made in the dark, and after illumination of the sample using an LED. All the wafers (1, A and B) show similar properties, with a maximum mobility of $\approx 360,000 \text{ cm}^2 \text{V}^{-1} \text{s}^{-1}$. This value is typical of wafers from the same source and indicates that the mobility is limited by the background impurity level, and not by additional defects due to growth on the LT GaAs layer.

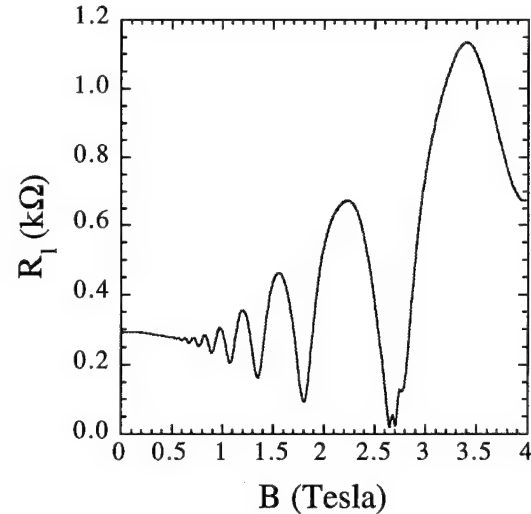


Figure 3. Longitudinal magnetoresistance of wafer B at 4.2 K showing SdH oscillations.

Wafer	In dark			Illuminated		
	n_s (10^{11} cm^{-2})		μ ($\text{cm}^2 \text{V}^{-1} \text{s}^{-1}$)	n_s (10^{11} cm^{-2})		μ ($\text{cm}^2 \text{V}^{-1} \text{s}^{-1}$)
	SdH	R_H		SdH	R_H	
#1	2.60	2.64	139,000	4.06	4.22	358,000
A		3.09	211,000		4.26	360,000
B	2.58	2.60	198,000	3.55	3.62	357,000

Table III. Carrier concentration and mobilities of GaAs/AlGaAs 2DEG layers at 4.2 K.

In conclusion, high mobility 2DEG layers were grown on a $1 \mu\text{m}$ thick LT GaAs layer which exhibited a carrier lifetime of $\approx 0.5 \text{ ps}$. Such wafers are useful for monolithic integration of ultrafast photodetectors and high electron mobility transistors.

References

- ¹J. Allam, K. Ogawa, J. White, N. de B. Baynes, J.R.A. Cleaver, I. Ohbu, T. Tanoue and T. Mishima, *OSA Proceedings on Ultrafast Electronics and Optoelectronics*, 1993, (J. Shah and U. Mishra, eds.) Vol. **14**, p. 197.
- ²F.W. Smith, A.R. Calewa, C.L. Chen, M.J. Manfra and L.J. Mahoney, *IEEE Electron Device Lett.* **9**, 77 (1988)
- ³S.Gupta, M.Y.Frankel, J.A.Valdmanis, J.F.Whittaker, G.A.Mourou, F.W.Smith & A.R.Calewa, *Appl. Phys. Lett.* **59**, 3276 (1991).
- ⁴M.R. Melloch, N. Otsuka, J.M. Woodall, A.C. Warren and J.L. Freeouf, *Appl. Phys. Lett.* **57**, 1531 (1990).
- ⁵K. Ogawa, J. Allam, N. de B. Baynes, J.R.A. Cleaver, I. Ohbu, and T. Mishima, to be published in *Applied Physics Letters*.
- ⁶J.P. Ibbetson, C.R. Bolognesi, H. Weman, A.C. Gossard and U.K. Mishra, *GaAs and Related Compounds 1991*, (Inst. Phys. Conf. Ser. No. 120) p.37.

Manufacturable 200GHz, Low Noise P⁺-GaInAs/N-AlInAs/GaInAs JHEMT Technology

J.B. Shealy^{^*}, T.Y. Liu[†], M. A. Thompson[†], L.D. Nguyen[†], and U.K. Mishra

[^] Hughes Doctoral Fellow
[†] Hughes Research Laboratories
3011 Malibu Canyon Rd.
Malibu, CA 90265
(310) 317-5126

^{*} Department of Electrical and
Computer Engineering
University of California
Santa Barbara, CA 93106
(805) 893-3812

It is becoming increasingly critical to successfully develop a compound semiconductor IC technology which is both high performance and low cost to penetrate crucial large volume markets such as future mm-wave wireless communications. This requires a simple transistor technology which (i) exhibits high performance across a wide bias range to perform both transmit and receive operations, (ii) has high threshold uniformity to enable high density, high speed signal processing circuits, and (iii) has a basic technology which is relatively transparent to the two commercially important family of materials, namely, GaAs and InP based. The Junction HEMT (JHEMT) technology which is presented satisfies the above criteria.

The material system used is P⁺-GaInAs/N-AlInAs/GaInAs on InP. In contrast to a conventional Schottky-gated HEMT, the JHEMT uses a highly doped p⁺ region to modulate the 2DEG. The barrier height of a JHEMT is therefore both high (determined by the work function difference of the neutral p⁺ surface layer and the 2DEG, ~1.2eV) and uniform (solely determined by the MBE growth).

A schematic of the device is shown in

figure 1. The gate region is Be-doped with $p=1 \times 10^{20} \text{ cm}^{-3}$. A pseudo-delta doping scheme is employed using a thin Si-doped donor layer with $n=1.2 \times 10^{19} \text{ cm}^{-3}$. High sheet charge ($2.5 \times 10^{12} \text{ cm}^{-2}$) and low resistance ($300 \Omega/\text{sq}$) access regions are achieved, because the low surface work function of the AlInAs (~0.5eV) adjacent to the gate. This is crucial in ensuring that the access regions do not limit device current and gain_[1]. The energy band diagrams for the gate and access regions are shown in figure

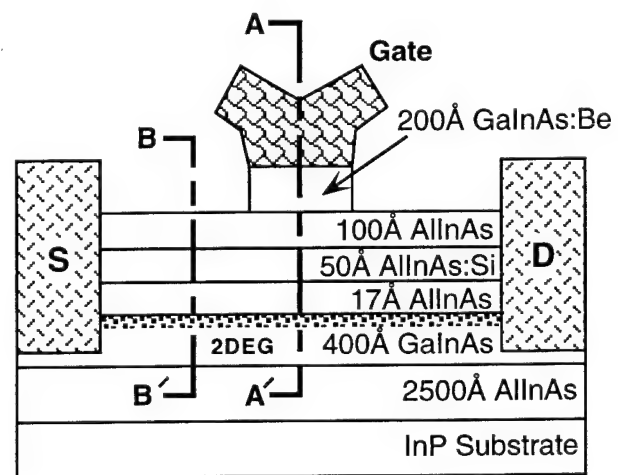


Figure 1. Device schematic of fabricated 0.2 μm gatelength JHEMTs. A-A' and B-B' denote cross-sections of the gate and access regions, respectively.

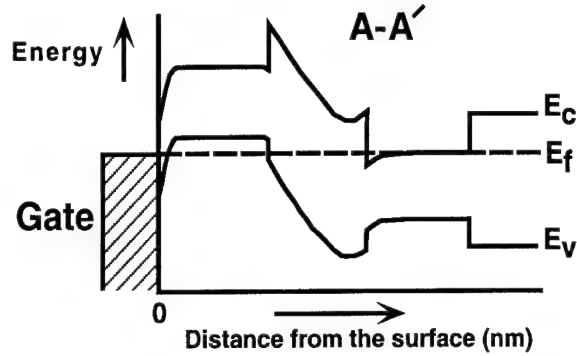
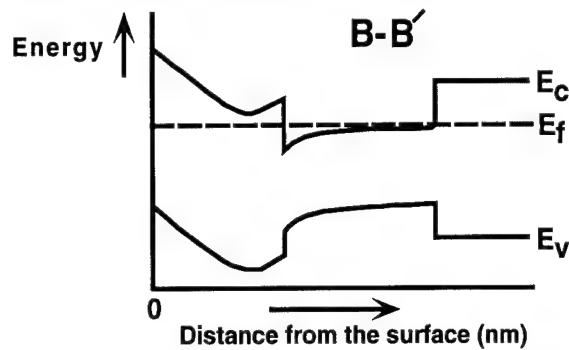
Band Diagram under the Gate:**Band Diagram outside the Gate:**

Figure 2. Energy band diagram of JHEMT at cross-section A-A' (Top) and cross-section B-B' (Bottom).

2. The variation of the channel sheet concentration and mobility as the access region is etched is shown in figure 3.

JHEMTs in the AlGaAs/GaAs system were first demonstrated by Ohata *et al.*_[2] in 1984. Recently, we demonstrated a P⁺-GaInAs/P⁺-AlInAs/N-AlInAs/GaInAs on InP JHEMT_[3] with an f_{max} of 110 GHz. The performance of that device was limited by a poor aspect ratio and high gate contact and feed resistance. The device presented here has both an improved aspect ratio and a reduced gate resistance by eliminating the P⁺-AlInAs layer. Furthermore, an improved ohmic contact technology and the incor-

poration of a T-shaped gate metal dramatically reduces the input resistance.

The record results achieved from devices with 0.2 μm gate length are presented below. The full channel current and transconductance for a 100 μm wide device is 460 mA/mm and 520 mS/mm, respectively, with a gate-source separation of 0.5 μm . Figure 3 shows the dc I-V characteristics of the P⁺-GaInAs/N-AlInAs/GaInAs JHEMT. Simultaneously, the two-terminal gate-drain breakdown voltage was over 10V for a gate-drain spacing of 1.5 μm . For

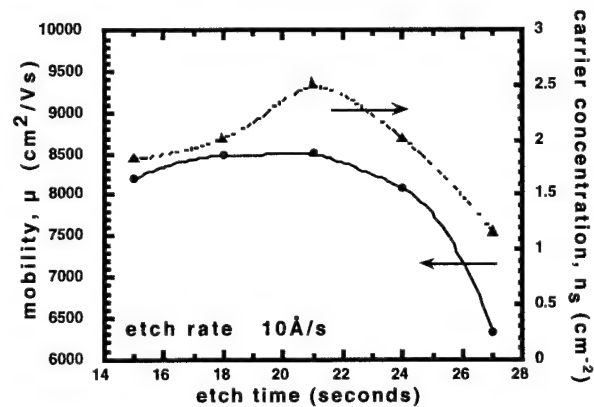


Figure 3. Electron mobility and carrier concentration versus etching time of the access regions.

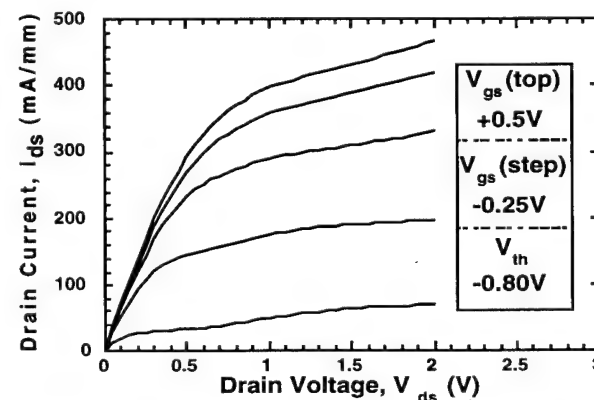


Figure 4. Drain I-V Characteristics of a 0.2 μm x 100 μm P⁺-GaInAs/N-AlInAs/GaInAs JHEMT.

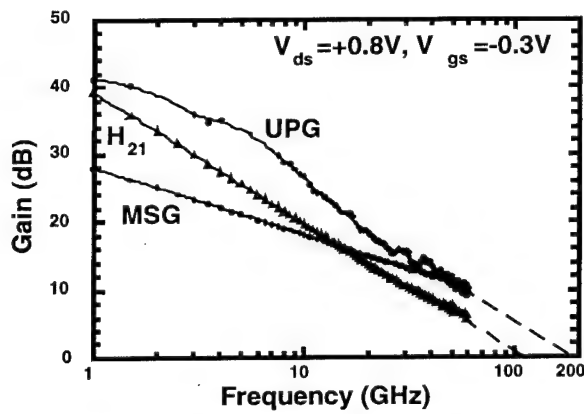


Figure 5. Small-Signal gain versus frequency of a $0.2\mu\text{m} \times 100\mu\text{m}$ P⁺-GaInAs/N-AlInAs/GaInAs JHEMT.

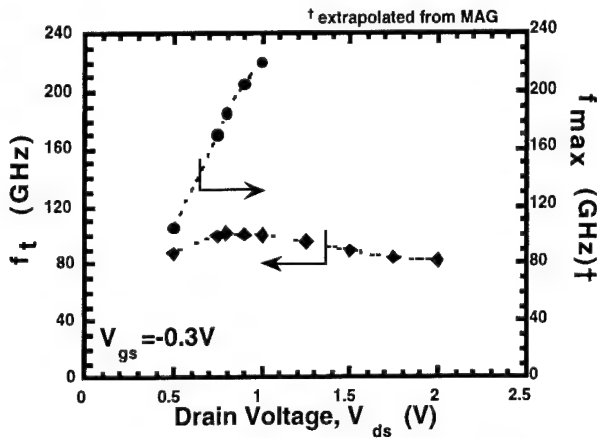


Figure 6. f_t and f_{max} versus drain voltage of a $0.2\mu\text{m} \times 100\mu\text{m}$ P⁺-GaInAs/N-AlInAs/GaInAs JHEMT.

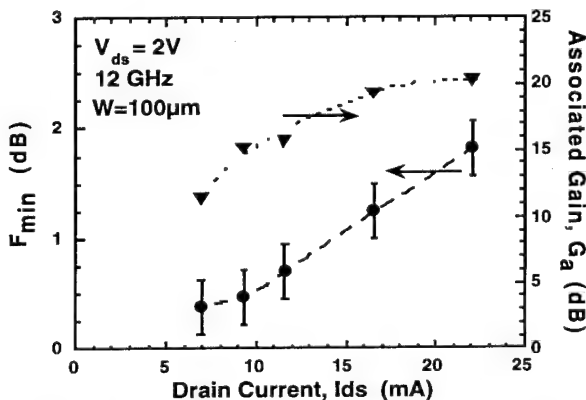


Figure 7. Minimum noise figure and associated gain of a $0.2\mu\text{m} \times 100\mu\text{m}$ P⁺-GaInAs/N-AlInAs/GaInAs JHEMT at 12GHz.

devices with a gate-drain spacing of $2.5\mu\text{m}$ the two-terminal breakdown voltage was 16V.

For a source-drain spacing of $2\mu\text{m}$, the f_t and f_{max} were as high as 100 GHz and 220 GHz, respectively at a drain voltage as low as 1V. Figure 4 shows the RF gain versus frequency and figure 5 shows the drain voltage dependence of f_t and f_{max} . The decrease in f_t at higher drain voltages is due to higher parasitic transit delay caused by an increasing output conductance^[4]. As previously mentioned, the threshold voltage in such devices is solely determined by the uniformity of the growth. Thus, the standard deviation of threshold voltage for 50 devices across a $1 \times 1.5 \text{ in}^2$ sample was 13.7mV. Finally, state-of-the-art minimum noise figure (0.4dB) and associated gain (15dB) at 12GHz are also obtained at a drain bias of $2V_{\text{gs}}$ ^[5]. The minimum noise figure and associated gain is plotted versus drain current in figure 6. In summary, we believe that no technology to date incorporates all these features and satisfies the requirements presented above.

Acknowledgements: The authors would like to acknowledge the support of Dr. Paul Greiling at Hughes Research Laboratories.

References

- [1] Greenberg *et al.*, IEEE Trans. Electron Dev., Vol.41, No.8, August 1994.
- [2] Ohata *et al.*, IEEE Int. MTT-S Microwave Symp. Dig., pp. 434-436, 1984.
- [3] Shealy *et al.*, 1994 Device Research Conference, Boulder Co., June 1994.
- [4] Tasker *et al.*, IEEE Electron Device Lett., Vol. 10, No. 7, July 1989.
- [5] Nguyen *et al.*, Proc. of the IEEE, Vol. 80, No. 4, April 1992.

Tuesday, March 14, 1995

Terahertz Dynamics

UTuD 3:45 pm-5:30 pm
Ballrooms VI-VIII

Dan Grischkowsky, *Presider*
Oklahoma State University

Probing Terahertz Dynamics in Semiconductor Nanostructures with the UCSB Free-electron Lasers

S.J. Allen, J.P. Kaminski, B.J. Keay, J.S. Scott, M. Wanke
Center for Free-electron Laser Studies
UC Santa Barbara, CA 93106
Tel: 805-893-7134 FAX: 805-893-4170

K.L. Campman, A.C. Gossard
Materials Department
UC Santa Barbara, CA 93106

U. Bhattacharya, M.J.M. Rodwell
Department of Electrical and Computer Engineering
UC Santa Barbara, CA 93106

D.H. Chow, M. Lui, and T.K. Liu
Hughes Research Laboratory
Malibu, CA 90265

Non-linear electron dynamics in semiconductor nano-structures define a rich scientific arena with potential impact on novel devices in the terahertz regime, a relatively technology poor part of the spectrum. Experiments abound that explore the spectrum of collective and single particle excitations in nanostructures in the terahertz regime, but "real devices" are inevitably driven far-from equilibrium and there are few experiments that address non-linear dynamics in nanostructures. Here we describe two related experiments that attempt to address the terahertz dynamics of quantum transport in resonant tunneling structures. In the first, we determine the intrinsic relaxation time in resonant tunneling diodes by measuring the "rectified" response from 120 GHz to 3.9 THz. In the second, photon assisted tunneling is explored in sequential resonant tunneling superlattices. Finally, we return to resonant tunneling diodes and speculate on the prospects of recovering photon assisted tunneling and narrow band terahertz gain in resonant tunneling diodes.

These experiments are made possible by the UCSB free-electron lasers that deliver kilowatts of tunable radiation from 120 GHz to 4.8 THz. A third FEL, coming on-line, is designed to generate frequencies as high as 10 THz. The FELs produce a quasi-CW pulse that can be varied from 1 μ sec to 10's of μ sec. A μ sec, quasi-CW, pulse appears to be a contradiction in terms. However, the characteristic elastic and inelastic relaxation times in semiconductor systems is orders of magnitude faster than the μ sec long pulse. At the same time the operating frequencies of these FEL's cover the important relaxation rates and resonant frequencies of semiconductor systems and dynamical information is recovered in the frequency domain.

Intrinsic Relaxation of Resonant Tunneling Diodes. Resonant tunneling diodes, (RTD's), exhibit strong differential negative resistance and are potentially important for high speed switching¹ and terahertz oscillators². The resonant tunneling structure used here consisted of an InGaAs/AlAs/InGaAs/AlAs/InGaAs double barrier heterostructure grown on InP. The room temperature I-V is shown in Fig. 1.

To determine the high frequency behavior of the resonant tunneling, we would ideally like to measure this I-V at THz frequencies. This is not practical. Rather we measure the second derivative of the I-V by treating the RTD as a detector. At low enough frequencies the "rectified response" will simply be proportional to the DC second derivative, while at frequencies where the device can no longer follow the high frequency fields, the response will "roll-off". It is important to point out that the observation of a rectified response at some frequency does not provide much information. It is only the broad band frequency dependence of this response that conveys dynamical information.

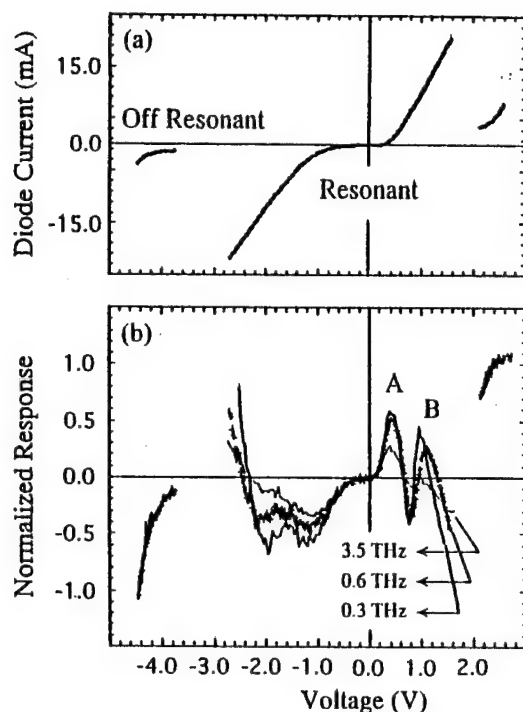


Fig. 1. The DC I-V characteristic of the RTD, top. The normalized rectified response at 300 GHz, 600 GHz, and 3.5 THz, bottom.

resonant tunneling regime, is normalized by the off resonant response for positive bias, beyond the negative resistance region.

In Fig. 1, the normalized response is shown for three different frequencies, 300 GHz, 600 GHz and 3.5 THz. It is gratifying to find that the off-resonant response for negative bias, beyond the negative resistance region, shows little frequency dependence while the resonant tunneling regime shows a strong relaxation at high frequencies.³

The normalized, rectified response is shown in Fig. 2 from 120 GHz to 3.8 THz for two different bias points. Both have a relaxation frequency of the order of 650 GHz but the behavior near threshold exhibits a plateau. This implies that there are contributions to resonant tunneling, and its rectified response at threshold, that are extremely fast and suffer no relaxation in our frequency range.

The roll-off at 650 GHz implies a relaxation time of 240 femtoseconds. It is tempting to ascribe this to the quasi-bound state lifetime, the time it takes an electron to tunnel through the double barrier/quantum well system. But, recent theory of quantum rectification in these devices, by Wingreen⁴, argues against this interpretation. It is possible that the time represents the relaxation time of the screening space charge in the structure, but this interpretation must be confirmed by a systematic study of the dependence of this relaxation time on material parameters. Although the relaxation behavior is not easily reconciled with existing theory, it does present a measure of the intrinsic relaxation of these quantum transport devices, at frequencies some two orders of magnitude higher than previously measured.

Photon Assisted Tunneling. If $\omega\tau > 1$ in a system that supports coherent transport, classical rectification is described as photon assisted tunneling. Here electrons tunnel through an insulating barrier but gain or lose energy equal to one or more photons. This process is particularly important, for it has the potential to make possible a tunable laser⁵ or a medium with tunable narrow band gain.⁶

The device is electrically probed in a conventional probe station, while it is irradiated by the free-electron laser. The probe tip acts as an antenna to couple the radiation into the device but the coupling is a very strong function of frequency, varying like ω^{-4} . To remedy this defect the response in the important part of the I-V characteristic, the

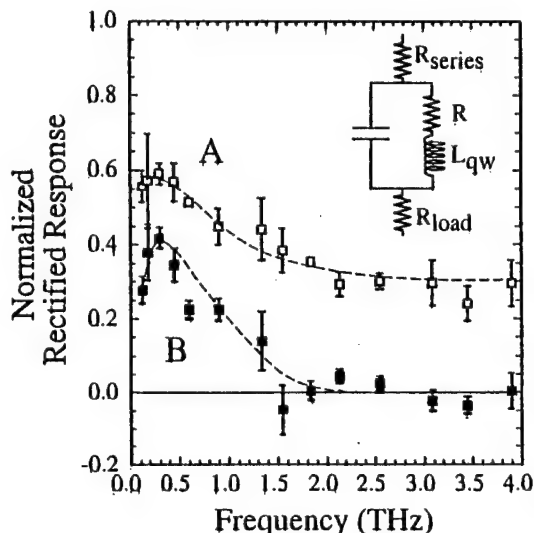


Fig. 2. The normalized rectified response at two different bias points in the resonant tunneling regime. Relaxation at 650 GHz implies a relaxation time of 240 fsec.

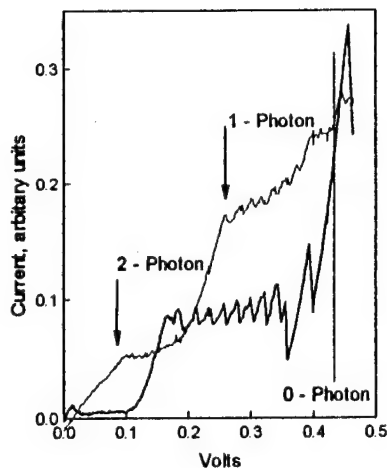


Fig. 3. Superlattice current-voltage characteristics in a "bow tie" antenna at 12 K, with and without the presence of radiation at 3.43 THz.

the excited state of a neighboring well. The dependence of the photon assisted tunneling on the radiation intensity exhibits a non-monotonic behavior, in semi-quantitative agreement with the theory of Tien and Gordon.

An important goal of the current research is to establish photon assisted tunneling in RTD's, to open the possibility of a material system with narrow band gain. If successful we will have driven RTD's from the electronic side of the electronic/photonic side of the technology ledger, with descriptions of gain in terms of negative resistance, to the photonic side, and concepts such as population inversion.

The essential physics governing photon assisted tunneling is found in the early work of Tien and Gordon⁷ that explained quasi-particle tunneling in superconductor-insulator-superconductor, (S-I-S), junctions. Singular features in the current voltage characteristic, $I(V)$, are replicated as features at $I(V \pm n\hbar\omega)$, where $n\hbar\omega$ is n units of photon energy. Specifically the $I(V)$ characteristic becomes

$$I = \sum_{n=-\infty}^{n=\infty} J_n^2 \left(\frac{eaE}{\hbar\omega} \right) \cdot I(V + n\hbar\omega),$$

where J_n is the n^{th} order Bessel function and e , a , and E are the electron charge, junction barrier thickness and high frequency electric field, respectively.

The early work by us simply bonded a wire to a relatively large mesa and relied on the bond wire to both measure the current-voltage characteristic and couple the FEL radiation into the device.⁸ More recently we have integrated these superlattices into "Bow Tie" antennae which has enhanced the coupling and exposes multi-photon assisted resonant tunneling.⁹

The current voltage characteristic of a ten period superlattice that supports sequential resonant tunneling is shown in Fig. 3 at 12 K, with and without radiation at 3.43 THz. Features appear that correspond to sequential resonant tunneling into one and two photon side bands of

1. E. Ozbay, D.M. Bloom, D.H. Chow and J.N. Shulman, IEEE Electron Device Lett. **14**, 400 (1993).
2. E.R. Brown, J.R. Soderstrom, C.D. Parker, L.J. Mahoney, K.M. Molvar and T.C. McGill, Appl. Phys. Lett. **58**, 2291 (1991).
3. J.S. Scott, J.P. Kaminski, M. Wanke, S.J. Allen, D.H. Chow, M. Lui and T.Y. Liu, Appl. Phys. Lett. **64**, 1995 (1994).
4. N.S. Wingreen, Appl. Phys. Lett. **56**, 253 (1990).
5. J. Faist, F. Capasso, D.L. Sivco, C. Sirtori, A.L. Hutchinson and A.Y. Cho, Science **264**, 553 (1994).
6. R.F. Kazarinov and R.A. Suris, Sov. Phys. Semicond. **6**, 120 (1972).
7. P.K. Tien and J.P. Gordon, Phys. Rev. **129**, 647 (1963).
8. P.S.S. Guimaraes, B. J. Keay, J.P. Kaminski, S.J. Allen, P.F. Hopkins, A.C. Gossard, L.T. Florez, and J.P. Harbison, Phys. Rev. Lett. **70**, 3792 (1993).
9. B.J. Keay, S.J. Allen, Jr., J.P. Kaminski, K.L. Campman, A.C. Gossard, U. Bhattacharya, M.J.M. Rodwell, J. Galan, to be published, Proceedings of the 22nd International Conference on the Physics of Semiconductors.

Bloch oscillations in GaAs/AlGaAs superlattices following excitation of continuum states: physics and application perspectives

H. G. ROSKOS, C. WASCHKE, P. LEISCHING, and H. KURZ

Institut für Halbleitertechnik II, Rheinisch-Westfälische Technische Hochschule (RWTH) Aachen,
Sommerfeldstr. 24, D-52056 Aachen, Germany, Tel.: +49-241-80-7806 (-7890),
Fax: +49-241-8888-246, Email: roskos@zyklop.basl.rwth-aachen.de

K. VICTOR

Institut für Theoretische Physik B, RWTH Aachen, Sommerfeldstr. 26, D-52056 Aachen, Germany

K. KÖHLER

Fraunhofer-Institut für Angewandte Festkörperphysik, Tullarstr. 72, D-79108 Freiburg, Germany

Time-resolved terahertz (THz) emission spectroscopy is a powerful tool to investigate coherent processes in semiconductors. With this measurement technique, Bloch oscillations of optically excited electron wave-packets in GaAs/AlGaAs semiconductor superlattices have been observed [1]. All time-resolved experiments carried out up to now with this and other techniques [2,3] concentrated on wave-packets generated by resonant excitation of excitonic and free-carrier states of the Wannier-Stark (WS) ladder at the fundamental bandedge of the conduction band. Here, we present evidence for Bloch oscillations obtained by excitation of WS ladder states at photon energies as high as 70-80 meV above the fundamental bandgap. This surprising result is interpreted as evidence for carrier scattering processes that preserve the relative phase of the Wannier-Stark states forming the wave-packets. Our observation suggests that Esaki-Tsu emitters based on electrical injection of electron wave-packets into a superlattice may be realized.

THz emission for above-bandgap excitation has been observed for six GaAs/Al_{0.3}Ga_{0.7}As superlattices with calculated zero-field e1-miniband widths of 8-45 meV. The superlattices consist of 35 periods of nominally 13.6-nm- to 6.1-nm-thick GaAs well layers, and barrier layers with a thickness of 1.7 nm for all samples.

In the time-resolved measurements, the sample, held at a temperature of 10 K, is excited by 150-fs laser pulses from a Ti:sapphire laser. Wave-packet oscillations induced by the simultaneous excitation of several WS ladder states lead to the emission of submillimeter-wave radiation that is detected with an optically gated photo-

conductive dipole antenna.

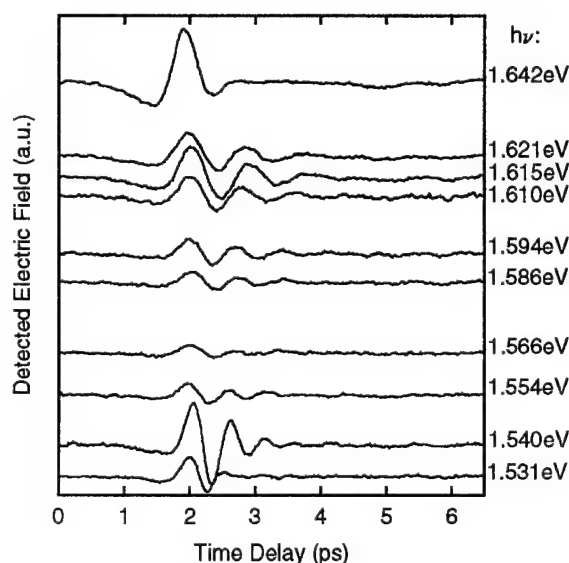


Fig. 1. THz transients at different photon energies of the excitation pulse. Bias: -1.5 V (Wannier-Stark regime); T = 10 K.

In Fig. 1, detected THz transients from a sample with an e1-miniband width of 13 meV are plotted for different photon energies of the optical excitation pulses. The sample is biased into the WS regime (voltage: -1.5 V). Time-delay zero is chosen arbitrarily. The photon energy is tuned from 1.531 eV just below the fundamental bandgap to 1.642 eV exciting into the second (e2) miniband (hh2-e2 transition: onset estimated to be at 1.624 eV; lh2-e2 transition: onset at 1.657 eV). For bandedge excitation, the signal consists of a single-cycle transient emitted during excitation of the superlattice. It is attributed to instantaneous polarization [4]. For excita-

tion at higher photon energies, an oscillatory transient is observed for all energies up to 1.642 eV. The amplitude of the oscillations peaks at about 1.540 eV, close to the strongest hh1-e1 exciton resonances at the fundamental bandgap. For higher energies, the oscillation amplitude first decreases but increases again to reach a second maximum at 1.61-1.62 eV, in the energy range of the excitonic hh2-e2 transitions. The oscillations are observed for photon energies as high as 80 meV above the bandgap. They disappear at 1.642 eV. The frequency of the oscillations changes slightly with the photon energy. This is a consequence of the fact that the internal electric field is not independent of the excitation conditions. Field screening leads to a reduction of the internal electric field - and hence of the oscillation frequency - e.g., when the density of the excited charge carriers rises as a result of an increase of the absorption coefficient at higher photon energies [2].

The oscillating THz radiation emitted after coherent excitation at photon energies of approx. 1.54 eV is known to result from Bloch oscillations of e1 wave packets [1-3]. A feature characteristic of Bloch oscillations is the bias-field tunability of the oscillation frequency. This is il-

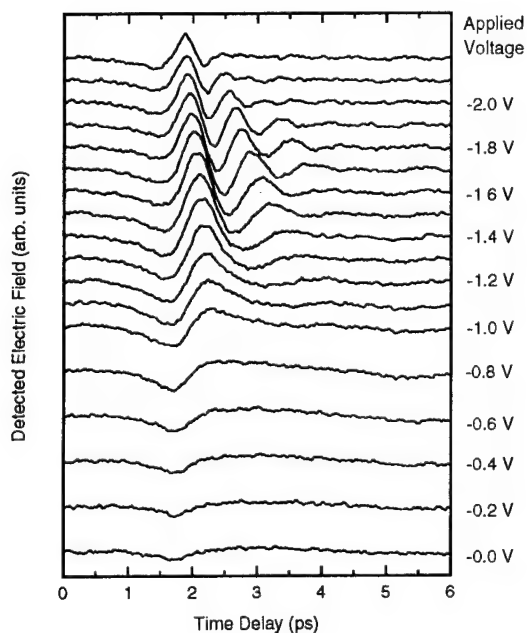


Fig. 2. Bias-voltage dependence of the detected electromagnetic signals at a photon energy of 1.540 eV of the excitation pulse.

lustrated in Fig. 2, where THz transients for excitation at 1.540 eV are shown for a series of bias voltages. Below a reverse bias of -1.0 V, the external voltage is screened by photogenerated charge carriers accumulating at the boundaries of the superlattice. The THz signal consists mainly of an instantaneous contribution. Bloch oscillations can only be excited for higher reverse bias when the internal field increases linearly with the bias voltage and WS resonances evolve from the e1 miniband. Above -1.0 V, Bloch oscillations are detected via an oscillatory THz signal with a frequency depending linearly on the bias voltage as expected for Bloch oscillations. Frequencies up to 3 THz are resolved in this measurement.

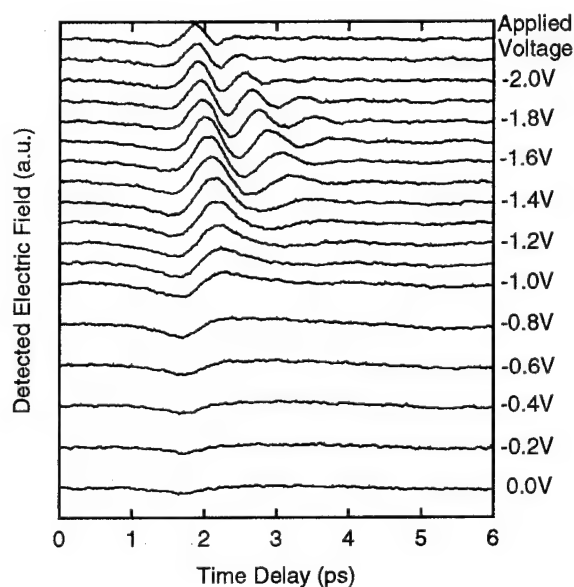


Fig. 3. Bias-voltage dependence of the detected electromagnetic signals at a photon energy of 1.615 eV of the excitation pulse.

To determine the origin of the oscillatory signal for excitation at higher photon energies, we trace the THz transients at 1.615 eV for different reverse bias voltages. There, transitions from the hh2 to the e2 miniband are excited, whereas the lh2-e2 transitions are not reached yet. Figure 3 shows detected THz transients for a series of bias voltages. At low reverse bias up to -1.2 V, when the external voltage is screened, only an instantaneous THz signal is resolved [4]. In the WS regime, above a reverse bias of -1.2 V, several cycles of a strong oscillation become visible. The frequency of the oscillations rises linearly with increasing field.

The results for a photon energy of 1.615 eV

bear a strong similarity to those at 1.540 eV. For that reason and specifically because of the linear bias-dependence of the oscillation frequency, we conclude that the oscillatory signals in the data of Fig. 3 originate from Bloch oscillations. At other photon energies, equivalent results are obtained allowing us to extend this conclusion to all oscillatory signals observed in Fig. 1.

It is emphasized that we have only established Bloch oscillations as the origin of the signal; for excitation well above the bandgap it is, however, not evident what states contribute to the formation of the Bloch wave packets responsible for the emission of electromagnetic radiation.

The most likely interpretation of the data [5] assumes excitation of states in the e and lh minibands above the bandedges and subsequent ultrafast scattering in k-space. The Bloch wavepacket emitting THz radiation is probably continuously reformed during scattering events (the final states of scattering processes are again WS ladder states) or formed by coherent WS states at the bandedges after scattering has taken place.

Based on four-wave-mixing data, it is generally assumed that a relaxation process destroys the phase of a quantum-mechanical system. In this picture, coherent phenomena like Bloch oscillations would be disrupted by the scattering process. Our data, however, indicate that scattering processes exist that preserve the relative phase (what we may call the *intraband* or quasi-static phase) of the excited WS states forming the Bloch wave-packets even though the *interband* (optical) phase, probed by four-wave-mixing, is lost.

The experiments provide a further hint of such an interpretation: The maximum resolved frequency of the Bloch oscillations is always lower for excitation high above the bandgap than for bandedge excitation. In Fig. 3, the maximum frequency is 1.7 THz, significantly smaller than the 3 THz resolved in the data for bandedge excitation of Fig. 2. This difference might result from an incomplete phase memory of the relaxation process. High-frequency signals are expected to be more strongly affected by a partial loss of phase information than low-frequency transients.

The role of different scattering processes is speculative at the moment. The data suggest conservation of the intraband phase during carrier-carrier scattering expected to rapidly redi-

tribute the carriers in k-space for all excitation energies. The data are less clear in disclosing the role of LO-phonon scattering, to be considered for excitation of states located at least one LO-phonon energy (36 meV) above the fundamental bandedges. The cut-off for Bloch oscillations at an excess photon energy of 70-80 meV seems to suggest that a single LO-phonon scattering event destroys the intraband phase. However, this conclusion is based on the assumption that the excess energy of 70-80 meV (approx. twice the LO-phonon energy) is distributed evenly between conduction and valence band. As this is not supported by the calculation for the relevant optical transitions, the role of LO-phonon scattering at present remains unclear.

We indicate a practical significance of our observation. A question of great interest is whether it is possible to obtain Bloch oscillations after *electrical* (not optical) injection of electron wave-packets into a superlattice. It is believed that scattering destroys the coherence so rapidly that electrical injection is of no avail. This assumption may well be incorrect (at least for low temperatures) as intraband phase information apparently survives during scattering.

It appears then feasible to realize optically or electrically driven Bloch oscillators based on coherent emission of electromagnetic radiation. We have recently analyzed theoretically the efficiency of emitters pumped with optical pulses [6]. An interesting feature of such emitters is the *superradiant* character of the emission resulting from the coherence of the optically excited dipoles. Superradiant emitters can be optimized in such a way that as many dipoles as possible contribute to cooperative emission into the same electromagnetic mode. It can be shown that it is theoretically possible to extract the energy available for emission (energy between the optically excited states forming the WS wave-packets) completely with a radiation pulse [6]. Furthermore, amplification of a THz wave by phase-correct feedback of the wave into a coherently prepared material is viable, e.g. with the help of an external cavity.

REFERENCES

- [1] Roskos, in "Festkörperprobleme/Advances in Solid State Physics" **34**, Vieweg Verlag (1994) p. 297.
- [2] Leisching et al., Phys. Rev. **B50** (1994), in press.
- [3] Dekorsy et al. Phys. Rev. **B50**, 8106 (1994).
- [4] Chuang et al., Phys. Rev. Lett. **68**, 102 (1992).
- [5] Roskos et al., Superlat. & Microstruc., in press.
- [6] Victor et al., J. Opt. Soc. Am. **B11** (1994), Dec. issue

Terahertz Spectroscopy of a Mesoscopic Tunnel Barrier

C. Karadi, S. Jauhar, L. P. Kouwenhoven, K. Wald, J. Orenstein, P. L. McEuen, Y. Nagamune, J. Motohisa, and H. Sakaki

Department of Physics, University of California, Berkeley and Materials Science Division, Lawrence Berkeley Laboratory, M/S 2-300, Berkeley, CA. 94720

Tel: (510) 486-5879

FAX: (510) 486-5996

Recently, considerable theoretical and experimental effort has been directed towards understanding the frequency-dependent response functions of mesoscopic structures. This work bears directly on controversial issues such as the tunneling time through a barrier [1], and the complex admittance of mesoscopic systems [2]. At terahertz frequencies the admittance is predicted to crossover to a frequency-dependent regime.

Although direct measurements of the terahertz admittance are extremely difficult, measurements of the change in *dc* current due to terahertz excitation are relatively straightforward. Such measurements can also reveal the predicted crossover. Above the crossover frequency the induced current (photocurrent) is predicted to be *frequency-dependent*, with high frequencies producing a greater photocurrent than low frequencies. This regime is conventionally termed "photon-assisted transport (PAT)".

In this paper, we report the first measurements of the photocurrent ΔI_{dc} as a continuous function of frequency ν in a 2DEG tunnel barrier. The spectra were measured as a function of both barrier height and perpendicular magnetic field. The results provide strong evidence that the time-averaged current is due to PAT.

A description of the device [3] and measurement setup can be found in [4,5]. Briefly, the device consists of a 460 nm wide channel etched in a 2DEG with mobility 800,000 cm²/V-s and density 1.6×10^{11} cm⁻² at 4.2 K, at a AlGaAs/GaAs heterojunction. The channel widens into millimeter-sized regions of 2DEG to which standard ohmic contacts are made. Application of a negative voltage, V_g , to a metallic gate of width 230 nm across the narrow section of the channel creates a barrier of adjustable height, E_0 (see Figure 3). In the measurements reported here, a *dc* bias of 100 μ V was applied between source and drain. The sample was immersed in ³He at 500 mK in the center of a split coil superconducting magnet.

To measure the frequency dependence of ΔI_{dc} we use a pulsed rather than *cw* source and a novel method for coupling radiation to the tunnel barrier [5]. Nearly single-cycle electric-field pulses of 5 ps duration are generated by femtosecond laser excitation of antenna-coupled Auston switches external to the cryostat. The pulses are coupled quasi-optimally from free space to the sample assembly placed in the bore of the magnet. The sample assembly consists of a receiver chip and a chip which contains the tunnel barrier. A 600 μ m dipole antenna on the receiver couples the pulse to an impedance matched coplanar transmission line 5mm in length. The transmission line is connected *via* wire bonds to the gate electrode and one of the 2DEG contacts.

To determine $\Delta I_{dc}(\nu)$ we first measure the current, $\Delta I_{dc}(\tau)$, generated by a pair of pulses as a function of the time delay, τ , between them. $\Delta I_{dc}(\nu)$ is then simply obtained from the Fourier transform of $\Delta I_{dc}(\tau)$.

We discuss first the dependence of the spectra on B . Figure 1a shows the real part of $\Delta I_{dc}(\nu)$ at several magnetic fields, measured at the value of V_g which gives the maximum response (point O in inset of Figure 2a). The spectrum with $B=0$, shown in the lowest curve in of Fig. 1a, has two main features: a peak at ≈ 25 GHz and a broadband response from ≈ 100 -200 GHz whose shape is largely determined by the spectral density of the excitation pulse. These two features differ dramatically in their dependence on B , as the spectra indicate. At a relatively small field, 0.25 T, the 25 GHz peak disappears, and a peak with reversed sign appears at 100 GHz. With increasing B the negative-going peak continues to shift to higher frequency while the broad component of the spectrum remains relatively unchanged for fields up to 1 T.

The dependence of the sharp peak on B is indicative of a magnetoplasmon excitation of the 2DEG. The lower panel of Fig. 1 is a plot of the peak frequency *vs.* B , including both the positive peak at $B=0$ and the negative peak at nonzero field. The solid line is the upper branch of the magnetoplasmon spectrum expected for the GaAs 2DEG. It has been demonstrated experimentally that the higher magnetoplasmon mode is well described by $\nu_+^2(B) = \nu_p^2 + \nu_c^2$, where ν_p and ν_c are the 2D plasma and cyclotron frequency, respectively [15]. The fit was obtained with $\nu_p = 25$ GHz, which corresponds to a confinement length of 0.8 μ m, using the measured 2DEG density and a GaAs band mass of 0.07 m_e . The confinement length scale suggests that the plasmon is an excitation of the mm scale 2DEG "leads" to the quasi-1D wire.

The behavior of the spectra as a function of B suggests that heating due to magnetoplasmon absorption by the 2DEG cannot explain the broadband component of the induced current. If this were the mechanism then we expect $\Delta I_{dc}(\nu)$ to peak only near frequencies at which the 2DEG absorbs energy from the electromagnetic field. Instead, the magnetoplasmon appears only as a perturbation of the field-insensitive continuum.

Next, we consider the dependence of $\Delta I_{dc}(\nu)$ on barrier height E_0 , depicted in Figures 2a and 2b. The main part of panels (a) and (b) compare spectra recorded at the operating points labeled in the inset of Fig. 2a by primed and unprimed letters, respectively. Both panels include the spectrum at the point "O" where $E_0 \approx E_f$ and the magnitude of the induced current is greatest. For $E_0 < E_f$ (Fig. 2b) the low-frequency response is strongly suppressed with increasing $|E_0 - E_f|$. For example, at 100 GHz the magnitude changes by a factor of five over the full range of V_g , while the response at 200 GHz changes by a factor of two. The suppression of low-frequency response is emphasized in the inset of Fig. 2b, in which the curves are normalized to the spectrum recorded at point "O." For $E_0 > E_f$ (Fig. 2a) the change in response is qualitatively similar, but the magnitude of the effect is much weaker. For example, at 125 GHz the magnitude drops by 32% as the response at 200 GHz changes by 25%.

In addition to the data described above, we have recorded spectra at $B=1$ T where the magnetoplasmon absorption of the 2DEG is well above the spectral range of the pulse. The behavior in Figs. 2a and 2b is observed at this high field as well; suppression of the low-frequency response as E_0 is varied away from E_f , and a much stronger effect when $E_0 < E_f$.

The observation of a frequency dependent photoresponse, which depends on barrier height, is strong evidence that the terahertz radiation couples directly to the barrier region. In addition, the suppression of the low frequency response for $E_0 > E_f$ is consistent with an intuitive picture of PAT: a high frequency photon can provide an electron with enough energy to surmount a potential barrier while a low frequency photon cannot. It may appear surprising, however, that suppression of low frequencies is observed for $E_0 < E_f$ as well. Understanding this behavior requires a more realistic model of photon-assisted transport. The dashed curves in Fig. 2 are a simple fit to a model for photon-assisted transport [6].

Figure 3 shows a sketch which helps to illustrate the frequency dependence expected for PAT in a degenerate Fermi system. In the presence of an harmonically varying potential, V_v , an electron incident from the left-hand side will undergo inelastic in addition to elastic scattering. To first order in V_v the inelastic processes are transmission with the absorption or emission of a single photon. As Fig. 3a illustrates, when $E_0 > E_f$ overcoming the barrier requires that $h\nu \geq E_0 - E_f$. For $E_0 < E_f$ (Fig. 3b), $h\nu \geq E_f - E_0$ is required in order to reach unoccupied states above the Fermi level. Therefore spectra for E_f above and below the barrier are expected to show a threshold when $h\nu \approx |E_f - E_0|$.

Finally, we consider other mechanisms for the observed photocurrent: differential heating due to absorption in the ohmic contacts or wire bonds and classical rectification. Both appear to be ruled out immediately because the photocurrent spectra are sensitive to the properties of the device, i.e., they depend on gate voltage. However, it may be argued that the spectral shifts reflect a V_g dependence of the spectral density of terahertz radiation coupled to the device rather than PAT. To explain the observed behavior, low-frequency radiation would have to couple poorly to the device for $E_0 > E_f$, go through a maximum when $E_0 \approx E_f$, and decrease again for $E_0 < E_f$. The coincidence of maximum coupling at $E_0 \approx E_f$, particularly when the device impedance is varying monotonically, seems unlikely. As a result, we believe that PAT provides the most reasonable description of the data.

In conclusion, this experimental study has demonstrated that PAT provides a consistent explanation for dc current induced across a tunnel barrier by terahertz radiation.

We wish to thank Jeff Beeman for technical assistance. This work was supported by the U.S. Department of Energy Contract No. DE-AC03-76SF00098, the Packard Foundation, the Sloan foundation (P.L.M.), and the Royal Netherlands Academy of Arts and Sciences (L.P.K.).

References

- [1] M. Buttiker and R. Landauer, *Phys. Rev. Lett.* **49**, 1739 (1982);
- [2] Y. Fu and S.C. Dudley, *Phys. Rev. Lett.* **70**, 65 (1993); M. Buttiker *et. al* *Phys. Rev. Lett.* **70**, 4114 (1993); H.C. Liu, *Phys. Rev. B* **43**, 12538 (1991).
- [3] Y. Nagamune *et. al.*, *Appl. Phys. Lett.* **64**, 2379 (1994).
- [4] S. Verghese *et al.*, *Appl. Phys. Lett.* **64**, 915 (1994).
- [5] C. Karadi *et al.*, to be published in *JOSA B*, Dec. 1994.
- [6] C. Karadi *et al.*, to be published.

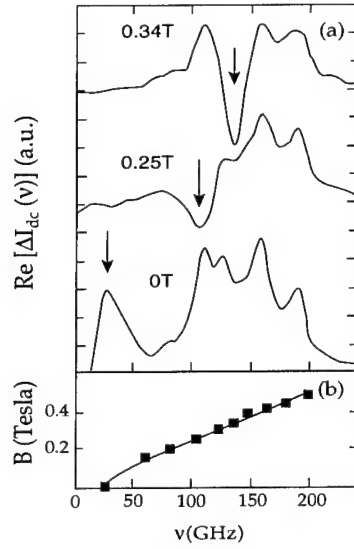


Figure 1: (a) $\text{Re}[\Delta I_{dc}(\nu)]$ at typical magnetic fields. (b) Plot of low frequency resonance at 25 GHz vs. magnetic field (boxes). Solid line is a fit to the magnetoplasmon dispersion relation.

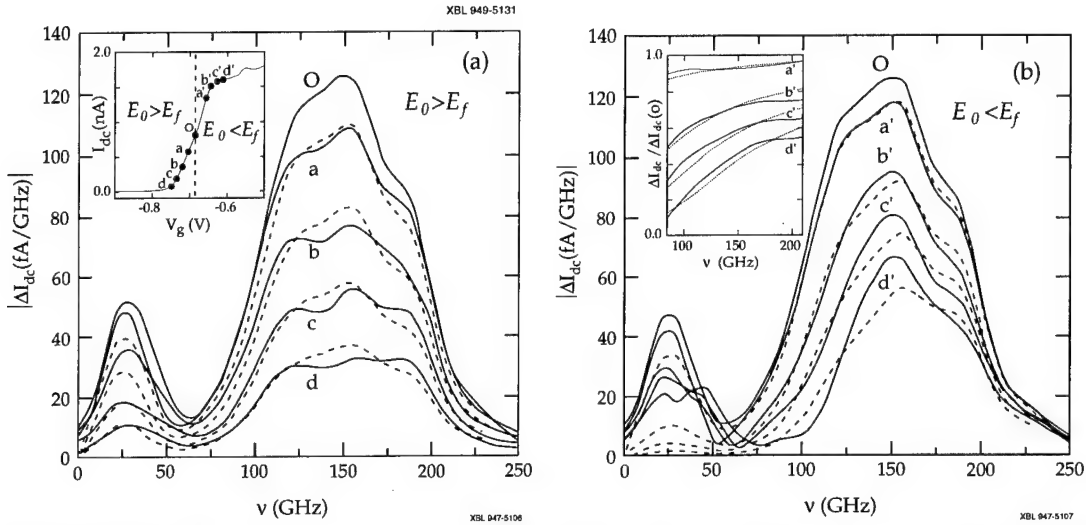


Figure 2: $|\Delta I_{dc}(\nu)|$ at different gate voltages indicated in the inset. The solid curves correspond to measured data. The dashed lines are a fit to a photon assisted transport model. (a) $|\Delta I_{dc}(\nu)|$ for $E_0 > E_f$. (inset) The dc current flowing through the tunnel barrier vs. gate voltage in the absence of pulsed excitation. (b) $|\Delta I_{dc}(\nu)|$ for $E_0 < E_f$. (inset) Ratios of $|\Delta I_{dc}(\nu)|$ relative to spectra "O". The spectra were further apodized to mitigate the effects of standing waves in the ratios.

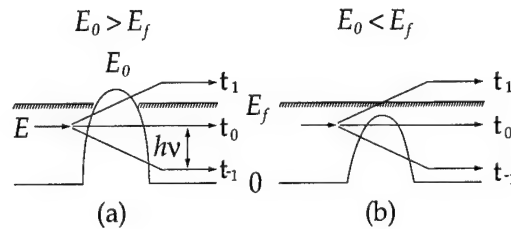


Figure 3: (a) Tunnel barrier with barrier height, E_0 , greater than the Fermi Energy, E_f . An electron incident at energy, E , is scattered by a harmonically varying potential at frequency ν into three channels characterized by amplitudes t_0 and $t_{\pm 1}$. (b) Similar to (a) but with $E_0 < E_f$.

Micromachined Three-Dimensional Photonic Band Gap Crystals

E. Özbay^{1,2}, and G. Tuttle¹

1. *Microelectronics Research Center and DOE Ames Laboratory, Iowa State University, Ames, IA 50011
(515)-294-1814, (515)-294-9584 (fax)*

2. *Department of Physics, Bilkent University, Bilkent, Ankara 06533, TURKEY
011-90-312-266-4380, 011-90-312-266-4579(fax)*

In analogy to electrons in a crystal, the propagation of electromagnetic (EM) waves in a three-dimensional dielectric structure can be forbidden for a certain range of frequencies. These three-dimensional structures that are called photonic band gap crystals, have recently received both theoretical and experimental attention[1-3]. The early research in the field has concentrated on possible optical frequency range applications that take advantage of reduced spontaneous emission, such as thresholdless semiconductor lasers and single-mode light-emitting diodes. The proposed applications were later extended to the millimeter and sub-millimeter wave regime, like efficient antennas, sources, waveguides and other components that take advantage of the unique properties of photonic bandgap materials[4]. But, the difficulties associated with the fabrication of smaller scale structures along with the unfeasible three-dimensional structure designs, have restricted the experimental demonstration of the basic photonic band gap crystals to microwave frequencies (12-15 GHz).

We have recently designed a new three-dimensional structure that may alleviate some of the problems associated with earlier photonic band gap designs[5]. The new structure, shown in Fig. 1, is constructed of layers of dielectric rods. The stacking sequence repeats every four layers, corresponding to a single unit cell in the stacking direction. In order to build a 500 GHz crystal, we have used silicon micromachining techniques[6-8]. Fabrication consisted of defining stripes that were parallel to (111) planes and subsequently etching the wafers in an KOH etch solution.

The testing of the crystal was performed by using a terahertz free-space spectroscopy setup. The dynamic range of the system was around 30 dB for frequencies up to 550 GHz. The crystal consisted of 16 stacked silicon wafers (corresponding to 4 unit cells) for transmission measurements. The characteristics along the stacking direction were obtained by placing the structure on the beam path, so that the transient radiation propagated in a plane perpendicular to the top surface of the structure. Figure 3 shows the transmission characteristics of the propagation along the stacking direction. The lower edge of the photonic gap is at 370 GHz, while the upper edge is at 520 GHz. This is very close to the calculated bandgap edges of 378 GHz and 518 GHz. The average measured attenuation within the bandgap was around 30 dB which was limited by the dynamic range of the experimental setup. Our calculations for the bandgap frequencies predicted the attenuation to be as low as 65 dB. We are currently working to improve this frequency performance by building a 2 THz crystal.

Although silicon micromachining has been very successful to build three-dimensional photonic crystals, the relatively low resistivity of silicon can be a problem for certain applications. Alumina with a typical resistivity six orders of magnitude larger than the resistivity of silicon would be a good dielectric material to build photonic crystals. In order to build alumina based millimeter wave photonic crystals, we have patterned the wafers by means of laser machining.

The square-shaped alumina wafers (Kyocera 96% alumina: resistivity $> 10^{10} \Omega\text{-cm}$) used in this work were each 2.54 cm x 2.54 cm, and 380 μm thick. The pattern consists of 24 parallel stripes, each 460 μm wide and separated by 840 μm wide gaps. These stripe dimensions and the wafer thickness determine the center of the forbidden photonic gap—calculated to be 95 GHz in this case. The stripes are 3.1 cm long so that the 24 stripes form a square 3.1 cm x 3.1 cm pattern. The stripes are cut by means of laser machining the alumina crystals, where a high power carbon

dioxide laser cuts the separation gaps between the stripes. The laser machining was performed by a commercial vendor (Accumet Engineering, Hudson, MA).

Once the wafers were laser machined, we have stacked them to build a photonic crystal. The crystal is then tested with a W-band transmission measurement set up[6]. Figure 3 shows the transmission characteristics obtained, when the EM waves are incident at the front surface of the crystal with an incidence angle of 45 degrees. For such a propagation direction, the band gap falls within the measurement limits of the experimental set up. The valence band edge occurs at 92 GHz, while the conduction band edge is at 108 GHz. The transmission characteristics of the structure along these directions and for other directions and angles, are all in good agreement with our theoretical calculations which predicted a full band gap from 92 GHz to 105 GHz.

Besides testing the transmission properties of the new crystal, we have also fabricated defect structures by means of removing material from the crystal. Figure 4 shows the transmission characteristics of a defect structure. The defect is built by removing a portion of one of the alumina stripes. The defect occurs at a frequency of 98 GHz, and has a peak amplitude 26 dB below the incident signal level. To our knowledge this is the first demonstration of a three-dimensional photonic band gap defect structure at millimeter wave length regime. The availability of such defect structures at this wavelength scale will be useful for a number of millimeter wave applications including filters, resonators and sources.

References

1. K. M. Ho, C. T. Chan, and C. M. Soukoulis, Phys. Rev. Lett. **65**, 3152 (1990).
2. E. Yablonovitch, T. J. Gmitter, and K. M. Leung, Phys. Rev. Lett. **67**, 2295 (1991).
3. For a recent review, see the articles in *Photonic Bandgaps and Localization*, C. M. Soukoulis, Ed. (Plenum, New York, 1993).
4. See the articles in the J. Opt. Soc. Am. B 10 (1993), a special feature edited by C.M. Bowden, J.P. Dowling, and H.O. Everitt.
5. K. M. Ho, C. T. Chan, C. M. Soukoulis, R. Biswas, and M. Sigalas, Solid State Comm. **89**, 413 (1994).
6. E. Ozbay, E. Michel, G. Tuttle, M. Sigalas, R. Biswas, and K. M. Ho, Appl. Phys. Lett. **64**, 2059 (1994).
7. E. Ozbay, E. Michel, G. Tuttle, R. Biswas, K. M. Ho, J. Bostak, and D. M. Bloom, Optics Lett. **19**, 1155 (1994).
8. E. Ozbay, G. Tuttle, M. Sigalas, R. Biswas, K. M. Ho, J. Bostak, and D. M. Bloom, Appl. Phys. Lett. **65**, 1617 (1994).

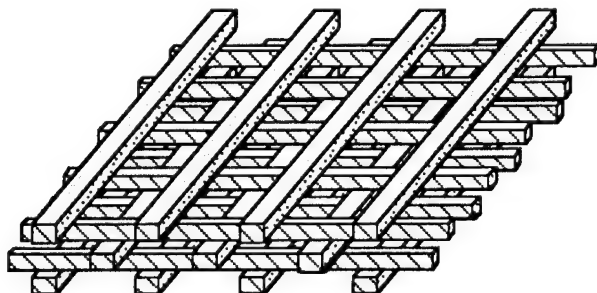


Figure 1. This figure schematically illustrates the design of the three-dimensional photonic bandgap crystal. The structure is built by an orderly stacking of dielectric rods and repeats every four layers in the stacking direction.

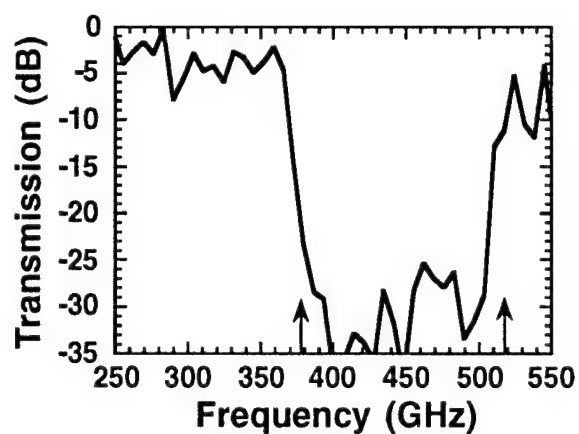


Figure 2. EM wave transmission through the micromachined crystal in which the wavevector of the incident radiation is normal to the wafer surfaces. The arrows indicate calculated band edge frequencies.

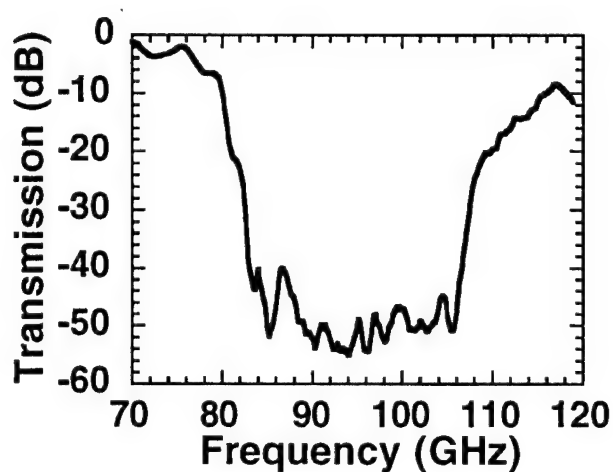


Figure 3. Transmission characteristics of laser micromachined alumina based photonic crystal.

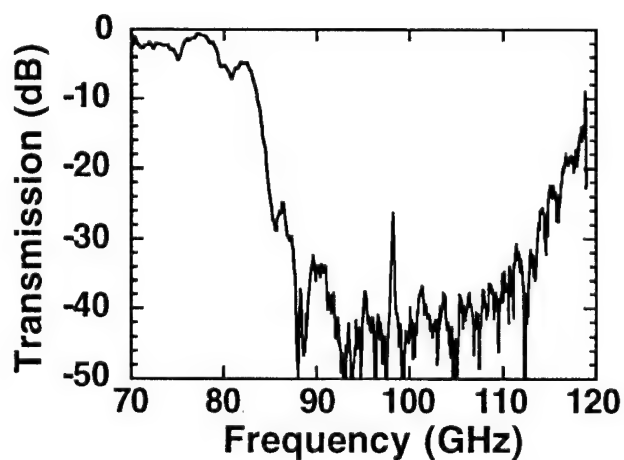


Figure 4. A defect structure appears at 98 GHz, when a portion of the alumina stripe is removed from the crystal.

Measurement and Analysis of THz Radiation from Bulk Semiconductors

L. Ming, G.A. Wagoner, M. Alexander^{a)}, and X.-C. Zhang

Physics Department
Rensselaer Polytechnic Institute
Troy, NY 12180-3590 USA
Tel: (518) 276-3079
Fax: (518) 276-6680
Email: zhangx2@rpi.edu

When illuminated by femtosecond laser pulses, where the photon energy lies above the optical absorption bandedge, GaAs emits pulsed submillimeter-wave (THz) radiation via ultrafast photocarrier transport. The radiation emitted from the semiconductor surface has both forward (transmitted direction) and backward (pseudoreflected direction) components. This radiation has been used to coherently probe the ultrafast electronic properties of the semiconductor. However due to technical difficulties associated with THz beam measurements, there are still many unanswered questions. For example, a detailed comparison and analysis of amplitude and phase of the forward and backward THz radiation has not reported. In this talk, we present recent measurements and analysis of the amplitude and phase of both forward and backward THz radiation via ultrafast photocarrier transport. Based on these results we are able to qualitatively and quantitatively explain anomalous THz emission from metal/semiconductor interfaces. All these interesting results which have not been reported before will improve our understanding of THz emission from semiconductors.

A summary of our recent measurements indicates that:

- [1] For the component of the optically induced electromagnetic transient perpendicular to the semiconductor surface, the amplitude of backward component is greater than forward component. For example, from an unbiased GaAs wafer at a 45° angle of incidence, the field strength of the backward signal (in air) is

^{a)} Rome Laboratory, Hanscom Air Force Base, MA 01781

approximately 40% stronger than that of the forward signal (in air). However the component of the electromagnetic transient parallel to the surface, such as that produced in a biased semiconductor at normal optical incidence, the backward field strength is about 33% weaker than the forward field. These measurements are consistent with the predictions of our model of ultrafast photocarrier transport, which is based, in part, on the method of images, as used in classical electrodynamics.

[2] The forward and backward THz radiation have opposite polarity if the transient photocarriers move perpendicular to the semiconductor surface, as in the presence of a surface depletion field, and the same polarity if the photocurrent propagates parallel to the semiconductor surface, as in the presence of a planar bias field. The direction and polarity of the backward, forward, and first reflected THz signals are consistent with the dipole radiation model.

[3] Due to the polarity flip between the forward and backward THz fields, generated via the static surface depletion field, by adding an optically transparent conducting plate (ITO film) on the top of the semiconductor surface, we can redirect (reflect) the backward THz field into the forward direction, thereby enhancing the total forward propagating signal. Since the backward field undergoes a phase reversal after it reflects from metal film, it propagates in phase and constructively interferes with forward field, increasing the total forward field. Our preliminary measurements have indicated an increase in the forward signal exceeding over 81%.

[4] In a previous publication (Appl. Phys. Lett., **65**, 682, 1994), the anomalous behavior of THz beams emitted from metal/GaAs interfaces was reported. Therein, we observed that at normal incidence, the THz signal decreased with increasing metal film thickness, which we attributed to both an increase in reflectivity and absorption in the thicker films. However, at oblique incidence, THz emission increased with increasing metal thickness until reaching a maximum when the film was approximately 80 Å thick. Now this observation can be explained by considering a partial reflection of the backward THz field into the forward direction by the ultrathin conducting film on the GaAs. The reflected backward signal then

adds or subtracts to the initial forward signal depending on the direction of the optically induced electrical transient.

[5] Since the backward radiation is stronger than the forward radiation. Figure 1 plots a THz waveform from an unbiased GaAs wafer. The signal to noise ratio is better than 250 with a lock-in time constant of 300 microseconds (not milliseconds)! We used a Coherent MIRA laser and 100 μm photoconducting antenna detector. The backward signal can be directly measured by connecting the photoconducting antenna to an oscilloscope. Our measurements indicate an average peak signal exceeding 7 mV, which corresponds to a low limit of 7 V radiated from an unbiased wafer. Further we expect an over 10 V radiation field can be achieved by coherently combining both forward and backward signals with the use of an ITO plate on the front surface of unbiased wafer.

In summary, we report our recent measurements and analysis of both the amplitude and phase of forward and backward propagating THz radiation from bulk semiconductor, via ultrafast photocarrier transport. We also present the detailed measurement of backward THz signal from an unbiased wafer versus polar angle.

Tuesday, March 14, 1995

Poster Session

UTuE 5:30 pm-6:30 pm
Ballrooms IV-V

Electro-Optic Probes: High-Permittivity Crystals vs. Low-Permittivity Polymers

H.-J. Cheng and J.F. Whitaker, Center for Ultrafast Optical Science, University of Michigan, 2200 Bonisteel Blvd., Rm. 1006, Ann Arbor, MI 48109-2099; Tel.: 313-763-4875

K.J. Herrick, N. Dib, and L.P.B. Katehi, Radiation Laboratory, Dept. of Electrical Eng. and Computer Science, University of Michigan, Ann Arbor, MI 48109-2122; Tel.: 313-747-1796

J.-L. Coutaz, LAHC, Universite de Savoie, Campus Scientifique, 73 376 Le Bourget du Lac Cedex, France; Tel.: 33 79 75 87 50

Despite the success of external electro-optic (EO) probing in measuring ultrafast time-domain signals with an extremely large bandwidth [1], issues involving the invasiveness of the probe, the repeatability of the measured results, the ability to measure low-frequencies, and the calibration of voltage signals have served to impede the impact of EO sampling on high-speed-device and circuit testing. The main problem associated with the external probe is the high permittivity of the EO material used (*e.g.*, lithium tantalate has a relative permittivity which is as high as 44). This probe not only creates an impedance mismatch and reflections, but it also renders the measurement results somewhat unreliable by preferentially excluding electric fields of certain frequencies depending on the height of the probe, h , with respect to the circuit under test.

This paper presents two novel solutions to the problems associated with situating an EO probe in a fringing field while still maintaining the positioning flexibility of the external probe: the use of stable, electro-optic, polymer-film probes with relative permittivities of approximately 3 [2]; and the correction of the frequency dependence of the probe by application of its inverse transfer function to the Fourier transform of the measured data. Furthermore, we demonstrate for the first time the frequency-dependent behavior (from dc to the terahertz regime) of the electric field interaction between either a high- or low-permittivity EO probe and a coplanar transmission-line circuit using a finite-difference, time-domain (FDTD) computational analysis. The simulations substantiate the dramatic benefit afforded by the use of the polymer probe.

The problems encountered with LiTaO₃ probes can be virtually eliminated by changing the crystal to a low-permittivity, electro-optic polymer. While this scheme has been considered previously for measurements on circuits coated with an EO polymer [3], this investigation employs a polymer-probe tip that can be freely positioned. Figure 1 shows an FDTD analysis of picosecond-duration waveforms measured by both a LiTaO₃ crystal and a probe fabricated from a polymer of 10- μ m thickness and $\epsilon_r = 3$. Both probes produce virtually the same waveform when $h = 0$, but when they are raised above the lines by 50 μ m, the LiTaO₃ probe gives a distinct negative component, while the waveforms from the polymer probe are qualitatively nearly identical. Simulations for the LiTaO₃ probe indicate that the negative 'tail' appears due to the concentration of electric field, and especially low-frequency signal components, between the high-permittivity material and the circuit under test. The electric field is essentially avoiding the high-permittivity material when another path is available. In contrast, there is no loss in low-frequency components for the low-permittivity probe. This result is significant because of the previous perception that bipolar time-domain signals implied the coupling of radiation into LiTaO₃ probes. Simulations of the dynamic electric-field patterns have been compiled in a movie to demonstrate how the electric field is concentrated below the surface of a dielectric probe, to the point of extending significantly up the side of a LiTaO₃ crystal elevated even a small distance above a transmission line.

One concern regarding an EO-polymer probe is sensitivity. Since the EO modulation depth is determined by $m \propto n^3 r_{ij}$, where n is the index of refraction, and r is the electro-optic coefficient, sensitivity will be lower for typical polymers which have r_{ij} and n values smaller than those of EO crystals. However, for the high-permittivity probe to have the same low invasiveness as that of the low-permittivity one, it has to be elevated, sacrificing sensitivity. Therefore, if both

types of probes are applied in a low-invasive configuration, their sensitivities are approximately the same. However, one avoids the elevation-dependent frequency response of the LiTaO₃ probe by employing the polymer. In addition, for some EO polymers, when the probing wavelength is decreased to be closer to the absorption peak, the induced nonlinearity leads to an enhanced EO coefficient without excessive absorption. The r can be as high as 100 (which is three times higher than that of the LiTaO₃) while the absorption is low enough to make high-speed measurements. With the advancement of short-pulse laser sources in the 400 - 450 nm region (either by optical upconversion or frequency doubling), the low permittivity probe has the potential to out-perform its LiTaO₃ counterpart from every perspective. In addition, the reflection from the low-permittivity probe is less than 5% even when in contact with a circuit, which is very good in comparison with a 30% reflection for the high-permittivity probe [4].

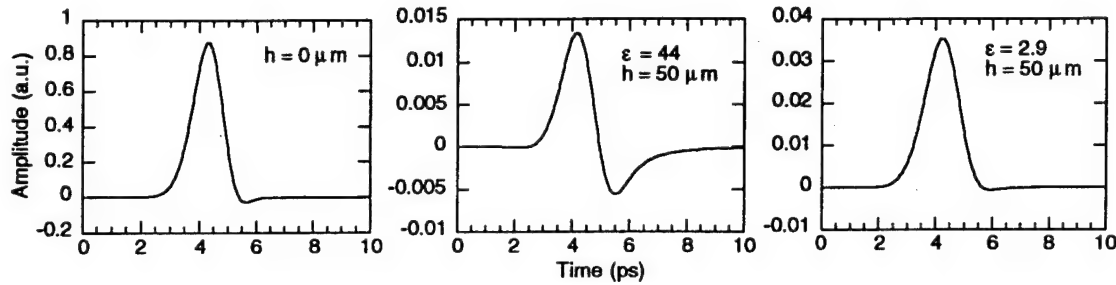


Figure 1. Time-domain waveforms measured by electro-optic probes as simulated using finite-difference, time-domain computations: (left) arbitrary probe in contact with circuit under test; (middle) LiTaO₃ probe elevated above the circuit by 50 μm ; (right) polymer probe elevated above the circuit by 50 μm .

Polymers with relatively high electro-optic coefficients that are also stable in air are now being synthesized [2]. When problems in our facilities with poling the materials (*e.g.*, application of an electric field of 100 V/ μm at nearly 100°C) are solved, we believe that it will be possible to fashion these materials into small probes to demonstrate their functionality for electro-optic sampling.

Although a high-permittivity LiTaO₃ probe will always be more invasive or have a greater frequency dependence than a low-permittivity probe, there is one method that can be used to obtain a more faithful version of a waveform measured with this probe. This involves the use of the inverse transfer function from the LiTaO₃ probe response to correct for distorted transients measured when $h > 0$. A semi-empirical analysis similar to that used for planar transmission lines [5], where the effective permittivity increases with frequency due to the frequency-dependent hybrid-mode behavior, is used to arrive at a system response for the probe

$$H(f) = \frac{\sqrt{\epsilon_q} + [(\sqrt{\epsilon_r} - \sqrt{\epsilon_q}) / (1 + a(f_e/f)^b)]}{\sqrt{\epsilon_r}}$$

where ϵ_r is probe permittivity, ϵ_q is the low-frequency effective permittivity (which can be determined in practice by solving the 2-D Poisson's equation), f_e is a transition frequency, f is frequency, and a and b are geometry-dependent terms. As a demonstration of the utility of the inverse transfer function, the negative component in an experimental waveform measured by a LiTaO₃ probe raised 5 μm above a coplanar stripline (Fig. 2) – which results from low-frequency field expulsion – has been removed by simply dividing the spectrum of the waveform by the system response function. Figure 3 shows the waveform measured by the LiTaO₃ probe at $h = 0$, along with the waveform from Fig. 2 after application of the inverse transfer function. The waveforms are virtually identical, except for the small positive tail that was measured with the LiTaO₃ probe contacting the circuit. This may indicate that the probe system response is not completely accurate for the low-frequency electric fields, but it still allows for a dramatic improvement of a measured signal by a high-permittivity probe that is elevated above a circuit in

order to decrease invasiveness.

Very significant benefits realized by the use of an external electro-optic probe of low permittivity have been demonstrated through a detailed full-wave analysis. Experiments and simulations for LiTaO_3 high-permittivity probes have also helped to prove that the field concentrates between the probe and the circuit under test, and it does so with a frequency dependence that leads to measured signals that exhibit negative tails. It is possible to correct high-permittivity probe effects through the application of an inverse transfer function, although not with the accuracy afforded by using a polymer probe.

REFERENCES

- [1] J.A. Valdmanis, *Electron. Lett.* **23**, 1308 (1987).
- [2] *Molecular Nonlinear Optics*, J. Zyss ed., Academic Press, New York 1994.
- [3] P.M. Ferm, et al., *Appl. Phys. Lett.* **59**, 2651 (1991).
- [4] D. Conn, et al., 1992 *IEEE MTT-S International Microwave Symposium Digest*, 665.
- [5] G. Hasnain, A. Dienes, J.R. Whinnery, *IEEE Trans. Microwave Theory Tech.* **34**, 738 (1986).

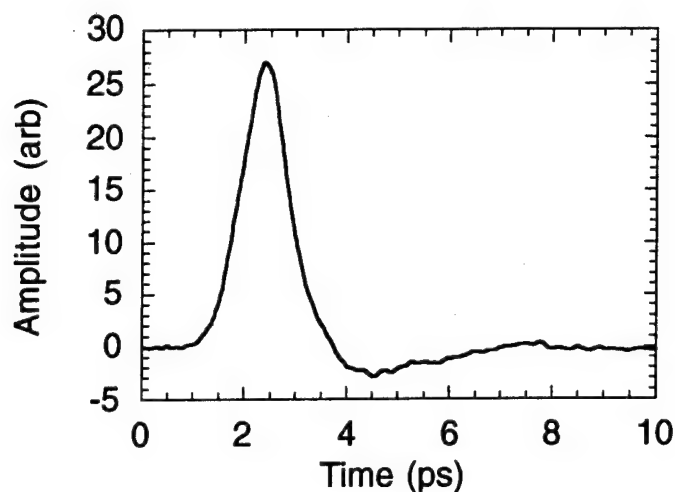


Figure 2. Short pulse measured by high-permittivity LiTaO_3 probe elevated $5\ \mu\text{m}$ above circuit.

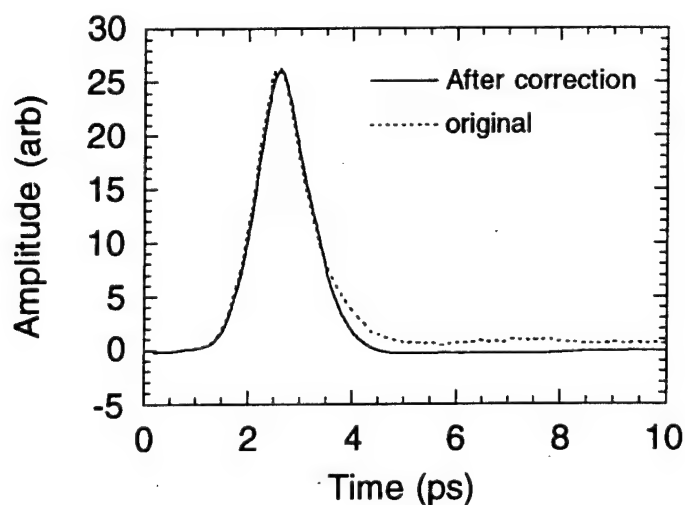


Figure 3. Short pulse measured by LiTaO_3 probe in contact with circuit (original), along with waveform from Fig. 2 modified by probe inverse transfer function (after correction).

Picosecond Pulse Generation by Edge Illumination of Si and InP Photoconductive Switches

Marc Currie, Chia-Chi Wang, Roman Sobolewski, and Thomas Y. Hsiang

LABORATORY FOR LASER ENERGETICS
and DEPARTMENT OF ELECTRICAL ENGINEERING

University of Rochester
250 East River Road
Rochester, NY 14623-1299

Phone: (716) 275-4709

Fax: (716) 273-1014

Ultrafast electrical pulses are beginning to be used for performing broadband frequency domain characterization of circuits^{1,2} and for test and failure analysis of digital circuits.³ With frequency components in the terahertz regime, these pulses have been used for the characterization of transmission lines for high-speed interconnections on integrated circuits,¹ and for measuring microwave S-parameters.² Generation of ultrafast electrical pulses has been developed using pulsed lasers on semiconductors.⁴⁻⁶ Some of these techniques require special materials or geometries, which makes it difficult to use these methods as an analysis tool as in Ref. 2. However, edge illumination requires no special designs other than a coplanar transmission line.

Subpicosecond electrical pulse generation by edge illumination occurs by illuminating, with a laser pulse, a small area of a semiconductor between an electrically biased transmission line. This phenomenon has been well studied on GaAs substrates.^{6,7} The experiments of Alexandrou *et al.*⁷ thoroughly characterized the mechanism of edge illumination on GaAs and provided motivation for further studies by strongly supporting the material-independent theory of Sano and Shibata.⁸ To further reinforce this theory, the effect of edge illumination must be shown on semiconductors other than GaAs.

We report on our experimental studies of edge illumination of coplanar transmission lines on Si and InP. Our experiments add further evidence that the ultrafast electrical pulses produced by edge illumination are a result of an electromagnetic field disturbance. By applying the method of edge illumination to Si, we demonstrate a mechanism for generating the fastest electrical pulses on Si to date.

A Ti:sapphire laser (with ~140-s pulses) was used in conjunction with our electro-optic sampling system⁹ to excite and measure the ultrafast phenomena. Figure 1 shows the experimental setup of our coplanar transmission lines, excitation area, and sampling points. A coplanar transmission line on an InP substrate is excited with 720-nm light and generates the subpicosecond pulses with full-width at half-maximum (FWHM) of 550 fs shown in Fig. 2. Of particular interest is the difference in the shoulders following the pulses. Probing ~100 μm from the excitation, we can observe the local field by studying the pulse shoulders. Sampling the electric field on the same side as the excitation (point A) results in the observation of a positive shoulder, while testing on the opposite side (point C) we observe a negative shoulder. Finally, by sampling near the center (point B, or more precisely in the gap at the edge of the excitation pulse), the effect of the local field is balanced and only the propagating pulse is observed.

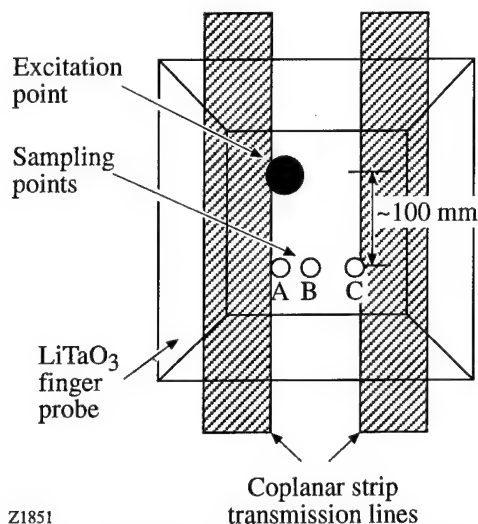


Fig. 1. An electro-optic finger probe is placed on top of a coplanar transmission line to optically detect electrical transients. The metal-semiconductor interface is illuminated by an ultrafast laser pulse, and the electrical response is measured at points A, B, and C.

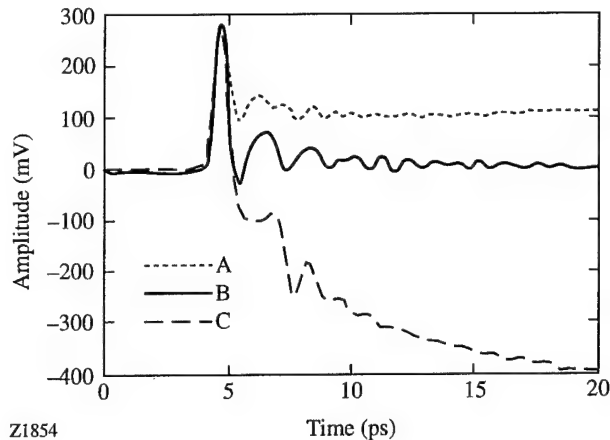


Fig. 2 The metal-semiconductor interface of InP is illuminated with red light. The electrical transient response is electro-optically sampled between the coplanar electrodes at three points ~100 μm away from the excitation: (A) at the excitation electrode, (B) near the center of the gap between the two electrodes, and (C) at the un-excited electrode.

Si has a large penetration depth at 720 nm; therefore, we decided to use 400-nm excitation, which has a much smaller penetration depth. As shown in Fig. 3, these pulses with ~1.0-ps FWHM are similar in shape and duration to those of InP excited with red light, and also of those previously obtained on GaAs.⁷ Once again we observe the effects of the local electric field: positive shoulder at point A, negative shoulder at point C, and no shoulder in the center (point B). Moving our probing beam ~20 μm from the excitation beam, Fig. 4 shows the 1.1-ps FWHM pulse shape on Si when sampled with a balanced local field (similar to point B in Figs. 2 and 3).

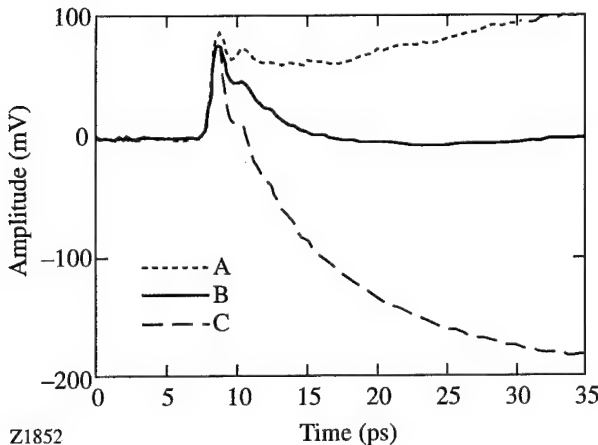


Fig. 3. Exciting Si by edge illumination with blue light produces ultrafast pulses. The electrical response of Si at the three sampling points is similar to InP as shown in Fig. 2.

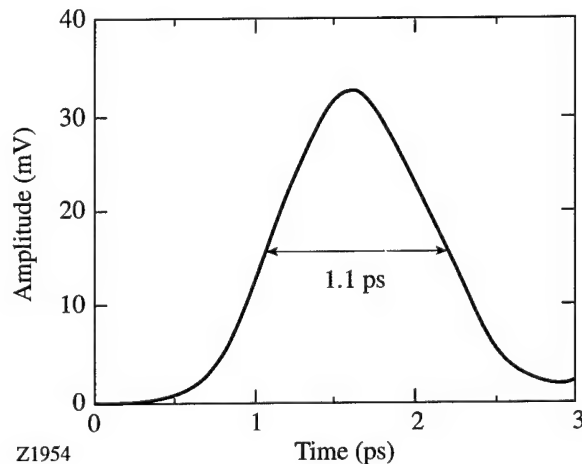


Fig. 4 An electrical pulse of 1.1-ps FWHM was measured on Si ~20 μm from the excitation point.

Our results directly support the Sano and Shibata theory. The local field in the vicinity of the excitation is observed, and only the subpicosecond pulse propagates down the transmission line. We believe our success in generating a pulse on Si is due to our choice of excitation wavelength. The only other successful ultrafast pulse generation on Si was performed on a silicon-on-sapphire (SOS) substrate where the Si layer was much less than the penetration depth at the excitation wavelength.⁵

The band structure in Si is totally different from that of InP and GaAs. Thus, our results show that the mechanism behind edge illumination is not material dependent. Therefore, it appears unlikely that electrical pulses arising from edge illumination are a result of intervalley scattering, as was suggested for GaAs.⁶ The applicability of this method to a variety of materials (Si, GaAs, and InP) makes edge illumination a powerful technique for ultrafast pulse generation in semiconductors. Another useful feature of edge illumination is that it can be performed with existing transmission lines on integrated circuits; it requires no additional designs.

By utilizing edge illumination, broadband frequency domain characterization of devices fabricated on Si and InP can be as easily performed as those on GaAs, as was shown by Alexandrou *et al.*¹ When combined with an electro-optic sampling system, edge illumination is a simple and powerful tool for *in situ* characterization of circuits.

This research is supported by University Research Initiative at the University of Rochester sponsored by the Army Research Office grant No. DAAL03-92-G-0112. C.-C. Wang acknowledges support from the Frank Horton Graduate Fellowship Program.

REFERENCES

1. S. Alexandrou, C.-C. Wang, M. Currie, R. Sobolewski and T. Y. Hsiang, in *Technologies for Optical Fiber Communications*, edited by G. J. Brown, D. J. Decoster, J. S. LaCourse, Y. S. Park, K. D. Pedrotti and S. R. Sloan (SPIE, Bellingham, WA, 1994), Vol. 2149, pp. 108-118.
2. M. Frankel, IEEE Microwave and Guided Wave Lett. **4**, 118 (1994).
3. J. A. Valdmanis, Electron. Lett. **23**, 1308 (1987).
4. S. Alexandrou, C.-C. Wang, and T. Y. Hsiang, Appl. Phys. Lett. **62**, 2507 (1993).
5. D. Krökel, D. Grischowsky, and M. B. Ketchen, Appl. Phys. Lett. **54**, 1046 (1989).
6. U. D. Keil and D. R. Dykaar, Appl. Phys. Lett. **61**, 1504 (1992).
7. S. Alexandrou, C.-C. Wang, R. Sobolewski, and T. Y. Hsiang, IEEE J. Quantum Electron. **30**, 1332 (1994).
8. E. Sano and T. Shibata, Appl. Phys. Lett. **55**, 2748-2750 (1989).
9. S. Alexandrou, R. Sobolewski, and T. Y. Hsiang, IEEE J. Quantum Electron. **28**, 2325 (1992).

Paper Withdrawn

Impact ionization in wide-band-gap materials under high-field

D. Du, X. Liu, J. Squier, and G. Mourou

Center for Ultrafast Optical Science,
The University of Michigan,
2200 Bonisteel Blvd., Room 1006
Ann Arbor, MI 48109-2099

Impact ionization coefficient under extremely high electric field is a very important parameter in electron transport. Because of the electric breakdown under high electric field, the impact ionization parameter is measured at DC fields up to 15 MV/cm in SiO₂[1]. In this paper, we report that by employing femtosecond laser pulses, we were able to measure the impact ionization parameters of SiO₂ and MgF₂ in electric fields as high as 280 MV/cm.

We utilized a Ti:sapphire laser system based on the chirped pulse amplification (CPA)[2] in our experiment. The laser wavelength was 780 nm. Laser pulses with adjustable pulse width from 150 fs to 7 ns were focused onto SiO₂ and MgF₂ samples. An electron avalanche process happens when the laser electric field exceeds the breakdown threshold. The general equation to describe the growth of the electron density is given by

$$\frac{dn_e(t)}{dt} = \eta(E)n_e(t) + \left(\frac{dn_e(t)}{dt}\right)_{PI} - \left(\frac{dn_e(t)}{dt}\right)_{loss}, \quad (1)$$

where $n_e(t)$ is the free electron (plasma) density, and $\eta(E)$ is the avalanche coefficient. The second term on the right hand side is the photoionization contribution, and the third term is the loss due to electron diffusion, recombination, etc. When the pulse-width is in the picosecond regime, the loss of electrons is negligible during the duration of the short pulses. We have shown that avalanche ionization is the dominant process under our experimental conditions[3]. Therefore, neglecting the last two terms on the

right, the electron density at the end of the pulses is given by

$$n(\tau) = n_0 \exp(-\eta\tau) \quad (2)$$

where n_0 is the initial electron density (which is about $10^8 \sim 10^{10} \text{ cm}^{-3}$), τ is the pulse duration, and η is the avalanche ionization coefficient. In our experiments, we measured the laser fluences when the final electron density reaches the critical plasma density ($\sim 2 \times 10^{21} \text{ cm}^{-3}$ in our case) at different pulse durations. We obtained the avalanche coefficient η as a function of the electric field. The impact ionization parameter is related to η by $\eta = \alpha v_{\text{drift}}$. Under the high electric field the drifting velocity of the electrons is saturated at about 10^7 cm/sec . Therefore, by measuring the electric breakdown threshold as a function of laser pulses, we can derived the impact ionization parameter as a function of the electric field.

The impact ionization coefficient has been studied theoretically first by Wolff and Shockley[4][5]. Thornber[6] has derived an expression for $\alpha(E)$, which applies to the entire electric field strength, which is important for us to compare with our experimental results:

$$\alpha(E) = \frac{eE}{U_i} \exp \left(-\frac{E_i}{E(1 + E/E_p) + E_{kT}} \right), \quad (3)$$

where U_i is the ionization energy, E_{kT} , E_p , and E_i are threshold fields for carriers to overcome the decelerating effects of thermal, phonon, and ionization scattering, respectively. In Fig. 1, we show our experimental and calculated results. As can be seen, the experiment agrees with the theory very well.

In summary, for the first time, we have measured the impact ionization parameter of a wide band gap material up to 280 MV/cm. Impact ionization parameter at high electric field can be measured by femtosecond lasers using laser induced breakdown in a regime where avalanche ionization is the dominant mechanism, and with electric field that are orders of magnitude stronger than that can be applied with dc or switching techniques.

References

- [1] D. Arnold, E. Cartier, and D. J. Dimaria, Phys. Rev. **B49** 10278 (1994)
- [2] D. Strickland and G. Mourou, Opt. Commun. **56**, 219 (1985)
- [3] D. Du *et al.*, Appl. Phys. Lett. **64**, 3071 (1994)
- [4] P. A. Wolff, Phys. Rev., **95**, 1415 (1954)
- [5] W. Shockley, Czech. J. Phys., **B11**, 81 (1961)
- [6] K. K. Thornber, J. Appl. Phys. **52**, 279 (1981)

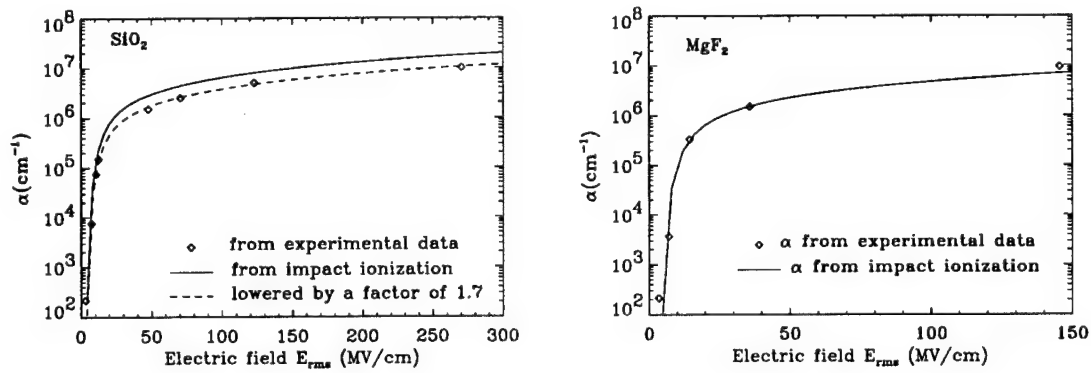


Figure 1: Impact ionization rate per unit distance α determined from experiment and theory in SiO_2 and MgF_2 .

Step Function Photoconductive Signal Generation in Integrated Coplanar Test Fixtures

A. Zeng and M.K. Jackson

*Dept. of Electrical Engineering, University of British Columbia
2356 Main Mall, Vancouver, B.C., V6T-1Z4, Canada
tel. (604)822-6348, fax (604)822-5949*

M. Van Hove and W. De Raedt

*Interuniversity Microelectronics Center
Kapeldreef 75, B-3001 Leuven, Belgium
tel. 32-16-28-13-80, fax 32-16-28-12-14*

Electro-optic sampling has been used in the ultrafast time-resolved characterization of active devices such as modulation-doped field-effect transistors (MODFETs) [1,2] and heterojunction bipolar transistors. One of the most interesting measurements is the large-signal response of an active device, because it gives information on an ultrafast time scale about the nonlinear response of the device. Such measurements require a photoconductive switch geometry that allows independent control of the device operating point and the photoconductive excitation; these have been developed by Frankel et. al. [1]. Ideally, to reduce and control access parasitics, the device under test should be monolithically integrated with the coplanar test fixture. In this paper we report a study of photoconductive signal generation in structures similar to those of Ref. 1, monolithically integrated with high-performance MODFETs. We show the results of photoconductive excitation, and show how positioning of the excitation beam affects the generated signal. Our results show that changes in the direction of the photogenerated current with respect to the coplanar stripline has little effect on the signal observed 1.5 mm away. We show that the photogenerated signal is step-like in form, and compare our results with a 2-D model of the carrier transport including Schottky contact effects. The process is composed of a rapid screening of

the field by photogenerated carriers, followed by a slower process of charge collection.

In Figure 1 we show the top-view of the input side coplanar stripline fixture that is integrated with a pseudomorphic AlGaAs/InGaAs MODFET. The MODFET, which is at the right-hand end, is mesa isolated and the gate and source are integrated with the metallic coplanar electrodes. The drain and source are integrated with a similar coplanar line extending to the right. The coplanar electrodes are formed by first mesa etching into the nominally undoped MBE-grown GaAs buffer, followed by evaporation of a metal stack consisting of Ti, Pt, Au and TiW. Finally, $2\mu\text{m}$ of Au is plated to lower the electrode resistance. A SiN passivation layer is deposited over the entire coplanar electrode area including the GaAs buffer. This is removed by CF_4 reactive ion etching outside the active area of the MODFET. All gaps are $5\mu\text{m}$, and the coplanar electrode widths are $55\mu\text{m}$ to the right of the switch; to the left the three electrode widths are 25, 25, and $55\mu\text{m}$, respectively.

Electro-optic measurements are made

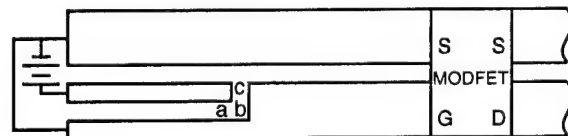


Fig.1 Coplanar stripline test fixture geometry and excitation positions (not to scale). S, D, and G are the integrated MODFET contacts.

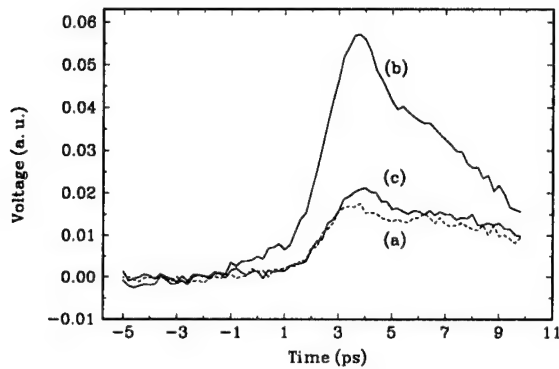


Fig.2 Response for excitation at the three pump positions shown in Fig. 1.

with 150 fs pulses from a Ti-Sapphire laser operating at approximately 830 nm, a mixer-based detection scheme, and an external electro-optic sampling tip. The pump is focused on the gap through an $f=10\text{mm}$ lens followed by a subminiature right prism that turns the beam; incorporation of ccd-camera-based microscope systems in both pump and probe paths allows us to observe the exact position and focusing of the two beams.

In Fig. 2 we show the voltage measured at a location 1.5 mm from the excitation position. The three curves correspond to pump excitation at three different locations in the L-shaped gap, as shown in Fig. 1, where the bias voltage is 5V. Positions (a) and (c) involve excitation of identical carrier distributions with identical electric fields, because the interelectrode gap is the same in both locations. The only difference between excitation at (a) and (c) is the direction of the photogenerated carrier motion. Such a difference might be expected to lead to differing excited signal amplitudes, because of differences in the electromagnetic coupling between the photocurrent and the propagating modes on the coplanar striplines. However, little difference between the two generated signals is observed. We also note that excitation at the corner of the L-shaped gap, position (b), leads to a significantly larger generated signal.

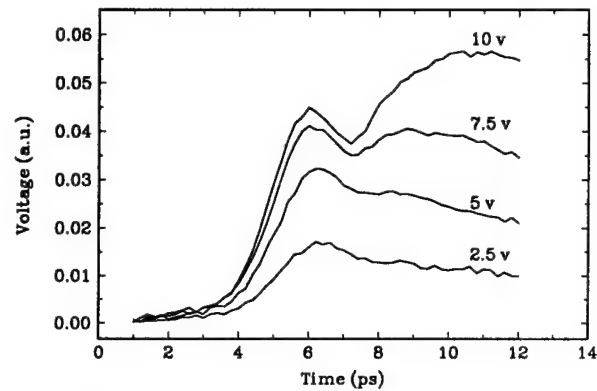


Fig.3 Response for excitation at position (b) as a function of switch bias, as labelled.

In Fig. 3 we show the generated signal as a function of DC bias across the switch, measured 1.5 mm from pump excitation at position (b) of Fig. 1. It is interesting to notice that the initial pulse-like part of the pulse starts to saturate at a bias of approximately 7.5V. However, the latter part of the pulse does continue to increase in amplitude with increasing bias, and starts to show an increasing delay before reaching a peak amplitude. The behavior seen in Fig. 3 suggests that the response can be separated into two events: the first is a rapid pulse-like response, and the second a slower step-like response. The slight difference in decay time seen compared to Fig. 2 is attributed to slightly differing excitation conditions.

We have modelled the photoconductive switch using the MEDICI two-dimensional simulator, which incorporates drift, diffusion, and thermionic current self-consistently with Poisson's equation. The simulation is intended to model excitation at point (a) or (c) of Fig. 1. We incorporate photogeneration with a 150 fs FWHM Gaussian temporal profile, and a peak integrated photocharge density of 10^{18}cm^{-3} , corresponding to experimental conditions; the pulse peak occurs at $t=300\text{fs}$. The spatial distribution of photogeneration is also Gaussian, with a profile $\exp\{-r^2/a^2\}$ where $a = 1\text{ }\mu\text{m}$. In Figs. 4(a), (b), and (c), we show

the electron density, hole density, and potential contours at $t=300\text{fs}$. The $5\mu\text{m}$ electrode gap is in the vertical direction, and Schottky contacts lie along the top and bottom of the areas shown. Even at this early time, the electric field is nearly completely screened in the middle of the excitation area, as can be clearly seen in rhw potential contours of Fig. 4(c). In Fig. 4(d) we show the contact current as a function of time. The behavior is similar to the experiment, showing a rapid peak as the photogenerated carriers screen the applied bias. Once the field is screened, current drops and a slower process occurs consisting of electron and hole collection by diffusion in the center of the excitation area and drift near the contacts. The slight oscillations visible on the calculated current are due to the finite simulation grid density. Finally we compare our results with those of Ref. 3, in which the role of hot-carrier scattering to satellite valleys was discussed. Because we use lower energy excitation, this cannot be a factor in our experiments. We also note that the form of the current shown in Fig. 4(d) is strikingly similar to the experimental measurements in InP reported in [3], which suggests that hot-carrier effects may not be necessary to explain the sharp peak they observed.

This work was supported by the Natural Sciences and Engineering Research Council of Canada.

References

- [1] M.Y. Frankel, J.F. Whitaker and G.A. Mourou, I.E.E.E. J. Quantum Electron. **28**, 2313(1992) and references therein.
- [2] M.K. Jackson, M.Y. Frankel, J.F. Whitaker, G.A. Mourou, D. Hulin, A. Antonetti, M. Van Hove, W. De Raedt, P. Crozat and H. Hafdallah, Appl. Phys. Lett. **61**, 1187(1992).
- [3] U.D. Keil and D.R. Dykaar, Appl. Phys. Lett. **61**, 1504(1992).

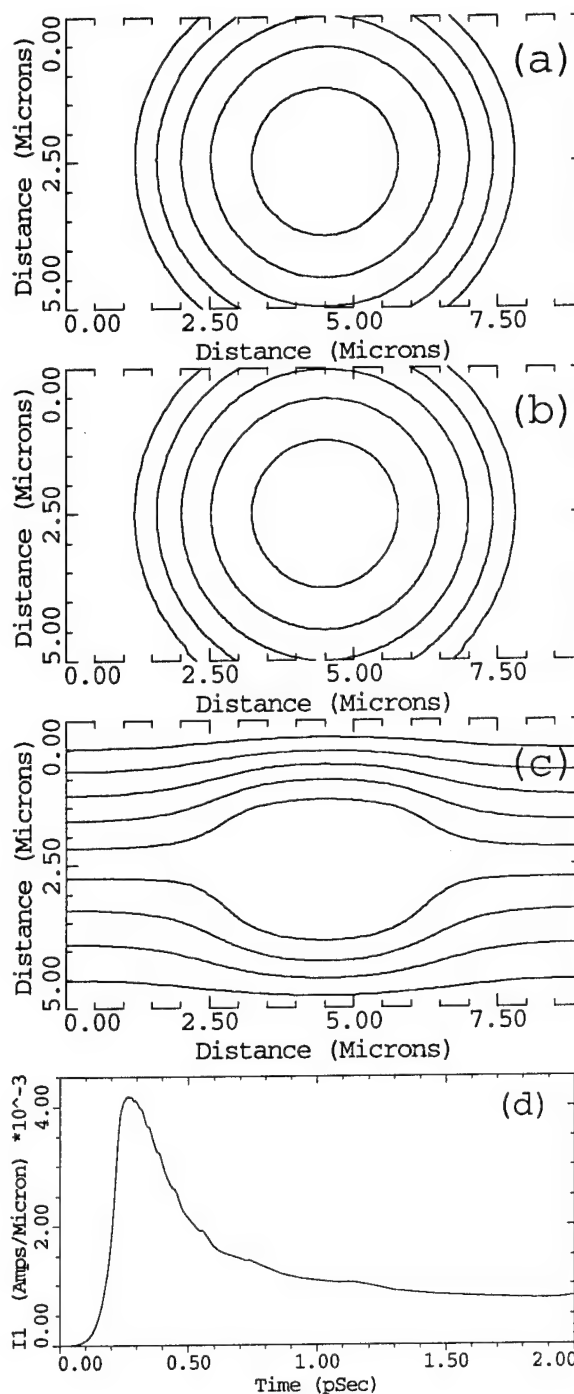


Fig. 4 (a) electron and (b) hole density contours, each representing drop by factor of 10, largest is 10^{17}cm^{-3} . (c) potential contours, separation is 0.5V. (d) electrode current.

**Ultrafast Carrier Relaxation in Semi-insulating GaAs Implanted with Arsenic Ions
(GaAs:As)**

Gong-Ru Lin, Feruz Ganikhanov, Wen-Chung Chen, C.-S. Chang, and Ci-Ling Pan

Institute of Electro-Optical Engineering, National Chiao Tung University

Hsinchu, Taiwan 300, Republic of China

Phone: 886-35-712121 x 56321, FAX: 886-35-716631

E-mail: clpan@cc.nctu.edu.tw

Ultrafast carrier dynamics in damaged and nonstoichiometric Gallium arsenide (GaAs:X) has attracted much attention.^{1,2} Among those materials, the arsenic-rich GaAs film grown by molecular beam epitaxy (MBE) at low substrate temperatures of about 200 °C (so-called LT-GaAs), exhibits the shortest carrier relaxation time reported to date, about 200 femtoseconds (fs).² Recently, the electrical properties of arsenic-rich GaAs layer fabricated by arsenic implantation of GaAs substrates (GaAs:As) have also been studied.^{3,4} This material exhibits similar electrical characteristics as the MBE grown LT-GaAs materials and requires simpler and less costly fabricating process. These advantages would make GaAs:As an attractive alternative to LT-GaAs which have been shown to be very promising for applications in ultrafast electronics and optoelectronics.⁵ In the present paper, we report preliminary data on ultrafast carrier dynamics of As-ion implanted GaAs samples. The carrier lifetimes have been determined for substrates implanted with different dosage of arsenic ions.

Semi-insulating (100) GaAs substrates were implanted by dense arsenic ions with dosages of 10^{13} to 10^{16} ions·cm⁻² and energy of 200 keV. The distributing depth of the implanted layer is about 2000 Å.³ The resulting As excess concentrations were estimated to be a maximum of 2%, at a depth of about 90 nm. Time-resolved reflectivity measurements were performed with 80-90 fs pulses of a mode-locked

Ti:sapphire laser at 786 nm (≈ 1.58 eV), i.e. the photon energy is approximately 150 meV above the bandgap of normal GaAs. The absorption depth at this wavelength is approximately 0.7 μm at room temperature. The carrier density at the surface is estimated to be less than 10^{18} cm^{-3} . Typical detection sensitivity as small as one part in 10^5 .

Transient responses for arsenic-ion-implanted GaAs are shown in Fig.1 for the substrates damaged by As ions at dosages of 10^{13} and $10^{15} \text{ ions/cm}^2$. Decay time as short as 160 fs is already attained at dosage of $10^{13} \text{ ions/cm}^2$. At 10^{15} cm^{-2} , the result is system-limited and should be ≤ 160 fs. The response is fitted well over 2 orders of magnitude by a single exponential function with a time constant of 160 fs. This is already shorter than those reported for LT-GaAs,^{5,6} thus proving the potential of As-ion-implanted GaAs as candidate for ultrafast optoelectronic applications.

REFERENCES

1. M. B. Johnson, T. C. McGill, and N. G. Paulter, **Appl. Phys. Lett.** 58 (1989) 2424.
2. E. S. Harmon, M. R. Melloch, A. J. Woodal et al., **Appl. Phys. Lett.** 63 (1993) 2248.
3. A. Claverie, F. Namaver, and Z. Liliental-Weber, **Appl. Phys. Lett.** 62 (1993) 1271.
4. G. R. Lin, W. C. Chen, C. -S. Chang, and C. -L. Pan, to be published in **APPL. Phys. Lett.** (1994).
5. S. Gupta, J. F. Whitaker, G. A. Mourou, **IEEE J. Quant. Electron.** 28 (1992) 2464.
6. X.-Q. Zhou, H. M. van Driel, W. W. Ruhle, Z. Gogolak, and K. Ploog, **Appl.Phys.Lett.** 61 (1993) 3020.

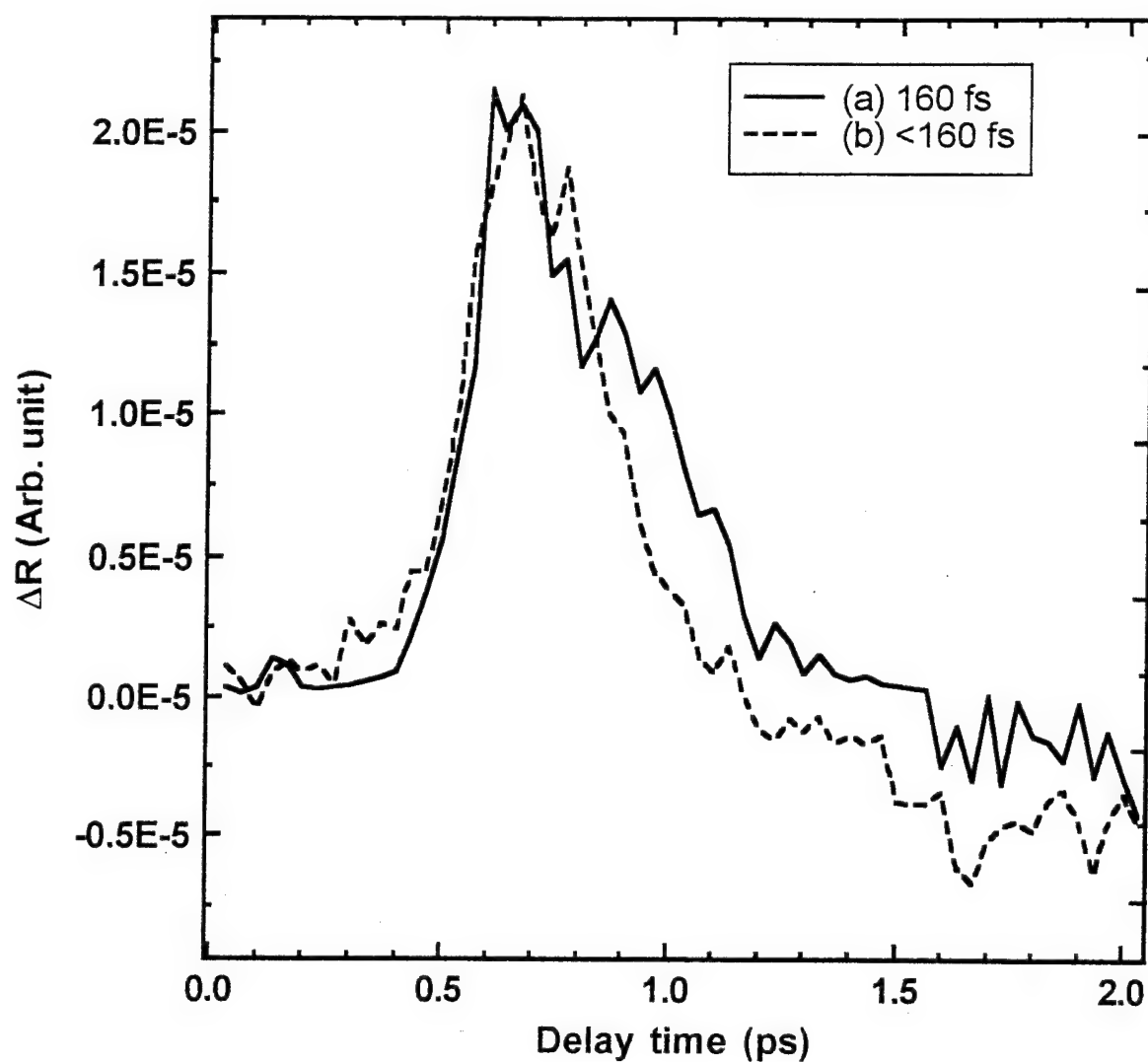


Fig.1 Transient reflectivity of from the S.I. substrate implanted with different dosages of As-ions: (a) 10^{13} ions/cm²; (b) 10^{15} ions/cm².

All-Silicon, Ultrafast, Integrable Optoelectronic Interface

Chia-Chi Wang, Marc Currie, and Thomas Y. Hsiang

LABORATORY FOR LASER ENERGETICS
and DEPARTMENT OF ELECTRICAL ENGINEERING
University of Rochester, Rochester, NY 14623-1299
Tel. (716) 275-1808, Fax. (716) 273-1014

We report on the computed and experimental studies of an ultrafast, all-silicon optical receiving and modulating system that is compatible in processing with the integrated-circuit technology. A silicon metal-semiconductor-metal (MSM) photodiode is demonstrated to be an optical receiver with resolvable bit rate as high as 60 Gb/s. An all-silicon light-intensity modulator is proposed as an optical transmitter. The field-effect nature of this proposed modulator provides high-speed performance in addition to low-power dissipation. A sample device with 300- μm interaction length is calculated to have a modulation depth of $\sim 40\%$ with 5-V bias, and the operational speed is expected to be 70 GHz, limited by the RC time constant.

Experimentally, an MSM diode with 200-nm electrode separation was made on crystalline silicon. A subpicosecond electro-optic sampling system was used to measure the response of this diode to femtosecond laser pulses. Figure 1 shows that the response of a 200-nm diode to blue light has a full-width at half-maximum of 3.7 ps. Furthermore, it recovers fully to its original, nonconductive state within 16.5 ps, which infers that it provides a resolvable bit rate as high as 60 Gb/s.

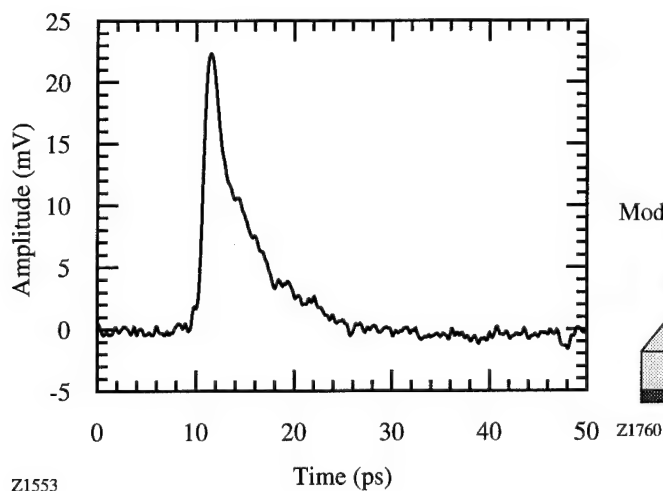


Fig. 1 A 200-nm silicon MSM diode recovers fully to its original, nonconductive state within 16.5 ps after its excitation.

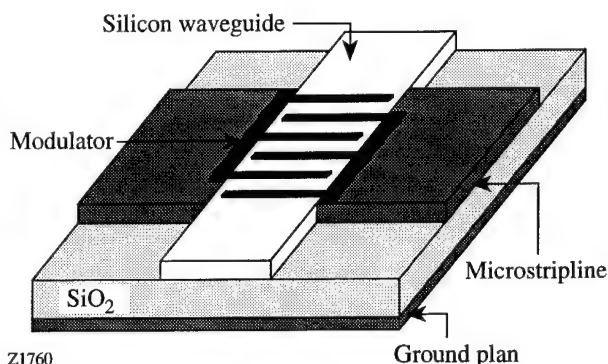


Fig. 2 Schematic view of the SOI waveguide modulator.

Since silicon is not a suitable material for semiconductor lasers, we propose an all-silicon, ultrafast, integrable light-intensity modulator as the optical transmitter. Figure 2 shows the schematic view of the modulator. The silicon-on-insulator (SOI) structure forms an optical waveguide. An interdigitated structure is deposited on top of the silicon layer to form the interaction region of a distributed modulator in the form of a Bragg reflector. A microstrip line guides the electrical signal to the metal fingers and alternately biases the fingers, forming forward- and reverse-biased Schottky junctions with silicon. There are larger depleted regions on the reverse-biased sides, as shown in the shaded part of Fig. 3. In the depleted regions, the carrier concentration is lower, and the optical index of refraction is larger, known as the carrier-refraction effect. If the optical wavelength is $1.55\text{ }\mu\text{m}$, the difference of refractive index between depleted and undepleted regions is 0.005 for a p-type silicon with carrier concentration of $3 \times 10^{18}/\text{cm}^3$.¹ Thus, there is a field-induced Bragg reflection, with reflectivity modulated by the applied electric field.

To obtain the maximum modulation depth, Bragg condition must be satisfied, i.e., $\Lambda = \lambda/2$, where Λ is the period of finger electrodes, as shown in Fig. 3, and λ is the guided wavelength. If the thickness of the silicon layer is chosen to be 100 nm to sufficiently guide the TE_0 mode of $1.55\text{-}\mu\text{m}$ light, then the modulation depth can be calculated using coupled-mode theory² as a function of bias voltage and the interaction length, as shown in Fig. 4. The carrier concentration in this calculation is $p = 3 \times 10^{18}/\text{cm}^3$. Figure 4 shows that a modulator with 300- μm interaction length has a modulation depth of $\sim 40\%$ with 5-V bias, which is adequate for most applications.

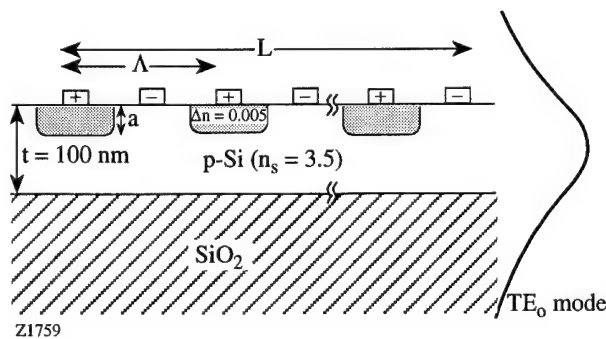


Fig. 3 The depleted and undepleted regions form a field-induced Bragg reflector, which converts the index modulation to light-intensity modulation. The TE_0 mode profile is shown to the right of the modulator.

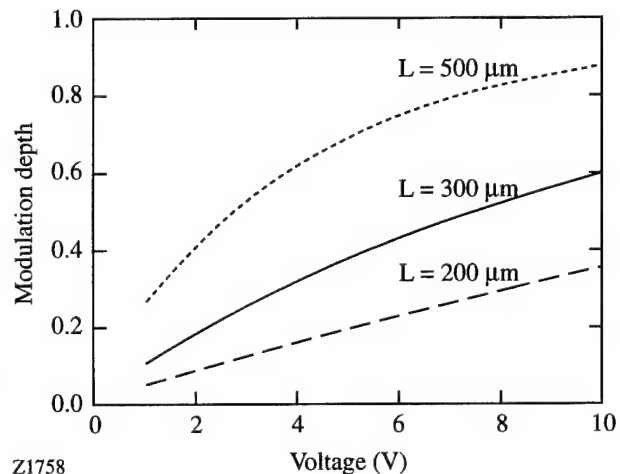


Fig. 4 The modulation depth is a function of interaction length and applied voltage. The thickness of the guiding layer is 100 nm, and doping is $p = 3 \times 10^{18}/\text{cm}^3$.

Because it is a field-effect device, the operational speed is dominated by the RC time constant. For example, a modulator with 60-nm finger width, 120-nm finger spacing, 3- μm finger length, and 300- μm interaction length is calculated to have a capacitance of 0.22 pf.³ If a microstrip line with 10- Ω impedance is used, the bandwidth of this modulator would then be $1/2\pi RC$, or about 70 GHz.

Combining the MSM diode and the modulator, an all-silicon, ultrafast, optoelectronic interface is proposed.

This research is supported by University Research Initiative at the University of Rochester sponsored by the Army Research Office grant No. DAAL03-92-G-0112. C.-C. Wang acknowledges support from the Frank Horton Graduate Fellowship Program.

REFERENCES

1. R. A. Soref and B. R. Bennett, IEEE J. Quantum Electron. **QE-23**, 123 (1987).
2. A. Yariv and P. Yeh, *Optical Waves in Crystals: Propagation and Control of Laser Radiation* (Wiley, New York, 1984), Chap. 11.
3. Y. C. Lim and R. A. Moore, IEEE Trans. Electron Devices **ED-15**, 173 (1968).

Fast Vertical Silicon Photodetectors with Buried CoSi₂ Contact

H. G. ROSKOS, J. P. HERMANN, F. RÜDERS,* E. STEIN VON KAMIENSKI, O. HOLLRICHER,* C. BUCHAL,* S. MANTL,* and H. KURZ

Institut für Halbleitertechnik II, Rheinisch-Westfälische Technische Hochschule (RWTH) Aachen, Sommerfeldstr. 24, D-52056 Aachen, Germany
Tel.: +49-241-80-7806 (-7890), Fax: +49-241-8888-246,
Email: roskos@zyklop.basl.rwth-aachen.de

* Institut für Schicht- und Ionentechnik II, Forschungszentrum Jülich, D-52425 Jülich, Germany

Si-based integrated optoelectronics for high-speed applications demands ultrafast photodetectors with a good quantum collection efficiency (QCE). Several approaches towards such diodes have been pursued in the past: (i) Ultrashort electric transients of 5 ps duration (FWHM) can be derived from planar metal-semiconductor-metal (MSM) photodiodes with interdigitated metal finger structures [1]. The speed is determined by the sweep-out time of the photogenerated carriers. However, for very fast response, a metal finger separation of typically 300 nm is required and electron-beam lithography has to be employed in the fabrication process [1]. (ii) Electric pulses with a sub-ps FWHM are derived from conductance-lifetime-limited photodetectors such as photoconductive switches [2]. Unfortunately, those detectors suffer from a very low QCE on the order of 10^{-5} .

As an alternative, sweep-out-limited MSM detectors with *vertical* electrode arrangements promise a good compromise of high speed and high QCE *without* the need for electron-beam lithography in the fabrication process. The basic idea is to achieve a small conductor spacing with the help of a buried conductor instead of laterally extended interdigitated electric contacts [3]. In contrast to lateral photodetectors, the temporal response of vertical Si photodiodes should not depend on the wavelength (i.e. the penetration depth) of the incident optical pulses. Here, we present a detector based on single-crystalline Si(100) wafers with a

buried layer of single-crystalline metallic CoSi₂ under the Si surface grown by molecular beam epitaxy (allotaxy) [4] and by ion-beam synthesis (mesotaxy) [5]. The top Si films are 370 nm and 70 nm thick, respectively. In the latter case, 380 nm poly-Si is deposited onto the 70 nm Si film to increase the photoactive-layer thickness.

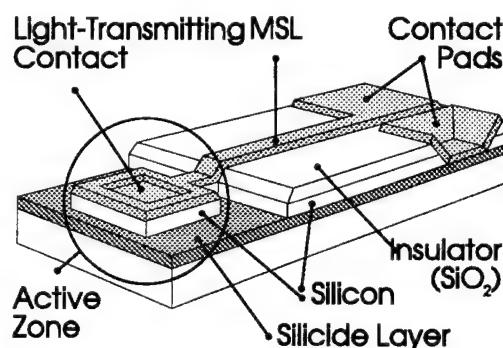


Fig.1. Design of the vertical Si MSM photodetector. The detector mesa is integrated into an Al-SiO₂-CoSi₂ MSL of 5 mm length.

Figure 1 illustrates schematically the structure of our vertical MSM photodiodes [6]. The active zone consists of a Si mesa with a semi-transparent 10-nm Al top metalization (window size: $20 \times 20 \mu\text{m}^2$) in between an Al ring electrode. The electrode is connected to the top conductor of a 5 mm long microstrip transmission line (MSL). The CoSi₂ layer underneath the photosensitive Si film serves as the back Schottky contact of the diode, a buried light reflector ($R \approx 40\%$) and the ground plane of the MSL. The mesa structure prevents speed-limiting

carrier diffusion into low-field regions. To gain maximum speed, the dimensions of the photodiode have to be chosen carefully. With a Si layer thickness of 370 nm and 450 nm for the diodes, carrier sweep-out is expected to occur within 4-11 ps when a carrier drift velocity on the order of $4\text{-}10 \times 10^6$ cm/s is taken into account. The area of each ring electrode is $30 \times 30 \mu\text{m}^2$ to ensure a RC time constant below 4 ps (MSL impedance $R=12 \Omega$).

To determine the temporal response of the photodetectors, we employ electro-optic (EO) sampling in a conventional pump-probe scheme. We illuminate the active zone of the vertical photodetector with 150-fs Ti:Sapphire-laser pulses at a wavelength of 720 nm. Photogenerated electric pulses are probed electro-optically with a LiTaO₃ crystal placed onto the MSL 200 μm away from the photodiode. On this length scale, dispersion and attenuation of ps-electric transients are negligible for this type of MSL [7].

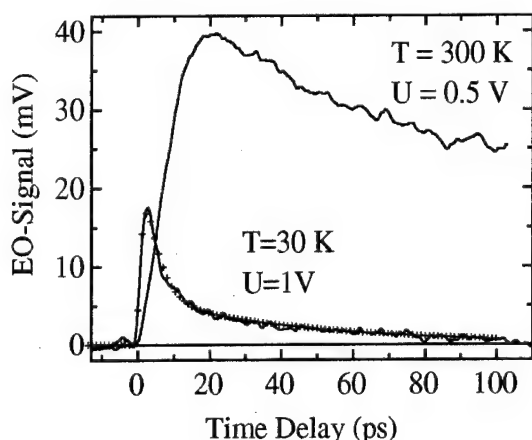


Fig. 2. Pulse response of a vertical Si MSM photodetector fabricated on allotaxially grown Si-CoSi₂-Si substrates at room temperature and at 30 K.

In Fig. 2, the temporal response of a vertical photodetector on an allotaxially grown substrate is depicted for various temperatures. At room temperature and 0.5 V bias, the signal rise occurs on a time scale of 15-20 ps. A peak amplitude of 40 mV is

obtained. The signal decays rather slowly with a time constant of approximately 180 ps. At 30 K, the speed of the photodetector is considerably enhanced. For a bias of 1 V, the signal increases with a time constant of 4.4 ps to a peak amplitude of 17.5 mV. The signal decreases biexponentially with time constants of 3 ps and 40.6 ps. The temporal response of the photodetector depends only weakly on the external bias. The peak amplitude rises only by a factor of 2 when the external bias is increased from 0.5 V to 7 V while the shape of the electric pulses remains identical.

We attribute the much slower speed of the vertical photodetector at room temperature to the presence of shallow traps leading to thermally activated hopping transport of the carriers. This type of transport is strongly suppressed at 30 K resulting in the long pedestal in the trailing part of the electric transients. The observed lower peak amplitude and reduced average photocurrent at 30 K as compared to 300 K result from the fact that fewer carriers contribute to the signal output at low temperatures. The traps are likely to be associated with dislocations in the Si film on top of the buried CoSi₂ layer created during the growth process.

With 1 V of reverse bias of the Al/Si contact, one obtains a sensitivity of 6 mA per Watt of incident optical power. This translates into an external QCE of 0.5%. As 2-3 % of the incident photons are absorbed in the top Si layer (at a wavelength of 720 nm), 17-25 % of the photogenerated carriers are collected at the contacts.

Photodetectors realized on mesotaxially grown Si-CoSi₂-Si substrates with an additional poly-Si layer show lower speed and efficiency even at low temperature (compare Fig. 3). This is to be expected from the crystal quality of the photactive layer consisting mainly of poly-Si with a high density of defects. However, it is possible to apply very high external voltages (up to 50 V) and to achieve optically switched voltage pulses on the order of 0.5-1 V.

In conclusion, we demonstrate a new

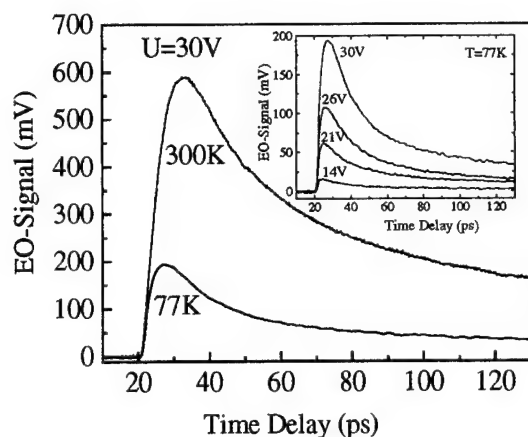


Fig. 3. Pulse response of a vertical Si MSM photo-detector fabricated on mesotaxially grown Si-CoSi₂-Si substrates for various bias voltages at 77 K.

concept for fast Si photodetectors based on Si-CoSi₂-Si substrates. No electron-beam lithography is needed in the fabrication process. Characterization of the detectors via time-resolved electro-optic sampling establishes the high-speed potential. The carrier collection efficiency at present is 17-25 %. There is substantial room for improvement of both speed and collection efficiency by further advances in the growth of defect-reduced Si-CoSi₂-Si substrates.

REFERENCES

- [1] S. Alexandrou, C.-C. Wang, and T. Y. Hsiang, *Appl. Phys. Lett.* **62**, 2507 (1993).
- [2] M. B. Ketchen, D. Grischkowsky, T. C. Chen, C.-C. Chi, I. N. Duling III, N. J. Halas, J.-M. Halbout, J. A. Kash, and G. P. Li, *Appl. Phys. Lett.* **48**, 751 (1986).
- [3] A. M. Johnson, A. M. Glass, D. H. Olson, W. M. Simpson, and J. P. Harbison, *Appl. Phys. Lett.* **44**, 450 (1984).
- [4] S. Mantl and H. L. Bay, *Appl. Phys. Lett.* **61**, 267 (1992).
- [5] A.E. White, K. T. Short, R. C. Dynes, J. P. Garno, and J. M. Gibson, *Appl. Phys.* **50**, 95 (1987).
- [6] J. P. Hermanns, F. Rüders, E. Stein v. Kamienski, O. Hollricher, C. Buchal, S. Mantl, H. G. Roskos, and H. Kurz, *Appl. Phys. Lett.*, submitted.
- [7] H. Roskos, M. C. Nuss, K. W. Goossen, D. W. Kisker, A. E. White, K. T. Short, D. Jacobson, and J. M. Poate, *Appl. Phys. Lett.* **58**, 2604 (1991).

Diffraction effects in spatial and spectral properties of THz radiation from bulk GaAs excited by ultrashort pulses

N. Sarukura, Z. Liu, Y. Segawa

Photodynamics Research Center,

The Institute of Physical and Chemical Research (RIKEN),
Nagamachi Koeji 19-1399, Aoba-ku, Sendai, Miyagi 980, Japan
Telephone: +81 22 228 2012 Facsimile: +81 22 228 2010

S. Koshihara

Department of Applied Physics, Tokyo Institute of Technology

K. Shimoyama, Y. Kondo

Department of Applied Physics, Tohoku University,

Y. Shibata, T. Takahashi, S. Hasebe, M. Ikezawa

Research Institute for Scientific Measurements,
Tohoku University

The mechanism and potential application to ultrafast optoelectronics of THz radiation excited by ultrashort pulse lasers have been studied intensively.^{1,2} With regard to its mechanism, the THz radiation from semiconductor surfaces has been explained by the dipole induced during the relaxation process of the surface surge current or optical rectification.³ With regard to its application, this phenomena can be a good interface between well-developed ultrafast optics extending to the sub 10-fsec region, and ultrafast electronics around the picosecond region. Additionally, this radiation is an attractive light source for studying time-resolved far-infrared spectroscopy of phonons in solids and gaps of superconductors. For this purpose, the properties of this radiation should be known in detail. In this presentation, we will describe spatial and spectral properties of THz radiation from bulk GaAs excited by ultrashort-laser pulses and the diffraction effects.

The excitation sources were the mode-locked Ti:sapphire lasers with 1-psec or 100-fsec pulse duration. The THz-radiation was collected by a concave Al-mirror and detected by a silicon bolometer. A black-polyethylene filter was inserted to cut excitation laser light. A non-doped, semi-insulating bulk GaAs sample with a (100) surface was used as the emitter. The radiation intensity depends on the 1.5-th power of the excitation. This power dependence demonstrates that this radiation cannot be explained by a simple optical rectification process. The spectra of the THz radiation were obtained by the Fourier transformation of the autocorrelation of the radiation from a Martin-Puplett interferometer. To avoid water-vapor absorption, the interferometer was purged by dried nitrogen. Broad spectra were obtained both for 1-psec and 100-fsec pulse excitation. The peak positions of radiation

were 0.2 THz for both cases, and for the 100-fsec excitation frequency component over 1-THz was observed. We found that the center frequency is lower than the expected value assuming optical rectification. However, the spectral information contains the information on excitation pulse duration. Furthermore, the polarization characteristics of this radiation were found to be independent of the polarization direction of the excitation light from the transmission measurement of THz radiation through the wire-grid polarizer. The radiation was completely horizontally polarized.⁴ This result indicates that the radiation has lost the memory of excitation polarization, unlike a coherent process. For application as a probe light for time-resolved spectroscopy, polarized white radiation will be more useful than unpolarized, narrow band light.

The angular distributions of this radiation were also examined by the rotation of the detector position. The angular distributions were recorded for various incidence angles as shown in Fig. 1. The radiation was only detected in the reflection and transmission direction. This suggests that the radiation retains the memory of excitation direction like the coherent process. The excitation spot-size dependence of the radiation beam divergence was measured using the same configuration. The beam-divergence angle (FWHM) depends on the inverse of the excitation-spot size. This dependence clearly shows the diffraction effect (Fig. 2). This diffraction effect was also seen in the spectral shape (Fig. 3). As the excitation spot size became smaller, the longer wavelength side was more easily diffracted and the shorter wavelength component was emphasized. From this information, the excitation spot-size in the probe emitter should be large enough in pump and probe experiments to avoid distortion in the white spectrum or low spatial resolution.

In conclusion, properties of THz radiation from GaAs excited by ultrashort-laser pulses were examined, and most of these properties in our experiments can be understood by assuming a surface surge current model rather than the simple optical rectification process or fluorescence. We also found that the diffraction effects in spatial and spectral properties of THz radiation should be considered carefully for the future application of this THz radiation as white probe light for time-resolved far infrared spectroscopy.

References

1. D. H. Auston, Appl. Phys. Lett. 43, 713 (1983).
2. P. C. M. Planken, M. C. Nuss, W. H. Knox, D. A. B. Miller, and K. W. Goossen, Appl. Phys. Lett. 61, 2009 (1992).
3. S. L. Chuang, S. Schmitt-Rink, B. I. Greene, P. N. Saeta, and A. F. J. Levi, Phys. Rev. Lett. 68, 102, (1992).
4. 22nd International conference on the physics of semiconductors (Canada, 1994), paper TuP-117, N. Sarukura, Z. Liu, Y. Segawa, S. Koshihara, Y. Kondo, Y. Shibata, T. Takahashi, M. Ikezawa.

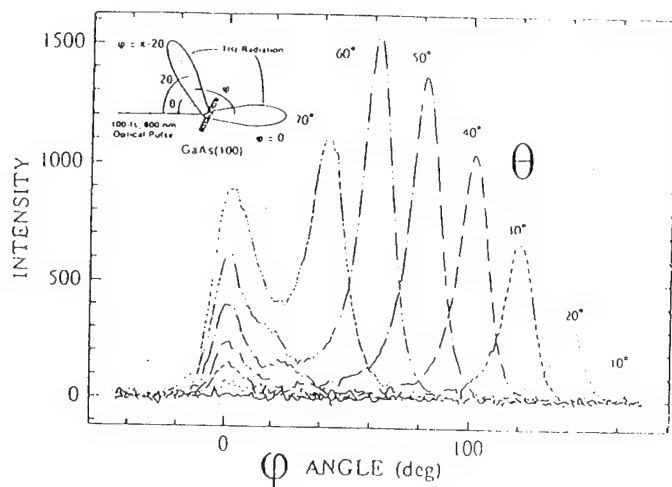


Fig. 1 The angular distribution of THz radiation excited by 100-fsec pulses for various incidence angles. The radiation was only detected in the reflection and transmission direction.

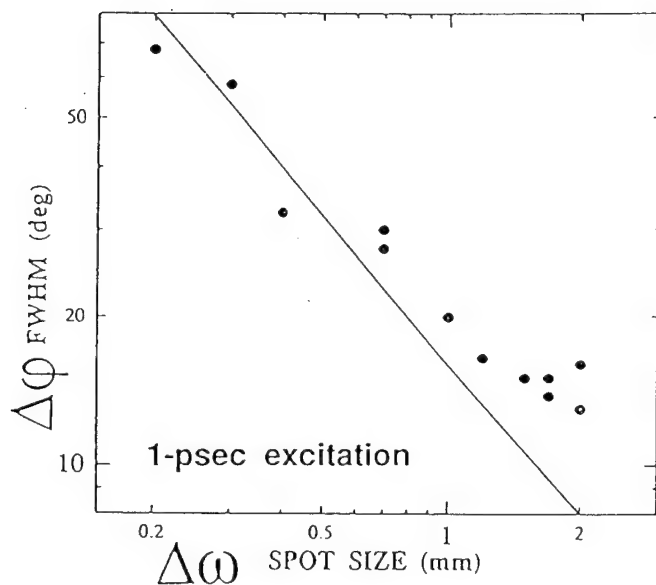


Fig. 2 The excitation spot-size dependence of the radiation beam divergence. (1-psec excitation pulse duration). The beam divergence angle (FWHM) depends on the inverse of the excitation-spot size. This dependence clearly shows the diffraction effect.

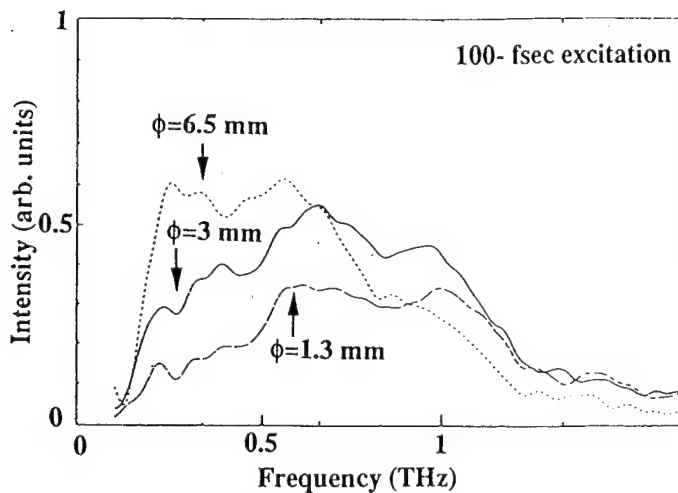


Fig. 3 The diffraction effect in the spectral shape (100-fsec excitation pulse duration). As the excitation-spot size became smaller, the longer wavelength side was more easily diffracted and the shorter wavelength component was emphasized.

Ultrafast characterisation of parasitics in in-plane-gate field-effect transistors

K. Ogawa, J. Allam and J.J. Baumberg

*Hitachi Cambridge Laboratory, Hitachi Europe Ltd.,
Cavendish Laboratory, Madingley Road, Cambridge CB3 0HE, U.K..
Telephone: (44 223) 467944 Facsimile: (44 223) 467942*

*N. de B. Baynes and J.R.A. Cleaver
Microelectronics Research Centre, University of Cambridge,
Cavendish Laboratory, Madingley Road, Cambridge CB3 0HE, U.K..*

*T. Mishima and I. Ohbu
Central Research Laboratory, Hitachi Ltd.,
1-280, Higashi-koigakubo, Kokubunji-shi, Tokyo 185, Japan.*

The in-plane-gate field-effect transistor (IPGFET) with gate-channel isolation by mesa trench exhibits very small gate-channel capacitance¹ due to the planar geometry. In this paper the parasitic capacitance is measured using electro-optic sampling² of the displacement current induced on the drain.

Device IPGFET1 consisted of a narrow channel of 2D electron gas with width $1\text{ }\mu\text{m}$ and length $20\text{ }\mu\text{m}$ connected at each end to a rectangular contact. The channel was laterally gated by a voltage applied to the 2DEG in the gate region adjacent to the channel. The gate consisted of a finger of width $\sim 0.8\text{ }\mu\text{m}$ and length $\sim 5\text{ }\mu\text{m}$, perpendicular to and separated from the channel by a distance of $\sim 0.5\text{ }\mu\text{m}$.

In order to minimise the parasitic impedances associated with electrical connection to the device, the IPGFET was monolithically integrated into a photonic sampling circuit³ consisting of low-temperature-grown GaAs photoconductive switches (PCS's) and coplanar waveguide (CPW). Picosecond pulses on the gate were generated by illuminating a PCS with pulses from a Ti:sapphire laser. The voltage transients on the gate and drain were measured using electro-optic sampling.

The drain transient at drain voltages V_D between 0 V and 3 V is shown in Fig. 1(a). The signal is dominated by the displacement current due to capacitive coupling between gate and drain,

$$I_d = C_{GD} dV_G/dt,$$

where C_{GD} is the gate-drain capacitance. Figure 1(b) shows the measured dV_G/dt superimposed on a step-like background. C_{GD} is determined by comparing the measured values of V_D and dV_G/dt .

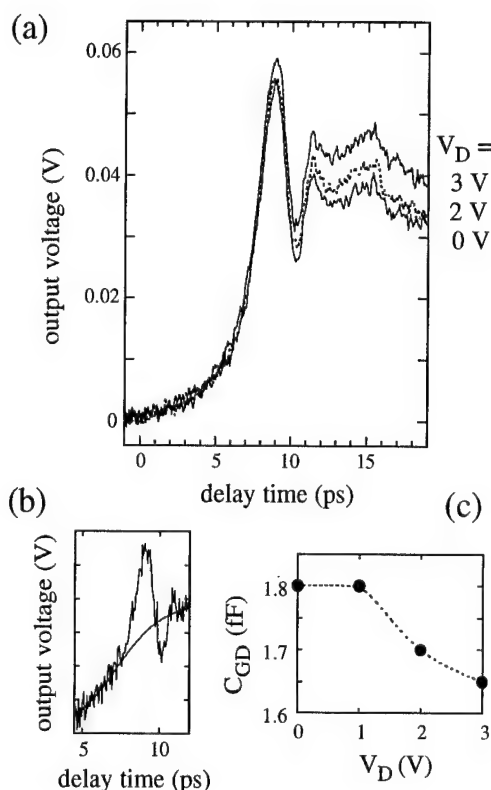


Fig. 1: (a) Output voltage measured at $V_D = 0, 2,$ and 3 V . (b) Transient reproduced from time derivative of input voltage on step-like background (at $V_D = 0\text{ V}$). Smooth step-like line shape represents asymptotic background with 6.6 ps rise time. (c) Gate-drain capacitance C_{GD} as function of V_D .

The gate-drain capacitance has been determined as 1.8 fF at $V_D = 0$ V.

The dependence of C_{GD} on the drain voltage is shown in Fig. 1(c). The decrease in C_{GD} as V_D increases is related to the formation of a stationary Gunn domain in the gated region of the channel, which cuts off the intrinsic gate-drain capacitance.⁴ The decrease in C_{GD} (≈ 0.15 fF) must be nearly the intrinsic gate-drain capacitance. The remaining gate-drain capacitance of ≈ 1.65 fF is extrinsic to the channel and represents the parasitic capacitance C_{GD}' between gate and drain contact pads. This interpretation is confirmed by a numerical computation of the planar capacitance.

The physical origin of the parasitics is shown in Fig. 2(a) and the corresponding equivalent circuit in Fig. 2(b). Common-source gain S_{21} of IPGFET1 is calculated and plotted as a function of frequency up to 1 THz in Fig. 2(c) with the parameters obtained by DC and ultrafast measurements. The curve with $V_D = 0$ V represents the characteristics of the displacement current. In the frequency region above 1 GHz, the displacement current overwhelms the particle current even in the velocity saturation regime with V_D as high as 3 V. This is due to the small transconductance $g_m \ll \omega C_{GD}$. The result is consistent with the characterisation of an ion-implanted IPGFET up to 1 GHz, where the displacement current was comparable with the particle current.⁵

The capacitance C_{GD} of this device is dominated by extrinsic parasitics. Furthermore, the transconductance g_m is small (≈ 7 mS/mm) and seems to be reduced by a channel resistance of ~ 70 k Ω associated with the long channel length. The parasitics can be reduced by decreasing the channel length (decreasing R_D and R_S), and by decreasing extrinsic gate-source and gate-drain parasitic capacitances (C_{GD}' , C_{GS}'). Two new IPGFET structures with reduced parasitics are shown in Fig. 3. The tapered connections from the source, drain and gates to their respective contacts represent a compromise between reducing the parasitic series resistances and increasing the extrinsic parasitic capacitances. The transconductance measured from DC characteristics was increased to ≈ 40 mS/mm.

IPGFET2 (Fig. 3(a)) has ≈ 0.25 μ m channel width over a ≈ 1.2 μ m channel length. The drain transient for IPGFET2 is shown in Fig. 4, and is independent of drain voltage between 0 and 3 V. Also shown is a fit to the derivative of the gate transient (solid curve). The drain transient is clearly broadened compared to dV_G/dt . This is due to the distributed nature of C_{GD}' and the finite time taken for the electrical transient to propagate from the CPW to the gate. Also shown in Fig. 4 is

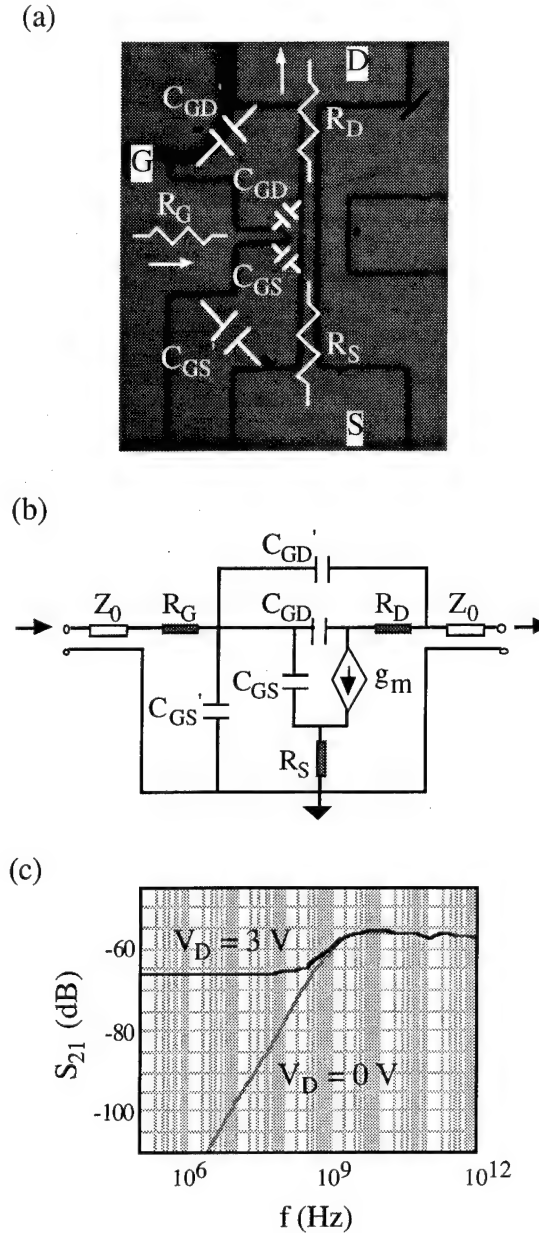


Fig. 2: (a) Physical origin of parasitics illustrated on the top view of IPGFET1. (b) the corresponding equivalent circuit. (c) Common-source gain (S_{21}) versus frequency up to 1 THz for the equivalent circuit.

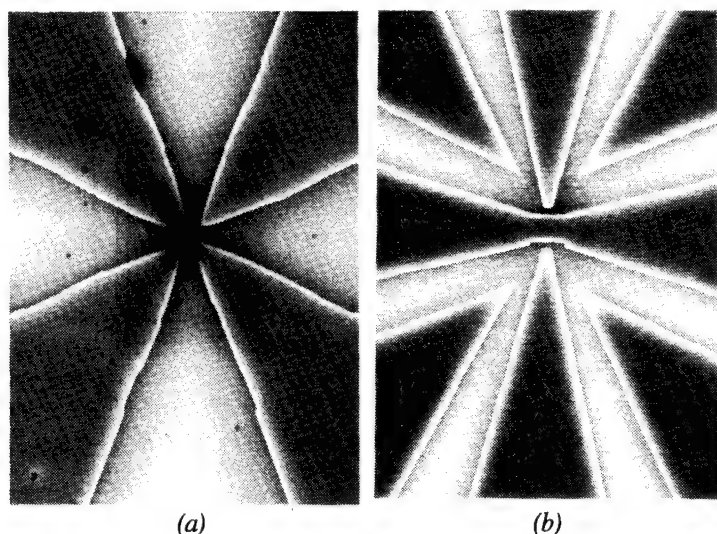


Fig. 3: Scanning electron micrographs of IPGFET2 (a) and IPGFET3 (b).

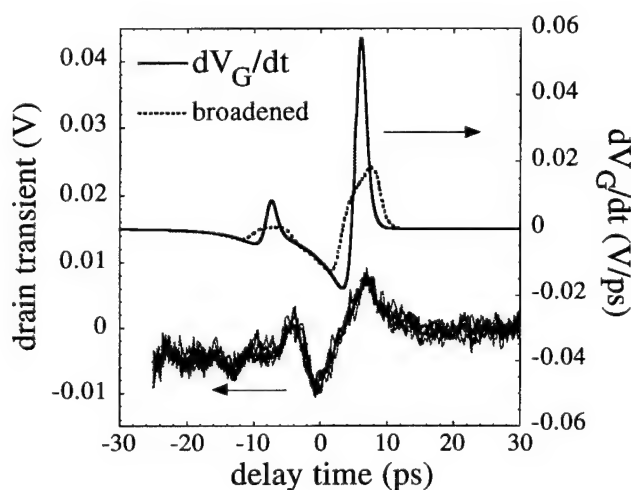


Figure 4. Drain transient of IPGFET2. Also shown is a fit to dV_G/dt , and dV_G/dt broadened by a 3 ps square pulse.

dV_G/dt broadened by a 3 ps square pulse, which shows closer agreement with the measured drain transient. The value of C_{GD}' is estimated between 1.6 and 4.8 fF depending on the degree of pulse broadening. Numerical calculations predict $C_{GD}' \approx 2$ fF for 30 μm distance from the channel to the CPW. The intrinsic capacitance C_{GD} is estimated < 0.1 fF.

IPGFET3 (Fig. 3(b)) has channel width 1.5 μm over a channel length of 2.5 μm . This device has grounded shields between the gates and the source / drain to reduce extrinsic parasitic capacitance. The ratio of the conductor width to the separation from the ground shields is the same as that of the CPW, in an attempt to guide the wave as close as possible to the device. The displacement current induced on the drain was reduced compared to IPGFET2 by a factor of ≈ 2 , with similar broadening compared to dV_G/dt . This indicates a reduction in C_{GD}' , although detailed comparison is difficult due to the uncertainty associated with the degree of pulse broadening. Numerical calculation of the electrostatic capacitance predicts a factor of ≈ 2 decrease in C_{GD}' for IPGFET3 due to the grounded shields.

In conclusion, parasitic capacitances have been determined in IPGFET's via electro-optic sampling of the displacement current. The extrinsic parasitics dominate C_{GD} , although these may be reduced by extending

the waveguide very close to the active region of the device. The high frequency performance of these devices is limited by the small value of (g_m / C_{GD}) .

References

- ¹J. Nieder, A. D. Wieck, P. Grambow, H. Lage, D. Heitmann, K. v. Klitzing and K. Ploog, Appl. Phys. Lett. **57**, 2695 (1990).
- ²M. Y. Frankel, J. F. Whittaker and G. A. Mourou, IEEE J. Quantum Electron. **28**, 2313 (1992).
- ³J. Allam, K. Ogawa, J. D. White, N. de B. Baynes, J. R. A. Cleaver, I. Ohbu, T. Tanoue and T. Mishima, OSA Proceedings on Ultrafast Electronics and Optoelectronics **14**, 197 (1993).
- ⁴R. W. H. Engelmann and C. A. Liechti, IEEE Trans. Electron Devices, **ED-24**, 1288 (1977).
- ⁵J. S. McLean, A. D. Wieck, M. Bledner and K. Ploog, Appl. Phys. Lett. **61**, 1324 (1992).

Picosecond Photoconductive Sampling with Nanosecond Carrier Lifetimes Using an Integrated Inductive Loop

Andrew C. Davidson and Frank W. Wise

Department of Applied Physics, Cornell University, Ithaca, NY 14853
ph. 607-255-9956 fax. 607-255-7658

Richard C. Compton

School of Electrical Engineering, Cornell University, Ithaca, NY 14853
ph. 607-255-9231 fax. 607-255-2792

High-speed optical sampling of electrical signals is usually carried out by either electro-optic¹ or photoconductive² sampling. These methods are capable of sub-picosecond temporal resolution and have found widespread use in the characterization of optoelectronic devices, but suffer certain drawbacks. To achieve responses in the one-picosecond regime^{3,4}, photoconductive techniques rely on short-lifetime material such as low-temperature-grown or ion-damaged GaAs. Short-lifetime material may be well-suited for devices such as photodetectors, but more complicated integrated circuits generally use high-quality, long-lifetime material. Photoconductive measurements on such circuits can be accomplished by selectively ion-damaging the desired region, but this requires additional processing steps. The method of electro-optic sampling^{5,6} is capable of sub-picosecond resolution but has more complicated optical requirements and several limitations. With substrate probing, the substrate must exhibit the Pockels effect and must be transparent to the probe beam. With external-crystal probing, a sufficiently small electro-optic crystal is required and must be positioned within the electric field of the signal to be sampled. This paper describes a new high-speed method of photoconductive sampling intended to overcome these drawbacks. The method relies on electromagnetic coupling to generate the time derivative of a signal; a slow sampling gate fabricated on long-lifetime material then integrates the coupled signal to produce the desired waveform.

In standard photoconductive sampling, a signal waveform with voltage $v_{sig}(t)$ is sampled at a variable time τ after its generation. The result of sampling, $I_{std}(\tau)$, appears as a DC current in the measurement and is given by⁷,

$$I_{std}(\tau) = \int_{-\infty}^{+\infty} v_{sig}(t) \cdot f_{samp}(t - \tau) dt \quad (1)$$

where $f_{samp}(t)$ is the sampling result produced by a delta-function signal waveform and is thus ideally a delta function. Its risetime is determined by the gap capacitance and the duration of the optical pulse, and can be under 1 ps. The falltime reflects the time-dependent conductivity of the gap and is therefore determined by the carrier lifetime, which is typically nanoseconds or longer. This limits the temporal resolution of the measurement.

To overcome the limitations imposed by a long carrier lifetime, the approach presented here uses a small sampling circuit placed in close proximity to a conductor of the transmission line to produce weak electromagnetic coupling. This coupling is assumed to be proportional to the time derivative of the signal waveform, as would result if the coupling were a mutual inductance L producing an induced voltage $L \cdot di_{sig}/dt = (L/Z_0) dv_{sig}/dt$. A sampling device is placed in the circuit and illuminated with delay τ relative to the signal waveform. Defining $f_{samp}(t)$ now as the sampling result produced by a step-function signal waveform and noting that for finite lifetimes it approaches zero at $\pm\infty$, the DC signal produced by the sampling circuit, $I_{coup}(\tau)$, will be given by

$$I_{coup}(\tau) = \int_{-\infty}^{\infty} \frac{d}{dt} v_{sig}(t) \cdot f_{samp}(t - \tau) dt = - \int_{-\infty}^{\infty} v_{sig}(t) \cdot \frac{d}{dt} f_{samp}(t - \tau) dt \quad (2)$$

Comparison with (1) shows that this electromagnetically coupled sampling is equivalent to standard sampling with the effective sampling response $-df_{samp}/dt$. Sampling in this manner is closely related to the differential photoconductive sampling introduced by Paslaski and Yariv⁸.

The ideal form of $f_{samp}(t)$ for coupled sampling is a step function. For signal waveforms with fall times below ~ 100 ps, the slow response of sampling devices fabricated on long-lifetime (~ 1 ns) material will approximate a step function and thus are well suited for this application.

To demonstrate coupled sampling, circuits were fabricated on semi-insulating GaAs. An interdigitated metal-semiconductor-metal (MSM) detector ($1 \mu\text{m}$ fingers, $2 \mu\text{m}$ gaps, $40 \times 40 \mu\text{m}^2$ active area) was placed at one end of a coplanar waveguide transmission line to generate a short, ~ 30 -ps electrical pulse. An inductive sampling loop $100 \mu\text{m}$ long was embedded in one of the transmission line's outer conductors as shown in Figure 1, and a device identical to the generating detector was placed in the loop to gate the coupled signal. As will be seen below, this detector is operated so as to have the desired step-function response. The detectors were illuminated with 100-fs pulses from a mode-locked Ti:sapphire laser.

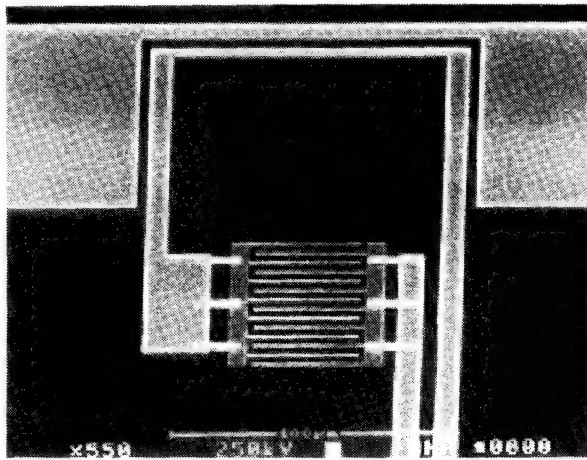


Figure 1. Sampling loop with MSM detector imbedded in outer conductor of CPW transmission line.

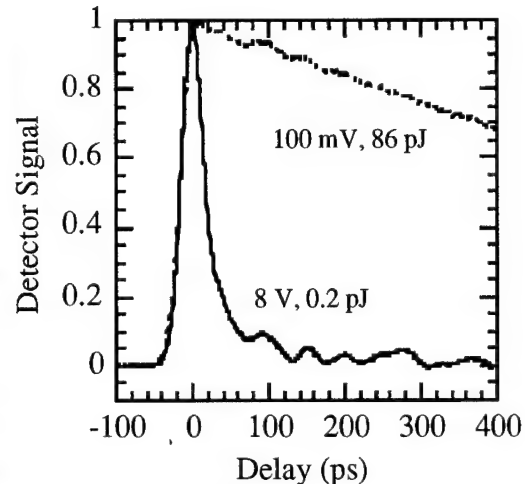


Figure 2. Fast and slow response of a detector measured with sampling oscilloscope.

The generating and sampling photodetectors were operated under different conditions to generate a short electrical pulse and to produce a step-function response, respectively. The generating device was biased at 8 V and illuminated with pulses of low energy (0.2 pJ) to produce the short electrical pulse shown in Figure 2 as measured with 50-ohm coplanar probes. The response is limited by the rise time of the oscilloscope, and has a full-width at half-maximum (FWHM) of 30 ps. At low bias and intense (86 pJ) illumination the same device has a fall time of 1 ns. When compared with the response obtained with high bias and low pulse energy, this approximates the step-function desired for the sampling device. This slow response is caused by the low electric field and the high photogenerated carrier concentration. The low field results in longer transit times and carrier screening effects diminish the field further causing the device response to be lifetime-limited.

Several factors improve the sensitivity of our measurement which otherwise might be expected to suffer as a result of the weak coupling to the sampling circuit. Both the interdigitated geometry of the sampling detector and the high photogenerated carrier density increase the photoconductance, which, due to the weak coupling, can be made as large as desired without loading the circuit being tested. Although the sensitivity limit has not yet been explored, measurements thus far demonstrate adequate sensitivity for signal magnitudes of a few tens of millivolts.

Figure 3 shows the measured current $I_{\text{coup}}(\tau)$. The observed risetime is 5 ps, and the FWHM is ~ 20 ps. The longer falltime is caused by the carrier transit time in the generating device, while the uneven nature of the decay is probably due to reflections in the loop circuit; better termination of this circuit should improve this result. Circuit simulations indicate that the 5 ps risetime reflects the measurement resolution, which is limited by the self inductance of the loop and the sampling device capacitance. These parasitic elements may be decreased by making appropriate modifications to circuit dimensions and geometry such that a factor of 3-4 improvement in measurement speed should be possible.

In summary, a high-speed sampling technique has been introduced which is well-suited for sampling on long-lifetime material. A sampling response with a FWHM of 5 ps was achieved on semi-insulating GaAs with a lifetime of ~ 1 ns. By minimizing circuit parasitics the sampling response is expected to reach the 1-2 ps range.

This work was supported by the Joint Services Electronics Program.

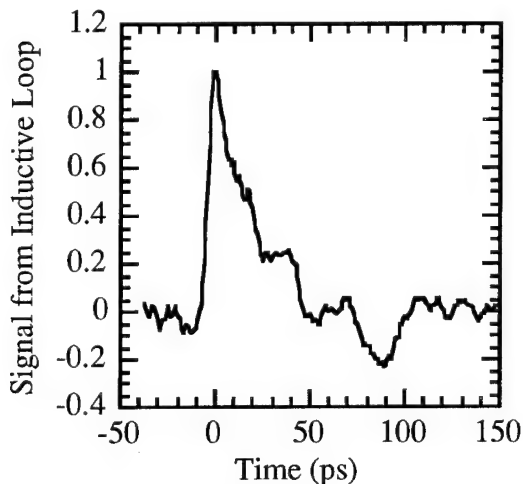


Figure 3. Measurement result from sampling with the integrated loop. The 5 ps risetime reflects the sampling resolution, and is dominated by the self inductance of the loop and the sampling detector capacitance. The 30 ps decay was measured with a 1 ns sampling device. The feature at 90 ps is a reflection off the end of the transmission line.

References

1. J. A. Valdmanis, G. Mourou, and C. W. Gabel, *Appl. Phys. Lett.* **41**, 211 (1982).
2. D. H. Auston and P. R. Smith, *Appl. Phys. Lett.* **41**, 599 (1982).
3. F. W. Smith, H. Q. Le, V. Diadiuk, M. A. Hollis, A. R. Calawa, S. Gupta, M. Frankel, D. R. Dykaar, G. A. Mourou, and T. Y. Hsiang, *Appl. Phys. Lett.*, **54**, 890 (1989).
4. D. R. Grischkowsky, M. B. Ketchen, C-C. Chi, I. N. Dulling III, N. J. Halas, and J. M. Halbout, *IEEE J. Quantum Electron.* **QE-24**, 221 (1988).
5. J. A. Valdmanis and G. Mourou, *IEEE J. Quantum Electron.* **QE-22**, 69 (1986).
6. B. H. Kolner and D. M. Bloom, *IEEE J. Quantum Electron.* **QE-22**, 79 (1986).
7. D. H. Auston, *IEEE J. Quantum Electron.* **QE-19**, 639 (1983).
8. J. Paslaski and A. Yariv, *Appl. Phys. Lett.* **55**, 1744 (1989).

Measurement of intensity-modulated signal generated by a two-wavelength laser diode array up to 7 THz

Ci-Ling Pan and Chi-Luen Wang

Institute of Electro-Optical Engineering, National Chiao Tung University

1001, Ta Hsueh Rd., Hsinchu, Taiwan 300, Republic of China

Fax: +886-35-716631 E-mail: clpan@cc.nctu.edu.tw

An optical beam which is intensity-modulated at terahertz (THz) rate is desirable for many applications such as wideband optical communication, heterodyne interferometry for absolute distance measurement, four-wave mixing in the laser diode, soliton pulse train generation, and THz radiation generation. Generation of modulated signal by direct modulation of a high-speed laser diode or by external waveguide modulator were limited 30 GHz [1] and 150 GHz [2], respectively. Optical generation of narrow band millimeter wave signal up to 60 GHz was demonstrated by mixing two lasers in a HEMT device [3]. Experimentally this requires precision alignment of two frequency-stabilized lasers, at least one of which is tunable. By recombining a linear chirped optical pulse through a Michelson interferometer, a tunable optical quasi-sinusoidal intensity modulation up to 1 THz but with a duty cycle of less than 0.3% was achieved recently [4]. In this work we report the generation and measurement of an cw intensity-modulated optical beam at the highest modulation frequency reported to date, 7 THz.

Figure 1 shows the experimental setup. The light source which provides the intensity-modulated output is a tunable two-color laser diode array ($\lambda = 0.81\mu\text{m}$) in an external grating-loaded cavity with a novel V-shaped double-stripe end mirrors [5,6]. This is shown in the inset of Fig. 1. The primary output of the laser consists of two wavelengths which are coaxial. The wavelength separation can be tuned by varying the separation of the two stripe mirrors. The length of each stripe is 15 mm and the angle between the two stripes is 15 degrees. The width of each stripe is 0.167 mm, corresponding to an equivalent spectral filter with a bandwidth of 0.27 nm. This is just smaller than the mode spacing of the diode chip, 0.32 nm. By vertically moving the stripe mirrors out of or into the plane of the inset of Fig. 1, we can tune the spectral separation of the two wavelengths continuously from 0.32 nm to 15 nm by multiples of 0.32 nm. This is shown in Fig. 2. The output power of each wavelength at maximum and minimum spectral separation are respectively 10 and 1 mW when the diode is biased at 300 ± 1 mA and 20 ± 0.1 °C. The threshold current of the laser is 260 mA.

The coaxial 2-color output of the laser is an intensity-modulated optical beam. The modulation frequency is just the beat frequency of the two resonant frequencies of the laser, which can be tuned from 0.15 to 7 THz. Since sensitive detectors with terahertz bandwidth is not yet available, we employ instead a noncollinear autocorrelator to characterize the multi-THz intensity-modulated signal. It can be readily shown that the time-averaged background-free correlation function of the laser output intensity is

$$G^{(2)}(\tau) = (I_1(t) + I_2(t-\tau))^2 + 2 I_1 I_2 \cos(2\pi\nu_b\tau), \quad (1)$$

where I_1 and I_2 are respectively the intensity at the two resonant frequencies, ν_1 and ν_2 , $\nu_b = \nu_1 - \nu_2$ is the beat frequency. If I_1 and I_2 are equal and ν_1 and ν_2 are phase-locked, the contrast ratio of $G^{(2)}(\tau)$ is equal to three.

Figure 3 shows the output of the correlator as a function of the delay time. The circles are experimental data points. The solid curve is a sinusoid at 7 THz, which corresponds to the beat frequency for the maximum spectral separation (14.89 nm) for the two-color laser diode array. The contrast ratio of the correlation trace in Fig. 3 is smaller than 3. There are several possible reasons for the smaller value. First of all, the far-field pattern of the laser output at the two wavelengths do not overlap

completely [5]. This increases the background level. Secondly, since the laser is not frequency-stabilized, residue fluctuations in the beat frequency could also contribute to the background. Furthermore, the output power of the laser at the maximum spectral separation is relatively low (≈ 1 mW). We also expect to improve the S/N ratio of the measurement by employing a thicker nonlinear crystal (1-mm-thick LiIO_3 was used).

In summary, we have demonstrated generation and detection of intensity-modulated optical signal at multi-THz rate. The frequency of the modulation signal can be tuned quasi-continuously from 0.15 to 7 THz by varying the spectral separation of the dual-wavelength laser output. Still higher frequency can be realized by biasing the laser at higher current. The multi-THz signal is measured using a non-collinear autocorrelator.

References

1. S. Weisser, J.D. Ralston, E.C. Larkins, I. Esquivias, P.J. Tasker, J. Fleissner, and J. Rosenzweig, *Electron. Lett.*, vol. 28, pp. 2141-2143, 1992.
2. K. Noguchi and K. Kawano, *ibid.*, vol. 28, pp. 1759 - 1761, 1992.
3. D.V. Plant, D.C. Scott, H.R. Fetterman, L.K. Shaw, W. Jones, and K.L. Tan, *IEEE Photon. Technol. Lett.* vol. 4, pp. 102 - 105, 1992.
4. C.-L. Wang and C.-L. Pan, *Appl. Phys. Lett.*, vol.64, pp. 3089- 3091, 1994.
5. C.-L. Wang and C.-L. Pan, *Opt. Lett.*, vol. 19, pp. 1456 - 1458, 1994.

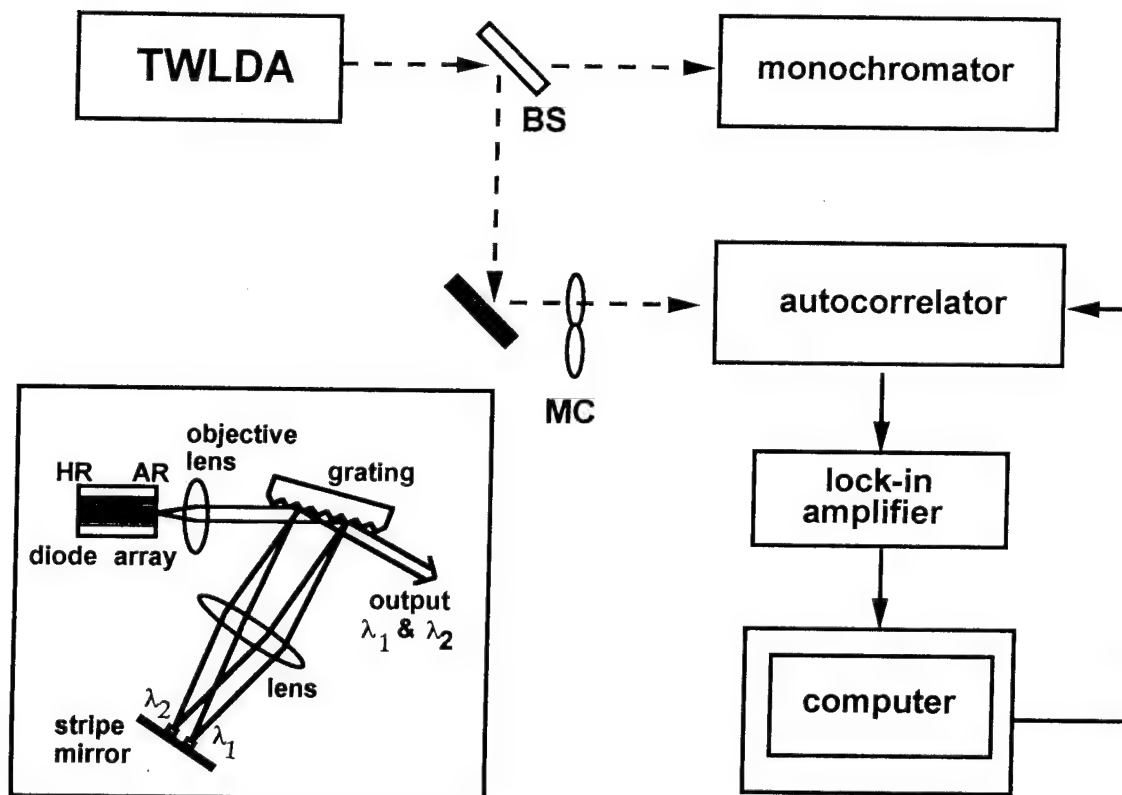


Fig.1 Experimental setup. TWLDA : 2-wavelength laser diode array; BS: beam splitter; MC: mechanical chopper. Inset shows the configuration of the TWLDA.

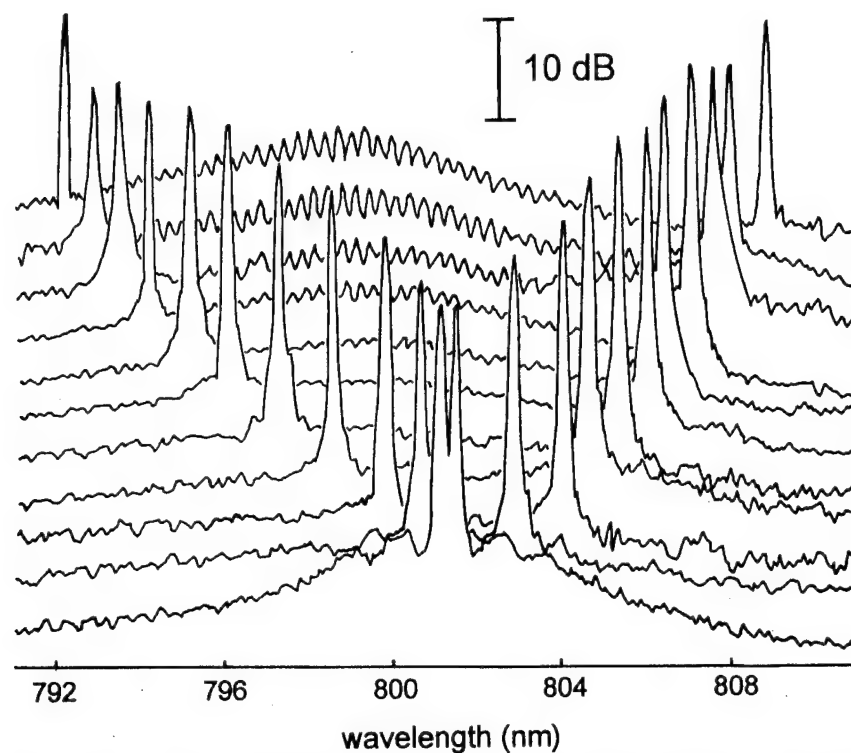


Fig.2 Spectral separation of the output of the TWLDA biased at 300 mA can be tuned from 0.32 to 15 nm. The side mode suppression ratio is 15 to 20 dB over this tuning range.

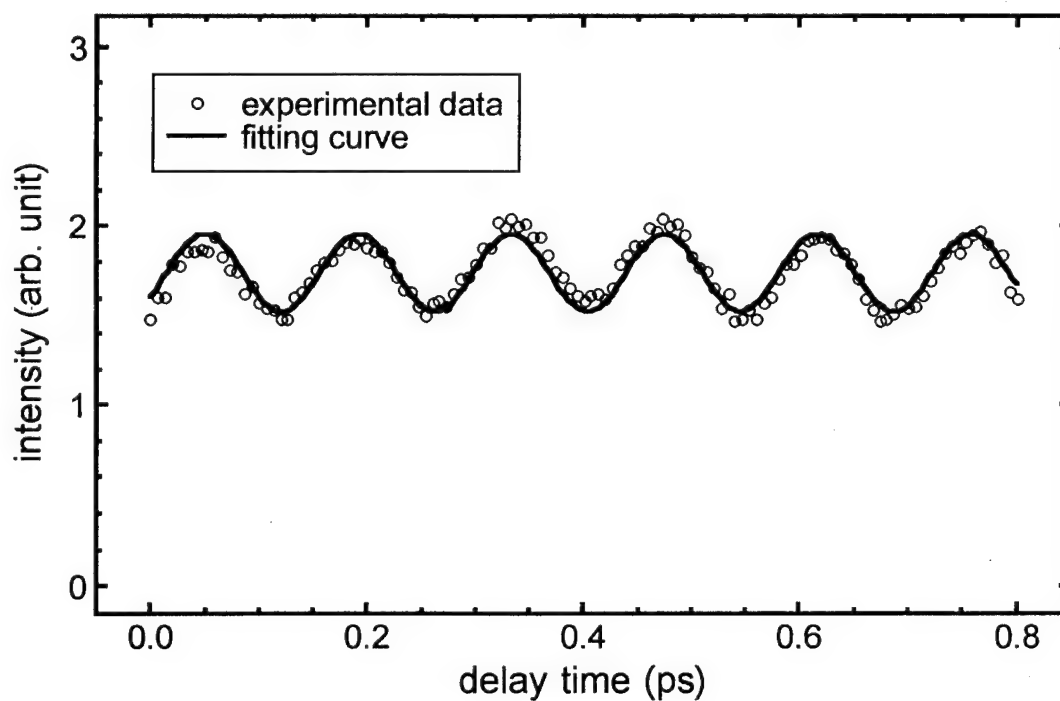


Fig.3 Intensity autocorrelation trace of a sinusoidal intensity-modulated optical signal at 7 THz.

Dependence of Large Signal Response on the Transverse Mode Structure in Vertical-Cavity Lasers

H. Deng, D.L. Huffaker, J. Shin, and D.G. Deppe

Microelectronics Research Center
Department of Electrical and Computer Engineering
The University of Texas at Austin, Austin, Texas 78712-1084
Tel.: (512) 471-4960
Fax: (512) 471-8575

The understanding of the limitations in the switching speed and the resulting mode behavior of the vertical-cavity surface-emitting laser (VCSEL) is important for its use in high speed optoelectronics. Previous studies have emphasized the speed limitations associated with the gain region and photon lifetime as set by the cavity length and mirror reflectivities [1,2]. Here we present data demonstrating the additionally strong interdependence of the transverse mode structure of the cavity and the temporal response of lasing, and show that the gain-switched response of the VCSEL can be substantially improved through the use of high contrast mirrors. The interdependence of the transverse mode structure and laser speed is demonstrated through direct comparisons of laser structures with differing gain regions and cavity designs.

Results from measurements of three different VCSEL structures are presented below. The laser structures differ in both the number of quantum wells (QWs) used for the gain regions as well as the type of mirrors used on the full-wave cavity spacer. A schematic illustration of two of the different types of cavity structures used in the experiment are shown in Fig.1. In the experiment three different VCSELs are used which have the same bottom mirror consisting of 26 pairs of AlAs/GaAs quarter-wave distributed Bragg reflector (DBR). For the upper mirrors, the first VCSEL has 16 pairs of AlAs/GaAs DBRs, while the second and third VCSELs have a single pair of quarter-wavelength layers of AlAs/GaAs followed by five pairs of high contrast ZnSe/CaF DBR. The two different VCSELs which use the ZnSe/CaF DBR are contrasted by one of which uses a three InGaAs QW active region, and a second which uses a single QW active region. The VCSEL with the 16 pair AlAs/GaAs upper DBR contains a three QW active region.

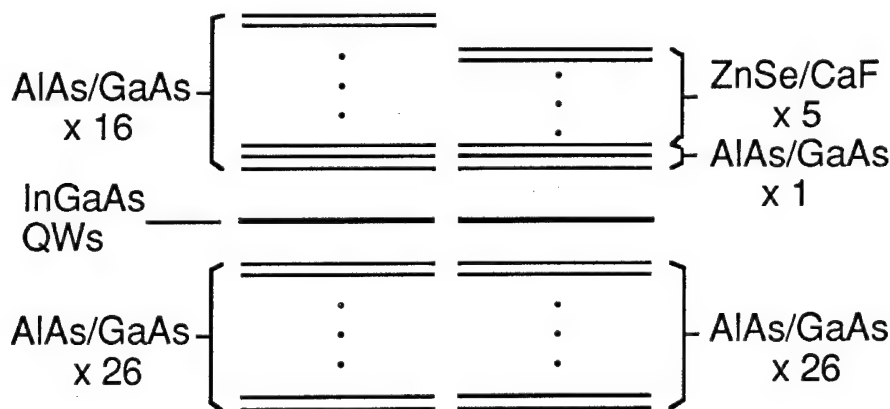


Fig.1 Schematic structures of the two different cavities studied.

First the lasing threshold versus temperature is measured for each VCSEL to determine the optimal temperature for gain tuning to the cavity mode. Subsequent measurements of each laser are carried out at its minimum threshold temperature where the quantum well gain peak matches the lowest order cavity resonance. The three different VCSELs are then characterized versus pump rate in terms of their optically gain-switched temporal response, far-field radiation pattern, and

spectral response. The temporal responses as measured by a streak camera are shown in Figs. 2 and 3, respectively, for the VCSELs with the three QW active regions and either 16 pair AlAs/GaAs DBR or the ZnSe/CaF DBR. For the first laser with the AlAs/GaAs top DBR, the FWHM of the emitted pulses are 60ps at $P=1.05P_{th}$, 54ps at $P=1.3P_{th}$, and 40ps at $P=4P_{th}$, with the corresponding delays of the pulse peaks of 90ps, 84ps and 64ps. For the shorter cavity VCSEL with the ZnSe/CaF DBR we see a much faster response, with the FWHM of the emitted pulses measured to be 36ps at $P=1.05P_{th}$, 20ps at $P=1.3P_{th}$, and 14ps at $P=4P_{th}$, and with the corresponding delays of the pulse peaks of 70ps, 38ps and 24ps, respectively. The single QW VCSEL which uses the ZnSe/CaF DBR has a slower response than the similar cavity three QW VCSEL, with FWHM of the emitted pulses measured to be 66ps at $P=1.05P_{th}$, 50ps at $P=1.3P_{th}$, and 40ps at $P=4P_{th}$, with the corresponding delays of the pulse peaks of 100ps, 68ps and 56ps.

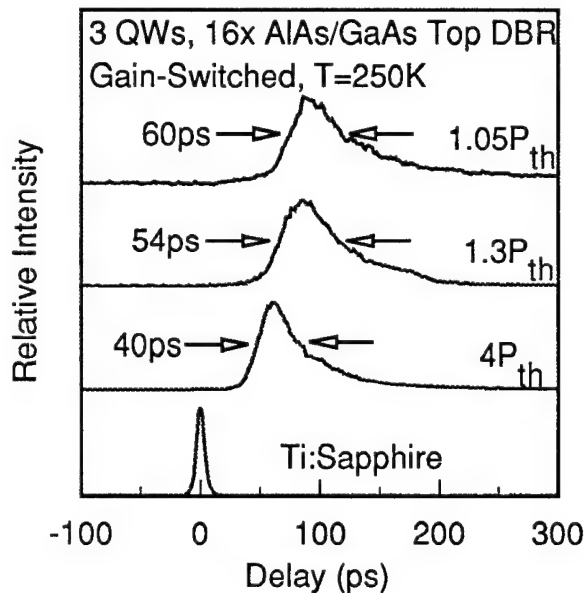


Fig.2 Temporal response of the three QW VCSEL with AlAs/GaAs top DBR.

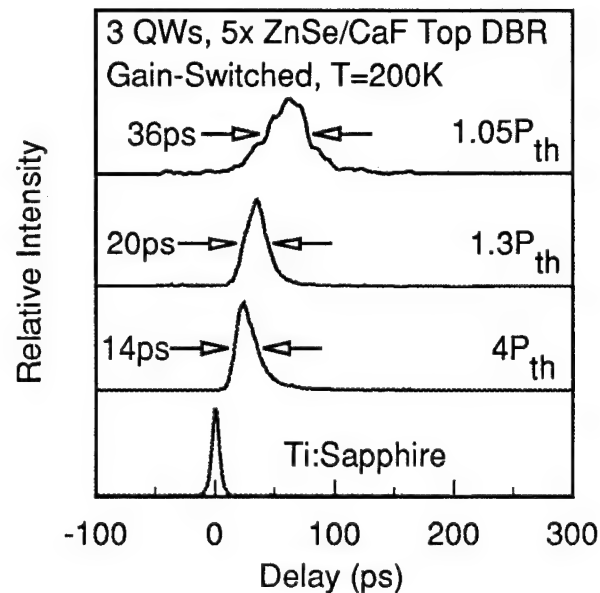


Fig.3 Temporal response of the three QW VCSEL with ZnSe/CaF top DBR.

The transverse lasing mode behavior as measured by the far-field radiation patterns are shown in Figs. 4 and 5 for the three QW VCSELs of Figs. 2 and 3. For reference, the radiation patterns with a quasi-continuous wave (CW) (pulses of 100ns) pump source are also shown. Little change is observed in the lobe widths under quasi-CW operation for pump powers up to 4 times threshold. However, for gain switched response the far-field radiation pattern broadens in accordance with a decrease in the temporal pulse width. This can be seen by directly comparing the radiation patterns and temporal responses of the VCSEL with the AlAs/GaAs top DBR, Figs. 2 and 4, in which both the temporal response and the broadening of the far-field radiation pattern saturates at higher pump rates. Not only does the three QW VCSEL with the upper CaF/ZnSe DBR show a decreased temporal response (Fig. 3), but the radiation pattern continues to broaden at higher pump powers for decreasing temporal pulse widths (Fig. 5). Measurements of the single QW VCSEL with the upper CaF/ZnSe DBR demonstrate the importance of both the optical gain region and the cavity in setting both the temporal response and the resulting transverse mode structure. The reduced gain of the single QW active region leads to a saturation of the broadening of the far-field radiation pattern in accordance with its slower temporal response as compared to the three QW VCSEL with the same cavity.

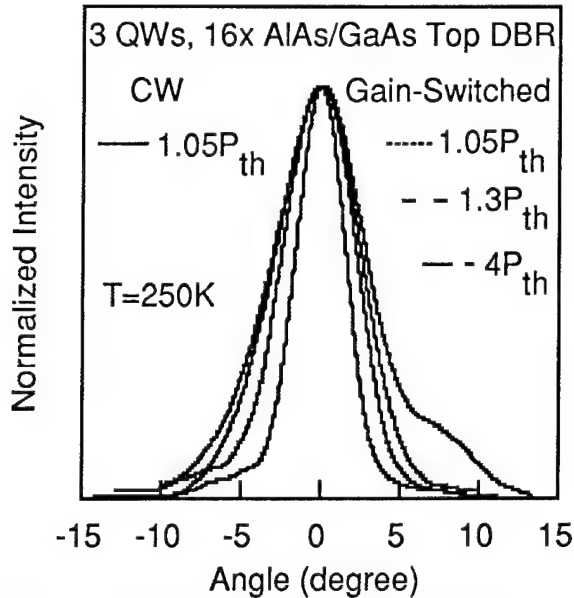


Fig.4 Far-field radiation patterns of the VCSEL with AlAs/GaAs top DBR.

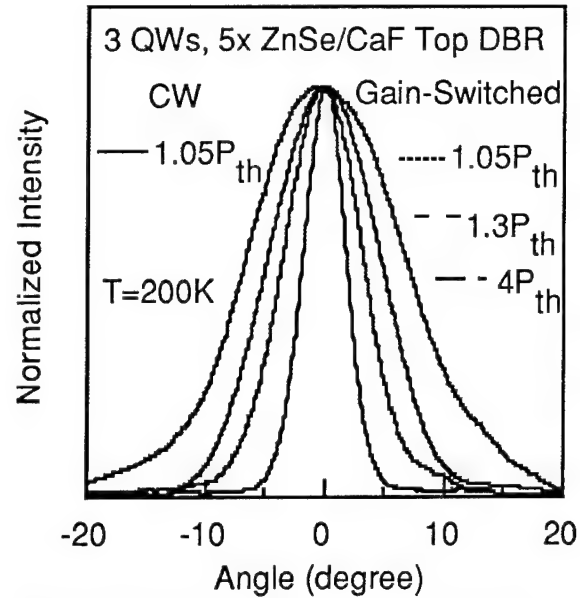


Fig.5 Far-field radiation patterns of the VCSEL with ZnSe/CaF top DBR.

In addition to the variety of data measured for the three VCSEL structures as presented above, we will also discuss the basis for the interdependence of the transverse mode structure and the temporal response. The interdependence arises due to the strong frequency dependence of the transverse mode structure in the short, high reflectivity cavity [3,4]. Spectral data will also be presented, as well as additional measurements underway for VCSELs fabricated with even higher contrast mirrors than presented above.

References

- [1] G. Hasnain, J.M. Wiesenfeld, T.C. Damen, J. Shah, J.D. Wynn, Y.H. Wang, and A.Y. Cho, IEEE Phot. Tech. Lett. **4**, 6 (1992).
- [2] J.M. Wiesenfeld and J. Stone, IEEE J. Quant. Electron. **22**, 119 (1986).
- [3] D.L. Huffaker, C.C. Lin, D.G. Deppe, B.G. Streetman, and T.J. Rogers, IEEE Phot. Tech. Lett. **6**, 135 (1994).
- [4] F. DeMartini, M. Marrocco, and D. Mura, Phys. Rev. Lett. **65**, 1853 (1990).

Wednesday, March 15, 1995

Nanometer Probing

JWA 8:30 am-10:00 am
Ballrooms VI-VIII

Gerard A. Mourou, *Presider*
University of Michigan

Applications of Scanning Force Microscopy for Voltage Measurements with High Spatial and Temporal Resolutions

Francis Ho, A. Samson Hou, Bettina A. Nechay, and David M. Bloom
Edward L. Ginzton Laboratory, Stanford University, Stanford, CA 94305

Introduction

To keep pace with device technology as it pushes towards 100-nm line widths and gigahertz operating speeds, new measurement tools are needed for studying mesoscopic device physics and for testing and designing the next generation of ultra-dense integrated circuits. A promising new direction is the use of scanning probe microscopes for such measurements, by utilizing probe tip nonlinearities for heterodyning very high-speed signals.[1-6] We have developed such an ultrafast system, based on the scanning force microscope (SFM), that should theoretically be able to map a voltage profile with subpicosecond temporal resolution and sub-micron spatial resolution. Furthermore, it is non-invasive, rugged, and does not require vacuum. By using the square-law force interaction between the SFM and sample for mixing and sampling, we have measured voltage transients as fast as 5 picoseconds. We have also used this system to probe VLSI integrated circuits.

Theory of Operation

Figure 1 shows the concept of an SFM probe system.[1] A scanning force microscope operates by using a CW laser and a position-sensitive detector to sense the deflection of a cantilever to which is attached a sharp tip. We operate an SFM in non-contact mode, in which a gap of approximately 10-100 nm is maintained between the tip and the circuit sample. There is a periodic high-speed voltage V_S on the sample that we wish to measure. We apply a pulse-train sampling voltage V_P to the tip. The voltage across the gap between the tip and the sample is $V_P - V_S$. The measured force is proportional to the square of this voltage and therefore contains a mixing term at an intermediate frequency (IF) corresponding to the offset frequency between V_P and V_S . This IF is chosen low enough so that the cantilever deflection can follow an equivalent-time representation of V_S .

Experiments

To illustrate the operation of the probe, we describe here the results from three experiments. In the first experiment, we probed various signals on an Intel 80486 microprocessor that had been depassivated. (We have also demonstrated non-invasive probing of circuits through passivating layers;[2] removal of passivation for devices that can tolerate it, however, yields improvements in voltage sensitivity and spatial resolution.) The experiment consisted of two parts. In the first part, we operated the microprocessor with a 20 MHz clock and probed the voltages on two metal lines on the microprocessor that carried opposite phases of

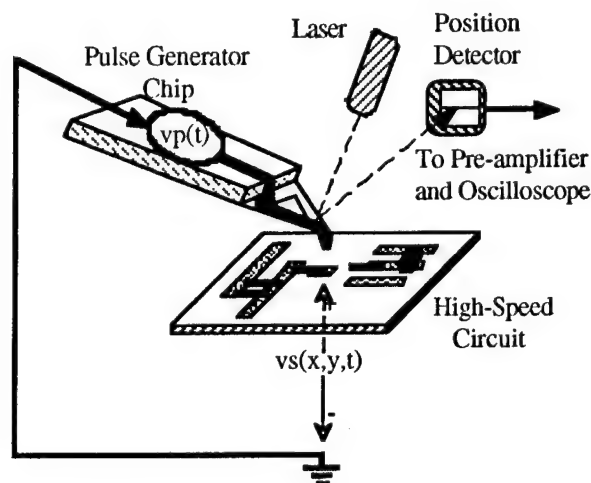


Figure 1. High-speed SFM probe system.

the clock; this is shown in Figure 2. The strobe pulses supplied to the tip were 2 ns in duration, which meant that the time resolution was 2 ns. Next, we operated the '486 in its self-test mode with a 10 MHz clock. In that mode, the microprocessor goes through a pre-defined series of logic states every time it receives a reset signal. By applying a reset every 20 clocks, we were able to measure a repeating self-test sequence, shown in Figure 3, using our probing system. The digital sequence can be easily discerned.

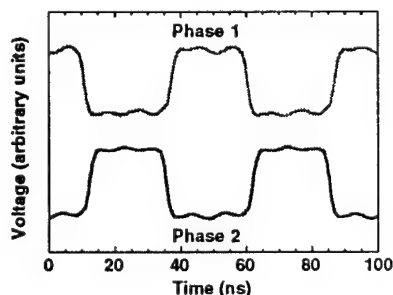


Figure 2. Two clock phases on the 80486 microprocessor.

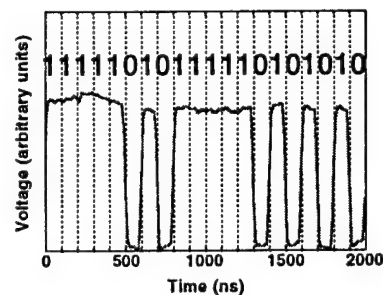


Figure 3. Self-test sequence of the 80486 microprocessor.

A second experiment, in which we probed National Semiconductor's AT/LANTIC (AT local area network twisted-pair interface controller) chip, further demonstrates the usefulness of this probe system for making precise timing and delay measurements. The AT/LANTIC incorporates a clock-recovery phase-lock loop to synchronize incoming ethernet data. A challenge in testing the AT/LANTIC was building the timebase electronics, shown in Figure 4, required for generating sampling pulses with proper timing with respect to the chip. Measured data from the chip are shown in Figure 5. PHCOMP is an asynchronous digital signal that requires about 250 ns to settle to a valid state. The first complete rising edge of PHCOMP (occurring at $t=330$ ns) is found to be significantly longer (15 ns) than subsequent edges (about 6 ns). The amount of edge broadening is a measure of the jitter in AT/LANTIC's phase-lock loop and also a function of the averaging time for the measurement. In comparison, a second, synchronous signal from the chip (DMUX) showed no significant difference in edge speeds from edge to edge. These results demonstrate the usefulness of the probe system for making precise timing and delay measurements.

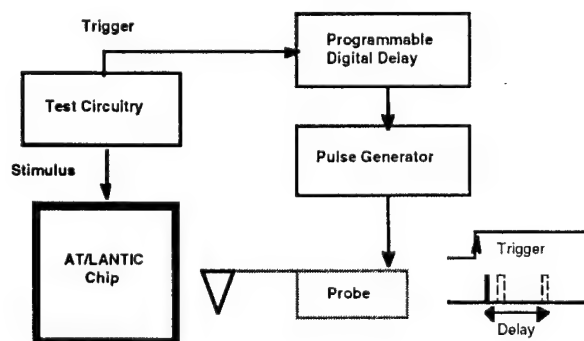


Figure 4. Timebase circuit for testing the AT/LANTIC.

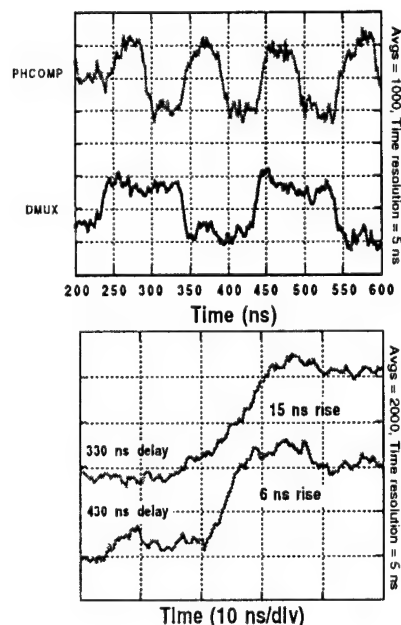


Figure 5. AT/LANTIC measurements.

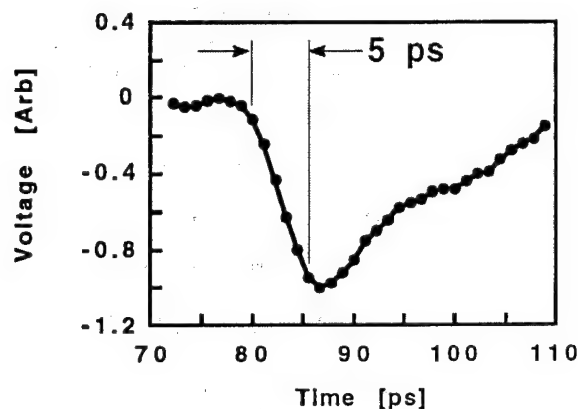


Figure 6. Probing of nonlinear transmission line.

The preceding experiments were all performed using gold-coated commercially available cantilevers, a scheme which does not work at frequencies greater than a few gigahertz. In order to obtain better temporal resolution, we microfabricated cantilevers with integrated transmission lines. Using these high-speed cantilevers, we were able to observe voltage steps as short as 5 picoseconds on circuits. This is shown in Figure 6. We used nonlinear transmission line (NLTL) circuits, which can generate subpicosecond voltage steps [7], to serve both as the source of the strobe pulses and as the circuit under test. In this experiment, the NLTL circuit and the cantilever chip were wire-bonded together. We anticipate that by integrating the NLTL circuit and the cantilever on the same substrate, we shall obtain sub-picosecond time resolution.

Conclusion

We have measured 5 ps voltage steps using equivalent time sampling, and probed various ICs, including an 80486 microprocessor and a National Semiconductor AT/LANTIC chip. In the future, we anticipate being able to probe with sub-picosecond and nanometer resolution by integrating pulse-generators with microfabricated cantilevers and tips.

This work is supported by ONR/ARPA under the Ultra program. We are grateful for the assistance of Bob Rao and Debbie Cook (both at Intel), Joe Byrne and William Ng (both at National Semiconductor), Pauline Prather, and David Su.

References

- [1] A.S. Hou, F. Ho, and D.M. Bloom, "Picosecond electrical sampling using a scanning force microscope," *Electronics Letters* **28**, 2302 (1992).
- [2] F. Ho, A.S. Hou, and D.M. Bloom, "High-speed integrated circuit probing using a scanning force microscope sampler," *Electronics Letters* **30**, 560 (1994).
- [3] D.M. Bloom, "Voltage-contrast scanning probe microscopy," *Proceedings of the 4th European Conference on Electron and Optical Beam Testing of Integrated Circuits*, Zurich, Switzerland 1-3 Sept. 1993. (To be published in *Microelectronic Engineering*.)
- [4] S. Weiss, D.F. Ogletree, D. Botkin, M. Salmeron, and D.S. Chemla, "Ultrafast scanning probe microscope," *Appl. Phys. Lett.* **63**, 2567 (1993).
- [5] K. Takeuchi and Y. Kasahara, "High-speed optical sampling measurement of electrical waveform using scanning tunneling microscope," *Appl. Phys. Lett.* **63**, 3548 (1993).
- [6] G. Nunes Jr. and M.R. Freeman, "Picosecond resolution in scanning tunneling microscopy," *Science* **262**, 1029 (1993).
- [7] M.S. Shakouri, A. Black, B.A. Auld, and D.M. Bloom, "500 GHz GaAs MMIC sampling wafer probe," *Electron. Lett.* **29**, 557 (1993).

Ultrafast Near-Field Optical Probing

Jason B. Stark

AT&T Bell Laboratories, Murray Hill, NJ 07974
908-582-2173 (voice), 908-582-4702 (fax), jstark@physics.att.com (email)

Umar Mohideen

Department of Physics, University of California, Riverside, CA 92521
909-787-5390 (voice), 909-787-4529 (fax), umar@ucrph0.ucr.edu (email)

Richart E. Slusher

AT&T Bell Laboratories, Murray Hill, NJ 07974
908-582-4094 (voice), 908-582-4702 (fax), res@physics.att.com (email)

Direct measurement of carrier dynamics, using femtosecond light sources, has yielded a wealth of understanding within the field of condensed matter physics^[1]. Also, recently, near-field optical probe techniques have enabled optical measurements with spatial resolution below the diffraction limit^[2]. An understanding of many scientifically and technologically important issues require a knowledge of the local behavior of carriers within materials and microstructures. We report the development of the required instrumentation, and the first measurement of carrier dynamics with spatial resolution below the diffraction limit and temporal resolution below 60 fs.

The experimental instrumentation consists of a broadband modelocked light source, a pair of acousto-optic modulators (AOMs), and a near-field optical microscope (Fig. 1). Modelocked pulses are separated into pump and probe, and chopped independently by the AOMs. Probe pulses are delivered to the optical fiber probe tip of the near-field microscope, and illuminate the sample. The transmitted light is collected by the objective of a far-field microscope, and delivered, through a multimode optical fiber, to a spectrometer where a photomultiplier tube registers the signal. The pump pulses are delivered through a beam-splitter to the same objective and focused to a far-field spot on the sample. The nonlinear optical response of the sample is recorded as the sample is scanned within the near-field of the fiber probe tip, taking one image for each setting of the time delay between pump and probe pulses. In this way, carrier dynamics within the sample can be imaged as a function of time after excitation, with a time resolution as low as 40 fs, and spatial resolution as small as 50 nm. The results can be displayed as a sequence of animated movie frames.

Infrared optical pulses are generated in a modelocked Ti:Sapphire laser, with a repetition rate of 82 MHz and average power of 400 mW. The spectral bandwidth is adjustable up to a maximum of 100 nm about the 800 nm center. The pulsewidth, from the 3 mm crystal, is below 15 fs. The output enters a two-pass prism-pair dispersive delay line, for compensation of the positive dispersion of the output coupler and subsequent optics. Within this delay line, the beam is spectrally separated into pump and probe. A pair of pick-off mirrors then direct the long-wavelength probe, and short-wavelength pump to the experiment. The pump beam passes through a variable delay line, followed by an AOM, operating at 3.1 MHz. It then enters the far-field microscope, and is reflected downwards from a beam-splitter, through the objective, onto the sample. This far-field pump is focused on the sample to a spot on the order of 5 μm , to uniformly excite the region probed by the fiber tip.

The probe beam enters a second dispersive delay line, using a two-pass grating-pair geometry, to pre-compensate the dispersion introduced during passage through the 1-meter fiber probe tip. The probe beam is modulated at 3.0 MHz. Pulses enter the probe tip and emerge with a pulsewidth of 50 fs. The fiber probe tip is a single-mode optical fiber whose end has been tapered and coated

with aluminum to leave a small aperture, typically 50-100 nm^[3]. Light propagating through this aperture is coupled into the far-field and subsequently detected. The coupling efficiency of such tips is typically -50 to -60 dB; the remaining light is absorbed in the aluminum, causing heating, and imposing an upper limit on average power of the order of 1 mW. Light levels in the far-field of the tip are then in the nW regime. The sample is held in the near-field of the fiber tip using a shear-force feedback technique^[4], stabilizing the tip-sample separation at around 50 nm. The fiber tip is imaged into a multimode optical fiber, and delivered to a spectrometer to control the probe bandwidth reaching the detector. In a transmission experiment, the absorption of the sample is measured locally by the fiber probe tip, and the sample scanned to form an image. In a nonlinear transmission measurement, the nonlinear response, at the 100 kHz modulation sideband, is recorded simultaneously.

Samples of GaAs quantum wells were etched to produce 150 nm thick disks, of varying diameters from 3 to 10 μm , with eight periods of 10 nm wells separated by 5 nm barriers. The room-temperature excitonic absorption edge is at 850 nm. Measurements made using the full laser spectrum indicate that the carrier recombination in the center of the microdisks is exponential, with a time constant of 500 ps. In the first set of measurements, the pump beam was filtered before the sample, to a 10 nm bandwidth about 800 nm, while the probe was filtered after the sample to 10 nm about 820 nm. In this case the probe measures carriers well above the bandedge, as they relax from their initial distribution, as injected by the pump. Figure 2 shows the nonlinear signal, measured by the probe, in two microdisks (upper right and lower left) of diameters 5 and 10 μm . The image is produced by linearly scanning the X- and Y-voltages on the sample piezoelectric tube (distortions of the circular shape are caused by a nonlinear relationship between the displacement and applied voltage). The nonlinear optical response at 67 fs delay (a) shows the carriers relaxing after excitation by the leading edge of the pump pulse. After 133 fs (b) the nonlinear response is near its peak, indicating a time resolution on the order of 60 fs. After the initial excitation, measurements (c,d,e) at 2, 20 and 67 ps, respectively, show that carriers relax in the microdisks with a time constant on the order of 80 ps. The measured recombination time was 500 ps, with the 80 ps relaxation rate indicating the rate of carrier cooling. Furthermore, carriers near the edges of the microdisks relax most quickly, leaving the nonlinear response peaked strongly toward the center for time delays beyond 1 ps. The spatial resolution in these images, though not rigorously characterized, is on the order of 400 nm. Ultimate resolutions are expected to be under 100 nm.

We demonstrate, for the first time, submicron spatially resolved images of carrier dynamics, with time resolution better than 60 fs. Carriers injected uniformly into the microdisks cool in a time of 80 ps, most quickly near the edges, where they may relax into surface trap states. Studies continue to measure the details of this relaxation, as a function of probe wavelength and with better spatial resolution. Similar studies are under way to study nonequilibrium transport in narrow channel electronic devices, as well as local carrier dynamics in operating semiconductor lasers. Measurements with high spatial and temporal resolution have now evolved from the stage of instrumentation development, to begin producing results having important scientific and technological implications. The rapid development of this field presents many exciting prospects, in the very immediate future, for the study of carrier dynamics in materials and microstructures.

- [1] *Hot Carriers in Semiconductor Nanostructures*, ed. Jagdeep Shah, Academic Press, San Diego, California, 1992
- [2] E. Betzig, J. K. Trautman, *Science* **257**, 189 (1992)
- [3] E. Betzig, J. K. Trautman, P. D. Harris, J. S. Wiener, R. L. Kostelak, *Science* **251**, 1468 (1991)
- [4] E. Betzig, P. L. Finn, J. S. Wiener, *Appl. Phys. Lett.* **60**, 2484 (1992)

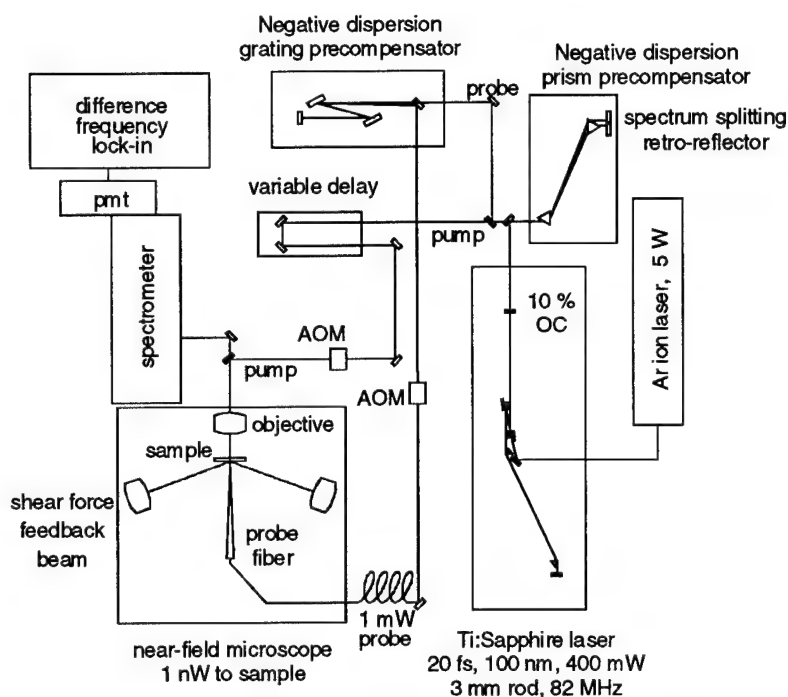


Figure 1. Ultrafast near-field probe. Ti:Sapphire laser pulses spectrally split into pump and probe. Probe precompensated for dispersion, pump delayed, each modulated by AOM. Probe coupled into fiber tip, through sample in near-field, into spectrometer. Pump focused onto sample. Difference frequency measured.

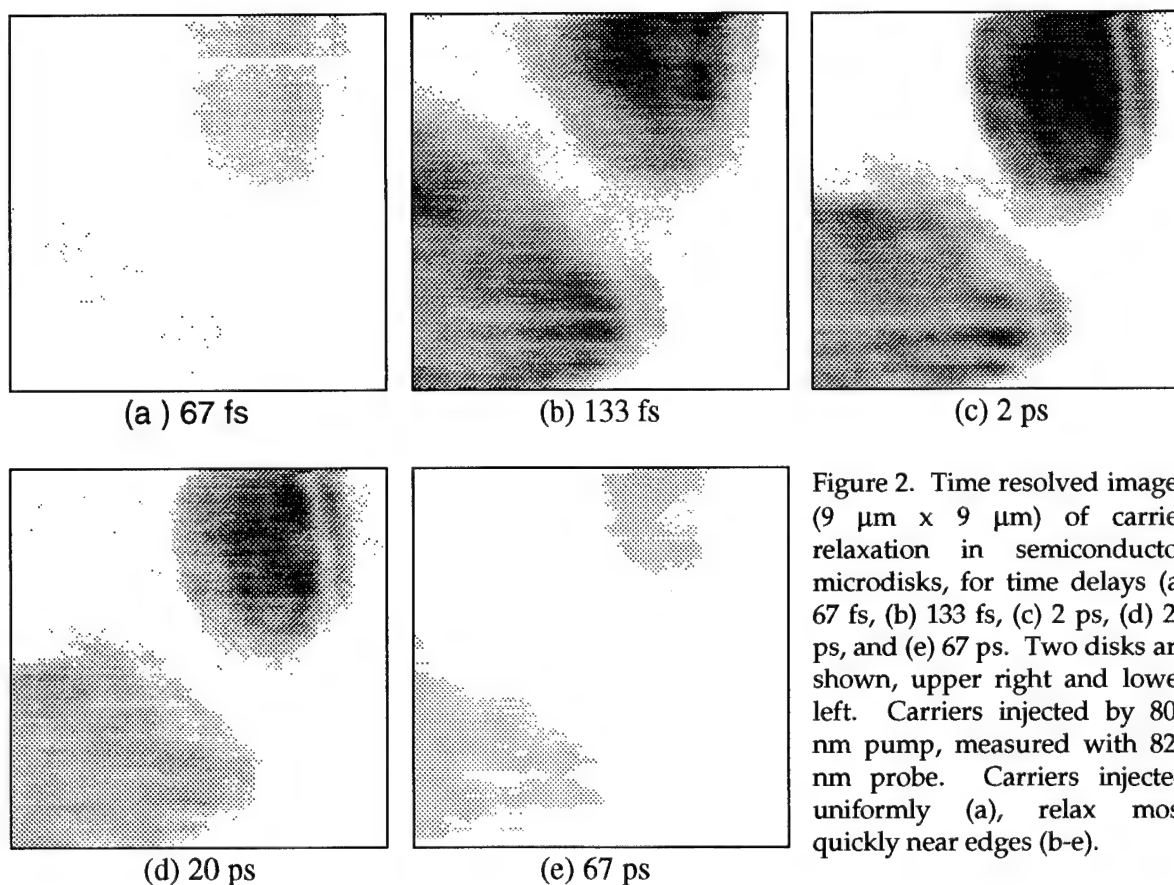


Figure 2. Time resolved images ($9\ \mu\text{m} \times 9\ \mu\text{m}$) of carrier relaxation in semiconductor microdisks, for time delays (a) 67 fs, (b) 133 fs, (c) 2 ps, (d) 20 ps, and (e) 67 ps. Two disks are shown, upper right and lower left. Carriers injected by 800 nm pump, measured with 820 nm probe. Carriers injected uniformly (a), relax most quickly near edges (b-e).

Laser-Diode Based Scanning Force Microscope and Ultrafast Sampling Probe

John Nees and Douglas Craig

University of Michigan, Ultrafast Science Laboratory 2200 Bonisteel Blvd. 1006/IST Ann Arbor MI 48109-2099
USA phone (313) 764-9271 fax (313)763-4876

Soichi Hama and Shin ichi Wakana

FUJITSU Laboratories Ltd. 1-10 Morinosato Wakana Atsugi, Kanagawa 243-01, Japan phone 81-046-248-4311,
fax 81-046-248-3896

Introduction

New discoveries in fabrication technology and in device physics have open the way for a class of electronic and optoelectronic devices with nanometer-scale dimensions. These devices offer the opportunity to work with electrons confined to 2-D, 1-D and 0-D in space. In an effort to understand how individual devices work it will be necessary to interrogate individual submicron structures. Aside from the fine dimensions of the contacts used for such measurements it will be necessary to make measurement with very low invasiveness and increasingly, with higher speed. To meet the challenges of new nano-technologies we have developed a probe which demonstrates high impedance voltage measurement using a 0.1-micron contacting tip. The voltage of the tip is photoconductively sampled allowing waveforms to be measured with picosecond resolution [1]. In this paper we describe the operation of the probe using a gain switched laser diode to make measurements which extract only a few fC from the device under test. We also show the probes value as a high-speed, high sensitivity probe for millimeter-wave circuits.

Probe fabrication

The probe is fabricated using Low Temperature grown GaAs (LT GaAs). That is, GaAs grown at 210°C rather than the conventional temperature of 600°C. A micron-thick layer of LT GaAs is grown on a half-micron-thick layer of AlGaAs on a semi-insulating GaAs wafer. Metal, defining the electrodes of a photoconductive switch, is patterned on the LT GaAs layer. The probe's perimeter is patterned by photolithography and defined by front-side etch penetrating through both epi-layers. A self-terminating lift off is used to define a fine probe tip having a tip radius below 0.1 μm [2, 3]. The GaAs substrate is chemically removed, freeing the 1.5 μm thick film of LT GaAs and AlGaAs as shown in figure 1. Following this UV curing cement is used to attach the probe to a glass support, and the finished probe is placed on a translation stage for use.

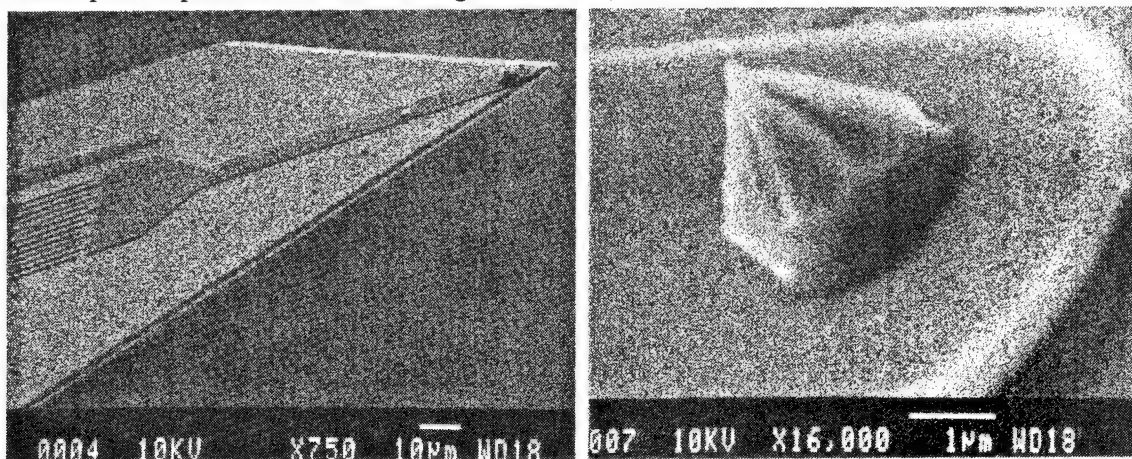


Figure 1 shows SEM pictures of the scanning force microscope probe and ultrafine tip.

Probe use

The probe is used in a Scanning Force Microscope (SFM) in the place of a conventional cantilever probe. It is mounted and aligned on the SFM stage and an image of the device-under-test is scanned. The probe tip is then positioned at the desired location and pressed into low-force contact with the signal-line to be interrogated. Picosecond resolution is obtained by photoconductively switching charge from the device under test during the picosecond on-time of the probes gate. This samples the electronic waveform on the device-under-test by allowing an amount of current proportional to the waveform voltage to pass on to the detection electronics. The delay of the switching beam is swept to perform equivalent time sampling of the repetitive waveform.

The experiment

A photoconductive SFM probe was made as described above. The gate was illuminated through a fiber-optic connection supported by the substrate used to support the probe on the SFM scanning arm. In this configuration the probe was scanned over the sample, rather than *vice versa*. In order to measure the effects of parasitic

capacitance on the circuit under test and amplifier was attached to the output of the probe. The *ac* transients measured without illumination of the gate switch agreed with the calculated capacitance of 10 fF. With illumination turned on and a dc voltage applied to the circuit under study a mapping of the tip contact was made over the active area of a test structure. The conductivity mapping was indicative of the uniformity of contact over the surface of the conductor. As may be seen in figure 2(a,b, c, and d) contact with the surface was not continuous during the scan, nor was it repeated from the forward scan (1b) to the reverse scan (1d).

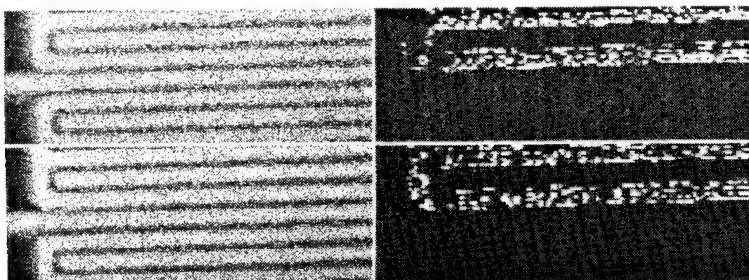


Figure 2 (row 1-a and b, row 2-c and d) shows topographic scans (a and c) of and electrode test pattern and scanned conductivity mapping (b and d) of the circuit. Note that only one loop is connected and that the contact for forward scan and reverse scan are neither identical, nor continuous.

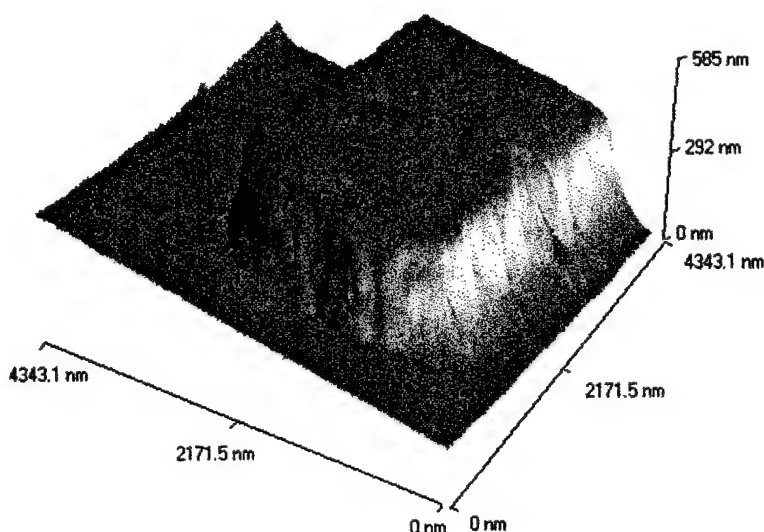
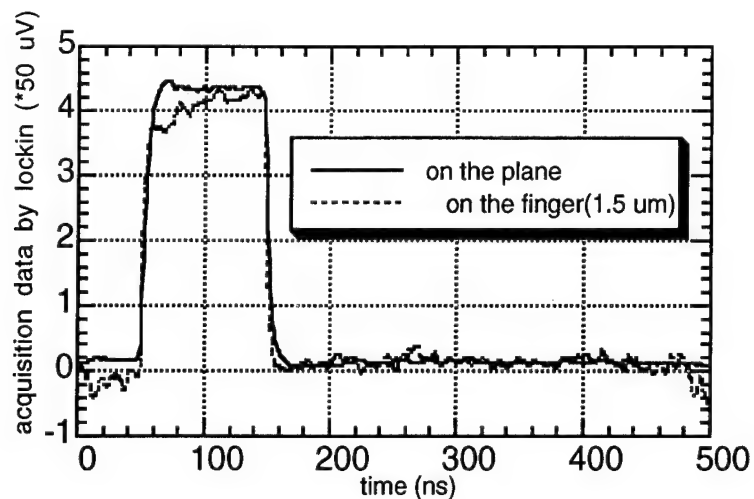


Figure 3 shows the topographic image of a 1.5 micron-wide metal finger on which transients are measured.

In low-force contact, our probe has a dark conductance of 0.05 nS as measured using a Fluke 27 multimeter. The test signal is generated by an electronic pulser and launched onto the device under test by an SMA connector. The measured signal is gated by a 30 x 30- μ m photoconductive switch integrated on the LT GaAs probe cantilever and carried on a coplanar stripline to a pre-amplifier and 20 MHz A/D converter. 810-nm, 100-ps optical pulses generated by a Hamamatsu gain switched laser diode are coupled to the probe by the optical fiber mounted with the probe. These pulses are estimated to have fJ of absorbed energy allowing only 5 fC of charge to be removed from the device under test. Delay between the optical sampling pulse train and the test signal is controlled by a computer controlled electronic delay circuit.

The results

Images scanned by the probe show 10 to 100-nm features. Signal-to-noise equal to unity is seen at 2V with a single shot measurement. With the same degree of invasiveness in the high speed signal single mV sensitivity is achieved at a sampling rate of 3 MHz.



Conclusions and References

Using a probe with demonstrated 2.5 ps temporal resolution and 100-nm spatial resolution we have been demonstrated laser diode-based sampling of integrated circuits. A single shot measurement of 2V sensitivity is possible with the removal of only 5 fC. This probe not only provides a critical solution to the problem of internal circuit testing on VLSI, but it also opens the door to investigation individual mesoscopic devices with unprecedented sensitivity.

The investigation of repeatability and continuity in these measurements is on-going.

D. R. Grischkowsky, *et al* IEEE J. Quantum Electron. QE-24, 221 (1988)

J. Kim, S. Williamson, J. Nees, S. Wakana, and J. Whitaker, Appl. Phys. Lett. 62 (18), 3 May 1993.

C.A. Spindt, L. Brodie, L. Humpfrey, and E. R. E. R. Westerberg, J. Appl. Phys. 47, 5248 (1976).

STOEM: Scanning Tunneling Optoelectronic Microscope

Koichiro Takeuchi, Akira Mizuhara
Teratec Corporation, 2-9-32 Naka-cho, Musashino-shi
Tokyo 180, Japan
FAX:81-422-52-2125, Phone:81-422-52-2102

Introduction

We applied a scanning tunneling microscope (STM) to optoelectronic sampling measurement of high-speed electrical waveform^[1]. An optical pulse train was used to turn on and off a photoconductive semiconductor switch (PCSS) made of low temperature GaAs on the STM probe. This special STM can be called scanning tunneling optoelectronic microscope (STOEM).

Because of Great advances in increasing the speed and in decreasing the size of electronic circuits and devices, a new measuring method with high temporal resolution in the order of pico seconds and spatial resolution in the order of sub-micro meters is required. In such high-speed, microscopic measurement, the high frequency signal must be converted to a signal with low frequency in a sufficiently small region at the point to be measured. Furthermore, the measurement must be carried out without mechanical contact or with so soft contact that the probe could not break the surface of devices under test (DUT).

Although an STM has been developed as a microscope with ultra-high spatial resolution since its invention in 1982^[2], its property of non-contact and high impedance is also useful for measuring high-speed electrical waveforms. Therefore an STM would be a powerful new instrument offering ultra-high temporal and spatial resolution.

Very recently, some groups have reported novel applications based on such concept^[1, 3-5]. Weiss et al.^[3] and Nunes et al.^[4] measured short electrical pulses using non-linearity of the tunneling current. By using an atomic force microscope (AFM) instead of an STM, Hou et al.^[5] measured a high-speed electrical waveform via the mechanical response of the AFM cantilever.

Experiments

Figure 1 shows a schematic view of the probe and the DUT. Our STOEM probe has a photo-conductive semiconductors switch (PCSS) on it. An optical pulse train with 100fs duration from a Ti-sapphire laser is used to turn on and off the PCSS. The periodic frequency of the optical pulse train is $80\text{ MHz} + 1\text{ kHz}$, which is synchronized to an external master oscillator, while the fundamental frequency of the DUT signal is 80MHz. The 1kHz frequency difference is the fundamental frequency of the sampled signal to be measured from the current. Therefore the electrical signal is extended 80,000 times along the time axis. This technique is similar to that used for a high-speed oscilloscope and E-O sampling.

Since the band width of the feedback circuit is set to be lower than 1kHz, control of the probe position is not disturbed by the waveform measurement.

The PCSS was fabricated by sputter-evaporating Au/Ti films in interdigitated feature on a semi-insulating GaAs crystal. The line width and the gap distance of the switching region are $5\text{ }\mu\text{m}$ each. The GaAs photoconductive layer was grown by MBE at low temperature ($<300\text{deg.}$) to introduce carrier recombination centers[6]. As the result, the PCSS response time was shortened better than 1.8ps. After fabricating the PCSS, the GaAs wafer was cleaved and the metal tip on the cleaved corner was used as the STOEM probe tip. The tip part of the GaAs wafer was removed by wet etching to make the metal tip protruding.

The schematic view of the experimental arrangement for testing the PCSS response is illustrated in figure 2. There are 5mm long coplanar strips (CPS) on a low temperature grown GaAs layer, and an additional electrode connected to the CPS via an interdigitated PCSS. The CPS has design impedance of $50\text{ }\Omega$ and consists of two parallel $60\text{ }\mu\text{m}$ wide strips separated from each other by $5\text{ }\mu\text{m}$. The design of the PCSS is the same as that mentioned above.

When a charged strip line is shorted via the photocarriers generated by an laser pulse, an electrical pulse is generated and propagates toward the PCSS. Under this condition we focused sampling pulse beam on the PCSS. Both the 10 mW exiting and 10mW sampling beams were from one Ti-sapphire laser which is the same as that used for the STOEM

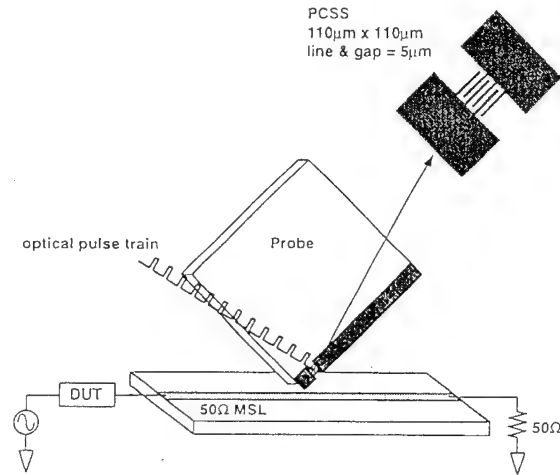


Fig. 1 Schematic view of the probe and DUT

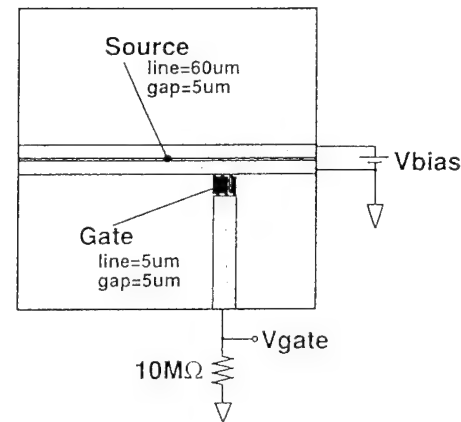


Fig. 2 Schematic view of the sample for testing the PCSS response

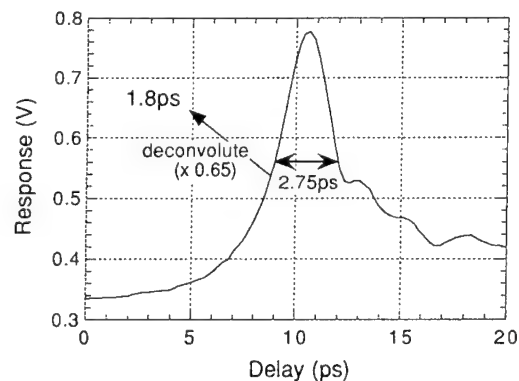


Fig. 3 Pulse shape of photogenerated pulse. Actual pulse width and PCSS response should be shorter than 1.8ps.

measurement. The focused beam size was approximately $50 \mu\text{m}$ in diameter. The sampling beam propagates through a delay line, and we measured the pulse shape of the photogenerated electrical pulse by scanning the delay.

Figure 3 shows a result when the distance between the exciting and sampling beam spots is $300 \mu\text{m}$. Since measured pulse width is 2.75ps , the deconvoluted value is about 1.8ps . Therefore the response time of the PCSS is at least 1.8ps . When the PCSS is used for the measurement using the STOEM, the time resolution is expected to be close to this value. The DC component in figure 3 may be due to unexpected photocarriers generated by sampling beam itself at the gap near the PCSS.

Using the probe with the PCSS, we measured the pulse shape from a comb generator on a 50Ω micro strip line made of an Au film. Details of the electronic system setup were described in the previous work [1]. Figure 4 shows the resulted pulse shape with 117ps FWHM. The following oscillation may be due to reflections of the electric pulse. The pulse width is almost the same as the actual value of 113ps .

Conclusion

We fabricated a probe which has a low temperature grown GaAs PCSS. The PCSS response time was 1.8ps . Using this new probe for the STOEM, we measured the pulse shape with 117ps FWHM that is almost the same as the actual value.

REFERENCES

- [1] K. Takeuchi and Y. Kasahara, Appl. Phys. Lett. Vol. 63, no. 26, pp. 3548 (1993)
- [2] G. Binning, H. Rohrer, C. Gerber, and E. Weibel, Phys. Rev. Lett. Vol. 50, pp. 120 (1983)
- [3] S. Weiss, D. F. Ogletree, D. Botkin, M. Salmeron, and D. S. Chemla, Appl. Phys. Lett. Vol. 63, no.18, pp. 2567 (1993)
- [4] G. Nunes, Jr. and M. R. Freeman, Science Vol. 262, pp1029 (1993)
- [5] A. S. Hou, F. Ho, and D. M. Bloom, Electron. Letters Vol. 28, no. 25, pp. 2302 (1992)
- [6] S. Gupta, M. Y. Frankel, J. A. Valdmanis, J. F. Whitaker, G. A. Mourou, F. W. Smith, and A. R. Calawa, Appl. Phys. Lett. Vol. 59, no. 25, pp. 3276 (1991)

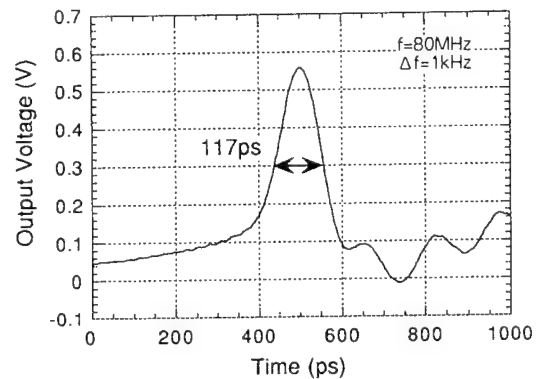


Fig. 4 Pulse shape of the comb generator measured by STOEM.

High-Frequency On-Wafer Testing with Freely Positionable Silicon-on-Sapphire Photoconductive Probes

T. PFEIFER, H.-M. HEILIGER, H. G. ROSKOS, and H. KURZ

Institut für Halbleitertechnik II, Rheinisch-Westfälische Technische Hochschule (RWTH) Aachen, Sommerfeldstr. 24, D-52056 Aachen, Germany

Tel.: +49-241-80-7806 (-7890), Fax: +49-241-8888-246,

Email: roskos@zyklop.basl.rwth-aachen.de

Electronic and optoelectronic devices have become available with cut-off frequencies up to several hundreds of GHz. This technological push necessitates the development of new measurement techniques, because conventional electronic measurement equipment such as network analyzers or sampling oscilloscopes are limited in bandwidth to 40 - 100 GHz.

Considering *optically-assisted* high-frequency measurement techniques, the recent advance in photoconductive (PC) sampling with freely positionable probes significantly extends the potential of on-chip characterization of high-speed devices and circuits [1,2]. The probes are utilized to measure electric voltage transients in direct or tunneling contact with a conductor. The spatial resolution can be pushed far below the micron scale. A sensitivity of 1 μ V has been reported for freely positionable PC probes made from LT-GaAs [1]. PC probes based on silicon-on-sapphire (SOS) technology, though inferior in sensitivity to LT-GaAs-based probes, are cheaper and easier to manufacture, and they are optically transparent per se facilitating alignment. In this contribution, we present a detailed characterization of freely positionable SOS PC probes both as *detectors* and *generators* for ultrafast electric signals. The linearity, sensitivity, time resolution and invasiveness are discussed.

Our PC probes utilize a metal-semiconductor-metal interdigitated electrode structure as photoconductive switch (see Fig. 1). To facilitate contacting to a device-under-test (DUT), a 5- μ m-high Au-coated Ti tip is

located at the end of the short electrode. Fabrication of the finger structure is based on a standard lift-off process for patterning of the Cr/Au metallization on the SOS substrate. The Si layer is implanted with Si^+ and Ne^+ ions to reduce the carrier lifetime. For fabrication of the Ti tip, a special lift-off process with a several-micron-thick photoresist layer was developed [2].

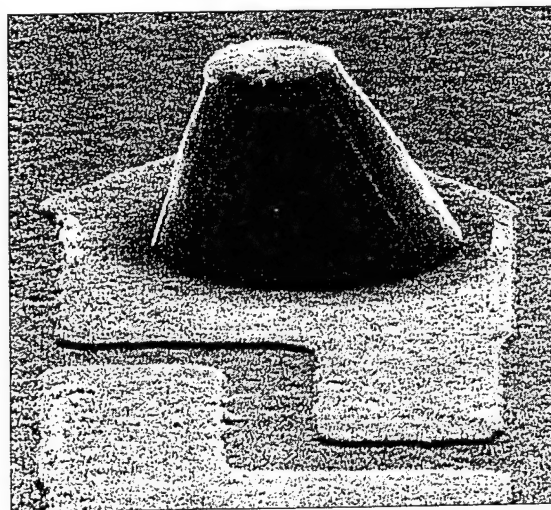


Fig. 1. SEM micrograph of a photoconductive sampling probe with an interdigitated switch. A 5- μ m-high Au-coated Ti tip facilitates contacting to a DUT.

The time-resolved characterization is performed with a 100-fs ring dye laser in a pump-probe setup. We utilize a THz dipole antenna [3] and coplanar waveguides (CPWs) with integrated photoconductive switches as DUTs.

In a first series of experiments, electric pulses on an antenna are sampled. The pulses are generated by the switch integrated

into the antenna. The transients are detected close to the generation point with the Ti tip of the PC probe positioned onto one of the arms of the Hertzian dipole of the antenna [2]. We investigate the response of the PC probe to electric pulses of 40 mV peak amplitude and 1.3 ps duration (FWHM). In these measurements, the intensity of the optical probe beam (beam impinging onto the PC probe) is varied, while the intensity of the pump beam (illuminating the antenna) is kept constant. As a measure for the photo-excitation of the PC probe, we determine the dc photocurrent I_{II} through the PC switch for a fixed bias of 1.5 V. Figure 2 shows

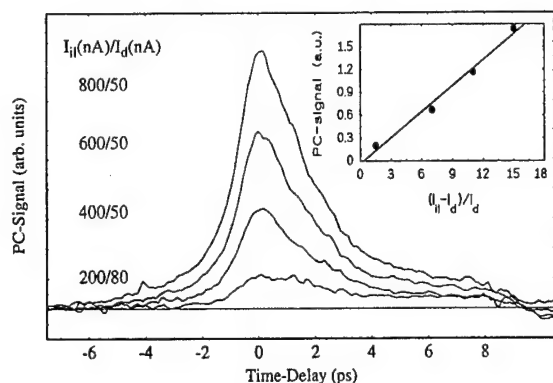


Fig. 2. Time-resolved PC probe signals of 40-mV electric pulses on an antenna. The probe-beam intensity is varied. Inset: dependence of the amplitude of the PC probe signal on the probe photocurrent I_{II} .

transients of the time-resolved experiment for various probe-beam intensities. The data are recorded in single scans (1-s lock-in time constant). The inset displays the peak amplitude of the transients as a function of $I_{II}-I_d$, with I_d being the dark current in the probe. We make the following observations: (i) No distortion in the shape of the electric pulses is found when the probe-beam intensity is raised. The transients have a duration of 2.7 ps (FWHM). This is longer than the electric-pulse width measured via electro-optic sampling technique (1.3 ps) [2]. A careful analysis of the measured data [2,4] shows that the time resolution of the PC probe is limited by the lifetime of the carriers in the Si layer of the probe. The lifetime is found to exhibit a bi-exponential

behavior with time constants of 0.6 ps and 2.2 ps. Model calculations [2] predict that a complete suppression of the slow component by optimized ion implantation will result in a time resolution of the probe of approx. 1.5 ps. (ii) The peak amplitude of the transients rises linearly with the illumination intensity of the probe. (iii) The sensitivity of the PC probe can be evaluated from the noise characteristics of the data in Fig. 2. The noise floor is estimated to be approx. 400 μ V for a single scan with 1-s lock-in time constant for all values of I_{II} . The sensitivity can be increased with the photoconductance of the PC switch [4]. The photoconductance is determined by the product of the mobility and the density of photoexcited carriers. To increase the sensitivity of SOS PC probes, higher excitation intensities and laser sources with better noise characteristics than that of dye lasers are necessary.

Additionally, we measure the response of the PC probe as a function of the amplitude of the electric transients on the DUT by varying the pump-beam intensity over two orders of magnitude (data not shown here, see [2]). The response of the PC probe reveals a linear dependence on the amplitude of the electric transients.

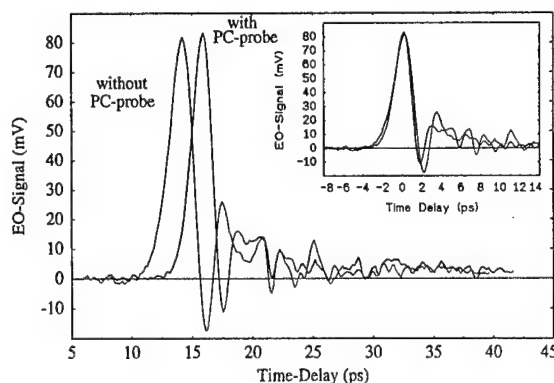


Fig. 3. Electro-optically detected electric pulses on a CPW with and without a PC probe in contact with the CPW. In the inset, the initial parts of the pulses are overlaid.

The invasiveness of our PC probes is investigated by measurements on a SOS CPW (one signal conductor surrounded by two ground conductors, conductor width: 60 μ m,

spacing: 30 μm) with integrated PC switch. We detect the electric pulses generated on the CPW behind a point where the tip of a freely positionable probe is in full contact with the signal conductor of the CPW. The transients are traced electro-optically at a point 1.92 mm away from the excitation spot. Fig. 3 shows waveforms detected with and without the PC probe in contact with the CPW 0.73 mm away from the excitation spot. The amplitude of the electric pulse is not measurably affected when the PC probe is brought into contact with the signal conductor. Hence, reflection losses by the PC probe must be small (below the detection limit, i.e. $\leq 5\text{--}10\%$). Although the probe apparently does not represent a significant inductive load of the CPW, a weak dielectric invasiveness modifying the effective refractive index of the CPW is found. This is evident in Fig. 3 from the shift of the peak by 1.6 ps towards longer delay times. The shift is explained with a 15-% increase of the refractive index of the CPW by the sapphire substate of the PC probe (substrate width: 1.33 mm). The dielectric invasiveness can be reduced strongly by a larger Ti tip height or by a smaller substrate width.

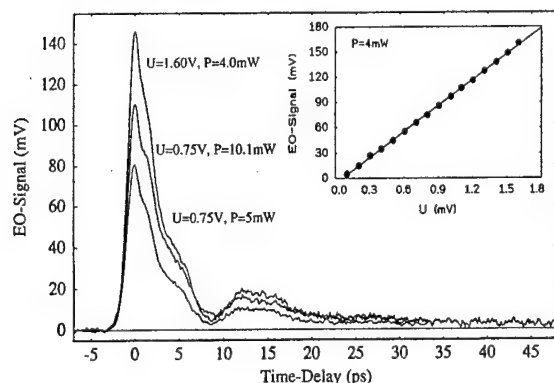


Fig. 4. Electro-optically detected electric transients generated by a PC probe positioned onto a CPW. The power of the optical pump beam and the bias voltage applied to the PC probe are varied. Inset: Peak amplitude of the electric signals for various bias voltages and a constant pump power of 4 mW.

In a last experiment, we demonstrate that freely positionable PC probes are not only capable to detect but also to generate ps electric transients. For this purpose, we

bring the PC probe into contact with the signal conductor of a 10-mm-long CPW fabricated on GaAs substrate. In contrast to the experiments presented above, the gap of the PC switch is biased and illuminated by the optical pump beam instead of the probe beam. The electric transients launched from the PC probe onto the CPW are detected via electro-optic sampling employing a LiTaO_3 crystal positioned onto the CPW approx. 300 μm away from the PC switch. Figure 4 depicts measured electric transients for various bias voltages (U) and average optical pump powers (P) on the PC probe. The amplitude of the generated electric pulses rises linearly with the bias voltage. A duration of the electric pulses of 3.3 ps (FWHM) is obtained. The amplitude of the transients is comparable to that of pulses launched directly from PC switches integrated into CPWs. These results illustrate that freely positionable PC switches can be used as efficient signal generators opening the way for all-photoconductive on-chip testing at any two electrically accessible points on a circuit without the need to integrate PC switches into the circuit.

REFERENCES

- [1] J. Kim, S. Williamson, J. Nees, S.-I. Wakana, and J. Whitaker, *Appl. Phys. Lett.* **62**, 2268 (1993).
- [2] T. Pfeifer, H.-M. Heiliger, E. Stein von Kamienski, H. G. Roskos, and H. Kurz, *JOSA B* (1994), Dec. issue.
- [3] H. G. Roskos, *Lithu. J. Phys.* **34**, 175 (1994).
- [4] D. H. Auston, "Picosecond Photoconductors", in *Picosecond Optoelectronic Devices*, C. H. Lee, ed., (Academic Press, Orlando, 1984), p.73-117.

Wednesday, March 15, 1995

Quantum Devices

JWB 10:30 am-12:00 m
Ballrooms VI-VIII

Jürgen Kühl, *Presider*
Max Planck Institute, Germany

Ultrafast All-Optical Switch with Switch-Off Time Unlimited by Carrier Lifetime

K. Tajima and S. Nakamura

Optoelectronics Research Laboratories, NEC Corporation

34 Miyukigaoka, Tsukuba, Ibaraki 305, Japan

Phone +81-298-56-6125 Fax +81-298-56-6125

All-optical switches are expected to become one of key elements in future ultrafast and flexible all-optical communication networks. And it has been generally believed that such all-optical devices would require very fast, as well as very efficient, nonlinear optical material (or phenomena). In fact, the well-known and often discussed figure of merit for nonlinear materials [$n_2/(\alpha\tau)$, where n_2 is the nonlinear refractive index change coefficient, α is the linear absorbance, and τ is the relaxation time] implies that it is the chosen nonlinear material that determines the basic device performance such as the switching speed and energy. In this paper, we show that this is not necessarily the case; the speed of a nonlinear optical switch proposed by the authors^{1,2} is not restricted by the slow relaxation time of high efficiency incoherent nonlinearities.

The proposed all-optical device is schematically illustrated in Fig. 1. This is similar to the well-known Mach-Zehnder (MZ) type device, but it differs in that it has nonlinear materials (waveguides) and control light injection ports in *both* arms. The nonlinear waveguides in both arms are identical. Thus, we call it symmetric Mach-Zehnder (SMZ) all-optical switch. Here we consider the usual case in which the control light photon energy is equal to or slightly lower than the band-gap energy of the nonlinear waveguides in order to efficiently generate photocarriers throughout the waveguides, while the signal light wavelength is much longer than the band-gap wavelength to achieve high transmission. The principle of operation of SMZ is as follows. The optical length of one arm of SMZ is modified by the induced nonlinear refractive index change caused by the first control pulse (leading control pulse) so that the signal output is switched to the other output port (switch-on). If we allow the nonlinear waveguide to relax back to its initial state, then the signal is gradually switched back to the initial port, following carrier recombination, as in the usual MZ all-optical switches³. However if the other arm is excited by the second control pulse (trailing pulse) shortly after the first pulse, we expect that the effect of residual nonlinear refractive index change in the first arm to be canceled by that in the second arm. Thus ultrafast switch-off can be achieved that is not restricted by the slow relaxation time of band-filling nonlinearity.

Experimental results are shown in Fig. 2. In this experiment, a pair of GaAs/AlGaAs waveguides with a core size of $0.5 \times 4 \times 500 \mu\text{m}$ are used. The signal and control pulse wavelengths are 900 and 875 nm, respectively. The control light pulse width is ~ 1.3 ps and the signal light is unmodulated CW light so that bare modulation characteristics of SMZ can be investigated. Fig.

2(a) shows an experimental result in which the time lag between the leading and trailing control pulses (or switching speed) is 56 ps. The square like modulation characteristic is evident. Here a nonlinear phase

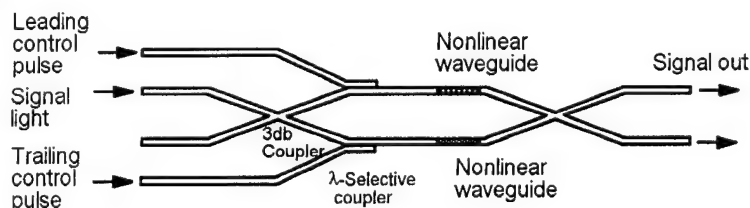


Fig. 1. The symmetric Mach-Zehnder all-optical switch.

shift of π (full switching) was achieved, which was verified by observing the characteristic periodic behavior of all-optical devices³. The control pulse energies required for full switching were 4 pJ for one waveguide and 7 pJ for the other, assuming a coupling efficiency of 10 %, estimated from a separate experiment. As the time lag is reduced to 6 ps, a faster switching speed of 8 ps was recorded, as shown in Fig. 2(b). Here the apparent modulation depth is less than 100 % and the square like modulation is no longer observed, because of the insufficient time resolution of the streak camera (~ 8 ps). Further increase in switching speed was only hindered by the time resolution, but clean square like modulation approaching 1 ps is expected to be possible.

In the above experiment, the control pulse repetition rate was only 82 MHz, allowing the nonlinear waveguides to relax back to the initial state before the next control pulse arrives. If, however, a series of high repetition control pulses are used, then the photocarriers become accumulated in the waveguides to a degree determined by the competition between the carrier generation rate and the carrier lifetime. The average carrier density would exceed $10^{18} / \text{cm}^3$ for repetition rates greater than 40 GHz, assuming a carrier lifetime of 1 ns and device parameters already cited. Even with this high background carrier density, the switching energy is expected to stay in the same range, because the change in nonlinear refractive index per photogenerated carrier is known⁴ to remain in the same range as in the case of low repetition operation ($\approx 3 \times 10^{16} / \text{cm}^3$). Here we assumed the carrier lifetime to be 1 ns, but it is actually a function of carrier density; as the carrier density becomes higher, the recombination process becomes faster. Further, various techniques have been developed to effectively reduce the carrier lifetime. Thus the background density mentioned earlier is probably an overestimation and faster repetition rates should be achievable; that is, if we ignore thermal effects, better than a few hundred GHz is expected for a carrier lifetime of 100 ps, following the earlier discussion. We are now obtaining experimental result which supports these observations and the result will be presented at the conference. We note that this type of strategy for high repetition operation does not work with the normal Mach-Zehnder type all-optical switches.

In conclusion, we have shown that ultrafast switching is possible with the symmetric Mach-Zehnder type all-optical switch, that is not restricted by the slow relaxation time of high efficiency incoherent nonlinearities. A switching speed as fast as 1 ps is expected without sacrificing the high efficiency of band-filling nonlinearity. It is also theoretically shown that a very high repetition rate exceeding hundred GHz is possible.

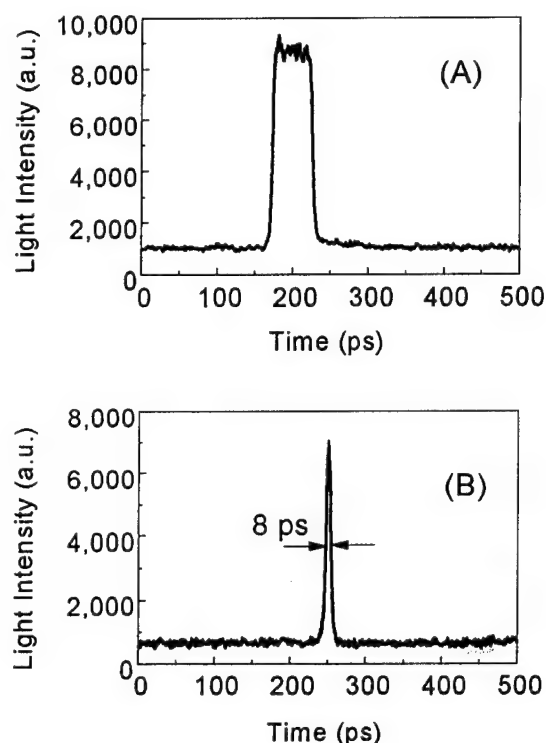


Fig.2. Switching Waveforms

[1] K. Tajima, Jpn. J. Appl. Phys. vol.32, p.L1749, (1993).

[2] S. Nakamura, K. Tajima, and Y. Sugimoto, Appl. Phys. Lett., vol.65, No.3, p.283, 1994.

[3] K. Tajima, S. Nakamura, N. Hamao, and Y. Sugimoto, Jpn. J. Appl. Phys. vol.33, pt. 1, no.1A, p. 144, (1994).

[4] Y. H. Lee, A. Chavez-Pirson, S. W. Koch, H. M. Gibbs, S. H. Park, J. Morhange, A. Jeffery, N. Peyghambarian, L. Banyai, A. C. Gossard, and W. Wiegman, Phys. Rev. Lett. vol.57, p.2446, (1986).

QUANTUM CASCADE LASERS

F. Capasso and J. Faist

AT&T Bell Laboratories
Murray Hill, NJ 07974

The recently demonstrated quantum cascade laser is a fundamentally new semiconductor laser.¹⁻³ It relies on only one type of carrier (unipolar laser) and on quantum jumps of electrons between discrete conduction band energy levels of quantum wells. As such the wavelength can be tailored over a very wide range from the mid-ir (a few microns) to the far-ir ($\sim 100\ \mu\text{m}$) by simply varying layer thicknesses. Two types of quantum cascade lasers will be discussed. In the original structure the relevant intersubband radiative transition is between states centered in different neighboring wells to facilitate population inversion, i.e. the transition is *diagonal* (Fig. 1). In this design, however, the width of the luminescence transition is relatively broad (FWHM $\sim 22\ \text{meV}$) due to the interface roughness since electrons traverse several heterointerfaces in the photon emission process. As a consequence the peak gain is reduced. To circumvent this problem we designed the structure of Fig. 2 where electrons make a vertical radiative transition essentially in the same well. This reduces considerably the width of the gain spectrum (FWHM $\approx 10\ \text{meV}$) and therefore the laser threshold current density. To prevent electron escape in the continuum, which is greatly reduced in the case of the diagonal transition, the superlattice of the digitally graded injector is designed to act as a Bragg reflector for electrons in the higher excited state and to simultaneously ensure swift electron escape from the lower states via a miniband facing the latter (Fig. 2). A crucial feature of both structures is that the lower state of the laser transition is separated by an optical phonon ($\approx 30\ \text{meV}$) from the $n = 1$ state. This strongly enhances the scattering of electrons out of the $n = 2$ state. The calculated time is $\tau_{21} \approx 0.6\ \text{ps}$ which is considerably less than the relaxation time between the $n = 3$ and $n = 2$ state (a few ps) thus creating the population inversion condition. Electrons can in turn tunnel out of the $n = 1$ state in a subpicosecond time to prevent electron build-up.

Quantum Cascade Laser with Diagonal Transition

The AlInAs/GaInAs structure grown by MBE comprises 25 stages, each consisting of a graded gap n-type injection layer and a three coupled-well active region, cladded by AlInAs waveguiding layers.¹⁻³ The undoped active region includes 0.8 nm and 3.5 nm thick GaInAs wells separated by 3.5 nm AlInAs barriers. 3.0 nm thick AlInAs barriers separate the active regions from the digitally graded n-type doped injectors ($\sim 10^{17}\ \text{cm}^{-3}$). The samples were processed into mesa etched ridge waveguides and the laser facets were obtained by cleaving. Powers $\approx 30\ \text{mW}$ in pulsed operation for a 2.8 mm long device and $\approx 6\ \text{mW}$ for a 1.2 mm long device have been obtained at $\lambda = 4.3\ \mu\text{m}$ and at a heat sink temperature $\sim 100\ \text{K}$. An outstanding feature of this laser is that the gain is much less sensitive to temperature than conventional semiconductor

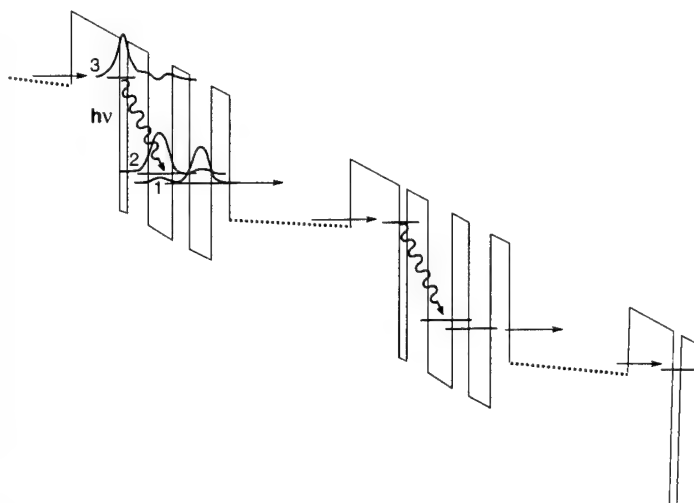


Figure 1. Energy diagram of the QC laser under bias showing the diagonal laser transition (wavy arrow). $E_3 - E_2 = 295$ meV.

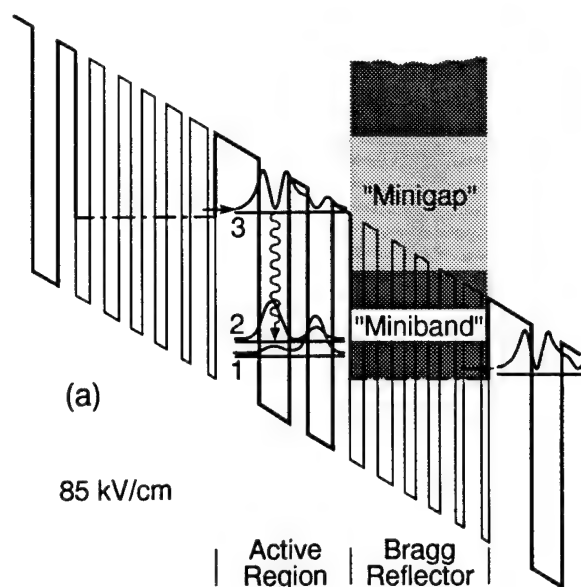


Figure 2. Energy diagram of QC laser under bias showing the vertical laser transition (wavy arrow). $E_3 - E_2 = 271$ meV.

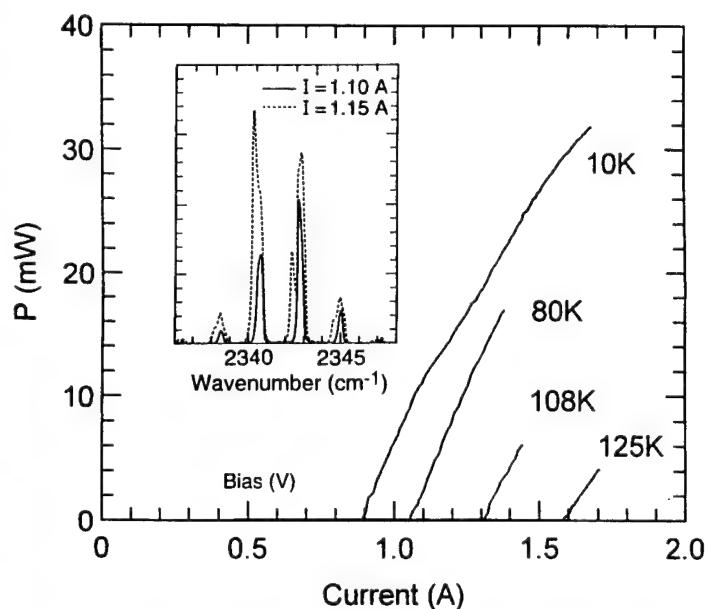


Figure 3. Peak optical power from a single facet vs. drive current for a 720 μm cavity length quantum cascade laser with diagonal transition at various heat sink temperatures. The inset shows the high resolution spectrum.

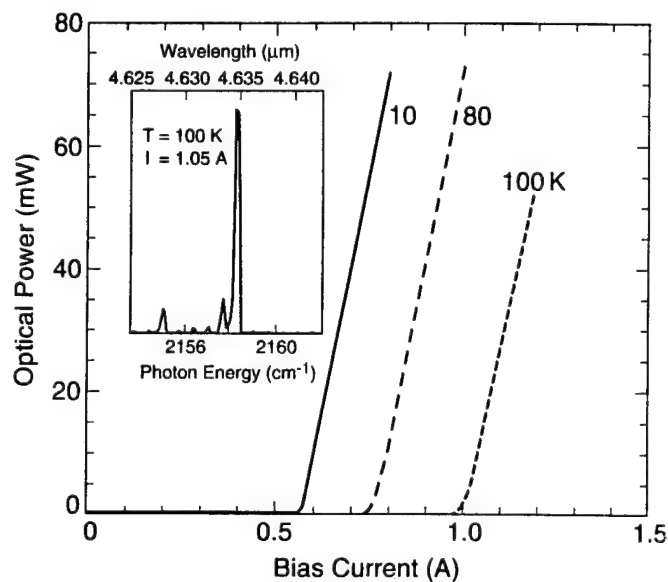


Figure 4. Peak optical output power from a single facet vs. drive current at various heat sink temperatures for the quantum cascade laser with vertical transition. The device is 2.4 mm long. Inset: high-resolution spectra of the sample above threshold.

lasers. The temperature dependence of the threshold indicates an exponential increase $\sim \exp(T/T_0)$ with a $T_0 = 110$ K (Fig. 3). Operating temperatures up to 125 K have been achieved with 5 mW of power (Fig. 3). The threshold is 7.7 kA/cm^2 at ~ 110 K and the measured slope efficiency $\sim 50 \text{ mW/A}$ per facet. The inset of Fig. 3 shows the high resolution spectrum at two different currents. Well defined longitudinal modes are observed. The mode spacing 2.16 cm^{-1} is in good agreement with the calculated one ($\frac{1}{2nL_{\text{cav}}} = 2.13 \text{ cm}^{-1}$ with $n = 3.26$). The linewidth of the dominant mode is presently limited by heating effects and mode hopping during the pulse. At higher currents an additional transverse mode emerge. The intrinsic linewidth of these lasers in cw single mode operation is expected to be Schawlow-Townes limited, similar to atomic lasers, without the linewidth enhancement factor typical of diode lasers.¹

Quantum Cascade Laser with Vertical Transition

In this structure (Fig. 2) the 25 active regions consist of a 4.5 nm GaInAs wells coupled to a 3.6 nm well by a 2.8 nm AlInAs barrier. Tunneling injection into the active region is through a 6.5 nm AlInAs barrier and electrons escape out of the $n = 1$ state through a 3.0 nm AlInAs barrier. The superlattice well and barrier thicknesses are respectively $\ell_w = 2.1, 2.1, 1.6, 1.7, 1.3$ and 1.0 nm and $\ell_b = 2.1, 1.9, 2.0, 2.3$ and 2.7 nm in going from left to right in Fig. 2. The waveguiding cladding regions are similar to those of the diagonal transition structure. After processing, the samples were cleaved in $L_{\text{cav}} = 2.4 - 3$ mm length bars. Current pulses of 30 ns were injected in the device with a 20 kHz repetition rate. Fig. 4 displays the peak optical power versus drive current obtained by focusing the light with a $f/0.8$ optics on a fast HgCdTe detector. The peak optical power is $\sim 80 \text{ mW}$ at 80 K. The measured slope efficiency is 300 mW/A per facet and essentially temperature independent and corresponds to a differential quantum efficiency per period of 4.5×10^{-2} when corrected for the collection efficiency of the apparatus. The threshold density has a value $J_{\text{th}} = 6.7 \text{ kA/cm}^2$ at 10 K and 3 kA/cm^2 at 100 K. The collaboration of C. Sirtori, D. L. Sivco, A. L. Hutchinson and A. Y. Cho is gratefully acknowledged.

REFERENCES

1. J. Faist, F. Capasso, D. L. Sivco, C. Sirtori, A. L. Hutchinson, and A. Y. Cho, *Science*, **264**, 553 (1994).
2. J. Faist, F. Capasso, D. L. Sivco, C. Sirtori, A. L. Hutchinson, and A. Y. Cho, *Electron. Lett.* **30**, 865 (1994).
3. J. Faist, F. Capasso, D. L. Sivco, A. L. Hutchinson, C. Sirtori, Sung N. G. Chu, and A. Y. Cho, *Appl. Phys. Lett.*, Dec. 5, 1994 (in press).

Scaling of Stark-Shifted Nonlinearities in Multiple Quantum Well Structures

A. N. Cartwright, X. R. Huang and Arthur L. Smirl
 Laboratory for Photonics and Quantum Electronics
 100 IATL, University of Iowa, Iowa City, Iowa 52242
 Tel. (319) 335-3460 Fax (319) 335-3462

Optical switching and logic devices require a large optical nonlinearity (absorptive or refractive) per absorbed photon (or injected charge), combined with a rapid excitation recovery time. The accumulated absorptive (or index) changes during a laser pulse are proportional to the shorter of either the pulse duration or the excitation lifetime. Optimally the two are matched, in which case the switching energy (power-time product) is determined primarily by the change in absorption coefficient (or refractive index) per photogenerated carrier-pair. Any mechanism, material or structure that will enhance the per-carrier nonlinear response is therefore of considerable interest. Device structures (such as self-electrooptic effect devices (SEED's), hetero *n-i-p-i*'s, and piezoelectric multiple quantum wells (MQWs)) that rely on the screening of applied, built-in or intrinsic fields are purported to have large per carrier nonlinearities primarily because the carriers generated in a single well can escape and move to screen multiple wells. As a class, we refer to the nonlinearities in such structures as Stark-shifted nonlinearities, since they arise from a reduction in the quantum-confined Stark effect (QCSE) as the field is screened by the photogenerated charge.

Here, we present the results of an extensive experimental investigation and phenomenological theoretical treatment of the per carrier optical nonlinearity in a number of hetero *n-i-p-i*, SEED and piezoelectric MQW structures. We have investigated how this commonly used figure-of-merit scales with excitonic linewidth, excitonic amplitude, electric field and the number of wells. These studies included the dependence of the per carrier nonlinearity on temperature, on materials system and on sample structure. Moreover, they included structures in which the electric fields were externally applied, built-in and intrinsic. We demonstrate that a single simple expression will account for the scaling of the per carrier nonlinearity with each of the stated parameters. This expression gives us predictive capabilities when designing new structures.

In direct contrast to nonlinearities associated with saturation (or bleaching), a true per-carrier nonlinear cross section cannot be defined for Stark-shifted nonlinearities. However, under a restricted set of conditions (analogous to those necessary for defining a

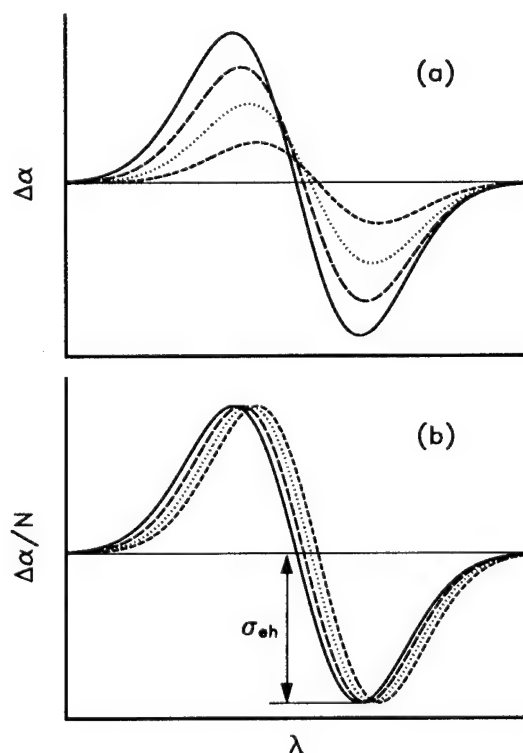


FIG. 1. (a) Change in absorption coefficient, and (b) the per-carrier change in absorption coefficient, $\Delta\alpha/N$, for a Stark-shifted nonlinearity.

bleaching cross section), a useful per carrier figure of merit, σ_{eh} , can be defined for Stark-shifting nonlinearities that obeys very simple scaling rules, as we shall demonstrate. The conditions necessary for defining σ_{eh} are that the photo-generated space-charge field must be small compared to the perpendicular field (whether it is applied, built-in or intrinsic), that each photo-generated carrier must escape the wells and move to screen the field, and that the area under the exciton must remain constant (e.g., bleaching is negligible). Under these conditions, the *peak* amplitude of the change in the absorption coefficient, $\Delta\alpha$, will increase linearly with incident fluence and, therefore, with the number density, N , of photoinjected electron-hole pairs in the well, as depicted in Fig. 1(a). Consequently, the blue shift will be small, and the spectra of the change in the absorption coefficient per carrier, $\Delta\alpha/N$, will have a constant amplitude and shape, but with a zero crossing that shifts linearly with excitation level, as shown in Fig. 1(b). It is this slight shift in the spectra as a function of carrier density that precludes the rigorous definition of a cross section that is constant for a given wavelength, as we do for bleaching. Nevertheless, we can still use the *peak* change in absorption coefficient per carrier as a measure of the strength of the nonlinearity:

$$\sigma_{eh}(peak) = \frac{\Delta\alpha_{peak}}{N}. \quad (1)$$

This figure of merit can be expected to obey simple empirical scaling laws, if the blue shift of the exciton (as the result of the screening of the QCSE) is represented as a shifted Lorentzian [1], or Gaussian [2] with amplitude α_o and a halfwidth at half maximum of Γ_o . Under conditions for which σ_{eh} can be defined, the per carrier figure of merit will have the following form:

$$\sigma_{eh} = \pm \frac{ql_w C}{\epsilon_s} \frac{m\alpha_o}{\Gamma_o} F(E_{\perp}), \quad (2)$$

where q is the fundamental charge, m is the number of quantum wells in the intrinsic region, l_w is the width of the quantum well, ϵ_s is the dielectric constant of the material, E_{\perp} is the perpendicular field (before screening), and C is a constant that depends on whether the lineshape is Lorentzian or Gaussian. The function $F(E_{\perp}) = E_{\perp}$ when the shift in wavelength from the zero field wavelength $\Delta\lambda(E_T) \propto E_T^2$, as it is in the low field limit, and $F(E_{\perp}) = 1$ when $\Delta\lambda(E_T) \propto E_T$, as it is in the high field limit [3], where $E_T = E_{\perp} - E_{sc}$ is the photogenerated space charge field.

The scaling of σ_{eh} with number of wells and excitonic amplitude and linewidth is illustrated in Fig. 2. For this demonstration, we measured σ_{eh} in seven separate structures by using a two

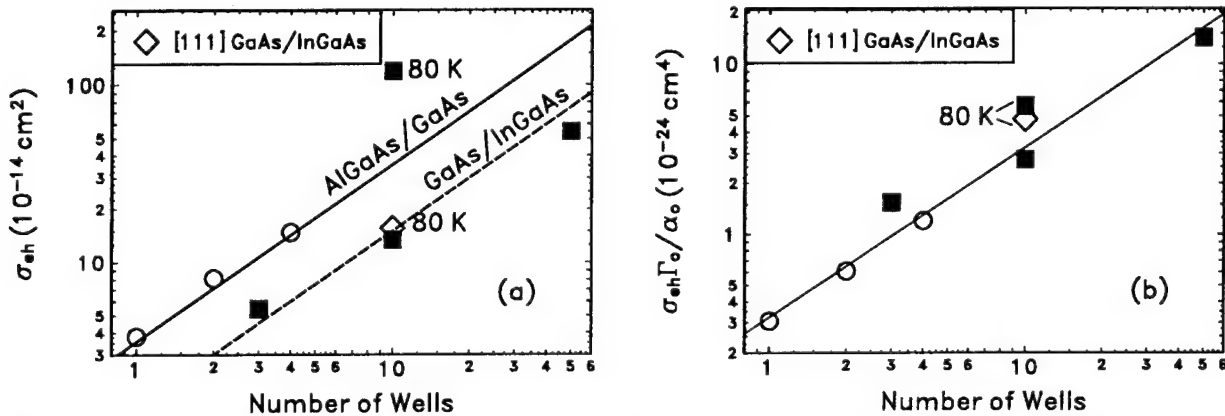


FIG. 2. (a) Measured per-carrier nonlinearity for seven separate structures at the same perpendicular electric field, and (b) the normalized quantity, $\sigma_{eh} \Gamma_o / \alpha_o$, as a function of the number of wells per intrinsic region.

color differential transmission technique. The measurements of the unscaled σ_{ch} 's are summarized in Fig. 2(a). All samples had approximately the same well widths and the same perpendicular fields. These samples included GaAs/AlGaAs hetero $n-i-p-i$'s with 1, 2 and 4 wells per intrinsic region; an InGaAs/GaAs hetero $n-i-p-i$ with 3 wells in the intrinsic region; an InGaAs/GaAs $p-i-n$ MQW structure with 10 wells and one with 50; and a InGaAs piezoelectric MQW $p-i-n$ structure grown in the [111] direction. All of the measurements were at 300 K, except for the two indicated. Notice that the unscaled σ_{ch} 's range over two decades and that they are consistently higher for AlGaAs/GaAs than for GaAs/InGaAs. Nevertheless, all of these σ_{ch} 's lie on a single straight line and are linearly proportional to the number of quantum wells per intrinsic region, as predicted by Eq. (2), when the normalized quantity $\sigma_{\text{ch}}\Gamma_0/\alpha_0$ is plotted as shown in Fig. 2(b)!

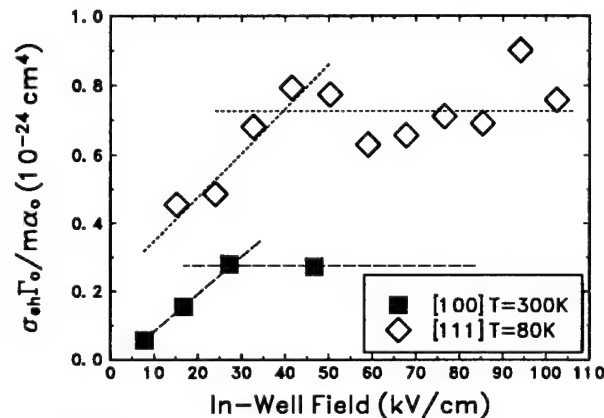


FIG. 3. The dependence of the normalized per-carrier nonlinearity on in-well field.

contrast, for large in-well fields we would expect $\Delta\lambda(E_{\perp}) \propto E_{\perp}$ and σ_{ch} should be independent of field [i.e., $F(E_{\perp}) = 1$]. In this regime, the normalized quantity $\sigma_{\text{ch}}\Gamma_0/m\alpha_0$ should be a constant independent of field. This is confirmed by the data in Fig. 3.

In summary, we have confirmed the validity of a simple scaling expression that allows one to predictably adjust for changes in well number and electric field in the design of Stark-shifted nonlinear devices, and to predictably correct for operation at other temperatures and predictably scale for conversions between material systems. Moreover, these measurements illustrate that the per-carrier nonlinearity can be improved by optimizing the in-well bias field and by increasing the number of wells per intrinsic region; however, they also demonstrate that when the measured per-carrier nonlinearities are corrected for material quality and temperature (i.e., excitonic amplitude and linewidth) that the per-carrier response does not depend appreciably on material system or on whether the fields are externally-applied, built-in, or intrinsic.

References

1. G. Lengyel, K. W. Jelley, R. W. H. Engelmann, *IEEE Journal of Quantum Electronics*, vol. **26**, pp. 296-304, 1990.
2. D. S. Chemla, D. A. B. Miller, P. W. Smith, A. C. Gossard, W. Wiegmann, *IEEE Journal of Quantum Electronics*, vol. **20**, pp. 265-275, 1984.
3. W. Chen and T. C. Andersson, *Semicond. Sci. Technol.* vol. **7**, pp. 828-836, 1992.

Dynamic Wannier-Stark Effect and Superradiance Switching in Semiconductor Superlattices

J. B. Khurgin^(a), S. J. Lee^(a),
N. M. Lawandy^(b), S. Li^(c)

^(a) Department of Electrical
and Computer Engineering
The Johns Hopkins University
Baltimore, MD 21218

^(b) Division of Engineering
and Department of Physics
Brown University
Providence, RI 02912

^(c) Dept. of Electrical Engineering
University of California
Los Angeles, CA 90024

We investigate the possibility of observing the transition between the localized states and the extended states in semiconductor superlattices (SL) in the presence of strong external ac field. i.e., the dynamic Wannier-Stark effect [1] and by switching of superradiance.

Let us consider the SL in Fig. 1a. The adjacent wells in this structure consist of materials with different bandgaps. This can be achieved by varying the Al mole fractions in $Al_xGa_{1-x}As$, for example. The SL parameters can be controlled so that the conduction band subbands are nearly in resonance while the valence band energy levels are well separated ($\Delta E_{v,12}^{(0)} \sim 50 meV$). When a strong optical field is applied (see Fig. 1b), the energy levels become "dressed" and the ac Stark effect moves conduction band energy level in well 1 by $(\mu_{cv}\mathcal{E})^2/\delta E$ and the level in well 2 by $(\mu_{cv}\mathcal{E})^2/(\delta E + \Delta E_{v,12} - \Delta E_{c,12}^{(0)})$ where $\mu_{cv} = e \langle r_{cv} \rangle$ is the dipole matrix element, \mathcal{E} is the optical field, and δE is the excitation detuning. The lower limit on detuning is put upon by absorption that might be caused by the miniband width and the line

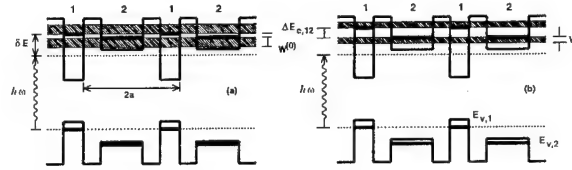


Figure 1: Energy levels and bands in the SL without (a) and with (b) the optical field. $2a$ is the unit period of the SL.

broadening. Since $\Delta E_{v,12}$ can be large, it is clear that the DWS shift of the level in well 2 is substantially larger than that in well 1. Thus, the energy level separation becomes wider and the miniband widths are substantially reduced, see Fig. 1b. Considering the miniband dispersion relation, as shown in Fig. 2, we see that the DWS effect results in a wider gap at $ka=\pi/2$ and a smaller miniband effective mass. Since the conductivity across the SL is decreased due to the optically-induced miniband effective mass change, a practical scheme to use this structure as an optical detector/switch can be considered.

In order to detect the effective mass change, we can apply a DC field to cause current flow in the SL growth direction. As long as the DC field is small enough not to cause energy level shifts, the Drude conductivity formula can be used. Then, the ac component of the current can be utilized in optical detection in a waveguide whereby the responsivity can be expressed as

$$R = \frac{16\pi\alpha_0}{15\sqrt{3}} Na \langle r_{cv} \rangle^2 \frac{e\tau}{\hbar} V \times \left(\frac{1}{\delta E} - \frac{1}{\delta E + \Delta E_{v,12}} \right) \left(\frac{L}{T} \right)$$

where α_0 is the fine structure constant, $L(T)$ is the waveguide length (thickness), V is the interwell coupling energy, N is the density of conduction electrons, and τ is the momentum

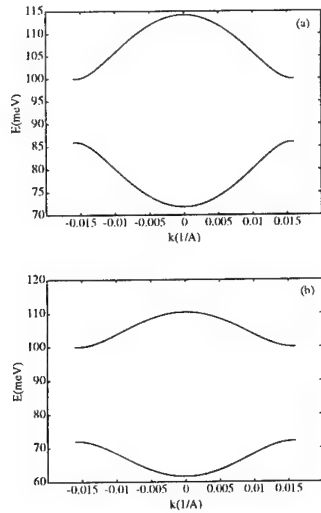


Figure 2: Miniband structure with (a) and without (b) the optical field. Note that the field increase the energy gap at $ka = \pi/2$.

relaxation time. The dimensional factors enter only when the light propagates along the interface. When the L/T ratio is equal to 1000, R can be as high as 0.1 A/W, a figure similar to that of a photodiode. Since no light absorption is involved in the process, the DWS detection scheme is suitable for nondemolition measurement. Compared to the “virtual conductivity” scheme [2], far greater responsivity can be obtained in the DWS scheme where the energy is supplied by the DC source [3]. Compared to the quantum wire interferometer method [4], the DWS device seems far easier to implement due to the confinement necessary in one direction and less stringent requirement of electron coherence. Also, using a differential scheme allows substantially reduction of the noise in this device by cancelling out the dc component.

Recently, excitonic superradiant decay in semiconductor quantum wells (QW) has been studied by a number of researchers [5] and



Figure 3: (a) Superlattice (SL) with minibands of width $4V$. (b) SL with $Q > V$. Excitons are confined in well regions, but are free to move around in the structure. (c) SL with $F \neq 0$. Exciton are confined in a single well.

verified experimentally by fast radiative lifetimes obtained in a single GaAs quantum well (~ 10 ps.) under the resonant excitation conditions [6].

In this study, we investigate spontaneous emission properties of the excitonic states in the superlattice (SL) undergoing the Wannier-Stark (WS) transition in the presence of external electric field. In a SL (Fig. 3a), as the period (barrier) increases, the Coulombic attraction energy between the electrons and holes becomes greater than the interwell coupling energy, V . As a result, the wannier exciton in the z -direction becomes Frenkel excitons, indicating that *an electron and an hole are always in the same well, but it is not known in which one* (see Fig. 3b) The oscillator strength (OS) of the exciton then becomes $f_x = N f_0 \phi_r^2(0)$ where N is the number of periods and $\phi_r(0)$ the in-plane part of the excitonic wavefunction. We see that there are two enhancement factors - ϕ_r^2 due to the formation of Wannier exciton in the parallel plane and N due to Frenkel exciton in the z direction.

When an electric field F larger than V is applied, the exciton wavefunction gets localized in *one particular* well, with no coherent coupling between adjacent states. Thus, the system can be described by N separate WS ladder wavefunctions, The OS of each state is $f_{WS} = f_0 \phi_r^2(0)$. The total OS of N states in the WS ladder is equal to the OS of the

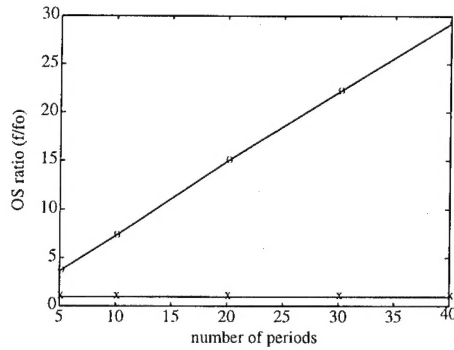


Figure 4: Oscillator strength ratio (f/f_0) vs. number of periods for a barrier width of 50 Å. f denotes the case where the Coulomb attraction is considered and f_0 the case where the Coulomb attraction is neglected. (a) no external bias (b) external bias applied.

superradiant state, indicating that the absorption strength is preserved, but for each particular state the superradiance enhancement is completely gone, thereby slowing down the radiative decay of the WS ladder states by a factor of N . Therefore, a sudden imposition of a relatively weak external field can cause large increase in the radiative lifetime of the SL, opening the possibility of modulating the spontaneous emission in SLs on a picosecond scale, far more efficient than switching of the OS in a single QW [7].

Our calculations are based on the linear combination of 1s exciton states with a single well basis [8] and on the tight-binding method in the non-zero field case for the WS ladder [9]. Fig. 4 shows the OS enhancement ratio after the excitonic effect is considered for both $F = 0$ and $F \neq 0$ cases. It is easily seen that both longitudinal and transverse excitonic components increase the OS dramatically as a linear function of N .

In practice, the enhancement is limited by the SL coherence length, l_c which depends

on the presence of scattering mechanisms and factors such as temperature and sample quality. Since the calculated and measured single well decay time is ~ 20 ps. [10], the corresponding value for the SL should be of the order of Thus, aside from observing direct modulation of spontaneous emission by electric field, the enhancement factor could provide a useful measure of the coherence length in SL's.

References

1. R. W. Boyd and M. Sargent III, J. Opt. Soc. Am. B. **5**, 99 (1988).
2. E. Yablonovich, *et. al.*, Phys. Rev. Lett. **62**, 28 (1989).
3. A. Shimizu and M. Yamanishi, Phys. Rev. Lett. **72**, 3343 (1994).
4. A. Shimizu, K. Fujii, and M. Okuda, Phys. Rev. B **40**, 1357 (1989).
5. Eiichi Hanamura, Phys. Rev. B. **38**, 1228 (1988).
6. B. Deveaud, *et. al.*, Surf. Sci. **263**, 491 (1992).
7. I. Suemune, T. Takoka, M. Yamanishi and Y. Lee, IEEE J. QE-**22**, 1900 (1988).
8. S. Li and J. B. Khurgin, Phys. Rev. B **46**, 12535 (1992).
9. J. Bleuse, G. Bastard, and P. Voisin, Phys. Rev. Lett. **60**, 220 (1988).
10. L. C. Andreani, Solid State Commun. **77**, 641 (1991).

- Ahmed, M. M. — UMD4
 Alexander, M. — UTuD5
 Allam, J. — UMD4, UTuC4, UTuE10
 Allen, S. J. — UTuB3
 Allen, S. T. — UTuD1
 Alphonse, G. — UTuA2

 Baumberg, J. J. — UTuE10
 Baynes, N., de B. — UMD4, UTuC4, UTuE10
 Bhattacharya, U. — UTuB3, UTuC3, UTuD1
 Bloom, David M. — JWA1
 Bowers, John E. — UMA1, UTuB, UTuC3
 Bronner, W. — UMA2
 Brown, E. R. — UTuA6
 Buchal, C. — UTuE8
 Bürkner, S. — UMA2

 Campman, K. L. — UTuD1
 Capasso, F. — JWB2
 Cartwright, A. N. — JWB3
 Chang, C.-S. — UTuE6
 Chen, Wen-Chung — UTuE6
 Chen, Y. K. — UTuC1
 Cheng, H.-J. — UTuE1
 Cho, A. — UTuC1
 Chow, D. H. — UMA3, UMB6, UTuD1
 Cleaver, J. R. A. — UMD4, UTuC4, UTuE10
 Compton, Richard C. — UTuE11
 Connolly, J. — UTuA2
 Coutaz, J. L. — UTuE1
 Craig, Douglas — JWA3
 Cunningham, J. E. — UMB1
 Currie, Marc — UMD5, UTuE2, UTuE7

 Davidson, Andrew C. — UTuE11
 De Raedt, W. — UTuE5
 de Souza, E. A. — UMB1, UTuA3
 Delfyett, Peter J. — UTuA2
 Deng, H. — UTuE13
 Deppe, D. G. — UTuE13
 Dib, N. — UTuE1
 DiNatale, W. F. — UTuA6
 Du, D. — UTuE4

 Eisenstein, Gadi — UTuA,

 Faist, J. — JWB2
 Fauchet, P. M. — UMB5
 Feldman, Marc J. — UMD5
 Fleissner, J. — UMA2
 Fujioka, H. — UMB7

 Gabel, K. — UTuA2
 Ganikhanov, Feruz — UTuE6
 Guggel, H. P. — UTuA5
 Gee, S. — UTuA2
 Gossard, A. C. — UTuD1
 Grantham, S. — UTuA2
 Grischkowsky, Dan — UTuD
 Guthrie, J. — UTuC3

 Hama, Soichi — JWA3
 Hamm, R. — UTuC1
 Haner, M. — UTuC1
 Hase, A. — UTuA5
 Hasebe, S. — UTuE9

 Hasenberg, T. C. — UMB6
 Hayduk, M. J. — UMB4
 Heberle, A. P. — UTuC4
 Hegmann, Frank A. — UMD2
 Heiliger, H.-M. — JWA5
 Hermanns, J. P. — UTuE8
 Herrick, K. J. — UTuE1
 Hillmer, H. — UTuA5
 Ho, Francis — JWA1
 Hofsäß, V. — UTuA5
 Hollricher, O. — UTuE8
 Hornung, J. — UMA2
 Hou, A. Samson — JWA1
 Hsiang, Thomas Y. — UMD2, UMD5, UTuE2, UTuE7
 Hu, B. B. — UMB1
 Huang, X. R. — JWB3
 Huffaker, D. L. — UTuE13
 Hughes, Robert A. — UMD2
 Humphrey, D. — UTuC1
 Hurtz, G. — UTuC3

 Ikezawa, M. — UTuE9

 Jackson, M. K. — UTuE5
 Jacobs-Perkins, Douglas — UMD2, UMD5
 Jauhar, S. — UTuD3

 Kaden, C. — UTuA5
 Kaminski, J. P. — UTuD1
 Kamiya, T. — UTuA4
 Karadi, C. — UTuD3
 Kash, J. A. — UMB3
 Katehi, L. P. B. — UTuE1
 Keay, B. J. — UTuD1
 Khitrova, G. — UMB4
 Khurgin, J. B. — JWB4
 Knox, W. H. — UMB1, UTuA1, UTuA3
 Köhler, K. — UTuD2
 Kondo, Y. — UTuE9
 Kopf, R. — UTuC1
 Koshihara, S. — UTuE9
 Kost, Alan — UMB6
 Kouwenhoven, L. P. — UTuD3
 Kovac, J. — UTuA5
 Krol, M. F. — UMB4
 Kühl, Jürgen — JWB
 Kuhn, J. — UTuA5
 Künzel, H. — UTuA5
 Kuo, J. — UTuC1
 Kurz, H. — UTuD2, UTuE8, JWA5

 Larkins, E. C. — UMA2
 Lawandy, N. M. — JWB4
 Lee, Chi-Hsiang — UMD
 Lee, S. J. — JWB4
 Leisching, P. — UTuD2
 Li, S. — JWB4
 Liliental-Weber, Z. — UMB7
 Lin, Gong-Ru — UMD3, UTuE6
 Lin, J. — UTuC1
 Liu, T. K. — UTuD1
 Liu, T. Y. — UTuC5
 Liu, X. — UTuE4
 Liu, Z. — UTuE9
 Lothian, J. — UTuC1
 Ludwig, R. — UMC2

 Lui, M. — UTuD1
 Lyszcza, T. M. — UTuA6

 Malik, R. — UTuC1
 Mantl, S. — UTuE8
 Martin, S. C. — UMA3
 McEuen, P. L. — UTuD3
 McGinnis, B. P. — UMB4
 McIntosh, K. A. — UTuA6
 McMahon, O. B. — UTuA6
 Miller, D. A. B. — UTuA3
 Ming, L. — UTuD5
 Mishima, T. — UTuC4, UTuE10
 Mishra, U. K. — UTuC5
 Mizuhara, Akira — JWA4
 Moffat, Steven H. — UMD2
 Mohideen, Umar — JWA2
 Molvar, K. M. — UTuA6
 Mondry, M. J. — UMA3, UTuC3
 Motohisa, J. — UTuD3
 Mourou, Gerard A. — UTuE4, JWA
 Muller, R. E. — UMA3
 Muto, Shunishi — UMC3

 Nagamune, Y. — UTuD3
 Nagarajan, Radhakrishnan — UMA1
 Nagatsuma, Tadao — UMD1, UMD6
 Nakamura, Satoshi — UMC3, JWB1
 Nechay, Bettina A. — JWA1
 Nees, John — JWA3
 Nguyen, Loi — UTuC, UTuC5
 Nichols, K. B. — UTuA6
 Nishikawa, Yuji — UMC3
 Nuss, M. C. — UMB1, UTuA3

 Ogawa, K. — UMD4, UTuC4, UTuE10
 Ohbu, I. — UTuC4, UTuE10
 Orenstein, J. — UTuD3
 Özbay, E. — UTuD4

 Pan, Ci-Ling — UMD3, UTuE6, UTuE12
 Patkar, Shekhar — UMB2
 Peyghambarian, N. — UMB4
 Pfeifer, T. — JWA5
 Pieper, W. — UMC2
 Preston, John S. — UMD2
 Püllela, R. — UTuB3, UTuC3

 Ralston, J. D. — UMA2
 Reddy, M. — UMA3, UTuC3
 Rella, C. W. — UMB5
 Ren, F. — UTuC1
 Richardson, M. — UTuA2
 Richman, B. A. — UMB5
 Rodwell, M. J. W. — UMA3, UTuB3, UTuC3, UTuD1
 Rosenzweig, J. — UMA2
 Roskos, H. G. — UTuD2, UTuE8, JWA5
 Rüders, F. — UTuE8

 Sah, R. E. — UMA2
 Sakaki, H. — UMB, UTuD3
 Sarukura, N. — UTuE9
 Saruwatari, Masatoshi — UMC1
 Schmidt, H. — UTuA5
 Schnabel, R. — UMC2
 Schulman, J. N. — UMA3

- Schüppen, A. — UTuB1
Schweizer, H. — UTuA5
Schwettman, H. A. — UMB5
Scott, J. S. — UTuD1
Segawa, Y. — UTuE9
Semenov, V. K. — UMA4
Sha, W. — UMB2
Shealy, J. B. — UTuC5
Shibata, Y. — UTuE9
Shimizu, N. — UMD6
Shimoyama, K. — UTuE9
Shin, J. — UTuE13
Shinagawa, M. — UMD6
Sivco, D. — UTuC1
Slusher, Richard E. — JWA2
Smirl, Arthur L. — UMB2, JWB3
Smith, R. P. — UMA3
Sobolewski, Roman — UMD2, UMD5, UTuE2
Sollner, T. C. L. G. — UMA
Squier, J. — UTuE4
Stark, Jason B. — JWA2
Stein Von Kamienski, E. — UTuE8
- Sun, Jack Y. C. — UTuC2
Suzaki, Tetsuyuki — UTuB2
- Tackeuchi, Atsushi — UMC3
Tajima, K. — JWB1
Takahashi, T. — UTuE9
Takeshita, H. — UTuA4
Takeuchi, Koichiro — JWA4
Tan, I. — UTuC3
Tate, A. — UTuC1
Ten, S. — UMB4
Thompson, M. A. — UTuC5
Tseng, W. F. — UMB2
Tsuchiya, M. — UTuA4
Tuttle, G. — UTuD4
- Van Hove, M. — UTuE5
Victor, K. — UTuD2
- Wagoner, G. A. — UTuD5
Waho, T. — UMD6
Wakana, Shin ichi — JWA3
Wald, K. — UTuD3
- Wang, Chi-Luen — UTuE12
Wang, Chia-Chi — UMD2, UMD5, UTuE2, UTuE7
Wang, H. H. — UMB7
Wanke, M. — UTuD1
Waschke, C. — UTuD2
Weber, H. G. — UMC2
Weiner, J. — UTuC1
Weisser, S. — UMA2
West, Linda — UMB6
Whitaker, J. F. — UMB7, UTuE1
Wicks, G. W. — UMB5
Wiesenfeld, Jay M. — UMC
Wise, Frank W. — UTuE11
Wu, Hsiao-Hua — UMD3
- Xu, Z. — UMB5
- Yokoyama, Naoki — UMC3
Yusim, A. — UTuA2
- Zeng, A. — UTuE5
Zhang, X-C — UTuD5

**ULTRAFAST ELECTRONICS AND OPTOELECTRONICS
TECHNICAL PROGRAM COMMITTEE**

Umesh Mishra, *Conference Chair, University of California, Santa Barbara*

Martin Nuss, *Program Chair, AT&T Bell Laboratories*

Elliott Brown, *MIT Lincoln Laboratory*

Peter Delfyett, *CREOL*

Gadi Eisenstein, *TECHNION, Israel*

Dan Grischkowsky, *Oklahoma State University*

Erich Ippen, *MIT*

Tadao Ishibashi, *NTT, Japan*

Takeshi Kamiya, *University of Tokyo, Japan*

Ursula Keller, *Federal Institute of Technology, Switzerland*

Brian Kolner, *University of California, Los Angeles*

Heinrich Kurz, *RWTH, Aachen, Germany*

Ted Norris, *University of Michigan*

Yasuo Ohno, *NEC Corporation, Japan*

Mark Rodwell, *University of California, Santa Barbara*

Ran-Hong Yan, *AT&T Bell Laboratories*

**ULTRAFAST ELECTRONICS AND OPTOELECTRONICS
ADVISORY COMMITTEE**

David Bloom, *Stanford University*

Chi Lee, *University of Maryland*

Gerard Mourou, *University of Michigan*

Jagdeep Shah, *AT&T Bell Laboratories*

T.C.L.G. Sollner, *MIT Lincoln Laboratory*